FREIE UNIVERSITÄT BERLIN

CUMULATIVE DOCTORAL THESIS

EXHUMATION MECHANISMS OF MIDDLE AND LOWER CRUST IN THE WESTERN TAUERN WINDOW, EASTERN ALPS

Author:

Susanne SCHNEIDER

Supervisors:

Prof. Dr. Claudio L. ROSENBERG

Dr. Konrad HAMMERSCHMIDT

A thesis in fulfilment of the requirements for the degree of Doctor of Natural Sciences

in the

Department of Earth Sciences,

Institute of Geological Sciences

June, 2014

Declaration of Authorship

I, Susanne Schneider, declare that this thesis, 'EXHUMATION MECHANISMS OF MIDDLE AND LOWER CRUST IN THE WESTERN TAUERN WINDOW, EASTERN ALPS' and the work presented in it are my own. I confirm that:

This work was done wholly or mainly while in candidature for a research degree at the Freie Universität Berlin.

Where any part of this thesis has previously been submitted for a degree or any other qualification at the Freie Universität Berlin or any other institution, this has been clearly stated.

Where I have consulted the published work of others, this is always clearly attributed.

Where I have quoted from the work of others, the source is always given. With the exception of such quotations, this thesis is entirely my own work.

I have acknowledged all main sources of help.

Where the thesis is based on work done by myself jointly with others, I have made clear exactly in the section 'organization of the thesis' what was done by others and what I have contributed myself.

This work has been approved by the Doctoral Committee of the Department of Earth Sciences of the Freie Universistät Berlin. The Doctoral Committee allowed me to write this thesis in English language.

Primary Reviewer: Prof. Dr. Claudio L. Rosenberg (Université Pierre et Marie Curie Paris)

Secondary Reviewer: Prof. Dr. Harry Becker (Freie Universität Berlin)

Date of disputation: September 25, 2014, 2 pm

Place of disputation: Freie Universität Berlin, Malteserstraße 74-100, 12249 Berlin, Building C, lecture hall

Signed: _____

Date: _____

Place: _____

…Feeling and passion are best painted in, and roused by, ornamental and figurative language; but the reason and the understanding are best addressed in the simplest and most unvarnished phrase. Pure reason and dispassionate truth would be perfectly ridiculous in verse, as we may judge by versifying one of Euclid's demonstrations. This will be found true of all dispassionate reasoning whatever, and all reasoning that requires comprehensive views and enlarged combinations. It is only the more tangible points of morality, those which command assent at once, those which have a mirror in every mind, and in which the severity of reason is warmed and rendered palatable by being mixed up with feeling and imagination, that are applicable even to what is called moral poetry: and as the sciences of morals and of mind advance towards perfection, as they become more enlarged and comprehensive in their views, as reason gains the ascendancy in them over imagination and feeling, poetry can no longer accompany them in their progress, but drops into the back ground, and leaves them to advance alone. Thus the empire of thought is withdrawn from poetry…

Thomas Love Peacock, ‘The four ages of poetry’ 1820

Acknowledgements

Before getting to the core, there were many experienced and successful scientists that contributed with their fruitful discussions and impartial view to the subjects of this thesis. Many thanks to Prof. Harry Becker for accepting the invitation of becoming the secondary reviewer of this thesis. Special thanks to Prof. Lothar Ratschbacher for waiting patiently until the completion of this thesis and for including me into his team. Many thanks to Prof. Stefan Schmid who, although having a different opinion on important aspects of the thesis, carefully commented two of the manuscripts in a very final stage. Many thanks to Prof. Ralf Schuster, Dr. Hannah Pomella, Dr. Matthias Konrad-Schmolke who all took their precious time to correct manuscripts or parts of it constructively. During seminars and discussions several colleagues helped to look from other points of view to the subjects or to better carve out the implications of the results, special thanks to Dr. Ekkehard Scheuber, Prof. Christoph Heubeck and Prof. Mark R. Handy. This thesis presents new analytical data measured in various laboratories. Thanks to Dr. Ralf Milke, Dr. Masafumi Sudo, Dr. Axel Gerdes and Dr. Dirk Frei who spend their precious time in installation, maintenance and improvement of the used measuring instruments. The technical staff provided the infrastructure to do proper science. Thanks to Martina Grundmann computer facilities were maintained and constantly improved. Thanks to Anna Giribaldi, Christiane Behr and Christine Fischer beautiful thin sections and sample mounts were fabricated. Special thanks to Monika Feth for improving my clean-lab skills and for helping me to install a mineral separation laboratory. For field accommodation, for no board to pay, for sharing good knowledge of places and for transporting sometimes heavy samples I am grateful to family Fankhauser, especially Georg Fankhauser and family Schwärzer, especially Markus Schwärzer.

This study has been designed under the supervision of Claudio L. Rosenberg and Konrad Hammerschmidt. Both supervisors supported my field work on-site that took in summary twelve months. They introduced me to the problems of structural geology and geochronology in the working area and they both helped me fundamentally with the interpretation of key outcrops. Each of them in his own way taught me how to collect not only good but geological meaningful samples in both senses, geochronologically and structurally. Both of them had a very special, intuitive and polite way to ask the right questions, to search for the right rocks and outcrops and by that to enthuse me for the Tauern Window. Claudio L. Rosenberg deeply participated in all aspects concerning structural geology, microtectonics and metamorphic petrology. He gave many useful advices and also thoroughly reviewed all manuscripts over and over. He involved several MSc-, PhD-students and Post-Docs into the project enlarging the Tauern-team not only by staff but also by content. His additional scientific contributions published in the last years were indispensable and considerably facilitated the scientific discussion in this study. I gained advanced knowledge in structural mapping, fieldwork in general, micro-tectonics and scientific writing. Konrad Hammerschmidt was deeply involved in all aspects concerning geochronology, microtectonics and metamorphic petrology. He accompanied me on several measuring instruments, taught me technical understanding and took my anxiety of these black boxes. His wholesome skepticism and his sharp analytical understanding delivered the fundament to most of the analytical data presented. Not till he thoroughly reviewed, re-calculated and statistically tested the data they became robust and meaningful. I gained advanced knowledge in data treatment, instrumental handling and clean-lab skills. Not only in the field but also in the office, behind the microscope, in the laboratories, at measuring instruments, during discussions, at conferences or even while being afar in different cities and countries Konrad Hammerschmidt and Claudio L. Rosenberg tried to understand me, supported me, taught me and last but not least they were both the most kindest persons around. Now, when it is almost done, I can state that missing only one of them I would have quit but thanks

to their enduring believe in this study I finally became a structural geologist as well as a geochronologist. So, this is for you Konrad and Claudio!

First field session, valley head of the Krimmler-Ache, Tyrol, Austria, left: Claudio L. Rosenberg, right: Konrad Hammerschmidt

I am pleased to get to know very special people (PhD-, MSc-students and Post-Docs) at the FU Berlin. Many thanks for unforgettable times, fruitful discussions, constructive controversies and debugging trash-talks to Alessandro Airo, Audrey Bertrand, Nadin Bungies, Paola Crupi, Silvia Favaro, Olga Frisch, Franziska Frütsch, Sebastian Garcia, Peter Gipper, Phillip Groß, Mario Fischer-Gödde, Friedrich Hawemann, Fabian Hecht, Simon Hohl, Martin Homann, Cornelia M. Kitzig, Moritz Liesegang, Ralf Milke, Kai Rankenburg, Sami Nabhan, Manuel Quiring, Andreas Scharf, Katharina Schmidt, Marina Spanka, Xiaojuan Sun, Kamil Ustaszewski, Clemens Ullmann, David van Aacken, Christina von Nicolai, Monique Wanner, Uwe Wichert, Marc Weynell, Sandra Wollnik, Frank Wombacher and Corinna Wutzke.

Kurzfassung

Die vorliegende kumulative Dissertation mit dem Titel „EXHUMATION MECHANISMS OF MIDDLE AND LOWER CRUST IN THE WESTERN TAUERN WINDOW, EASTERN ALPS“ wurde von mir, Susanne Schneider, am Fachbereich Geowissenschaften, Institut für Geologische Wissenschaften der Freien Universität Berlin unter Leitung von Prof. Dr. Claudio L. Rosenberg und Dr. Konrad Hammerschmidt in englischer Sprache verfasst. Es handelt sich dabei um eine interdisziplinäre Arbeit die in den beiden Arbeitsbereichen (1) Tektonik, gehörend zur Fachrichtung Tektonik und Sedimentäre Geologie, und (2) Geochemie, gehörend zur Fachrichtung Geochemie, Hydrogeologie und Mineralogie, anzusiedeln ist. Die beiden Gutachter der Arbeit sind Prof. Dr. Claudio L. Rosenberg (Erstgutachter) und Prof. Dr. Harry Becker (Zweitgutachter).

Das Tauernfenster, ein tektonisches Fensters, ist seit über einem Jahrhundert Gegenstand geowissenschaftlicher Forschung. Im westlichen Tauernfenster wurden während des Känozoikums Gesteine der europäischen Unterkruste, die einst bis in eine Tiefe von >35 km versenkt wurden, durch tektonische Prozesse an die Erdoberfläche gebracht. Trotz eingehender Studien existiert eine lebendige Debatte darüber welche geologischen Prozesse welchen Beitrag zur Hebung und Exhumierung geleistet haben auch darüber wann und in welcher Reihenfolge die geologischen Ereignisse stattfanden. Das Tauernfenster nimmt eine Schlüsselrolle ein, von der die Tektonik der Ostalpen maßgeblich abhängt.

Diese Arbeit leistet einen strukturgeologischen und einen geochronologischen Beitrag zu dieser Debatte. Umfangreiche strukturgeologische Messungen wurden durchgeführt um die dominanten tektonischen Strukturen zu erfassen. Systematisch wurden stark und möglichst wenig verformte Proben genommen um mikrostrukturelle, petrologische und geochronologische Untersuchungen durchzuführen. Die stark verformten Proben wurden mit der $^{40}Ar/^{39}Ar$ in situ Methode datiert um das Alter der Verformung zu erfahren. Die wenig verformten Proben wurden mit Hilfe des U-Pb Apatit Geochronometers datiert um die Abkühlung der Gesteine der lokalisierten Verformung zeitlich gegenüberzustellen.

Die Ergebnisse dieser Studie zeigen, dass das westliche Tauernfenster durch einen transpressiven Gürtel aus aufrechten Falten und sinistralen Scherzonen im orogenen Maßstab verformt würde. Es bildet eine blockierende Krümmung bestehend aus einem Krustenstapel zwischen zwei alpinen Hauptstörungssystemen. Das Abkühlmuster der U-Pb Apatit Alter wiederspiegelt eine Domstrutur im Einklang mit früheren Studien. Neu ist, dass ein frühes Stadium der Abkühlung im Unteren Oligozän datiert wurde. Damit wird die Dauer der Abkühlung, folglich auch die der verursachenden Prozesse, erheblich verlängern. Die Langlebigkeit der sinistralen Scherzonen umfasst für alle

datierten Strukturen mehrere Millionen Jahre. Ihr Ende konnte in einigen Fällen genau erfasst werden. Lokalisierte Verformung entlang der sinistralen Scherzonen beginnt im gesamten westlichen Sub-dom zeitgleich mit der oben beschriebenen Abkühlung. Sie dauert bis ins Obere Miozän an und folgt dabei zeitlich der Abkühlung des Doms vom Rand zum Zentrum. Die sinistralen Scherzonen und damit der gesamte transpressive Gürtel des westlichen Tauernfensters dominieren dessen Heraushebung.

Abstract

The present cumulative dissertation titled “EXHUMATION MECHANISMS OF MIDDLE AND LOWER CRUST IN THE WESTERN TAUERN WINDOW, EASTERN ALPS” was written in English language by me, Susanne Schneider, under supervision of Prof. Dr. Claudio Rosenberg and Dr. Konrad Hammerschmidt at the Department of Earth Sciences, Institute of Geological Sciences of the Freie Universität Berlin. This work is interdisciplinary connecting the two fields of studies (1) Tectonics, belonging to the branch of study Tectonics and Sedimentary Geology, and (2) Geochemistry, belonging to the branch of study Geochemistry, Hydrogeology and Mineralogy. Reviewers of this thesis are Prof. Dr. Claudio L. Rosenberg (primary reviewer) and Prof. Dr. Harry Becker (secondary reviewer).

The Tauern Window, a tectonic window, is subject to research in earth sciences for more than a century. European lower crustal rocks of the western Tauern Window, once buried below 35 km, were uplifted and exhumed to surface level during Cenozoic times. Although it has been studied exhaustively there is a vital discussion which geological processes contributed in which amount to uplift and exhumation and also when and in which temporal succession these processes occurred. The Tauern Window plays a key role and is significantly involved into Eastern Alps tectonics.

This work supplies contributions in structural geology and geochronology to this discussion. Comprehensive structural field measurements were performed to determine the dominant structural features. A systematic sampling strategy was performed where highly and almost not deformed samples were collected for microstructural, petrological and geochronological investigations. The highly deformed samples were analyzed with the $^{40}Ar/^{39}Ar$ in situ technique to obtain deformation ages. The almost not deformed samples were analyzed with the U-Pb apatite geochronometer to contrast the cooling history of the rocks with the timing of localized deformation.

The results of this study show that the western Tauern Window was deformed by a transpressive belt consisting of upright folds and sinistral shear zones that has the scale of an orogen. It forms a restraining bend by crustal buckling between two major Alpine fault systems. The obtained cooling

pattern from the U-Pb apatite ages indicates a dome structure in agreement with earlier studies. The novel aspect is that an early stage of this cooling event in the Lower Oligocene epoch was dated. Hence, the duration of cooling and the driving processes causing it were substantially extended. The longevity of sinistral shear zones comprises for all dated structures several million years. The termination of those structures was precisely figured out in some cases. Localized deformation initiated within the entire western sub-dome contemporaneously to the cooling mentioned above. It continued until the Upper Miocene and followed the cooling of the dome from the margins to the center. The sinistral shear zones and for this reason the entire transpressive belt dominated the uplift and exhumation of the western Tauern Window.

Organization of the thesis and contributions of the authors and co-workers

This thesis is a "cumulative dissertation" and consists of six chapters where three of them are complete manuscripts either published, in review or submitted to international journals. These latter three chapters 2, 3, and 4 form the heart of the thesis. The following paragraph clarifies the contributions of the involved authors and indispensable co-workers. The remaining three chapters are enveloping text strings connecting the manuscript chapters and unify them to this complete works. The first chapter gives a short but general introduction, an overview of the aim of the thesis and the driving scientific questions. A comprehensive or chronological review of previously published literature was avoided. In the end a closing chapter summarized the complete works and carves out the main conclusions of this thesis. The last chapter gives an outlook and ideas for future research tying this thesis to either methodological, regional-geological or global projects.

Chapter 1: The western Tauern Window a natural laboratory, refining geology after more than a century of research

By Susanne Schneider

Chapter 2: Dating the longevity of ductile shear zones: Insight from $^{40}Ar/^{39}Ar$ in situ analyses

By Susanne Schneider, Konrad Hammerschmidt, Claudio L. Rosenberg

Published in Earth and Planetary Science Letters, 2013, 369. 43-58.

The first author did the field work and collected the samples analyzed in this study. She performed preparation of the samples together with the competent assistance of the staff preparators Christiane Behr (Freie Universität Berlin) and Christine Fischer (Universität Potsdam). The first author examined the samples by microscopy and performed electron microprobe analyses with the competent assistance of the lecture and research associate PD Dr. Ralf Milke (Freie Universität Berlin). The first author performed in situ $^{40}Ar/^{39}Ar$ analyses with the competent assistance of the research associate Dr. Massafumi Sudo (Universität Potsdam). The first author evaluated the results, documented and visualized them in the tables and figures with the competent assistance of the second author lecture and research associate (Akademischer Oberrat) Dr. phil. nat. Konrad Hammerschmidt (Freie Universität Berlin). The first author wrote and revised the text for the manuscript together with the aid of careful and constructive reviews of the third author Prof. Dr. habil. Claudio L. Rosenberg (Université Pierre et Marie Curie Paris) and the second author Dr. Konrad Hammerschmidt. The manuscript was peer-reviewed in a very final stage by the research associate Dr. Matthias Konrad-Schmolke (Universität Potsdam) and by Prof. Dr. Stefan Schmid (ETH Zürich, emerit. Prof. University of Basel).

Chapter 3: Translation of indentation into lateral extrusion across a restraining bend: The western Tauern Window, Eastern Alps

By Susanne Schneider, Claudio L. Rosenberg, Andreas Scharf, Konrad Hammerschmidt

Submitted to Tectonics and under review since 11th March 2014

The first author did the field work and collected the structural measurements presented in this study. The field work was supported by the expert knowledge of the second author Prof. Claudio L.

Rosenberg and of the forth author Dr. Konrad Hammerschmidt. The first author evaluated the results, documented and visualized them in the tables and figures together with the aid of careful and constructive reviews of the second author Prof. Claudio L. Rosenberg and the fourth author Dr. Konrad Hammerschmidt. The first author performed a comprehensive literature compilation of structural data for the western and central Tauern Window. This picture was completed by a comprehensive literature compilation of structural data from the eastern Tauern Window performed by the third author Dr. Andreas Scharf (Freie Universität Berlin). The first author wrote and revised the text for the manuscript together with the aid of careful and constructive reviews of the second author Prof. Claudio L. Rosenberg, the third author Dr. Andreas Scharf and the forth author Dr. Konrad Hammerschmidt. The manuscript was peer-reviewed in a very final stage by the lecture associate Dr. Hannah Pomella (Universität Innsbruck) and by Prof. Stefan Schmid. The first figure was peer-reviewed in a very final stage by the research associate Prof. Dr. Ralf Schuster (Geologische Bundesanstalt Österreich).

Chapter 4: U-Pb ages of apatite in the western Tauern Window (Eastern Alps): Tracing the onset of collision-related exhumation in the European plate

By Susanne Schneider, Axel Gerdes, Konrad Hammerschmidt, Claudio L. Rosenberg, Dirk Frei, Audrey Bertrand

Published in Earth and Planetary Science Letters, 2015, 418. 53-65.

The first author did the field work and collected the samples analyzed in this study. The first author installed a laboratory for mineral separation at the Institute of Geological Sciences, Freie Universität Berlin and trained three scientific assistants (Moritz Liesegang, Peter Gipper and Sandra Wollnik). Together the first author and the tree scientific assistants separated the heavy minerals that were analyzed in this study. The first author prepared the sample mounts with the competent assistance of staff preparator Christine Fischer and the aid of the scientific assistant Manuel Quiring (Freie Universität Berlin). The first author and the second author research associate Dr. Axel Gerdes (Goethe-Universität Frankfurt) performed analyses of apatites in Frankfurt. The second author Dr. Axel Gerdes evaluated, documented and visualized the apatite results in tables and figures. The first and the third author Dr. Konrad Hammerschmidt revised the apatite results, figures and tables carefully and constructively. The third author Dr. Konrad Hammerschmidt and the first author performed the statistical tests of the apatite results. The fifth author research associate Dr. Dirk Frei (Central Analytical Facility at Stellenbosch University) performed analyses of zircons in Stellenbosch, South Africa. The fifth author Dr. Dirk Frei evaluated, documented and visualized the zircon results in tables and figures. The first and the third author Dr. Konrad Hammerschmidt revised the zircon results, figures and tables carefully and constructively. The sixth author Dr. Audrey Bertrand (National Football Center, Paris) performed fission track dating of six of the samples used in this study. These results are published elsewhere but the results were used to calculate cooling rates by the first author. The first author wrote and revised the text for the manuscript together with the careful and constructive reviews of the fifth author Prof. Claudio L. Rosenberg and the third author Dr. Konrad Hammerschmidt.

Chapter 5: The dynamic evolution of the Tauern Window: A crustal scale expression of upper mantle dynamics

By Susanne Schneider

Chapter 6: What will be next?

By Susanne Schneider

Table of content

1. The western Tauern Window a natural laboratory, refining the geodynamics after more than a century of research

The linkage of structural geology and geochronology is a powerful tool to understand the tectonic evolution during orogeny. Both localized and distributed deformation may cause differential movement of crustal blocks and rearrange them in space and time. Two fundamentally different geochronological approaches exist to decipher the dynamics of mountain belts. The first approach is the determination of cooling ages. It is based on empirical studies where systematic age variations of geochronometers were observed depending on the crustal level they were exhumed from. It is formulated by the concept of the closure temperature (Dodsen, 1973), which describes the accumulation of radiogenic nuclides within a given mineral depending mainly on the surrounding temperature but also on cooling rate, crystal geometry, and grain size. Below a critical temperature the so-called closure temperature radiogenic nuclides cannot escape the crystal diffusively and homogenize with the surroundings, they start to accumulate within the crystal and the isotopic clock starts to tick. The second approach is the determination of formation ages. Minerals may form even below their closure temperature due to fluid infiltration, metamorphic breakdown reactions or recrystallization (Villa, 1988). If mineral formation is syn-kinematic to localized deformation the isotopic age of a mineral may date one instant of the deformation event. The decision whether an isotopic age is a cooling or a formation age requires additional information about metamorphism, petrology, mineral chemistry and microstructure. It is not a priori straightforward.

The second Chapter presents in situ $^{40}Ar/^{39}Ar$ ages obtained by texturally-controlled laser ablation and Rb/Sr ages (microsampling) of pre-, syn-, and post-kinematic minerals of sinistral mylonites and their undeformed host rocks from the western Tauern Window. The major syn-kinematic mineral is phengite which formed due to the breakdown of K-feldspar and it is absent in the host rocks. The Tauern Window over the years has risen to the status of a natural laboratory where various novel approaches have been tested. By using the laser ablation approach dating carefully characterized micro-fabrics we demonstrate the viability of a whole new concept of targeting micro-fabric for selective dating, and by this approach we tread new ground in the geochronology of metamorphic processes. The longevity of ductile shear zones is deduced from the age range of syn-kinematic minerals that show systematic spatial age variations. The cessation of these ductile shear zones is dated by post-kinematic blasts. The youngest syn-kinematic minerals and the post-kinematic blasts overlap within error suggesting that the post-kinematic blasts grew immediately after differential stress has released.

The third chapter presents a comprehensive structural analyses of the western Tauern Window which experienced in parts a different tectonic evolution compared to the central and eastern Tauern Window. Nearly 7,000 structural measurements of thirteen fabric elements were summarized and grouped into five domains. Three of these domains form a connected transpressive system of tight upright folds and sinistral shear zones. To the southwest this transpressive system connects with the sinistral transpressive Giudicarie Belt, towards the northeast it enters the sinistral transpressive-transtensive SEMP Fault and forms a restraining bend between them. The map-scale restraining bend translates Dolomites indentation (Rosenberg et al., 2004) into lateral extrusion (Ratschbacher et al., 1991) and decouples the central and eastern Tauern Window. The faults and shear zones in and around the western Tauern Window play a major key in palinspastic restoration of the Eastern Alps. Amounts of shortening, extension and displacement were calculated using the mean values of the structural fabrics obtained in this study and assuming simplified geometric relations. Upright folding accommodated two third of the shortening caused by Dolomites indentation and sinistral shear zones translated the remaining one third of the shortening into east-west extrusion.

The forth chapter presents U-Pb ages of apatites and zircons obtained by laser ablation analyses from three sections crossing the western Tauern Window. Zircon analyses yield concordant crystallization ages whereas apatite analyses show two age clusters. A considerable number of apatite analyses for each sample reflect a relatively uniform cluster of younger age values. We

applied an age extractor algorithm (Ludwig and Mundil, 2002) to all apatite analyses of each sample to calculate median ages from the younger age cluster and asymmetric 2σ errors as their uncertainties. The median ages were interpreted as cooling ages. A second cluster reveals age values scattering between the zircon crystallization ages and the apatite cooling ages and were interpreted to reflect partly reset age values. The unconventional U-Pb apatite chronometer (Harrison et al., 2002) has a closure temperature of ~450 °C (Chamberlain and Bowring, 2000) and therefore, it is appropriate to date the mid-range cooling history of the Tauern Window. Although various mid-range geochronometers like $^{40}Ar/^{39}Ar$ and Rb/Sr of white mica exist, scattering over a wide age range, their interpretation as cooling or formation age remains ambivalent. The spatial distribution of the mid-range cooling ages obtained in this study shows two younging trends that were observed in previous studies for geochronometers having lower closure temperatures (Luth and Willingshofer, 2008). Additionally, cooling rates were calculated uncovering a rather uniform cooling history of the western Tauern Window. By extrapolating the cooling rates until the thermal climax that the samples experienced (Bousquet et al., 2012) the timing of Barrovian metamorphism could be obtained. New time constraints on the cooling and exhumation history challenges earlier interpretations of fast exhumation and rapid cooling and may shed more light on the temporality of high-pressure and Barrovian metamorphism of neighboring rock units in the Tauern Window.

The fifth chapter summarizes the main results of the thesis. A holistic conclusion combining all three studies will be presented. They will be linked to recent geophysical findings that might give a hint of the driving forces for the structures of the western Tauern Window and Eastern Alps tectonics.

The closing sixth chapter gives an outlook based on the results of this study. Possible future research studies will be proposed.

2. Dating the longevity of ductile shear zones: Insight from $^{40}Ar/^{39}Ar$ in situ analyses

2.1 Highlights and article information

We analyzed two undeformed host rocks and eight mylonites at sub-millimeter-scale.

We examined pre-, syn- and post-kinematic minerals with the $^{40}Ar/^{39}Ar$ in situ technique.

We defined ablation modes obtaining either high spatial resolution or high precision.

We deduced the longevity of ductile shear by dating syn-kinematic minerals.

We determined the end of ductile deformation by dating post-kinematic minerals.

Article history: Received 16 August 2012

Received in revised form 28 February 2013

Accepted 1 March 2013

Editor: T.M. Harrison

doi:10.1016/j.epsl.2013.03.002

2.2 Keywords

deformation dating; duration and termination of ductile shear; Ar/Ar in-situ analyses; pre-, syn- and post-kinematic mineral growth

2.3 Abstract

We attempt to improve temporal constraints on the longevity and the termination of ductile shear zones by performing texturally-controlled in situ $^{40}Ar/^{39}Ar$ analyses of pre-kinematic muscovite, biotite and K-feldspars, of syn-kinematic phengite and K-feldspar, and of post-kinematic phengite within the same samples of sinistral shear zones from the western Tauern Window (Eastern Alps). Additionally two samples were dated by the Rb/Sr method (microsampling). Relative sequences of mineral formation based on microstructural, cross-cutting relationships were confirmed by in situ $^{40}Ar/^{39}Ar$ analyses, showing that syn-kinematic minerals are, in general, younger than pre-kinematic minerals and older or of equal age than the post-kinematic minerals of the same sample.

From the rim to the core of the western Tauern Window syn-kinematic phengite and K-feldspar reveal a set of formation ages varying between 33 and 15 Ma for the northernmost and peripheral shear zone (Ahorn Shear Zone), between 24 and 12 Ma for the intermediate shear zone network (Tuxer Shear Zones), and between 20 and 7 Ma for the southernmost and central shear zone (Greiner Shear Zone). The age variation of syn-kinematic phengite and K-feldspar analyses is larger than the analytical error of each age obtained. In addition, isochron calculations of the syn-kinematic minerals reveal atmospheric-like $^{40}Ar/^{36}Ar$ intercepts. Therefore, the obtained age values of the syn-kinematic minerals are interpreted as formation ages which date increments of a long lasting deformation period. The time range of deformation of each shear zone system is bracketed by the oldest and youngest formation ages of syn-kinematic phengite and K-feldspar.

Post-kinematic phengite laths show the youngest formation ages and overlap with the youngest syn-kinematic formation ages. This relationship indicates that post-kinematic growth occurred immediately after syn-kinematic mineral formation at the end of ductile sinistral shear. Hence, the termination of deformation is dated by the ages of these post-kinematic phengite blasts.

Pre-kinematic minerals are characterized by breakdown and exsolution reactions and their age values are heterogeneous and often affected by the presence of extraneous Ar. These age values are usually older than, but sometimes overlapping with, ages of the syn-kinematic minerals.

Using the temporal constraints obtained by the ages of pre-, syn-, and post-kinematic minerals, we could assess partly overlapping time intervals of syn-kinematic mineral formation of 19 Myr (33–15 Ma) in the Ahorn Shear Zone, 13 Myr (24–12 Ma) in the Tuxer Shear Zones and 14 Myr (20–7 Ma) in the Greiner Shear Zone. This indicates successive localization and propagation of ductile shear zones in the western Tauern Window from lower metamorphic sites at the rim towards higher metamorphic sites in the center.

2.4 Introduction

Deformation within mountain belts is largely accommodated within fault systems which decouple coherent crustal blocks and rearrange them in space and time. Constraining the duration of deformation within these fault systems is a prerequisite to determine rates of shortening and orogen-parallel extension. Crosscutting relations were used to obtain maximum ages of ductile deformation by dating magmatic rocks which are overprinted by shear zones (e.g. Crawford et al., 1987 and Davidson et al., 1992) or to obtain minimum ages of ductile deformation by dating magmatic rocks which overprint shear zones (e.g. Paterson and Tobisch, 1988). Alternatively, comparison of cooling ages on either side of faults (e.g. Hurford et al., 1989) was used to detect and date differential cooling, hence differential exhumation. However, the latter approach cannot be applied to strike-slip faults because horizontal displacements do not offset horizontal isotherms, and therefore, cooling-age patterns in adjacent blocks may not be different. In these cases metamorphic fabrics need to be dated, which display tectonic phases (e.g. Steiger, 1964). Accessory minerals like monazite, titanite, xenotime, and zircon from deformational fabrics may be dated with high analytical precision and high spatial resolution (e.g. Oberli et al., 2004, Resor et al., 1996 and Rubatto, 2002). However, attributing dated compositional domains of the metamorphic texture within such accessory minerals to given tectonic phases remains difficult (Getty and Gromet, 1992, Resor et al., 1996 and Williams et al., 1999). Garnets commonly form porphyroblasts in metamorphic rocks and due to their high strength garnets might exhibit helicitic structures that formed syn-kinematically during ductile shear whose segments can be dated applying microsampling techniques (e.g. Christensen et al., 1994, Pollington and Baxter, 2010; 2011). In contrast to heavy minerals, micas within mylonites are commonly deformed, well suited as kinematic and petrologic indicators, and present in most crustal rocks deformed under greenschist and amphibolite facies conditions (e.g. Freeman et al., 1997, Kligfield et al., 1986, Massonne and Kopp, 2005 and Rolland et al., 2008). Isotopic analyses of several generations of micas of multi-stage deformed rocks may date different stages of deformation, but may also result in mixing ages if classical mineral separation techniques were applied (e.g. Beltrando et al., 2009; Hunziker and Zingg, 1980). Microstructural and chemical characterization of the minerals prior to isotopic analyses may help to discriminate age groups (e.g. Beltrando et al., 2009).

Regional metamorphism is a prerequisite for recrystallization of minerals, that can reset their isotopic ages, but the sufficient condition for age resetting is intense fluid–rock interaction and complete removal of pre-metamorphic radiogenic Ar. However, in blueschist-facies rocks metamorphic minerals may form out of pre-metamorphic ones and can be affected by extraneous Ar caught within crystals or along grain boundaries that was not effectively discharged during metamorphism (e.g. Warren et al., 2012). Shear zones are suitable pathways for fluid flow to remove pre-kinematic radiogenic Ar (McCaig, 1997) and syn-kinematic mineral reactions. In most

shear zones where pre-kinematic micas are affected by grain size reduction, age values may vary as a function of the grains analyzed, becoming younger for smaller grain fractions (e.g. West and Lux, 1993). This effect can be ignored where white mica grew syn-kinematically within mylonites that formed from white mica-free protoliths (e.g. Dunlap, 1997 and Rolland et al., 2008). However, no matter how precisely single grains or mineral aggregates are dated, classical isotope techniques provide only one age value for a shear zone that may persist over tens of million years (e.g. Phillips et al., 2004). This limitation was partly overcome by the use of in situ dating techniques (Cliff and Meffan-Main, 2003 and Kelley et al., 1994), which allow selective dating of minerals embedded in their textural and petrological context (Mulch et al., 2005, Müller et al., 2000 and Wells et al., 2008) and by that provide spatial age resolution. Segments of strain fringes formed around pyrite clasts were dated and integrated to a continuous time interval of deformation, suggesting that their formation during deformation lasted 31 Ma (Müller et al., 2000). Decreasing intra-grain formation ages from core to rim of syn-kinematic white mica (Mulch et al., 2005) and garnet (Christensen et al., 1994, Pollington and Baxter, 2010; 2011) were interpreted as dating the duration of ductile deformation. These studies give minimum ages for deformation initiation and maximum ages for its termination, hence minimum durations of the deformation phase. The difference between this geochronologically-defined minimum time interval and the longer real time of deformation activity largely depends on the stability of the dated mineral during the shear zone longevity.

In order to refine the age resolution on the initiation and termination of deformation activity we present in situ $^{40}Ar/^{39}Ar$ data of mylonites whose fabrics are characterized by syn-kinematic phengite and K-feldspar but also by preserved pre-kinematic clasts of K-feldspar, biotite, and by post-kinematic phengite blasts. Dating the syn- and post-kinematic minerals within the same sample allowed us to constrain the duration and the termination of deformation activity. Using $^{40}Ar/^{36}Ar$ intercepts we were able to identify or exclude extraneous Ar, hence making these mylonites an excellent natural example to refine deformation dating. In two cases we additionally performed Rb/Sr in situ analyses using a microscope-stage mounted micro mill gadget for mineral preparation (Supplement), which confirmed the $^{40}Ar/^{39}Ar$ ages.

2.5 Geological setting

The Tauern Window is the largest tectonic window in the Eastern Alps, consisting of an E–W elongate metamorphic and structural dome, bordered by normal faults at its eastern and western ends and by strike-slip faults along its northern and southern boundaries (Fig. 1). The deeper structural units of the Tauern Window consist of Late Variscan granites and granodiorites, intruded into Paleozoic country rocks (Schmid et al., 2013). This basement was overprinted by several metamorphic events in Cenozoic, during Alpine subduction and collision (Schmid et al., 2013). Exhumation of the Tauern Window took place in Miocene (e.g. Luth and Willingshofer, 2008 and Rosenberg and Berger, 2009) by a combination of extensional unroofing (e.g. Selverstone, 1988) and folding and erosion (e.g. Rosenberg and Garcia, 2011).

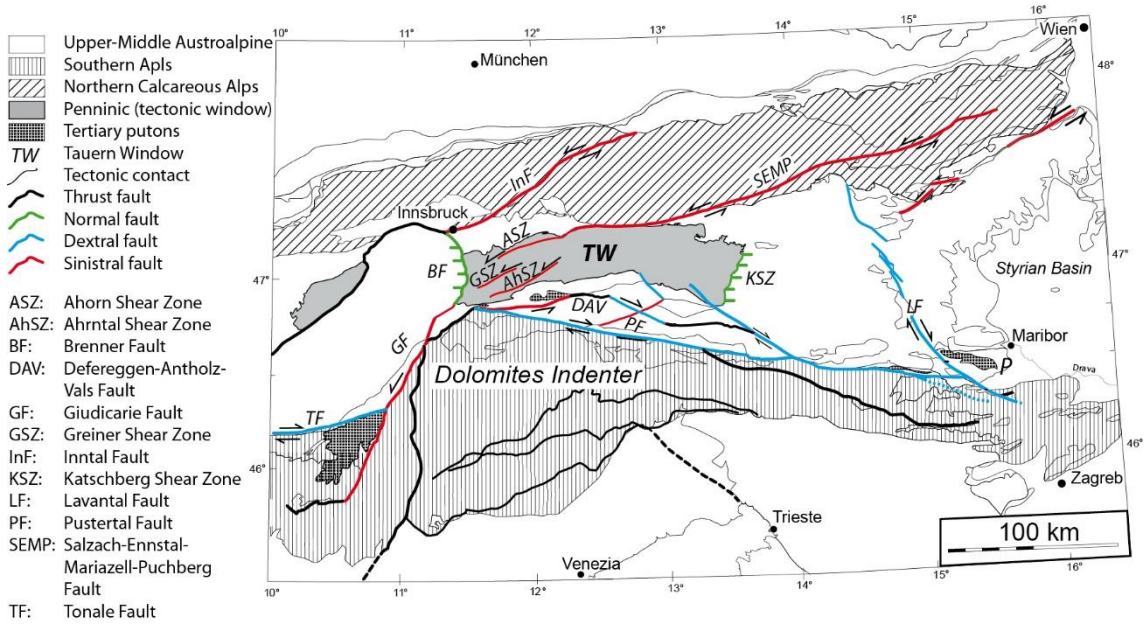

Figure 1: *Tectonic map of the Eastern Alps modified after Schmid et al., (2004). The major Cenozoic structures within and around the Tauern Window and the Dolomites Indenter are highlighted.*

The window is subdivided into an eastern WNW-striking and a western ENE-striking sub-dome (Fig. 2); the western sub-dome consists of three elongate upright antiforms which fold the nappe-contacts and the dominant Early-Alpine foliation. Locally a second sub-vertical axial plane foliation formed along steep limbs and within tight synclines of the upright folds. This foliation is co-genetic with large-scale and small-scale sinistral shear zones which are sub-parallel to the axial planes of the upright folds (Rosenberg and Schneider, 2008). The Early-Alpine foliation formed during north-vergent nappe stacking in Eocene (Kurz et al., 2008 and Schmid et al., 2004); whereas the second foliation resulted from folding and shearing of the nappe stack (Rosenberg and Schneider, 2008) in Oligocene and Miocene (Barnes et al., 2004, Glodny et al., 2008 and Selverstone et al., 1991). This second foliation within sinistral shear zones, contains phengite which is absent in the protolith, that are coarse grained and weakly foliated granites and granodiorites. The granites consist of *K-fsp+bt+plg+qtz±gnt* and sometimes muscovite forming 3–5 cm large clusters. The granodiorites consist of *plg+K-fsp+qtz+bt±zo* and are associated with 10–30 cm large mafic enclaves of biotite and amphibole.

In addition to four sinistral, ENE-striking, map-scale shear zones (Fig. 2), termed from N to S Ahorn Shear Zone, Olperer Shear Zone, Greiner Shear Zone, and Ahrntal Shear Zone, a large number of outcrop-scale sinistral shear zones occur in the central area of the western sub-dome suggesting the existence of an interconnected network that we term the Tuxer Shear Zones (Fig. 2). To the ENE all these shear zones merge into the sinistral SEMP fault (Fig. 2, Cole et al., 2007; Linzer et al., 2002; Rosenberg and Schneider, 2008), which accommodates lateral extrusion of the Eastern Alps (Ratschbacher et al., 1991). Given the parallelism between upright folds and sinistral shear zones, we consider that they formed in response to the same tectonic process, namely N–S shortening and orogen-parallel extension during late-stage collision. Both the cooling ages and the metamorphic isogrades of the western Tauern Window reflect an elongate, concentric pattern (Hoernes and Friedrichsen, 1974 and Luth and Willingshofer, 2008), whose longest axis coincides with the axial plane of the upright folds and with the slip planes of the sinistral shear zones. The Ahorn Shear Zone (Fig. 2), along the northern margin of the dome, formed under greenschist facies conditions (Cole et al., 2007 and Rosenberg and Schneider, 2008), the Tuxer Shear Zones under greenschist to amphibolite facies conditions, and the Greiner Shear Zone, located in the axial zone of the sub-dome, under amphibolite facies conditions (Selverstone et al., 1983 and Selverstone et al., 1991).

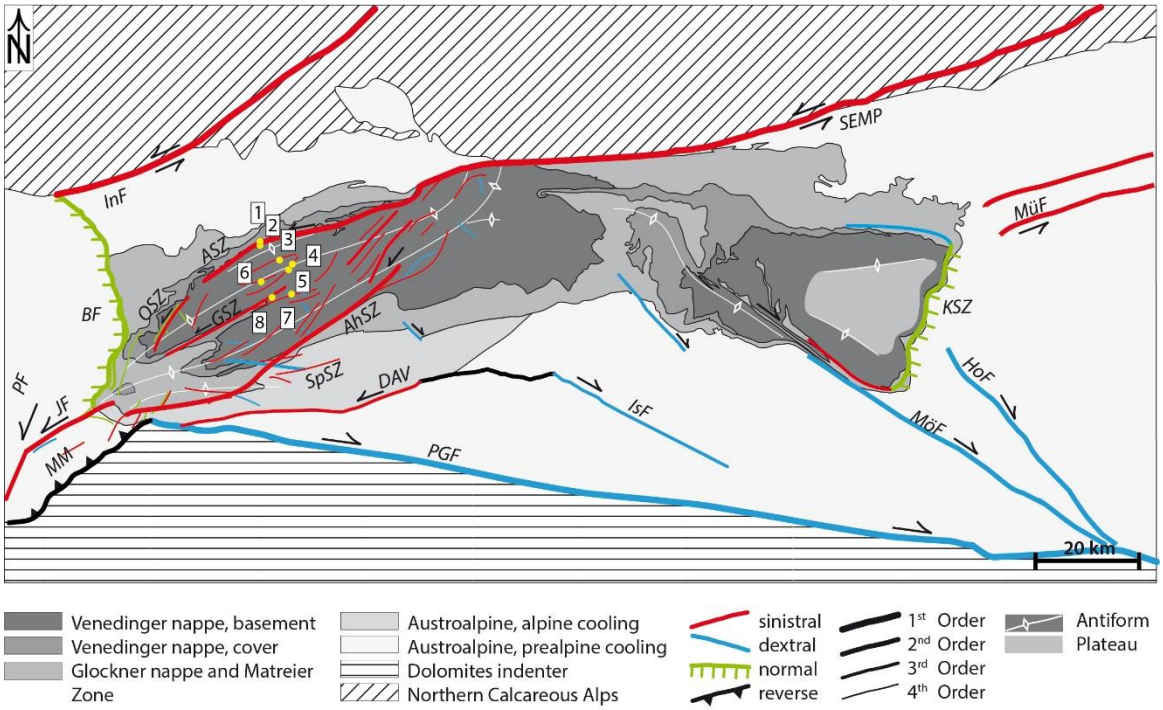

AhSZ=Ahrntal Shear Zone, *ASZ*=Ahorn Shear Zone, *BF*=Brenner Fault, *DAV*=Deferggen-Antholz-Vals Fault, *GSZ*=Greiner Shear Zone, *HoF*=Hochstuhl Fault, *InF*=Inntal Fault, *IsF*=Iseltal Fault, *JF*=Jaufen Fault, *KSZ*=Katschberg Shear Zone, *MM*=Meran-Maules Fault, *MöF*=Mölltal Fault, *MüF*=Mur-Müritz Fault, *OSZ*=Olperer Shear Zone, *PF*=Passeier Fault, *PGF*=Pustertal-Gailtal Fault, *SEMP*=Salzach-Ennstal-Puchberg-Mariazell Fault, *SpSZ*=Speikboden Shear Zone

Figure 2: *Tectonic map of the Tauern window, simplified after Bigi et al., (1990) modified after Schmid et al., (2013) showing the major Cenozoic faults and folds and the internal shear zone network of the western Tauern Window. Sample locations are marked with yellow dots and are also available as KML-file via Google Earth. Numbers correspond to the following samples: ST0559 (1), ST0505 (2), ST0732b and ST0734 (3), ST0730 (4), ST0727 and ST0728 (5), FT0728 (6), ST0706a (7) and FT0719 (8). Shear Zones are ordered according their mapped thickness 1st order ≥1 km, 2nd = 1000 to 100 m, 3rd order =100 – 10 m, 4th order ≤10 m.*

Previous Rb/Sr- and $^{40}Ar/^{39}Ar$-dating of micas of the sinistral shear zones resulted in ages varying between 35 and 15 Ma (Blanckenburg et al., 1989, Glodny et al., 2008 and Urbanek et al., 2002). Segments of one garnet porphyroblast, which was formed syn-kinematically within the Greiner Shear Zone (Selverstone et al., 1991), dated by the Sm/Nd method, cover the time interval of 28–20 Ma (Pollington and Baxter, 2010; 2011). This interval coincides with the age of cooling from higher than 550 °C (Most, 2003) to below 300 °C (Luth and Willingshofer, 2008) in the western Tauern Window. Therefore, most mineral ages, irrespective whether they derive from shear zones or host rocks, are expected to fall within this time interval. Therefore, establishing whether these ages date ductile deformation can only be successful by obtaining texturally-controlled ages (Müller, 2003).

2.6 $^{40}Ar/^{39}Ar$ methodology

The current investigation combined microstructural studies, in situ $^{40}Ar/^{39}Ar$ UV (ultra violet) LA (laser ablation) isotope analyses (Kelley et al., 1994, McDougall and Harrison, 1999 and Merrihue and Turner, 1966) and Rb/Sr in situ analyses. Numerous texturally-controlled in situ $^{40}Ar/^{39}Ar$ analyses were performed within 10 samples from the Ahorn Shear Zone, the Tuxer Shear Zones, the Greiner Shear Zone, and from their protoliths. The drilling locations of polished sections of 2 mm thickness, fixed on slides with thermoplastic glue, were chosen using a reflecting light

binocular. EMPA (electron microprobe analyses) were performed at each location using a JEOL JXA 8200 superprobe, results and technical explanations are summarized in Table 1.

Disc-shaped samples of Ø=1 cm were drilled with a gouge bit and detached from glass slides at 60 °C. Sample discs were cleaned from carbon coating by repeated polishing and from glue residues by solution in acetone for 24 h. After drying the sample discs were packed in aluminum foil, Cd-shielded, stacked in an Al N5 irradiation can, and irradiated with fast neutrons (neutron flux of 1×1012 n/cm^2/s) in Geestacht Neutron Facility for 97 h (e.g. Willner et al., 2009).

Samples were analyzed using the Ar isotope analytical facility system at the University of Potsdam. Suitable 6 mJ UV phase laser (wavelength 266 nm, frequency quadrupled) of a New Wave Gantry Dual Wave laser ablation system with an output rate of 80 % was used for sublimation of all minerals. Sample gas was cleaned within an ultrahigh vacuum purification line with a SAES getters and a cold trap. The gas was injected and analyzed in a Micromass 5400 noble gas mass spectrometer.

From each sample disc gas fractions of ablated phengite, biotite, K-feldspar, and/or sericitized albite were measured. Altogether 235 analyses were performed within the measuring session of 17 days, whereas blanks (B) were measured after three sample measurements (M) for background correction. For example: B_1–M_1–M_2–M_3–B_2–M_4–M_5–M_6–B_3, whereat M_1 was corrected with B_1, M_2 with the mean value ½(B_1+B_2) and M_3 and M_4 were corrected with B_2 using a Microsoft Excel spread sheet of M. Sudo, University of Potsdam. The measured ion intensities of the samples were always higher than those of the respective blanks, therefore, the corrected beam intensities, especially ^{36}Ar, were sometimes low but always positive. In particular, absolute ^{40}Ar contents of all blanks used for background correction vary between 2.5 and 37.3×10^{-12} cm^3 STP, and had an atmospheric-like ^{40}Ar/^{36}Ar, whereas absolute ^{40}Ar contents of the samples vary between 7.6 and 581.2×10^{-12} cm^3 STP (Table 2). However, due to small spot sizes and/or young age values the fraction of radiogenic Ar (^{40}Ar*) is sometimes <10 %; these 23 out of 142 results are given in brackets in Table 2. Since most of these analyses show ages which are similar to the ones of adjacent minerals with ^{40}Ar*>10%, they are also presented but their meaning will be discussed with caution.

Depending on the ablation mode used either a high precision or a high spatial resolution of the obtained age values was aspired. Four different ablation modes were carried out:

(a) Laser ablation along lines, raster (400–3000 µm length) or large spots (Ø≥100 µm) crossing grain aggregates were performed to obtain relative precise, integrated age values, however, with low spatial resolution.

(b) Small single spot analyses (Ø=30–50 µm) within syn-kinematic crystals performed with constant operating conditions were carried out to obtain age values with high spatial resolution. Special care was taken to locate the spots within individual crystals, avoiding grain boundaries, impurities, inclusions, and irregularities generated during sample preparation. Several measurements along sections within the same microstructural site were carried out to assess the repeatability and variance of the analyses.

(c) Large surface ablation (raster, large spots, curved lines) of or within single crystals was performed to maximize the ablation volume, hence to obtain age values with high precision.

(d) Ablations of several single spots within the same crystal were carried out to display intragrain variations of Ar isotopic composition with high spatial resolution (Mulch et al., 2005).

Four standards of Fish Canyon Tuff sanidine (fixed age of 27.5 Ma; Uto et al., 1997), used as neutron monitor, were stacked together with the sample discs vertically, upon each other in the irradiation can and analyzed by total fusion. The J-values for each sample were obtained by interpolation of these neutron monitors. The radial neutron fluence variation amounts to 2.6 %. The radial neutron fluence variation was estimated to be ∼1 % according to the pile geometry and additional eleven neutron monitors distributed in the irradiation can. For age comparison age

standards were analyzed before sample analyses. Four total fusion analyses of HDB-1 biotite yield a mean age of 25.0±1.4 Ma which agrees with 25.3±0.8 Ma (Fuhrmann et al., 1987). Four total fusion analyses of SORI93 biotite yield a mean age of 93.4±2.7 Ma which agrees with 92.6±0.6 Ma (Sudo et al., 1998).

2.7 Results

Table 1. Mean values and σ errors of Electron Microprobe Analyses

element oxides	n	K_2O	Na_2O	CaO	Al_2O_3	SiO_2	FeO	MgO	MnO	TiO_2	Total
Sample ST0732b, pre-kinematic muscovite											
mean	15	10.78	0.373	0.007	34.14	44.70	2.78	0.744	0.023	0.428	93.97
σ		0.13	0.082	0.013	0.42	0.34	0.15	0.072	0.013	0.068	0.44
Sample ST0734, syn-kinematic phengite											
mean	80	10.90	0.299	0.011	31.44	46.78	2.65	1.611	0.016	0.306	94.02
σ		0.18	0.062	0.020	0.40	0.32	0.18	0.090	0.015	0.038	0.44
Sample ST0730, pre-kinematic K-feldspar I											
mean	52	15.83	0.85	0.021	18.67	63.38	0.016	0.0050	0.010	0.007	98.79
σ		0.31	0.16	0.062	0.18	0.52	0.016	0.0063	0.012	0.011	0.53
Sample ST0730, syn-kinematic K-feldspar II											
mean	60	15.70	0.94	0.0130	18.32	63.40	0.013	0.0043	0.0059	0.012	98.40
σ		0.16	0.10	0.0093	0.12	0.38	0.016	0.0073	0.0074	0.014	0.41
Sample ST0559, pre-kinematic biotite											
mean	8	9.94	0.093	0.20	21.4	40.5	12.9	7.5	0.094	0.81	93.4
σ		0.83	0.035	0.24	3.4	2.5	3.7	2.0	0.039	0.22	1.4
Sample ST0732b, pre-kinematic biotite											
mean	16	9.57	0.058	0.23	18.25	35.06	24.60	4.62	0.408	2.67	95.47
σ		0.29	0.039	0.55	0.29	0.68	0.65	0.13	0.033	0.23	0.93
Sample FT0728, pre-kinematic biotite											
mean	6	7.57	0.084	0.018	16.41	28.01	25.48	6.39	0.185	3.92	88.07
σ		0.10	0.032	0.024	0.18	0.35	0.31	0.18	0.021	0.42	0.27
Sample ST0706a, syn-kinematic biotite											
mean	12	9.81	0.110	0.06	18.00	35.88	19.84	8.14	0.265	2.39	94.49
σ		0.41	0.042	0.14	0.17	0.41	0.21	0.18	0.031	0.12	0.91

atoms per formula	n	K	Na	Ca	Al	Si	Fe	Mg	Mn	Ti	Total
Sample ST0732b, pre-kinematic muscovite											
mean	15	0.939	0.049	0.0005	2.747	3.052	0.1586	0.0758	0.0013	0.0220	7.046
σ		0.015	0.011	0.0010	0.027	0.014	0.0090	0.0074	0.0007	0.0035	0.011
Sample ST0734, syn-kinematic phengite											
mean	80	0.947	0.0395	0.0008	2.524	3.186	0.151	0.1636	0.00092	0.0157	7.029
σ		0.015	0.0081	0.0015	0.031	0.016	0.010	0.0092	0.00086	0.0019	0.013
Sample ST0730, pre-kinematic K-feldspar I											
mean	52	0.947	0.077	0.0011	1.031	2.969	0.0006	0.00036	0.00039	0.00025	5.027
σ		0.040	0.028	0.0063	0.017	0.015	0.0012	0.00088	0.00093	0.00080	0.015
Sample ST0730, syn-kinematic K-feldspar II											
mean	60	0.941	0.085	0.00065	1.015	2.981	0.0005	0.0003	0.00023	0.00042	5.025
σ		0.023	0.018	0.00093	0.014	0.012	0.0013	0.0010	0.00059	0.00097	0.014
Sample ST0559, pre-kinematic biotite											
mean	8	0.937	0.0134	0.016	1.86	2.993	0.81	0.83	0.0060	0.045	7.51
σ		0.058	0.0052	0.019	0.24	0.086	0.25	0.25	0.0026	0.013	0.18
Sample ST0732b, pre-kinematic biotite											
mean	16	0.955	0.0088	0.020	1.682	2.743	1.609	0.538	0.0270	0.157	7.741
σ		0.021	0.0058	0.048	0.024	0.029	0.034	0.011	0.0022	0.015	0.013
Sample FT0728, pre-kinematic biotite											
mean	6	0.837	0.0142	0.0016	1.677	2.429	1.848	0.827	0.0136	0.256	7.903
σ		0.011	0.0055	0.0022	0.018	0.025	0.020	0.023	0.0016	0.027	0.016
Sample ST0706a, syn-kinematic biotite											
mean	12	0.966	0.0165	0.005	1.637	2.768	1.280	0.937	0.0173	0.1385	7.765
σ		0.034	0.0063	0.012	0.012	0.014	0.016	0.018	0.0021	0.0070	0.020

Notes: tungsten filament, beam current = 15 nA, acceleration voltage = 15 kV
natural standards of the FU Berlin were used for calibration:
sanidine (Al, K, Si), albite (Na), andesine (Ca), rutile (Ti), olivin (Fe, Mg), spessatite (Mn)

We use the term microstructural site, to define areas ≤1 cm^2 chosen for numerous $^{40}Ar/^{39}Ar$ analyses. These sites are characterized by a specific fabric element, which could be a clast with recrystallized grains in its pressure shadows, a shear band, a strain cap, or a post-kinematic blast.

2.7.1 Mineral reactions

Depending on the metamorphic facies of the investigated shear zones, we observed different mineral assemblages that we describe below. Syn-kinematic white micas within sheared samples consist of phengites that formed during the breakdown of biotite and K-feldspar according to the following reaction:

(1) K-fsp+bt+qtz+fluid=phe+ab

Muscovite, if any, is very rare and only occurs within the protolith. K-feldspar clasts (K-fsp I) selectively neo-/recrystallized into smaller K-feldspar grains (K-fsp II) of different major element compositions (Table 1, Fig. 10, Supplement).

2.7.2 Isotopic data

The results are presented as measured ^{40}Ar gas volumes, isotopic ratios, $^{40}Ar^*$, and calculated ages with their corresponding σ errors in Table 2. The J-value for each sample is given together with the sample identifier in the headings of each data set (Table 2). The amount of Ar released was corrected for blank, for interfering nuclides produced during irradiation, and for time elapsed after irradiation in a Microsoft Excel spread sheet programed by M. Sudo, University of Potsdam. All absolute errors are quoted at σ (confidence level=68.3 %). Numbers in the first left column of Table 2 relate the isotopic data to their analyzed microstructural sites in the corresponding sample figures (Figs. 3, 4, 5, 6, 7, 8). Analyses marked in the column "mineral" with the superscript suffix "iso" were used to calculate isochrons with the Isoplot add-in 3.41 (Ludwig, 2008). The $^{40}Ar/^{36}Ar$ intercepts are also shown in the respective sample headings (Table 2).

2.7.3 Isochron calculations

The main focus applying isochron calculation in this study was shifted from yielding new, reliable age information of the dated minerals, since there is no substantial gain in this age information, to rather testing whether the individual age values were affected by extraneous Ar. We considered the isochron age performed with age data of minerals from the same microstructural site as reliable if this isochron age agrees with the single age data used and if the $^{40}Ar/^{36}Ar$ intercept defined by the isochron reflects an atmospheric-like Ar composition. For this reason we selected those age values for isochron calculation which overlap within error and therefore, have similar $^{40}Ar^*/^{39}Ar_K$ values. The $^{40}Ar/^{36}Ar$ intercept of the isochron enables us to test for the presence of extraneous Ar (Kelley, 2002). If the $^{40}Ar/^{36}Ar$ intercept reflects an atmospheric-like Ar composition, we assume that the same was true for the remaining syn-kinematic minerals of the same microstructural site that were not taken into account for isochron calculation because of their different $^{40}Ar^*/^{39}Ar_K$ ratio.

Table 2. Results of $^{40}Ar/^{39}Ar$ In-Situ Laser Probe Analysis

No	Mineral	Mode, Ø and ~length (μm)	$^{40}Ar \times 10^{-12}$ (cm^3)	$^{40}Ar/^{39}Ar \pm \sigma$	$^{38}Ar/^{39}Ar \pm \sigma$	$^{37}Ar/^{39}Ar \pm \sigma$	$^{36}Ar/^{39}Ar \pm \sigma$	$^{40}Ar^*$ (%)	$^{40}Ar^*/^{39}Ar_K \pm \sigma$	Age ± σ (Ma)
				Sample ST0730 (J = 0.001729)						
1	bt	cL, 40, ~250	61.4	50.5 ± 0.4	0.040 ± 0.003	3.2 ± 2.6	0.117 ± 0.005	31.5	15.9 ± 1.5	48.9 ± 4.6
2	bt	cL, 20, ~350	40.6	21.3 ± 0.2	0.025 ± 0.002	1.5 ± 2.1	0.056 ± 0.004	22.8	4.9 ± 1.2	15.1 ± 3.6
3	bt	L, 40, ~100	28.5	52.0 ± 1.3	0.138 ± 0.009	7.2 ± 10.2	0.070 ± 0.012	56.0	31.2 ± 3.6	95 ± 11
5	bt	L, 40, ~400	50.1	21.4 ± 0.1	0.027 ± 0.001	2.1 ± 0.7	0.039 ± 0.000	46.0	9.9 ± 0.1	30.5 ± 0.4
6	bt	Ls, 35, ~400	37.5	28.5 ± 0.2	0.019 ± 0.005	0.0 ± 3.0	0.059 ± 0.004	39.1	11.1 ± 1.1	34.4 ± 3.4
7	bt	L, 50, ~350	65.3	25.5 ± 0.1	0.029 ± 0.001	1.2 ± 0.3	0.059 ± 0.002	31.5	8.0 ± 0.4	24.9 ± 1.4
8	bt	L, 40, ~450	54.2	25.4 ± 0.2	0.031 ± 0.002	0.0 ± 1.6	0.056 ± 0.002	34.3	8.7 ± 0.6	27.0 ± 2.0
9	bt	Ls, 20, ~250	66.7	66.4 ± 0.3	0.038 ± 0.006	0.9 ± 3.2	0.133 ± 0.005	40.8	27.1 ± 1.4	82.7 ± 4.2
10	k-fsp	cL, 40, ~300	45.3	21.6 ± 0.2	0.025 ± 0.003	2.2 ± 1.0	0.038 ± 0.003	48.6	10.5 ± 0.8	32.5 ± 2.5
11	k-fsp	cL, 75, ~300	56.7	9.4 ± 0.0	0.020 ± 0.000	0.5 ± 0.3	0.012 ± 0.001	62.0	5.8 ± 0.2	18.0 ± 0.7
12	k-fsp	cL, 40, ~550	78.8	11.9 ± 0.0	0.019 ± 0.000	0.2 ± 0.2	0.016 ± 0.000	59.8	7.1 ± 0.1	22.1 ± 0.4
13	k-fsp	cL, 40, ~250	52.3	15.6 ± 0.1	0.018 ± 0.001	0.4 ± 0.6	0.018 ± 0.001	66.3	10.3 ± 0.4	31.9 ± 1.3
14	k-fsp	cL, 50, ~500	94.7	12.3 ± 0.0	0.019 ± 0.000	0.0 ± 0.3	0.015 ± 0.000	62.9	7.7 ± 0.1	23.9 ± 0.3
15	k-fsp	R, 40, ~1200	58.2	16.8 ± 0.1	0.023 ± 0.001	0.2 ± 0.5	0.020 ± 0.001	64.7	10.9 ± 0.3	33.5 ± 1.0
16	k-fsp	R, 70, ~720	72.1	23.1 ± 0.1	0.023 ± 0.002	0.0 ± 0.6	0.026 ± 0.001	66.8	15.4 ± 0.3	47.4 ± 1.0
17	k-fsp	S, 75	49.5	24.9 ± 0.2	0.019 ± 0.002	0.0 ± 1.1	0.030 ± 0.003	64.6	16.1 ± 0.9	49.4 ± 2.6
				Sample ST0505 (J = 0.001723), bt^{iso} $^{40}Ar/^{36}Ar$ intercept = 298.9 ± 9.4, isochron age = 25.2 ± 8.8 Ma						
1	bt	S, 50	52.6	41.2 ± 0.3	0.038 ± 0.003	0.0 ± 2.2	0.106 ± 0.003	23.8	9.8 ± 1.0	30.2 ± 3.0
2	bt	S, 50	33.9	32.4 ± 0.3	0.031 ± 0.002	0.0 ± 2.3	0.060 ± 0.003	44.9	14.5 ± 0.9	44.6 ± 2.6
3	bt	S, 50	22.7	51.7 ± 1.0	0.026 ± 0.010	0.1 ± 6.7	0.121 ± 0.016	30.6	15.8 ± 4.8	46 ± 15
(4)	(bt^{iso})	(S, 50)	(145.6)	(144.6 ± 0.8)	(0.106 ± 0.003)	(0.0 ± 1.5)	(0.453 ± 0.005)	(7.5)	(10.8 ± 1.3)	(33.2 ± 4.1)
(5)	(bt^{iso})	(S, 50)	(98.4)	(98.6 ± 1.0)	(0.076 ± 0.003)	(1.6 ± 1.5)	(0.304 ± 0.004)	(8.8)	(8.7 ± 0.8)	(26.8 ± 2.4)
6	bt^{iso}	S, 50	37.0	41.2 ± 0.2	0.043 ± 0.003	2.5 ± 2.4	0.111 ± 0.006	20.0	8.2 ± 1.7	25.4 ± 5.1
7	bt^{iso}	S, 50	50.8	89.5 ± 1.1	0.066 ± 0.004	7.5 ± 3.7	0.272 ± 0.011	10.3	9.2 ± 3.0	28.4 ± 9.2
8	bt^{iso}	S, 50	33.5	26.2 ± 0.2	0.025 ± 0.003	1.6 ± 1.8	0.056 ± 0.005	36.6	9.6 ± 1.4	29.6 ± 4.3
9	bt	S, 50	39.6	19.6 ± 0.1	0.017 ± 0.001	0.0 ± 1.1	0.016 ± 0.002	75.8	14.8 ± 0.7	45.6 ± 2.0
10	bt	S, 50	33.9	21.2 ± 0.1	0.029 ± 0.001	0.0 ± 2.2	0.031 ± 0.003	56.3	11.9 ± 1.0	36.7 ± 2.9
11	bt	S, 50	49.5	21.3 ± 0.1	0.024 ± 0.001	0.0 ± 1.4	0.027 ± 0.002	62.8	13.4 ± 0.6	41.0 ± 1.9
12	phe	S, 40	38.4	39.4 ± 0.3	0.034 ± 0.003	0.0 ± 2.1	0.099 ± 0.003	25.7	10.1 ± 1.0	31.3 ± 3.1
13	phe	S, 40	31.7	13.5 ± 0.1	0.019 ± 0.002	0.0 ± 1.3	0.019 ± 0.001	58.2	7.9 ± 0.4	24.3 ± 1.2
14	phe	S, 40	23.4	9.7 ± 0.1	0.015 ± 0.001	0.0 ± 1.1	0.010 ± 0.001	70.1	6.8 ± 0.4	21.0 ± 1.3
15	phe	S, 40	27.3	11.0 ± 0.1	0.020 ± 0.002	0.0 ± 0.9	0.015 ± 0.003	59.6	6.6 ± 1.0	20.3 ± 3.0
16	phe	S, 40	26.8	10.6 ± 0.1	0.020 ± 0.002	0.6 ± 1.2	0.014 ± 0.003	60.3	6.4 ± 0.9	19.7 ± 2.9
17	phe	S, 40	38.8	16.1 ± 0.1	0.020 ± 0.001	0.0 ± 0.8	0.019 ± 0.002	65.5	10.6 ± 0.7	32.6 ± 2.2
19	phe	S, 100	39.6	17.6 ± 0.1	0.025 ± 0.001	0.0 ± 1.0	0.031 ± 0.002	48.8	8.6 ± 0.6	26.6 ± 2.0
				Sample ST0559 (J = 0.001722), phe^{iso} $^{40}Ar/^{36}Ar$ intercept = 296 ± 23, isochron age = 19.9 ± 7.1 Ma						
1	phe	S, 35	50.2	32.2 ± 0.5	0.027 ± 0.008	0.0 ± 2.8	0.092 ± 0.010	15.9	5.1 ± 3.0	15.9 ± 9.3
2	phe	L, 40, ~300	64.0	12.2 ± 0.1	0.022 ± 0.001	0.0 ± 0.5	0.031 ± 0.001	26.2	3.2 ± 0.5	9.9 ± 1.4
3	k-fsp	S, 40	92.2	29.3 ± 0.3	0.020 ± 0.002	1.3 ± 0.7	0.040 ± 0.003	60.0	17.6 ± 0.8	53.9 ± 2.4
4	phe	L, 35, ~220	58.8	31.5 ± 0.3	0.033 ± 0.003	0.4 ± 1.7	0.092 ± 0.004	13.8	4.3 ± 1.1	13.4 ± 3.5
5	k-fsp	L, 100, ~500	125.8	39.4 ± 0.3	0.032 ± 0.002	0.1 ± 0.6	0.085 ± 0.003	36.2	14.3 ± 0.9	43.8 ± 2.9
(6)	(ab)	(S, 50)	(83.4)	(60.7 ± 0.7)	(0.062 ± 0.006)	(0.0 ± 1.3)	(0.195 ± 0.006)	(5.3)	(3.2 ± 1.6)	(10.0 ± 4.9)
(7)	(phe)	(L, 35, ~260)	(77.8)	(48.3 ± 0.3)	(0.044 ± 0.005)	(0.3 ± 1.2)	(0.155 ± 0.003)	(5.1)	(2.5 ± 0.8)	(7.7 ± 2.6)
8	k-fsp	S, 35	56.7	47.7 ± 0.5	0.042 ± 0.009	0.0 ± 2.6	0.137 ± 0.004	15.2	7.3 ± 1.2	22.4 ± 3.8
(9)	(phe)	(S, 35)	(109.5)	(104.3 ± 0.5)	(0.079 ± 0.007)	(0.6 ± 1.7)	(0.336 ± 0.006)	(4.9)	(5.1 ± 1.9)	(15.7 ± 5.8)
(11)	(phe^{iso})	(S, 30)	(71.3)	(89.3 ± 1.1)	(0.073 ± 0.006)	(0.0 ± 2.5)	(0.276 ± 0.012)	(8.6)	(7.7 ± 3.5)	(24 ± 11)
12	phe^{iso}	S, 30	63.3	58.2 ± 0.4	0.053 ± 0.006	2.7 ± 2.1	0.173 ± 0.006	12.0	7.0 ± 1.8	21.5 ± 5.6
13	phe^{iso}	S, 30	46.2	31.4 ± 0.4	0.038 ± 0.006	3.3 ± 2.1	0.080 ± 0.007	24.8	7.8 ± 1.9	24.0 ± 5.9
14	phe^{iso}	S, 30	36.3	16.7 ± 0.2	0.026 ± 0.006	1.7 ± 2.1	0.030 ± 0.005	47.2	7.9 ± 1.6	24.3 ± 4.8
15	phe^{iso}	S, 30	41.0	23.2 ± 0.3	0.042 ± 0.005	0.0 ± 1.7	0.056 ± 0.004	28.3	6.5 ± 1.3	20.2 ± 4.1
16	phe^{iso}	S, 30	44.6	22.3 ± 0.3	0.019 ± 0.003	0.0 ± 1.9	0.056 ± 0.006	26.1	5.8 ± 1.9	18.1 ± 5.9
17	phe^{iso}	S, 30	47.6	30.5 ± 0.7	0.028 ± 0.004	0.0 ± 2.7	0.081 ± 0.006	21.6	6.6 ± 1.7	20.3 ± 5.3
18	phe^{iso}	S, 30	46.6	40.0 ± 0.5	0.050 ± 0.005	1.4 ± 3.2	0.119 ± 0.006	12.3	4.9 ± 1.8	15.2 ± 5.4
19	phe^{iso}	S, 30	34.3	20.1 ± 0.3	0.023 ± 0.006	0.6 ± 2.7	0.047 ± 0.005	30.9	6.2 ± 1.6	19.1 ± 4.8
20	phe	S, 30	34.8	23.1 ± 0.3	0.035 ± 0.005	0.4 ± 3.0	0.048 ± 0.007	38.6	8.9 ± 2.1	27.5 ± 6.4
22	bt	S, 30	36.9	24.6 ± 0.3	0.030 ± 0.006	0.0 ± 3.2	0.050 ± 0.006	39.6	9.7 ± 1.8	30.0 ± 5.5
23	bt	S, 50	36.8	22.4 ± 0.3	0.027 ± 0.005	6.7 ± 2.7	0.046 ± 0.005	39.2	8.8 ± 1.6	27.1 ± 5.0
24	bt	L, 20, ~150	46.6	33.1 ± 0.3	0.031 ± 0.005	0.0 ± 2.1	0.070 ± 0.005	37.3	12.4 ± 1.5	38.0 ± 4.5

No	Mineral	Mode, Ø and length (µm)	$^{40}Ar \times 10^{-12}$ (cm^3)	$^{40}Ar/^{39}Ar \pm \sigma$	$^{38}Ar/^{39}Ar \pm \sigma$	$^{37}Ar/^{39}Ar \pm \sigma$	$^{36}Ar/^{39}Ar \pm \sigma$	$^{40}Ar^*$ (%)	$^{40}Ar^*/^{39}Ar_K \pm \sigma$	Age ± σ (Ma)
				Sample ST0734 (J = 0.001724), phe^{iso} $^{40}Ar/^{36}Ar$ intercept = 296 ± 36, isochron age = 12.3 ± 4.3 Ma						
1	phe^{iso}	R, 50, ~2200	85.8	17.5 ± 0.2	0.024 ± 0.001	0.5 ± 0.4	0.046 ± 0.001	22.7	4.0 ± 0.3	12.4 ± 1.0
2	phe	L, 75, ~900	77.8	9.0 ± 0.1	0.022 ± 0.001	0.3 ± 0.2	0.014 ± 0.001	54.8	4.9 ± 0.2	15.2 ± 0.7
3	phe	S, 50	35.4	8.0 ± 0.2	0.027 ± 0.001	1.7 ± 1.1	0.004 ± 0.002	86.7	7.0 ± 0.6	21.5 ± 1.7
4	phe^{iso}	S, 50	28.5	6.3 ± 0.4	0.010 ± 0.002	0.1 ± 1.4	0.007 ± 0.003	66.1	4.2 ± 0.9	12.9 ± 2.8
5	phe^{iso}	S, 50	27.5	5.8 ± 0.5	0.020 ± 0.003	1.4 ± 1.6	0.007 ± 0.002	65.6	3.8 ± 0.9	11.8 ± 2.7
6	phe^{iso}	S, 50	28.4	6.3 ± 0.4	0.013 ± 0.003	0.8 ± 1.8	0.008 ± 0.003	61.3	3.9 ± 1.0	12.0 ± 3.0
7	phe^{iso}	S, 50	45.2	11.8 ± 0.3	0.016 ± 0.002	1.0 ± 1.0	0.026 ± 0.002	34.9	4.1 ± 0.6	12.7 ± 1.9
8	phe	S, 50	44.9	13.8 ± 0.3	0.029 ± 0.001	0.3 ± 1.3	0.027 ± 0.002	43.0	5.9 ± 0.6	18.3 ± 1.8
9	phe	R, 40, ~1400	60.7	12.8 ± 0.1	0.015 ± 0.002	0.4 ± 0.7	0.018 ± 0.001	58.4	7.5 ± 0.4	23.1 ± 1.2
10	phe	L, 100, ~1000	59.5	17.4 ± 0.3	0.023 ± 0.001	0.5 ± 1.1	0.039 ± 0.003	33.3	5.8 ± 0.9	17.9 ± 2.7
11	bt	L, 50, ~400	46.5	12.7 ± 0.1	0.024 ± 0.001	0.0 ± 0.7	0.025 ± 0.002	41.1	5.2 ± 0.4	16.1 ± 1.4
12	bt	L, 40, ~60	27.8	37.2 ± 0.7	0.020 ± 0.004	5.0 ± 4.7	0.090 ± 0.008	28.6	10.7 ± 2.3	32.8 ± 7.0
13	bt	Ls, 20, ~150	60.4	68.3 ± 0.6	0.047 ± 0.005	2.1 ± 2.9	0.155 ± 0.005	32.8	22.4 ± 1.6	68.5 ± 4.8
15	ab	R, 50, ~3000	43.8	65.7 ± 1.1	0.043 ± 0.007	0.0 ± 3.4	0.199 ± 0.006	10.4	6.8 ± 1.7	21.1 ± 5.2
				Sample ST0732b (J = 0.001726)						
1	ms	cL, 35, ~200	57.1	20.7 ± 0.1	0.022 ± 0.002	0.4 ± 0.6	0.042 ± 0.001	40.0	8.3 ± 0.4	25.5 ± 1.4
2	bt	cL, 50, ~400	114.6	24.1 ± 0.1	0.038 ± 0.001	0.2 ± 0.4	0.064 ± 0.001	21.9	5.3 ± 0.2	16.4 ± 0.6
3	k-fsp	cL, 50, ~300	106.0	34.0 ± 0.3	0.023 ± 0.002	0.1 ± 0.5	0.035 ± 0.001	70.0	23.8 ± 0.5	72.6 ± 1.4
4	k-fsp	cL, 50, ~250	52.6	12.3 ± 0.0	0.019 ± 0.001	0.1 ± 0.5	0.020 ± 0.001	51.4	6.3 ± 0.4	19.6 ± 1.2
5	bt	cL, 40, ~900	83.4	15.5 ± 0.0	0.029 ± 0.001	1.1 ± 1.0	0.030 ± 0.001	43.2	6.7 ± 0.3	20.8 ± 0.8
6	ms	cL, 40, ~800	58.5	10.7 ± 0.1	0.018 ± 0.002	0.2 ± 0.6	0.012 ± 0.001	66.3	7.1 ± 0.4	21.9 ± 1.2
7	bt	R, 40, ~1200	180.1	35.1 ± 0.2	0.042 ± 0.001	0.0 ± 0.4	0.104 ± 0.001	12.7	4.5 ± 0.2	13.8 ± 0.8
8	ms	R, 30, ~600	77.1	18.5 ± 0.1	0.029 ± 0.001	1.0 ± 0.7	0.035 ± 0.001	44.6	8.3 ± 0.3	25.6 ± 0.8
9	k-fsp	cL, 40, ~450	89.4	35.4 ± 0.3	0.025 ± 0.002	0.0 ± 0.7	0.035 ± 0.001	71.2	25.2 ± 0.5	76.9 ± 1.4
10	k-fsp	S, 35	37.7	32.7 ± 0.3	0.020 ± 0.005	0.0 ± 2.8	0.032 ± 0.004	71.1	23.3 ± 1.3	71.1 ± 4.0
11	k-fsp	S, 200	87.5	191.6 ± 2.8	0.099 ± 0.006	0.0 ± 3.3	0.436 ± 0.012	32.7	62.7 ± 3.1	185.3 ± 8.7
13	bt	cL, 40, ~550	71.6	25.3 ± 0.1	0.032 ± 0.003	0.3 ± 0.8	0.065 ± 0.002	24.7	6.3 ± 0.7	19.4 ± 2.2
14	ms	cL, 50, ~500	76.9	15.1 ± 0.1	0.020 ± 0.002	0.0 ± 0.3	0.014 ± 0.001	72.5	11.0 ± 0.3	33.8 ± 1.0
				Sample FT0728 (J = 0.001728), phe^{iso} $^{40}Ar/^{36}Ar$ intercept = 295 ± 25, isochron age = 15.1 ± 2.4 Ma						
(1)	(phe)	(S, 50)	(92.2)	(42.4 ± 0.3)	(0.045 ± 0.002)	(1.7 ± 1.3)	(0.131 ± 0.005)	(8.8)	(3.7 ± 1.4)	(11.6 ± 4.2)
2	phe^{iso}	S, 50	72.2	31.3 ± 0.3	0.033 ± 0.002	0.3 ± 1.4	0.090 ± 0.003	15.4	4.8 ± 0.9	14.9 ± 2.7
3	phe	S, 50	42.6	10.2 ± 0.1	0.019 ± 0.002	0.0 ± 1.1	0.008 ± 0.002	77.1	7.8 ± 0.6	24.2 ± 1.8
4	phe	S, 50	41.1	14.0 ± 0.1	0.018 ± 0.002	1.3 ± 1.6	0.024 ± 0.003	48.9	6.9 ± 0.9	21.2 ± 2.6
5	phe^{iso}	S, 50	29.3	10.9 ± 0.1	0.019 ± 0.004	0.7 ± 1.7	0.021 ± 0.003	44.2	4.8 ± 0.9	15.0 ± 2.9
6	phe^{iso}	S, 50	37.1	10.9 ± 0.2	0.015 ± 0.001	0.0 ± 0.8	0.020 ± 0.002	46.8	5.1 ± 0.5	15.8 ± 1.6
7	phe^{iso}	S, 50	33.7	8.2 ± 0.1	0.005 ± 0.001	0.0 ± 1.2	0.010 ± 0.002	64.4	5.3 ± 0.5	16.5 ± 1.5
8	phe	S, 150	33.7	7.9 ± 0.2	0.016 ± 0.003	0.0 ± 1.0	0.017 ± 0.002	37.7	3.0 ± 0.5	9.3 ± 1.7
9	bt	cL, 40, ~500	49.5	16.2 ± 0.2	0.031 ± 0.003	0.0 ± 1.1	0.047 ± 0.003	13.6	2.2 ± 0.8	6.9 ± 2.6
10	bt	cL, 50, ~800	69.0	30.7 ± 0.2	0.037 ± 0.001	0.0 ± 1.1	0.093 ± 0.002	10.3	3.2 ± 0.7	9.8 ± 2.2
11	bt	cL, 50, ~300	74.0	17.2 ± 0.1	0.028 ± 0.001	0.0 ± 0.4	0.047 ± 0.001	19.6	3.4 ± 0.3	10.5 ± 0.9
12	phe^{iso}	L, 75, ~850	69.2	10.6 ± 0.0	0.017 ± 0.001	0.0 ± 0.3	0.020 ± 0.001	43.1	4.6 ± 0.3	14.1 ± 0.9
13	bt	R, 40, ~400	85.4	27.5 ± 0.2	0.038 ± 0.002	0.0 ± 0.5	0.076 ± 0.002	17.9	4.9 ± 0.5	15.2 ± 1.5
16	k-fsp	R, 50, ~400	78.0	10.4 ± 0.1	0.022 ± 0.001	0.0 ± 0.2	0.019 ± 0.001	45.5	4.7 ± 0.2	14.7 ± 0.8
18	phe^{iso}	L, 50, ~200	47.4	12.3 ± 0.1	0.018 ± 0.002	0.0 ± 1.0	0.022 ± 0.002	46.1	5.7 ± 0.5	17.5 ± 1.6
				Sample ST0727 (J = 0.001727)						
(1)	(bt)	(L, 75, ~350)	(403.8)	(126.7 ± 0.5)	(0.098 ± 0.001)	(0.1 ± 0.6)	(0.409 ± 0.002)	(4.7)	(5.9 ± 0.5)	(18.4 ± 1.5)
(2)	(bt)	(L, 75, ~250)	(259.3)	(153.9 ± 0.6)	(0.112 ± 0.002)	(0.0 ± 0.8)	(0.496 ± 0.003)	(4.7)	(7.2 ± 0.7)	(22.3 ± 2.2)
3	bt	S, 40	54.1	133.6 ± 1.7	0.103 ± 0.008	2.3 ± 5.9	0.375 ± 0.011	17.0	22.8 ± 3.0	69.6 ± 9.0
(4)	(bt^{iso})	(S, 40)	(76.0)	(247.6 ± 4.0)	(0.158 ± 0.009)	(10.4 ± 7.9)	(0.797 ± 0.021)	(4.8)	(12.0 ± 4.9)	(37.1 ± 15.1)
(5)	(bt^{iso})	(S, 40)	(85.0)	(157.1 ± 1.5)	(0.118 ± 0.007)	(6.3 ± 3.6)	(0.489 ± 0.009)	(8.0)	(12.6 ± 2.2)	(38.9 ± 6.7)
(6)	(bt^{iso})	(S, 40)	(118.6)	(304.6 ± 4.7)	(0.217 ± 0.009)	(3.3 ± 4.2)	(0.982 ± 0.020)	(4.7)	(14.3 ± 3.9)	(44.0 ± 11.8)
(7)	(bt^{iso})	(S, 40)	(67.7)	(144.6 ± 2.7)	(0.111 ± 0.009)	(0.9 ± 2.9)	(0.451 ± 0.011)	(7.8)	(11.3 ± 2.1)	(34.9 ± 6.4)
(8)	(bt)	(S, 40)	(21.9)	(210.7 ± 5.7)	(0.112 ± 0.024)	(0.4 ± 16.8)	(0.696 ± 0.041)	(2.4)	(5.0 ± 10.9)	(15.6 ± 33.6)
9	bt	S, 40	68.9	203.6 ± 2.5	0.159 ± 0.009	0.1 ± 7.2	0.586 ± 0.013	15.0	30.5 ± 3.4	92.6 ± 10.1
10	bt	S, 40	37.4	202.6 ± 7.5	0.124 ± 0.017	26.6 ± 31.4	0.590 ± 0.038	13.9	28.1 ± 9.1	85.6 ± 27.2
				Sample ST0728 (J = 0.001726)						
1	bt	cL, 50, ~400	129.6	33.5 ± 0.1	0.041 ± 0.001	0.0 ± 0.6	0.092 ± 0.001	19.0	6.4 ± 0.3	19.7 ± 1.1
(2)	(bt)	(cL, 50, ~350)	(295.6)	(59.7 ± 0.1)	(0.057 ± 0.001)	(0.0 ± 0.3)	(0.187 ± 0.001)	(7.7)	(4.6 ± 0.4)	(14.3 ± 1.3)
(3)	(bt)	(cL, 75, ~250)	(306.8)	(57.0 ± 0.2)	(0.053 ± 0.001)	(0.0 ± 0.4)	(0.180 ± 0.001)	(6.6)	(3.8 ± 0.3)	(11.7 ± 0.9)
5	bt	L, 30, ~300	34.6	27.0 ± 0.2	0.035 ± 0.003	0.0 ± 1.5	0.057 ± 0.002	38.2	10.3 ± 0.5	31.8 ± 1.6
(6)	(bt)	(L, 75, ~300)	(581.2)	(85.3 ± 0.2)	(0.074 ± 0.001)	(0.0 ± 0.3)	(0.276 ± 0.001)	(4.4)	(3.8 ± 0.3)	(11.7 ± 0.8)
(7)	(bt)	(L, 50, ~200)	(313.1)	(111.4 ± 0.2)	(0.090 ± 0.001)	(0.0 ± 0.5)	(0.369 ± 0.002)	(2.1)	(2.3 ± 0.7)	(7.3 ± 2.1)
8	bt	S, 30	58.5	80.7 ± 0.8	0.066 ± 0.005	0.0 ± 2.8	0.227 ± 0.007	17.0	13.7 ± 2.1	42.1 ± 6.2
9	bt	L, 30, ~100	27.4	38.9 ± 0.6	0.039 ± 0.005	34.7 ± 6.6	0.080 ± 0.009	39.4	15.3 ± 2.6	47.1 ± 7.8
10	bt	L, 30, ~100	72.4	79.8 ± 0.6	0.074 ± 0.004	0.3 ± 2.3	0.237 ± 0.007	12.2	9.7 ± 1.9	30.1 ± 5.9

No	Mineral	Mode, Ø and length (µm)	$^{40}Ar \times 10^{-12}$ (cm^3)	$^{40}Ar/^{39}Ar \pm \sigma$	$^{38}Ar/^{39}Ar \pm \sigma$	$^{37}Ar/^{39}Ar \pm \sigma$	$^{36}Ar/^{39}Ar \pm \sigma$	$^{40}Ar^*$ (%)	$^{40}Ar^*/^{39}Ar_K \pm \sigma$	Age ± σ (Ma)
Sample ST0706a (J = 0.001724), bt^{iso} - $^{40}Ar/^{36}Ar$ intercept = 289 ± 14, isochron age = 11.0 ± 3.8 Ma										
1	phe	L, 35, ~300	50.7	11.6 ± 0.1	0.020 ± 0.001	0.0 ± 0.4	0.021 ± 0.001	47.8	5.6 ± 0.3	17.2 ± 0.9
2	phe	S, 35	31.9	16.6 ± 0.2	0.027 ± 0.003	0.0 ± 1.7	0.034 ± 0.002	39.5	6.6 ± 0.7	20.3 ± 2.0
3	phe	L, 20, ~300	67.9	14.3 ± 0.1	0.022 ± 0.002	0.0 ± 0.6	0.035 ± 0.001	28.1	4.0 ± 0.3	12.5 ± 0.8
4	phe	L, 20, ~500	69.1	11.5 ± 0.1	0.022 ± 0.001	0.0 ± 0.5	0.022 ± 0.001	42.8	4.9 ± 0.2	15.3 ± 0.6
5	bt^{iso}	L, 50, ~300	96.0	20.7 ± 0.1	0.037 ± 0.001	0.5 ± 0.6	0.060 ± 0.001	15.0	3.1 ± 0.3	9.6 ± 0.8
(6)	(bt^{iso})	(cL, 40, ~400)	(110.9)	(40.8 ± 0.1)	(0.045 ± 0.001)	(2.3 ± 0.7)	(0.130 ± 0.002)	(6.2)	(2.5 ± 0.6)	(7.9 ± 1.8)
7	bt	cL, 50, ~550	203.8	28.2 ± 0.1	0.030 ± 0.000	0.3 ± 0.1	0.082 ± 0.000	13.7	3.9 ± 0.1	12.0 ± 0.3
(8)	(bt^{iso})	(L, 100, ~600)	(214.9)	(32.3 ± 0.1)	(0.032 ± 0.001)	(0.0 ± 0.3)	(0.100 ± 0.001)	(8.9)	(2.9 ± 0.2)	(8.9 ± 0.7)
9	bt	L, 35, ~300	39.6	15.6 ± 0.7	0.034 ± 0.002	0.4 ± 1.1	0.035 ± 0.002	32.7	5.1 ± 0.8	15.8 ± 2.4
10	phe	cL, 35, ~600	65.0	11.0 ± 0.3	0.021 ± 0.001	0.6 ± 0.3	0.020 ± 0.001	46.3	5.1 ± 0.3	15.8 ± 1.0
11	bt	L, 30, ~250	36.8	25.5 ± 0.5	0.015 ± 0.005	1.0 ± 3.1	0.061 ± 0.006	29.6	7.6 ± 1.7	23.3 ± 5.1
Sample FT0719 (J = 0.001919), k-fsp^{iso} - $^{40}Ar/^{36}Ar$ intercept = 262 ± 65, isochron age = 10.1 ± 3.1 Ma										
4	bt	cL, 50, ~1300	59.5	18.1 ± 0.2	0.027 ± 0.001	0.3 ± 1.3	0.053 ± 0.001	12.7	2.3 ± 0.3	8.0 ± 1.0
(5)	(bt)	(cL, 50, ~850)	(31.7)	(13.4 ± 0.2)	(0.027 ± 0.002)	(0.7 ± 2.2)	(0.041 ± 0.002)	(9.5)	(1.3 ± 0.6)	(4.4 ± 2.1)
(6)	(bt)	(L, 50, ~1000)	(105.4)	(70.9 ± 0.6)	(0.062 ± 0.003)	(0.4 ± 2.4)	(0.226 ± 0.005)	(5.7)	(4.0 ± 1.5)	(13.9 ± 5.2)
(8)	(bt)	(L, 50, ~750)	(53.3)	(37.8 ± 0.2)	(0.042 ± 0.002)	(0.5 ± 2.5)	(0.123 ± 0.002)	(4.1)	(1.5 ± 0.7)	(5.3 ± 2.4)
10	bt	cL, 50, ~850	13.8	14.2 ± 0.2	0.026 ± 0.002	1.0 ± 4.8	0.039 ± 0.003	18.9	2.7 ± 0.8	9.2 ± 2.8
11	k-fsp	cL, 50, ~1000	13.0	6.6 ± 0.1	0.015 ± 0.002	0.5 ± 1.7	0.011 ± 0.001	51.9	3.4 ± 0.3	11.9 ± 1.1
12	k-fsp^{iso}	cL, 50, ~1000	18.6	6.6 ± 0.0	0.018 ± 0.001	0.3 ± 0.7	0.014 ± 0.001	36.7	2.4 ± 0.3	8.3 ± 0.9
13	k-fsp^{iso}	cL, 50, ~1000	17.5	7.9 ± 0.1	0.022 ± 0.002	0.4 ± 1.7	0.018 ± 0.001	31.1	2.5 ± 0.4	8.5 ± 1.5
14	k-fsp^{iso}	cL, 50, ~1000	8.8	4.4 ± 0.1	0.019 ± 0.001	0.4 ± 1.7	0.006 ± 0.001	61.7	2.7 ± 0.3	9.4 ± 1.1
15	k-fsp	cL, 50, ~850	16.4	6.6 ± 0.0	0.021 ± 0.001	0.2 ± 1.2	0.012 ± 0.001	47.0	3.1 ± 0.3	10.8 ± 1.1
16	k-fsp^{iso}	cL, 50, ~1000	7.6	8.9 ± 0.2	0.019 ± 0.003	1.3 ± 3.6	0.023 ± 0.003	23.7	2.1 ± 0.8	7.3 ± 2.7
17	k-fsp^{iso}	L, 50, ~500	7.9	4.3 ± 0.1	0.018 ± 0.002	0.6 ± 2.7	0.005 ± 0.001	65.1	2.8 ± 0.4	9.7 ± 1.4
19	k-fsp	cL, 50, ~1500	25.4	6.1 ± 0.0	0.020 ± 0.001	0.9 ± 1.0	0.010 ± 0.001	53.7	3.3 ± 0.2	11.4 ± 0.6

Notes: ab = albite; bt = biotite; k-fsp = k-feldspar; ms = muscovite; phe = phengite
L = line ablation (Ls = Lines); cL = curved line ablation; R = raster ablation; S = spot ablation;
$^{40}Ar^*$ = percentage of radiogenic ^{40}Ar
^{iso} indicates analyses used for isochron calculation
() indicates analyses where $^{40}Ar^* \leq 10$ %
all errors of the isotopic ratios, of the calculated $^{40}Ar/^{36}Ar$ intercepts and of the isochron ages are quoted as σ
isochron calculation was performed using the Microsoft Excel Add-In 3.41 (Ludwig, 2008)

2.7.4 Extraneous argon

$^{40}Ar/^{36}Ar$ intercepts of non-atmospheric-like composition as well as significant scatter of age values within single microstructural sites that cannot be explained by microstructural differences in the fabric are indicators of extraneous Ar, as discussed in detail for sample ST0730 (4 Fig. 2) from the Tuxer Shear Zones (Supplement). In addition, the results of the pre-kinematic minerals, which were

2.7.5 Syn- and post-kinematic minerals

2.7.5.1 Ahorn Shear Zone samples

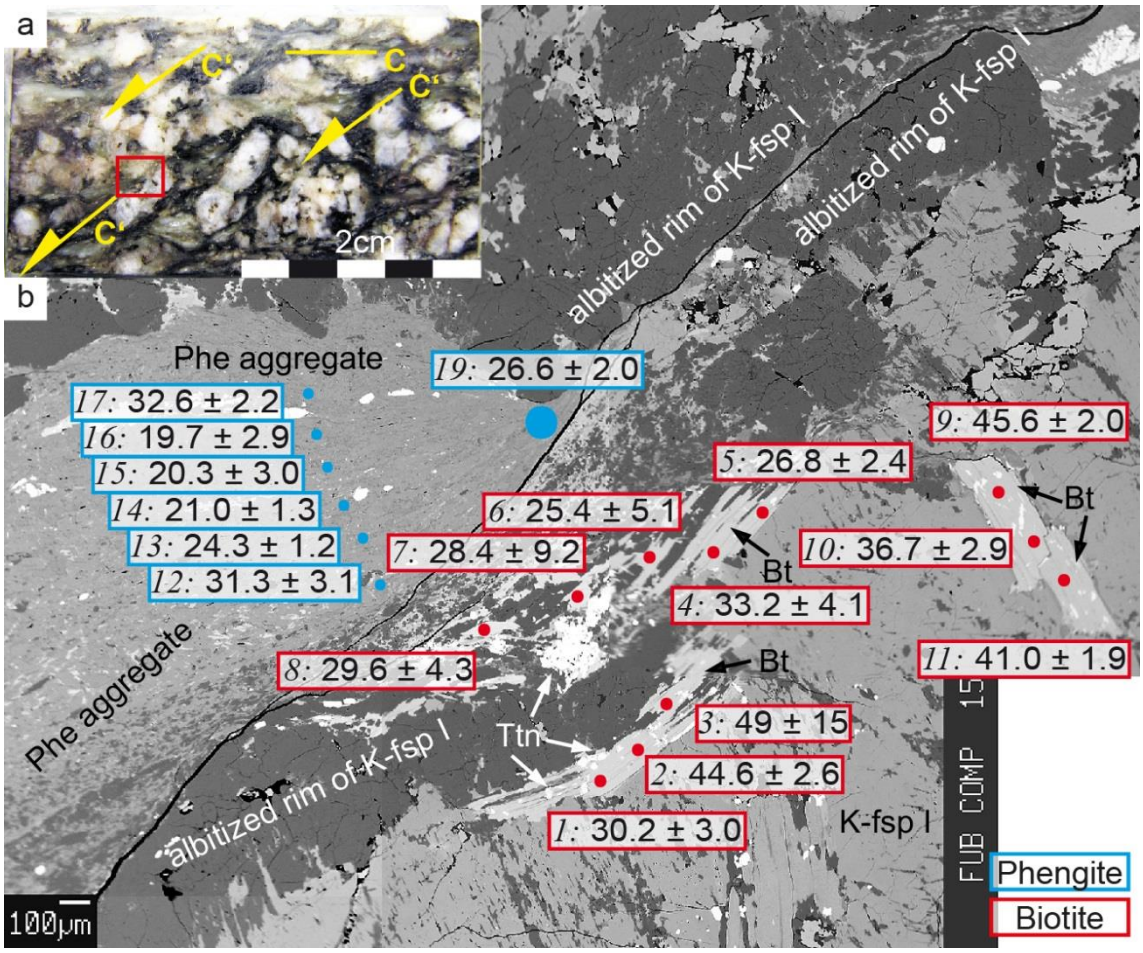

Figure 3a: *Photo of thick section of mylonite sample ST0505 (Ahorn Shear Zone). Yellow arrows indicate C-C'-fabric. Red square marks the drilling locality shown in Fig. 3b.* ***b:*** *Back scattered electron (BSE) images of sample ST0505 and $^{40}Ar/^{39}Ar$ age results. The size of the spot symbols approximately corresponds to the diameter of the laser ablation area. Biotites show titanite exsolution. K-feldspar clasts show albitized rims.*

Mylonites of the Ahorn Shear Zone (1, 2 Fig. 2, Fig. 3 and Fig. 4a) exhibit sinistral C–C′ fabrics and consist of K-feldspar clasts (0.5–1 cm) embedded in a matrix of fine-grained phengite, albite, quartz, calcite, and relics of magmatic biotite. The grain size of syn-kinematic phengite varies between 10 and 100 µm. Phengite preferentially grew along shear bands and within strain caps. K-feldspar clasts show remnants of magmatic zoning, perthitic exsolution, albitized rims and quartz- or calcite-filled fractures (Figs. 3 and 4b). Quartz show patchy, undulose extinction, healed cracks, incipient grain boundary migration and bulging with sub-grains of ~10 µm. Biotite show frayed grain boundaries, low [Ti] (Table 1) and exsolution of titanite (Figs. 3 and 4b). Biotite is intercalated with chlorite which is absent in the protolith. Quartz microstructures and biotite breakdown indicate that deformation temperatures of the Ahorn Shear Zone samples were at most 300 °C (Rosenberg and Schneider, 2008).

Single spot analyses of sample ST0505 (*12–17* Fig. 3a) of syn-kinematic phengites across a shear band yield ages varying between 32.6 and 19.7 Ma, with older ages located at both rims of the shear band. One integrated age obtained by large surface ablation (*19* Fig. 3b) yields 26.6±2.0 Ma (Table 2). Rb/Sr in situ analyses of this sample yield three albite–phengite isochrons varying between 21.1 and 24.4 Ma (Supplement), which are consistent with the $^{40}Ar/^{39}Ar$ ages.

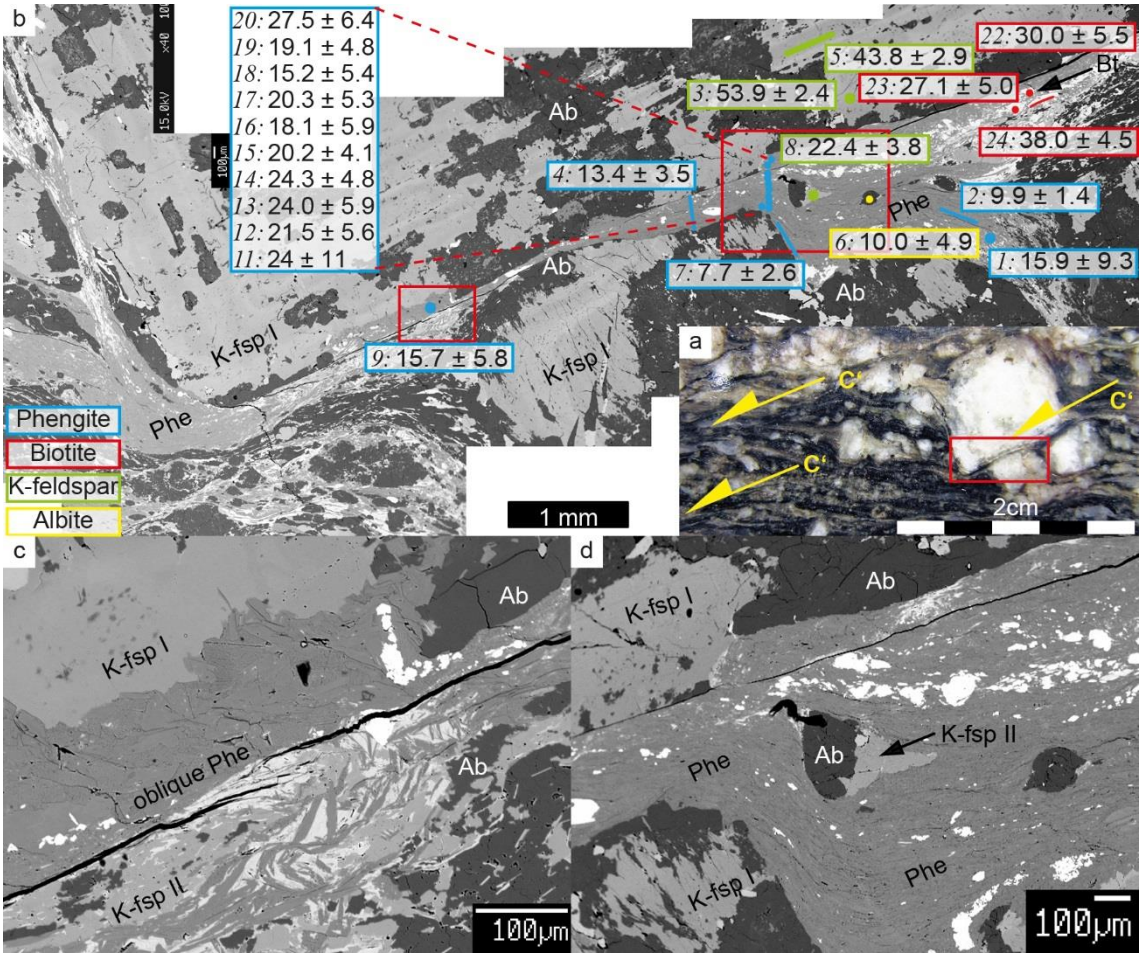

***Figure 4a**: Photo of thick section of mylonite sample ST0559 (Ahorn Shear Zone). Yellow arrows indicate C-C'-fabric, red square marks the drilling locality imaged in Fig. 4b. **b:** BSE image of sample ST0559 and $^{40}Ar/^{39}Ar$ age results. Nine spot analyses crossing the phengite aggregate are located along a section. The length of the colored lines corresponds approximately to the track length of line ablation. K-feldspar show patchy albitization and remnants of magmatic zoning. Red squares mark detail figures 4c and d. **c:** BSE detail of Fig. 4b (left red square) shows obliquely oriented cluster of phengite at the rim of the K-feldspar clast. White dots in the phengite aggregate are titanite. **d:** BSE detail of Fig. 4b (right red square) showing recrystallized K-feldspar in the pressure shadow of an albite clast within the phengite shear band.*

A similar age range of 27.5–15.2 Ma is observed in phengites of sample ST0559, where single spot analyses across a shear band (*11–20* Fig. 4b) were performed. Isochron calculation yields an age of 19.9±7.1 Ma and an $^{40}Ar/^{36}Ar$ intercept of 296±23 (Table 2). Single grain ablation analyses (*1, 9* Fig. 4b) yield 15.9±9.3 and 15.7±5.8 Ma, whereas line ablation analyses (*2, 4, 7* Fig. 4b) within the shear band reveal slightly younger ages ranging between 7.7 and 13.4 Ma. Due to the ablation mode used, crossing aggregates of small grains and grain boundaries, we suggest that Ar loss which is more effective at grain boundaries influenced the age values of the line ablations (see discussion on Geological errors). Analysis of a phengite grain (*9* Fig. 4b), out of a cluster grown into a K-feldspar clast, yields 15.7±5.8 Ma. These phengites are undeformed, obliquely oriented to the shear band, suggesting a post-kinematic formation with respect to sinistral shearing (Fig. 4c). Spot analysis (*8* Fig. 4b) of a recrystallized K-feldspar in the pressure shadow of an albite clast (Fig. 4d) yields an age of 22.4±3.8 Ma.

The large scatter of age values is influenced by low $^{40}Ar^*$ (2, 7, 9, 11 Table 2) and probably by an only locally achieved chemical equilibrium of the mineral assemblage due to low deformation temperature (Rosenberg and Schneider, 2008). However, the majority of phengite analyses yield ages which are consistent with the Rb/Sr and $^{40}Ar/^{39}Ar$ results of sample ST0505. Therefore, the ages of syn-kinematic phengite of the Ahorn Shear Zone bracket a time interval of 19 Myr (33–15

Ma). The age of 15.7±5.8 Ma of the post-kinematic blast leaves some doubts because of its low $^{40}Ar^*$. However, it is consistent with the remaining two young phengite ages obtained by spot analyses (1, 18 Fig. 4b).

2.7.5.2 Tuxer Shear Zones samples

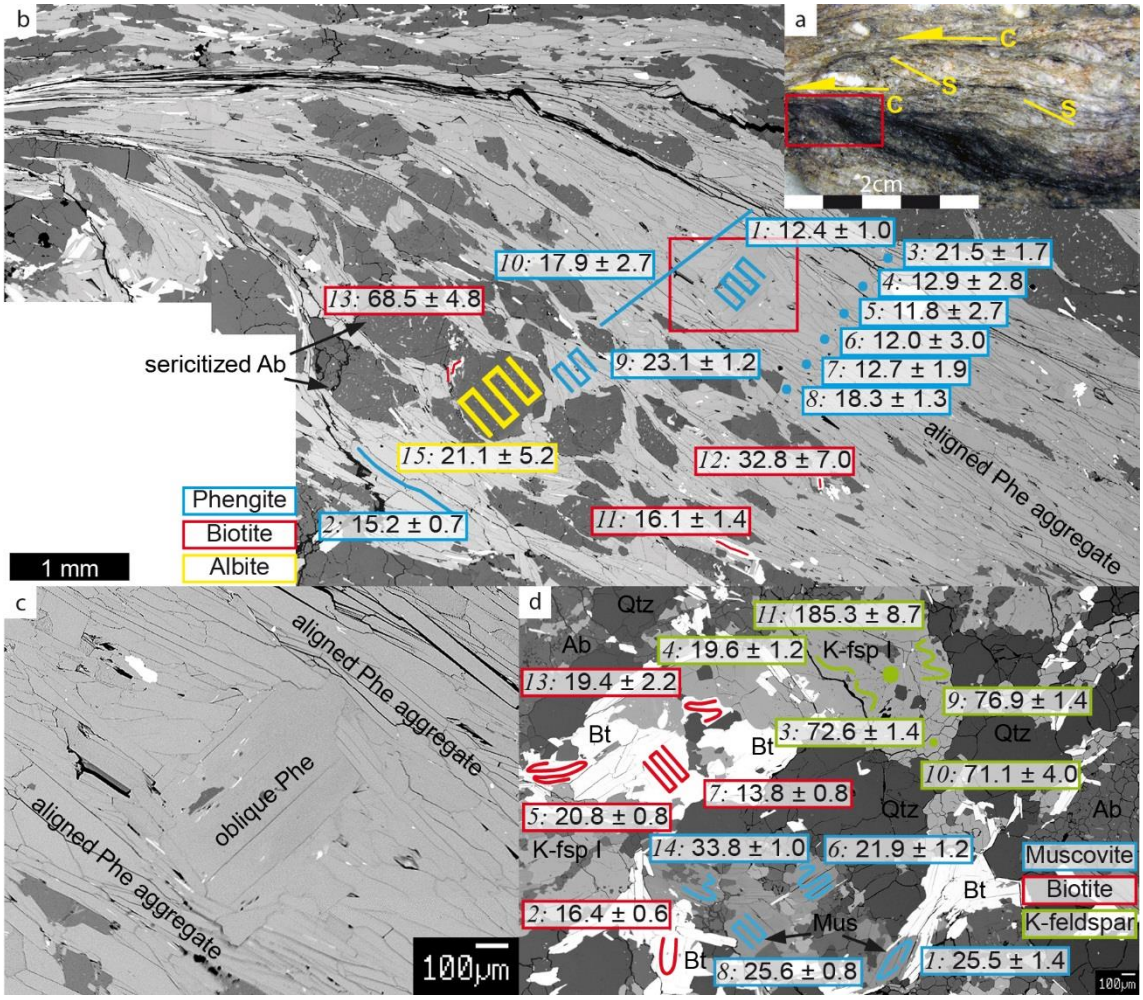

Figure 5a: *Photo of thick section of ultramylonite sample ST0734 (Tuxer Shear Zones). Yellow arrows indicate S-C-fabric; red square marks the drilling locality imaged in Fig. 5b.* ***b:*** *BSE image of sample ST0734 and $^{40}Ar/^{39}Ar$ age results. Phengite aggregate is surrounded by albite clasts which are sericitized. Angular lines indicate the tracks of raster ablation. Red square marks detail figure 5c.* ***c:*** *BSE detail of Fig. 5b, post-kinematic blast in the center of the phengite aggregate. The syn-kinematic phengite aggregate strikes from the upper left to the lower right corner, whereas the cleavage of the post-kinematic phengite is oblique, running from the upper right to the lower left corner.* ***d:*** *BSE image of the protolith sample ST0732b, from the same outcrop than sample ST0734. Note that white mica consists of pre-kinematic, randomly oriented muscovite blasts. Length of the curved lines images the track length of laser ablation.*

Proto- and ultramylonites of the Tuxer Shear Zones (Figs. 5a and 6a) are characterized by S–C fabrics and the presence of syn-kinematic phengite. Compared to the mylonites of the Ahorn Shear Zone the grain sizes of syn-kinematic phengite and recrystallized K-feldspar are larger (100–500 µm), and biotite is more abundant with higher [Ti] (Table 1). Feldspar is dynamically recrystallized (Supplement) and quartz recrystallized by sub-grain rotation. Syn-kinematic phengite occurs within strain caps, along S- and C-planes, and in pressure shadows of partly albitized K-feldspar clasts. These microstructures indicate deformation temperatures of 450–500 °C (Rosenberg and Schneider, 2008).

Line ablation across a syn-kinematic phengite aggregate (*10* Fig. 5b) of the ultramylonite sample ST0734 (3 Fig. 2) yields an integrated age of 17.9±2.7 Ma. Rb/Sr in situ analyses of phengite and albite of the same sample yield an isochron of 16.28±0.62 Ma (Supplement), hence confirming the integrated $^{40}Ar/^{39}Ar$ age. Spot analyses of neighboring phengites (*3–8* Fig. 5b) vary systematically between 21.5 and 11.8 Ma, whereas four central phengites yield an isochron age of 12.3±4.3 Ma and an $^{40}Ar/^{36}Ar$ intercept of 296±36 (Table 2). Phengites at the rim of the syn-kinematic aggregate (3, 8 Fig. 5b) yield older ages of 18.3±1.3 Ma and 21.5±1.7 Ma. In the center of the aggregate, an undeformed phengite lath, oriented oblique to the foliation, overgrew the syn-kinematic phengites (Fig. 5c). Large surface ablation of this post-kinematic blast yields an age of 12.4±1.0 Ma (*1* Fig. 5b), which is consistent with, but more precise than the isochron age of the youngest syn-kinematic phengites.

Line ablation (*12* Fig. 6b) in the protomylonite sample FT0728 (6 Fig. 2) across a syn-kinematic phengite aggregate at the strain cap of a K-feldspar clast yields an age of 14.1±0.9 Ma. Seven single spot ages across this aggregate (*1–7* Fig. 6b) vary between 11.6 Ma and 24.2 Ma, showing younger ages at the rim. Four analyses (*2, 5–7* Fig. 6b) of this section yield an isochron age of 15.1±2.4 Ma and an $^{40}Ar/^{36}Ar$ intercept of 295±25 (Table 2). At both margins of this aggregate undeformed phengites are oblique to the foliation of the syn-kinematic phengites (Fig. 6c and d) indicating a post-kinematic growth. Large surface ablation of one post-kinematic phengite (*8* Fig. 6b) yields 9.3±1.7 Ma, which is the youngest phengite age of the sample.

The dated age range of syn-kinematic phengite of the Tuxer Shear Zone samples lies between 24–12 Ma. The end of this time interval of 13 Myr, coincides with the older age of 12 Ma of the two dated post-kinematic phengite blasts.

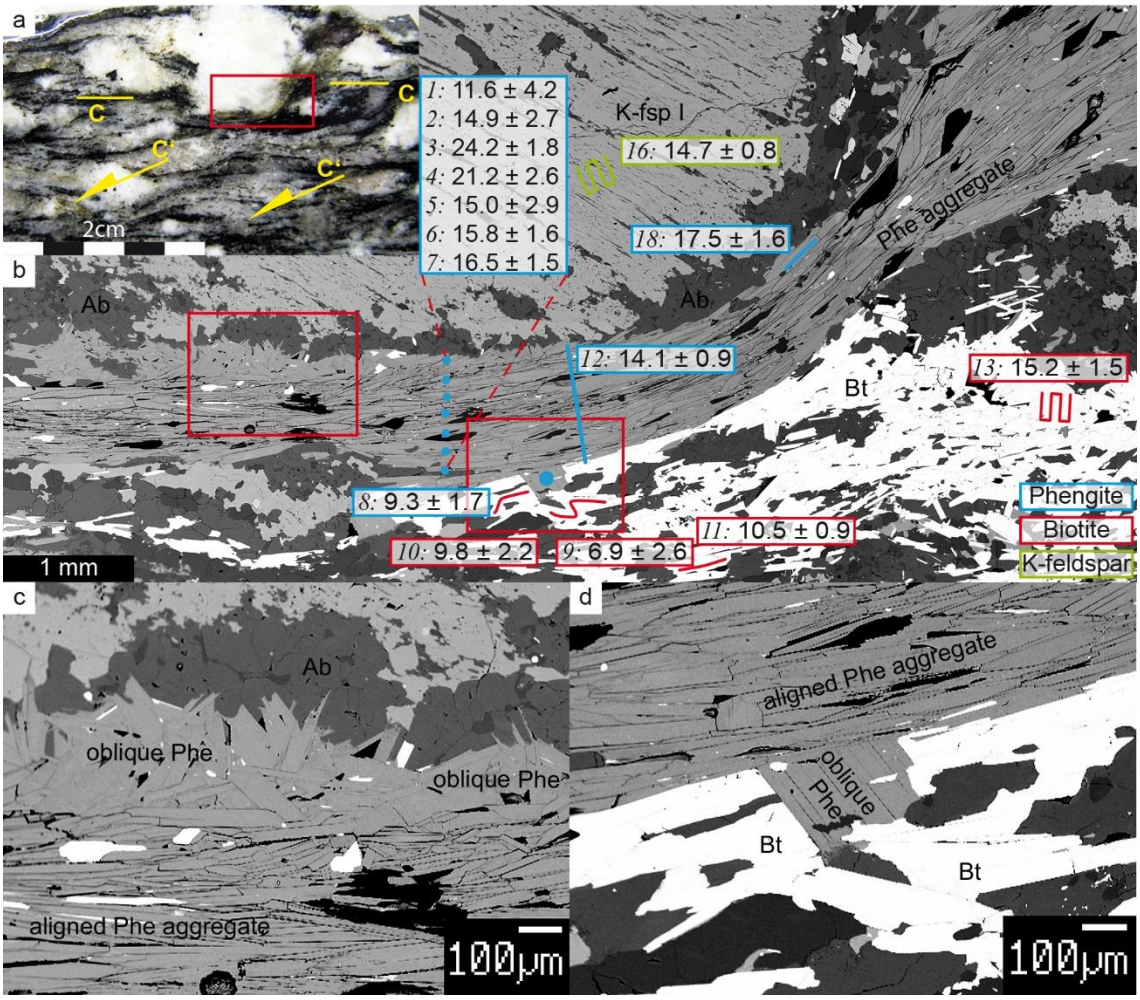

Figure 6a: *Photo of thick section of protomylonite sample FT0728 (Tuxer Shear Zones). Yellow arrows indicate S-C-fabric; red square marks the drilling locality imaged in Fig. 6b.* ***b:*** *BSE image of protomylonite sample FT0728 and $^{40}Ar/^{39}Ar$ age results. Single spot analyses of phengite across a syn-kinematic aggregate formed at a strain cap of a K-feldspar clast shows higher age variability than the neighboring line ablation. Red squares mark post-kinematic blasts shown in detail figures 6c and d.* ***c:*** *BSE detail of Fig. 6b (left red square) shows blasts of post-kinematic phengite which are located at the albitized rim of the K-feldspar clast. Their orientation is oblique to the direction of the syn-kinematic aggregate at the strain cap.* ***d:*** *BSE detail of Fig. 6b (right red square) shows one post-kinematic phengite which is oblique to the orientation of the biotite aggregate. This phengite blast is also obliquely oriented to the alignment of the phengite aggregate at the K-feldspar strain cap.*

2.7.5.3 Greiner Shear Zone samples

Granitic mylonites of the Greiner Shear Zone (7, 8 Fig. 2) are fine-grained and tightly foliated showing sinistral S–C fabrics (Figs. 7a, 8a). Syn-kinematic zoisite and biotite are stable during ductile shear and the latter shows higher [Fe], [Mg] and [Ti] than biotite of the Ahorn Shear Zone (Table 1). Feldspar is dynamically neo-/recrystallized, whereat syn-kinematic albite aggregates show an inverse [Ca] zonation. Syn-kinematic phengite has grain sizes of 50–600 µm (Fig. 7b). Quartz recrystallized by sub-grain rotation with grain sizes of 100–500 µm. The mineral paragenesis of bt+ab+qtz+zo±K-fsp±phe of the Greiner Shear Zone mylonites indicates metamorphic temperatures of at least 500 °C (Selverstone et al., 1983).

Sample ST0706a (7 Fig. 2) shows a saussuritized plagioclase clast with biotite inclusions (Fig. 7b). Large surface ablations (*1–4, 10* Fig. 7b) of syn-kinematic and foliation-parallel phengite that

formed along the margin of this clast yield ages between 20.3 Ma and 12.5 Ma (Table 2). Large surface ablations of biotite aligned parallel to the mylonitic foliation vary between 12.0 and 7.9 Ma. Three of these biotite analyses yield an isochron age of 11.0±3.8 Ma (*5, 6, 8* Fig. 7a, Table 2) with an $^{40}Ar/^{36}Ar$ intercept of 289±14.

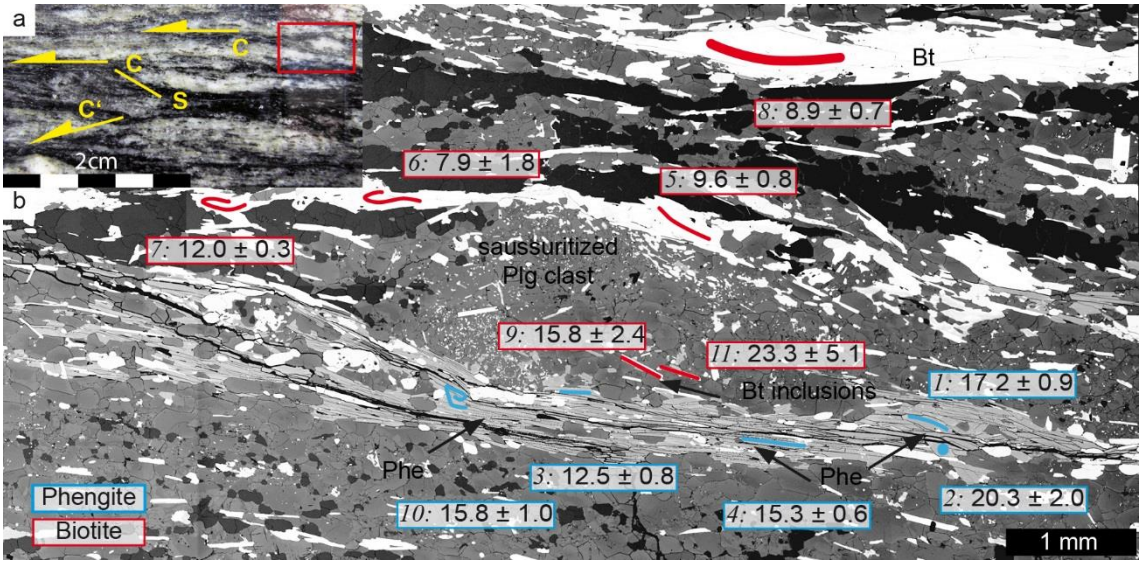

Figure 7a: *Photo of thick section of mylonite sample ST0706a (Greiner Shear Zone). Yellow arrows indicate S-C-fabric; red square marks the drilling locality imaged in Fig. 7b.* ***b:*** *BSE image of sample ST0706a and $^{40}Ar/^{39}Ar$ age results. Large surface ablations of phengite, located at strain cap of a pre-kinematic saussuritized plagioclase clast, are indicated by the spot and curved lines. Two analyses of biotite inclusions within the plagioclase are indicated by lines.*

K-feldspar clasts of FT0719 (8 Fig. 2) are dynamically recrystallized into xenomorphic albite and K-feldspar of Ø=300–800 µm grain size (Fig. 8a and b) forming ribbons. Single grain analyses of these recrystallized K-feldspars vary between 11.9 and 7.3 Ma, whereas five of them (*12–14, 16, 17* Fig. 8b) yield an isochron age of 11.9±3.1 Ma and an $^{40}Ar/^{36}Ar$ intercept of 262±65 (Table 2). Biotite analyses of ST0706a and the K-feldspar analyses of FT0719 yield ages in the same range, i.e. 12–7 Ma, which overlap with the youngest ages of syn-kinematic phengite of sample ST0706a. Half of these biotite results are characterized by low $^{40}Ar^*$ (Table 2), hence they will not be considered further.

In summary, ages of syn-kinematic phengite and dynamically recrystallized K-feldspar in the Greiner Shear Zone range between 20 and 7 Ma. The time interval of 14 Myr bracketed by syn-kinematic mineral formation overlaps largely with the time interval of the Tuxer Shear Zones.

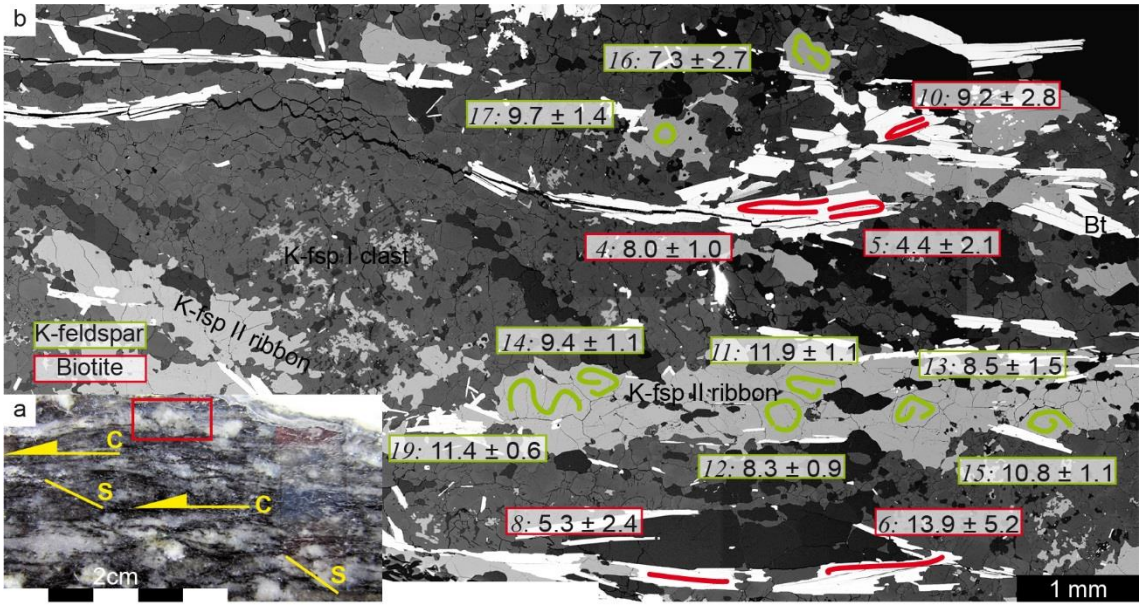

Figure 8a: *Photo of thick section of mylonite sample FT0719 (Greiner Shear Zone). Yellow arrows indicate S-C-fabric; red square marks the drilling locality imaged in Fig. 8b.* ***b:*** *BSE image of sample FT0719 and* $^{40}Ar/^{39}Ar$ *age results. Large surface ablations of recrystallized K-feldspar, aligned along a ribbon on the tail of a K-feldspar clast, are indicated by curved lines.*

2.8 Discussion

2.8.1 Errors

The age ranges obtained and the precision of these ages are influenced by analytical parameters and geological processes. Therefore the discussion on errors is divided into two sections.

2.8.1.1. Analytical errors

The used ablation modes and the resulting amount of ablated sample volume had the largest impact on the precision of the analyses. This is exemplarily shown for sample ST0734, where raster ablation (*1* Fig. 5b, Table 2) released 85.8×10−12 cm^3 STP of Ar gas and resulted in a 1σ error of 1.0 Ma. In comparison spot ablations of the single spot section (*3–8* Fig. 5b, Table 2) released approximately half as much 27.5–45.2×10−12 cm^3 STP Ar gas resulting in approximately twice as high σ errors between 1.7 and 3.0 Ma. The amount of blank affects the analytical precision, because of necessary background corrections. ^{40}Ar intensities of the measurements (Table 2) are at least three to ten times higher than the respective ^{40}Ar blank intensities. Based on the young absolute ages of the samples the irradiation time was chosen to produce an $^{40}Ar/^{39}Ar$ ratio of approximately unity to increase precision. Finally the accumulation of radiogenic Ar in young minerals is less than in old minerals as indicated by low $^{40}Ar^*$ values, therefore, the error increases due to background correction. The dated time range of the shear zones is manifold longer than the uncertainty given by the absolute errors, which are 5–30 %, allowing discrimination of spatially resolved ages. Errors due to axial and radial neutron fluence variance are already compensated by the interpolated J-values.

2.8.1.2 Geological errors

The systematic age variation of the syn-kinematic minerals and the large scatter of the pre-kinematic minerals cannot be exclusively explained by analytical errors. These age variations are influenced by several geological processes (Müller et al., 2000). The time scale of ductile deformation of major shear zone is in the range of tens of million years (e.g. Phillips et al., 2004). Therefore, the time window for syn-kinematic mineral growth might also last tens of million years if metamorphic conditions are maintained for this time range. Subtle isotopic disequilibria inherited from pre-kinematic minerals can be excluded for the syn-kinematic minerals, since isochron calculation yielded atmospheric-like $^{40}Ar/^{36}Ar$ intercepts, but it might explain the large age scatter of the pre-kinematic minerals (Warren et al., 2012, Supplement). The grain boundaries of the syn-kinematic minerals might be affected by Ar loss, which becomes vital in sample ST0559, where line ablation yield slightly younger age values than spot ablations. Since the difference between the youngest intragrain ages (15.9±9.3, 15.7±5.8, 15.2±5.4, *1, 9, 18,* Fig. 4b) and the ages obtained by ablation of grain aggregates (9.9±1.4, 13.4±3.5, 7.7±2.6, *2, 4, 7,* Fig. 4b) are not significant, we neglect drastic Ar loss. Two examples (Figs. 3b and 6b) show that pre-kinematic biotites spatially close to the syn-kinematic phengites have younger age values than pre-kinematic biotites afar from syn-kinematic phengites. This age difference of pre-kinematic minerals might be caused by sub-millimeter length scale of diffusion under greenschist to amphibolite facies conditions. Post-kinematic mineral ages overlap only with the youngest syn-kinematic minerals whose grain size is the same as that of the older syn-kinematic minerals. Therefore static crystallization or alteration phenomena with respect to grain size can be excluded.

2.8.2 Dating deformation

The large age scatter of biotite (95–4.4 Ma) indicates that its isotopic composition was only partly reset during mylonitization, even sometimes affected by excess Ar (Supplement). Pre-kinematic (Figs. 3b and 4b) and armored (Fig. 7b) biotites, which are unstable on the base of microstructural observations, have older ages than recrystallized biotites in the Greiner Shear Zone, where the metamorphic temperature were higher and biotite are inferred to be stable constituents of the mylonitic paragenesis. Interestingly, biotite and syn-kinematic K-feldspar in the Greiner Shear Zone give consistent age results. Analyses of K-feldspar clasts in samples of the Ahorn Shear Zone and the Tuxer Shear Zones (*3, 5* Fig. 4a, Supplement) yield systematically older age values than analyses of recrystallized K-feldspars (*8* Fig. 4a, Supplement). The only analysis yielding a younger age (14.7±0.8 Ma) is located in a clast showing perthitic exsolution (Fig. 6b). K-feldspar clasts in the protolith of the Tuxer Shear Zones (ST0732b, 3 Fig. 2, *3, 9–11* Fig. 5d) are even older than K-feldspar clasts in the mylonites. Therefore, we argue that K-feldspar clasts were affected by partial resetting during mylonitization. Recrystallized K-feldspar of the Greiner Shear Zone vary between 11.9 and 7.3 Ma and yield an atmospheric-like $^{40}Ar/^{36}Ar$ intercept, therefore, these ages are interpreted as formation ages. Age data of syn-kinematic phengite and recrystallized K-feldspar, 33–15 Ma (Ahorn Shear Zone), 24–12 Ma (Tuxer Shear Zones) and 20–7 Ma (Greiner Shear Zone), are more consistent, not affected by extraneous Ar and in two cases the ages of syn-kinematic phengite were confirmed by Rb/Sr analyses (Supplement). Therefore, these ages are interpreted as formation ages and the interpretation as cooling ages can be refused since these two chronometers have different closure temperatures for white mica.

Formation ages of syn-kinematic phengites across shear bands or strain caps show systematic spatial distributions indicating in two cases a younging trend from the rims to the center (Figs. 3b and 5b) and in one case a younging trend from the center to the rims (Fig. 6b). These different age trends suggest that the ages of syn-kinematic minerals depends on mineral formation in selected microstructural sites rather than on diffusional processes. If these age patterns arose from diffusion similar age trends within all the phengite aggregates would be expected. In addition, spatial age variations are not associated to changes in major and minor element composition across the

phengite aggregates (Supplement). These texturally-controlled age differences would not be preserved if minerals were affected by alteration or post-crystallization phenomena. Considering that the scatter of syn-kinematic minerals ages is larger than the analytical error of every formation age obtained (Figs. 3, 4a, 5b, 6b, 7b, and 8b), we conclude that each age value dates an increment of a long lasting deformation period (e.g. Christensen et al., 1994, Müller et al., 2000, Pollington and Baxter, 2010; 2011). Hence the interval bracketed between the youngest and the oldest syn-kinematic mineral ages represents the longevity of the respective shear zones.

In all cases analyzed post-kinematic phengites show the youngest ages of their microstructural site and are indistinguishable from the youngest ages of the adjacent syn-kinematic phengites (Figs. 5b, 6b and 7b). The temporal coincidence between youngest syn-kinematic formation ages and the age of post-kinematic blasts indicate that the latter immediately date the termination of ductile deformation.

The presence of pre-kinematic minerals in the protolith enables us to set some temporal constraints on the onset of deformation. The age values of pre-kinematic muscovites (33.8–21.9 Ma, *1, 6, 8, 14* Fig. 5d) of the protolith are older than but they overlap with the oldest ages of syn-kinematic phengites (24.2±1.8 Ma, *3* Fig. 6b) of the mylonites. This is constrained for the Tuxer Shear Zones, where muscovites might pre-date ductile deformation at 21.9±1.2 Ma.

The initiation of deformation cannot be constrained precisely, because of time possibly lacking between the onset of deformation and syn-kinematic mineral formation or a continuous recrystallization associated with age resetting during ongoing deformation. However, based on large scale considerations and on independent geochronological data (Glodny et al., 2008; Kurz et al., 2008) the onset of sinistral deformation cannot be older than our oldest age of 33 Ma for syn-kinematic phengites of the Ahorn Shear Zone, because sinistral shear zones of this study overprint a schistosity formed under high pressure metamorphism at 31 Ma (Glodny et al., 2008) or 38 Ma (Kurz et al., 2008). The oldest ages of syn-kinematic phengites in the Tuxer Shear Zones and in the Greiner Shear Zone are younger (24.2±1.8 Ma and 20.3±2.0 Ma, respectively) than the oldest syn-kinematic ages of the Ahorn Shear Zone. This relation is also true for the youngest ages of syn-kinematic minerals in the Greiner and Tuxer Shear Zones compared to the Ahorn Shear Zone. In summary, shear zone longevities of 19 Myr (33–15 Ma, Ahorn Shear Zone), 13 Myr (24–12 Ma, Tuxer Shear Zones), and 14 Myr (20–7 Ma, Greiner Shear Zone) appears to be partly coeval, but also show a southward shift of ductile shearing from the Ahorn Shear Zone to the Greiner Shear Zone.

2.8.3 Comparison with age results of previous studies

Age determinations on syn-kinematic white mica of the SEMP fault (Fig. 1) using $^{40}Ar/^{39}Ar$ step heating yield an age range of 35–28 Ma (Urbanek et al., 2002). These ages overlap with our results of the Ahorn Shear Zone (33–15 Ma), which is inferred to be the deep-seated, ductile continuation of the SEMP Fault (Rosenberg and Schneider, 2008).

Classical Rb/Sr and K/Ar analyses of "…strongly mylonitic shear zones …" (Blanckenburg et al., 1989) in the area of the Tuxer Shear Zone yield 20–14 Ma for phengite and 17–13 Ma for biotite, which are consistent with our results of the Tuxer Shear Zones (24–12 Ma).

Segments of syn-kinematic garnet of the Greiner Shear Zone dated with the Rb/Sr method yield ages of 35 Ma for the core and 30 Ma for the rim (Christensen et al., 1994). More recent Sm/Nd analyses of similar garnet segments span a formation age range between 28 and 20 Ma (Pollington and Baxter, 2010; 2011). Indeed, their youngest ages correspond to termination of garnet growth, but there is no independent evidence to infer that this coincided with termination of deformation. This limitation persists when dating syn-kinematic minerals only. Minerals can only be used to date the time of their stability, which does not necessarily coincide with the time of deformation activity.

Our study shows that syn-kinematic mineral formation continued until 7.3±2.7 Ma in the Greiner Shear Zone, under metamorphic conditions that did not permit the growth of garnet anymore. Combining the results of Pollington and Baxter, 2010; 2011 with ours, longevity of 22 Myr for the Greiner Shear Zone (28–7 Ma) can be inferred.

Dextral shear zones crosscutting the Greiner Shear Zone were dated at 29–20 Ma by in situ EMPA of monazites (Barnes et al., 2004). Monazites, inferred to have formed during dextral shear by fluid influx due to serpentinization and devolatilization, are "…individual grains, anhedral and embayed, suggesting that incipient breakdown of monazite occurred following the initial metasomatism…" (Barnes et al., 2004) but they lack of microstructural evidences to be certainly associated with dextral shear. In contrast, our results for the Greiner Shear Zone indicate that phengites were formed during sinistral shear between 20–13 Ma, in addition to K-feldspars and biotites that dynamically recrystallized until 7 Ma.

A comprehensive study, dating shear zones in the entire Tauern Window with the "Rb-Sr internal mineral isochron approach" (Glodny et al., 2008) suggested that sinistral shearing in the western Tauern Window was active between 31 and 15 Ma. The time of activity of sinistral shear zones proposed by this study (31–15 Ma) overlaps with our results (33–7 Ma). However, the implications of our results are fundamentally different assessing the textural and therefore, the geologic significance of these ages. The age span between 35 and 15 Ma corresponds to the age of collision and Barrovian-type metamorphism in the Eastern Alps. Therefore, metamorphic mineral ages and syn-kinematic formation ages of sinistral shear zones in the western Tauern Window fall in the same age interval, no matter whether they were deformed or undeformed. Since, the clear textural discrimination of the dated minerals is missing we abstain from evaluating the geologic significance of these earlier published Rb/Sr ages.

Assessing that sinistral displacement in the western Tauern Window took place between 33 and 7 Ma has some important implications for the tectonics of the Eastern Alps. Some models suggested that sinistral deformation in the Tertiary Eastern Alps terminated at 30 Ma and was overprinted by dextral deformation (e.g. Mancktelow et al., 2001, Neubauer et al., 1999 and Polinski and Eisbacher, 1992), whereas others suggested a contemporaneous activity of dextral and sinistral shear zones, forming a conjugate system that accommodated N–S shortening and E–W extension (e.g. Rosenberg et al., 2004, 2007). The continuation of sinistral deformation until 7.3±2.7 Ma, hence coeval with dextral displacements along the Pustertal Fault (Müller et al., 2001), implies a substantial support of the latter interpretation.

2.9 Conclusion

In situ dating of microstructurally defined pre-, syn-, and post-kinematic minerals confirms the relative age sequence assessed by textural arguments and allows us to attribute absolute ages to sinistral ductile shear in the western Tauern Window. Although pre-kinematic minerals appear to be affected by extraneous Ar, syn-kinematic and post-kinematic minerals yield reliable formation ages. Age differences of syn-kinematic minerals indicate different increments of a long lasting deformation history. Therefore, these ages can be interpreted to define longevities of ductile shear zones.

Since post-kinematic phengite ages coincide with the youngest syn-kinematic formation ages of the same microstructural site in one sample, the termination of ductile deformation is interpreted to be identical with the age of post-kinematic phengites. The initiation of deformation cannot be constrained as precisely as its termination but our results suggest that the three large-scale shear zones investigated were partly coeval each of them acting for time intervals of 19 Myr, 13 Myr and 22 Myr, respectively. The northernmost Ahorn Shear Zone was active under greenschist-facies conditions between 33 and 15 Ma and might have terminated at 15.7±5.8 Ma. The Tuxer Shear Zones were active under greenschist to amphibolite facies conditions between 24 and 12 Ma and

terminated at 12.4±1.0 Ma. The Greiner Shear Zone was active under amphibolite facies conditions between 28 and 7 Ma (Pollington and Baxter, 2010; 2011, this study). This result is a first step to assess how and when orogen-scale shear zone networking was active, hence to understand how deformation is accommodated and partitioned in space and time.

2.10 Acknowledgment

This work was funded by a grant of the Deutsche Forschungsgemeinschaft (Ro2177/4). We acknowledge Georg Fankhauser for field support and accommodation. For sample preparation we thank Christiane Behr (Freie Universität of Berlin) and Christine Fischer (University of Potsdam). Ralf Milke supported us at the EMPA facilities at the Freie Universität of Berlin. Masafumi Sudo introduced and supported us at the Ar isotopic analytical system at University of Potsdam and he provided a Microsoft Excel spread sheet for data evaluation and reduction. For helpful discussions we thank Audrey Bertrand, Sebastian Garcia, Andreas Scharf, Silvia Favaro, and Mark Handy. For critical and constructive reviews we thank Matthias Konrad-Schmolke, Stefan Schmid and two anonymous journal reviewers.

2.11 References

Barnes, J.D., Selverstone, J., Sharp, Z.D., 2004. Interaction between serpentinite devolatization, metasomatism and strike-slip strain localization during deep-crustal shearing in the Eastern Alps, J. Metamorph. Geol. 22, pp. 283–300.

Blanckenburg, F.v., Villa, I.M., Baur, H., Morteani, G., Steiger, R.H., 1989. Time calibration of a PT-path from the Western Tauern Window, Eastern Alps: the problem of closure temperatures, Contrib. Mineral. Petr. 101, pp. 1–11.

Christensen, J.N., Selverstone, J., Rosenfeld, J.L., DePaolo, D.J., 1994. Correlation by Rb-Sr geochronology of garnet growth histories from different structural levels within the Tauern Window, Eastern Alps. Contrib. Mineral. Petr. 118, pp. 1–18.

Cliff, R.A., Meffan-Main, S., 2003. Evidence from Rb-Sr microsampling geochronology for the timing of Alpine deformation in the Sonnblick Dome, SE Tauern Window, Austria, in: Linking the Isotopic Record with Petrology and Textures. Geol. Soc. London Spec. Publ. 220, pp. 93–117.

Cole, J., Hacker, B., Ratscbacher, L., Dolan, J., Seward, G., Frost, E., Frank, W., 2007. Localized ductile shear below the seismogenic zone: Structural analysis of an exhumed strike-slip fault, Austrian Alps, J. Geophys. Res. 112, doi:10.1029/2007JB004975.

Crawford, M.L., Hollister, L.S., Woodsworth, G.J., 1987. Crustal deformation and regional metamorphism across a terrane boundary, Coast Plutonic Complex, British Columbia, Tectonics 6, 343-361.

Davidson, C., Hollister, L.S., Schmid, S.M., 1992. Role of melt in the formation of a deep-crustal compressive shear zone: the MaClaren Glacier metamorphic belt, south central Alaska, Tectonics 11, pp. 348–359.

Dunlap, W.J. Neocrystallization or cooling? $^{40}Ar/^{39}Ar$ ages of white micas from low-grade mylonites, 1997. Chem. Geol. 143, pp. 181–203.

Finger, F., Roberts, M.P., Haunschmid, B., Schermaier, A., Steyrer, H.P., 1993. Variscan granitoids of central Europe: their typology, potential sources and tectonothermal relations. Miner. Petrol. 61, pp. 67-96.

Freeman, S.R., Inger, S., Butler, R.W.H., Cliff, R. A., 1997. Dating deformation using Rb-Sr in white mica: Greenschist facies deformation ages from the Entrelor shear zone, Italian Alps. Tectonics 16, pp. 57–76.

Getty, S.R. and Gromet, L.P., 1992. Geochronological constraints on ductile deformation, crustal extension, and doming about a basement-cover boundary, New England Appalachians. Am. J. Sci. 292, pp. 359–397.

Giogris D., Cosca, M., Li, S., 2000. Distribution and significance of extraneous argon in UHP eclogite (Sulu terrain, China): insight from in situ $^{40}Ar/^{39}Ar$ UV-laser ablation analysis, Earth Planet. Sc. Lett. 181 (2000) 605–615.

Glodny, J., Ring, U., Kühn, A., 2008. Coeval high-pressure metamorphism, thrusting, strike-slip, and extensional shearing in the Tauern Window, Eastern Alps. Tectonics 27, TC4004, doi:10.1029/2007TC002193.

Hoernes, S., Friedrichsen, H., 1974. Oxygen isotope studies on metamorphic rocks of the Western Hohe Tauern area (Austria). Schweiz. Mineral. Petrol. Mitt. 54, pp. 769–788.

Hunziker, J.C., Zingg, A., 1980. Lower Paleozoic amphibolite to granulite facies metamorphism in the Ivrea zone (Southern Alps, Northern Italy). Schweiz. Miner. Petrog. 62, pp. 181–213.

Hurford, A.J., Flisch, M., Jäger, E., 1989. Unraveling the thermo-tectonic evolution of the Alps: a contribution from fission track analysis and mica dating, in: Coward, M.P., Dietrich, D., Park, R.G. (Eds.), Alpine Tectonics. Geol. Soc. London Spec. Publ., 45 pp. 369–398.

Kelley, S., 2002. Excess argon in K–Ar and Ar–Ar geochronology, Chem. Geol. 188, pp. 1–22.

Kelley, S.P., Arnaud, N.O., Turner, S.P., 1994. High spatial resolution $^{40}Ar/^{39}Ar$ investigations using an ultra-violet laser probe extraction technique, Geochim. Cosmochim. Ac. 58, pp. 3519–3525.

Kligfield, R., Hunziker, J., Dallmeyer, R.D., Schamel, S., 1986. Dating of deformation phases using K-Ar and $^{40}Ar/^{39}Ar$ techniques: results from the Northern Apennines, J. Struct. Geol. 8, No. 7, pp. 781–798.

Kurz, W., Handler, R., Bertoldi, C., 2008. Tracing the exhumation of the Eclogite Zone (Tauern Window, Easter Alps) by $^{40}Ar/^{39}Ar$ dating of white mica in eclogites, Swiss J. Geosci. 3, pp. 1–16.

Linzer, H.G., Decker, K., Peresson, H., Dell'Mour, R., Frisch, W., 2002, Tectonophysics 354, pp. 211–237.

Luth, S.W., Willingshofer, E., 2008. Mapping of the Post-Collisional Cooling History of the Eastern Alps, Swiss J. Geosci. 101, pp. 207–223.

Ludwig, K., 2008. A Geochronological Toolkit for Microsoft Excel Berkeley Geochronology Center Spec. Publ. 4, pp. 1–84.

Mancktelow, N.S., Stöckli, D.F., Grollimung, B., Müller, W., Fügenschuh, B., Viola, G., Seward, D., Villa, I.M., 2001. The DAV and Periadriatic fault system in the Eastern Alps south of the Tauern window. Int. J. Earth Sci. 90, pp. 593–622.

Massonne, H.J., and Kopp, J., 2005. A low-variance mineral assemblage with talc and phengite in an eclogite from the Saxonian Erzgebirge, central Europe, and its P-T evolution, J. Petrol. 46, pp. 355–375.

McCaig, A.M., 1997. The geochemistry of volatile fluid flow in shear zones, In: Holness M.B. (Ed) Deformation-enhanced Fluid Transport in the Earth's Crust and Mantle, Chapman & Hall, London. ISBN: 0412752905, pp. 227–239.

McDougall, I., Harrison, M.T., 1999. Geochronology and Thermochronology by the $^{40}Ar/^{39}Ar$ Method, Oxford University Press, Oxford, 269 p.

Merrihue, C., Turner, G., 1966. Potassium-Argon Dating by Activation with Fast Neutrons, J. Geophys. Res. 71, pp. 2852–2857.

Most, P., 2003. Late Alpine cooling histories of tectonic blocks along the central part of the Transalp-Traverse (Inntal – Gadertal): constraints from geochronology, PhD-thesis Eberhardt-Karls-Universität Tübingen, pp. 1–151.

Müller, W., Aerden, D., Halliday, A.N., 2000. Isotopic Dating of Strain Fringe Increments: Duration and Rates of Deformation in Shear Zones, Science 288, pp. 2195–2198.

Müller, W., Prosser, G., Mancktelow, N.S., Villa, I.M., Kelley, S.P., Viola, G., Oberli, F., 2001. Geochronological constraints on the evolution of the Periadriatic Fault System (Alps), Int. J. Earth Sci. 90, pp. 623–653.

Müller, W., 2003. Strengthening the link between geochronology, textures and petrology, Earth Planet. Sc. Lett. 206, pp. 237–251.

Mulch, A., Cosca, M.A., Andresen, A., Fiebig, J., 2005. Time scales of deformation and exhumation in extensional detachment systems determined by high-spatial resolution in situ UV-laser $^{40}Ar/^{39}Ar$ dating, Earth Planet. Sc. Lett. 233, pp. 275–390.

Neubauer F. Genser, J., Kurz, W., Wang, X., 1999. Exhumation of the Tauern Window, Eastern Alps, Phys. Chem. Earth 24, No. 8, pp. 675–680.

Oberli, F., Rosenberg, C.L., Berger, A., Meier, M.G., 2004. U-Th-Pb and $^{230}Th/^{238}U$ disequilibrium isotope systematics: Precise accessory mineral chronology and melt evolution tracing in the Alpine Bergell intrusion. Geochim. Cosmochim. Ac. 11, pp. 2543–2560.

Paterson, S.R., Tobisch, O.T., 1988. Using pluton ages to date regional deformations: problems with commonly used criteria. Geology 16, 1108–1111.

Phillips R. J., Parrish, R.R., Searle, M.P., 2004. Age constraints on ductile deformation and long-term slip rates along the Karakoram fault zone, Ladakh, Earth Planet. Sc. Lett. 226, pp. 305–319

Polinski R.K., Eisbacher, G.H., 1992. Deformation partitioning during polyphase oblique convergence in the Karawanken Mountains, southeastern Alps, J. Struc. Geol. 14, No. 10, pp. 1203–1213.

Pollington, A.D., Baxter, E.F., 2010. High resolution Sm-Nd garnet geochronology reveals the uneven pace of tectonometamorphic processes, Earth Planet. Sc. Lett. 293, pp. 63–71.

Pollington, A.D., Baxter, E.F., 2011. High precision microsampling and preparation of zoned garnet porphyroblasts for Sm-Nd geochronology, Chem. Geol. 281, pp. 270–282.

Ratschbacher, L., Frisch, W., Linzer, H.G., Merle, O., 1991. Lateral extrusion in the Eastern Alps, Part 2: Structural Analysis, Tectonics 10, pp. 257–271.

Resor, P.G., Chamberlain, K.R., Frost, C.D., Snoke, A.W., Frost, B.R., 1996. Direct dating of deformation: U-Pb age of syndeformational sphene growth in the Proterozoic Laramie Peak shear zone. Geology 24, pp. 623–626.

Rolland, Y., Rossi, M., Cox, S.F., Corsini, M., Mancktelow, N., Pennacchioni, G., Fornari, M., Boullier, A.M., 2008. $^{40}Ar/^{39}Ar$ dating of synkinematic white mica: insights from fluid–rock reaction in low-grade shear zones (Mont Blanc Massif) and constraints on timing of deformation in the NW external Alps. In: Wibberley, C. A. J., Kurz, W., Imber, J., Holdsworth, R. E., Collettini, C. (Eds) The Internal Structure of Fault Zones: Implications for Mechanical and Fluid-Flow Properties, Geol. Soc., London, Spec. Publ., doi: 10.1144/SP299.18.

Rosenberg, C.L., Brun, J.P. Cagnard, F., Gapais D. 1997. Oblique indentation in the Eastern Alps: Insights from laboratory experiments, Tectonics 26, doi:10.1029/2006TC001960.

Rosenberg, C.L., Brun, J.-P., and Gapais, D., 2004. An indentation model of the Eastern Alps and the origin of the Tauern Window. Geology 32, pp. 997–1000.

Rosenberg, C.L., Berger, A., 2009. On the causes and modes of exhumation and lateral growth of the Alps, Tectonics 28, doi:10.1029/2008TC002442

Rosenberg, C.L., Garcia, S., 2011. Estimating displacement along the Brenner Fault and orogen-parallel extension in the Eastern Alps, Int. J. Earth Sci. 100, pp. 1129–1145.

Rosenberg, C.L., Schneider, S., 2008. The western termination of the SEMP Fault (eastern Alps) and its bearing on the exhumation of the Tauern Window, In: Siegesmund, S., Fügenschuh, B., Froitzheim, N. (Eds) Tectonic Aspects of the Alpine-Dinaride-Carpathian System, Geol. Soc. London Spec. Publ. 298, pp. 197–218.

Rubatto, D., 2002. Zircon trace element geochemistry: partitioning with garnet and the link between U–Pb ages and metamorphism, Chem. Geol. 184, pp. 123–138.

Schmid, S.M., Fügenschuh, B., Kissling, E., Schuster, R., 2004. Tectonic map and overall architecture of the Alpine orogen, Eclogae Geol. Helv. 97, pp. 93–117¬¬.

Schmid, S.M., Scharf, A., Handy, M.R., Rosenberg, C.L., 2013. The Tauern Window (Eastern Alps. Austria): a new tectonic map, with cross-sections and a tectonometamorphic synthesis, Swiss J. Geosci. 106, pp. 1–32.

Selverstone, J., 1988. Evidence for East-West crustal extension in the Eastern Alps: implications for the unroofing history of the Tauern Window, Tectonics 7, pp. 87–105.

Selverstone, J., Spear, F., Franz, G., Morteani, G., 1983. High-Pressure Metamorphism in the SW Tauern Window, Austria: P-T Paths from Hornblende-Kyanite-Staurolite Schists, J. Petrol. 25, pp. 501–531.

Selverstone, J., Morteani, G., Staude, J.M., 1991. Fluid channeling during ductile shearing: transformation of granodiorite into aluminous schist in the Tauern Window, Eastern Alps, J. Metamorph. Geol. 9, 419–431.

Singer, B. S., Wijbrans, J. R., Nelson, S. T., Pringle, M. S., Feeley, T. C., Dungan, M., 1998. Inherited argon in a Pleistocene andesite lava: $^{40}Ar/^{39}Ar$ incremental-heating and laser-fusion analyses of plagioclase, Geology 26, 427–430.

Steiger, R.H., 1964. Dating of orogenic phases in the central Alps by K-Ar ages of hornblende, J. Geophys. Res. 69, pp. 5407–5421. doi:10.1029/JZ069i024p05407.

Sudo M., Uto, K., Anno, K., Ishizuka, O., and Uchiumi, S., 1998. SORI93 biotite: A new mineral standard for K-Ar dating. Geochem. J. 32, pp. 49–58.

Urbanek, C., Frank, W., Grasemann, B., Decker, K., 2002. Eoalpine versus Tertiary deformation: Dating of heterogeneously partitioned strain (Tauern Window, Austria). PanGeo Austria 2002, abstract volume.

Uto, K., Ishizuka, O., Matsumoto, A., Kamioka, H. and Togashi, S., 1997. Laser-heating $^{40}Ar/^{39}Ar$ dating system of the Geological Survey of Japan: System Outline and Preliminary Results. Bull. Geol. Surv. Jpn. 48, 23–46.

Warren, C.L., Smye, A.J., Kelley, S.P., 2012. Using white mica $^{40}Ar/^{39}Ar$ data as a tracer for fluid flow and permeability under high-P conditions: Tauern Window, Eastern Alps. J. Metamorph. Geol. 30, pp. 63–80. doi: 10.1111/j.1525-1314.2011.00956.x

Wells, M.L., Spell, T.L., Hoisch, T.D., Arriola, T., Zanetti, K.A., 2008. Laser-probe $^{40}Ar/^{39}Ar$ dating of strain fringes: Mid-Cretaceous synconvergent orogen-parallel extension in the interior of the Sevier orogen, Tectonics 27, doi: 10.1029/2007TC002153.

West, D.P. Jr., Lux, D. R., 1993. Dating mylonitic deformation by the ^{40}Ar-^{39}Ar method: An example from the Norumbega Fault Zone, Maine. Earth Planet. Sc. Lett. 120, pp. 221–237.

Williams, M.L., Jercinovic, M.J., Terry, M.P., 1999. Age mapping and dating of monazite on the electron microprobe: Deconvoluting multistage tectonic histories. Geology 27, pp. 1023–1026.

Willner, A.P., Sepúlveda, F.A., Hervé, F., Massonne, H.J., Sudo, M., 2009. Conditions and Timing of Pumpellyite–Actinolite-facies Metamorphism in the Early Mesozoic Frontal Accretionary Prism of the Madre de Dios Archipelago (Latitude 508200S; Southern Chile), J. Petrol. 50, pp. 2127–2155.

2.12 Supplementary material

2.12.1 Extraneous argon

Two types of extraneous Ar can be distinguished: First, excess Ar, which is the component of radiogenic ^{40}Ar apart from atmospheric ^{40}Ar that was brought into minerals by processes not related to the in situ decay of ^{40}K, e.g. incorporation of excess Ar, derived from incomplete degasing of clasts or from Ar diffused out of a fluid or out of pre-kinematic mineral into neighboring newly formed minerals. The presence of excess Ar is best shown by $^{40}Ar/^{36}Ar$ values >295.5 (McDougall and Harrison, 1999). The second type is inherited Ar, which might be incorporated into or trapped within minerals during their formation. This may happen by incomplete diffusional resetting of minerals, which are overprinted by geologic events (e.g. metamorphism) after their formation without complete isotopic homogenization during this event. The resulting ages are termed partly reset ages (Giogris et al., 2000; McDougall and Harrison, 1999; Mulch et al., 2005; Singer et al., 1998). Another example might be the incorporation of inherited Ar during pseudomorphism, e.g. chlorite after biotite where chlorite exhibits unreasonable high ages and an atmospheric-like $^{40}Ar/^{36}Ar$ value. Since, in this case the $^{40}Ar/^{36}Ar$ values are preserved, only the apparent age might uncover the presence of inherited Ar.

2.12.2 Example ST0730 of the Tuxer Shear Zones

Sample ST0730 (Fig. 9) from the Tuxer Shear Zones shows age values affected by excess Ar and partial resetting. The asymmetric, sigmoidal K-feldspar clast (K-fsp I, ca. 3 mm) has albite- and K-feldspar domains within its core. The K-feldspar domain is characterized by lower [Al], remnants of perthite and cracks (Tab. 1, Figs. 9, 10a). The asymmetric tail of the sigma clast consists of recrystallized elongate K-feldspar grains (K-fsp II, ca. 100–200 µm) with higher [Al] and without cracks and perthite exsolution (Tab. 1, Figs. 9, 10a). Three (*15–17* Fig. 9) out of eight analyses of K-feldspar are located within the K-feldspar clast and yield 33.5±1.0 Ma, 47.4±1.0 Ma and 49.4±2.6 Ma. Isochron calculation using analyses *16* and *17* (Fig. 9) yield a non-atmospheric-like $^{40}Ar/^{36}Ar$ value. Therefore, we argue that the isotopic composition of this K-feldspar clast is affected by excess Ar. Since the age range between 33.5 and 49.4 Ma of the protomylonite sample ST0730 of the Tuxer Shear Zones is even lower than most ages of K-feldspar clasts of 71.1–76.9 Ma observed in the protolith sample ST0732b the age values of sample ST0730 are probably affected by partial resetting. The remaining five analyses (*10–14* Fig. 9) of recrystallized K-feldspar vary between 32.5 and 18.0 Ma, whereat three analyses (*11, 12, 14* Fig. 9) overlap with the ages of syn-kinematic

phengite of the Tuxer Shear Zones. Hence, the latter ages may also reflect the timing of sinistral shear.

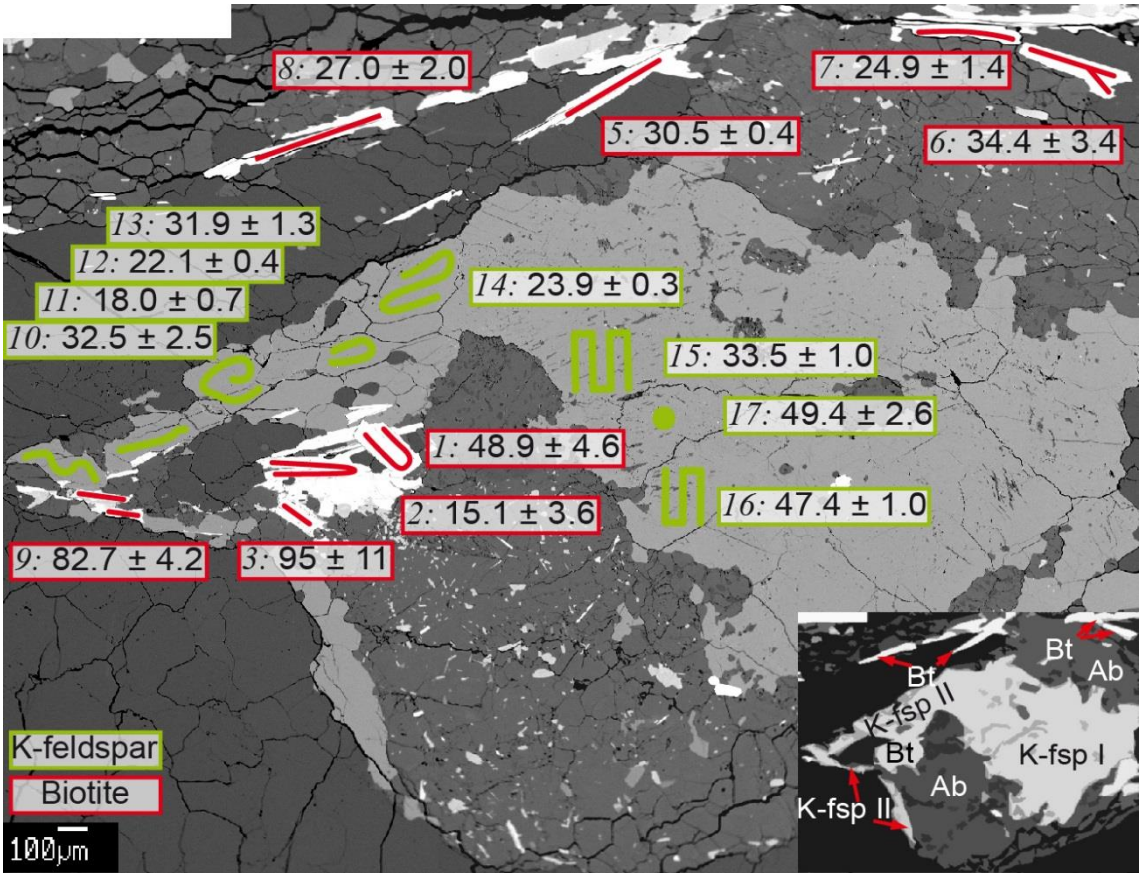

Figure 9: *BSE image of protomylonite sample ST0730 (Tuxer Shear Zones) and $^{40}Ar/^{39}Ar$ age results. In the lower right corner a simplified sketch overview of mineralogy is shown. The asymmetric, sigmoidal K-feldspar clast (ca. 3 mm length) consists of a K-feldspar and two albite-domains (K-fsp I, Ab). The K-feldspar clast domain shows remnants of perthite and cracks. The asymmetric tail of the sigma clast consists of recrystallized elongate K-feldspar grains (K-fsp II, 100–200 µm) without cracks and perthite exsolution. Biotite occurs aligned and parallel to the foliation and randomly oriented in the pressure shadow of the K-feldspar clast.*

Eight whole grain ablation analyses of biotite, whereat four analyses (*1–3, 9* Fig. 9) are located within the pressure shadow of the asymmetric K-feldspar clast, yield heterogeneous or unreasonably high age values of 48.9±4.6 Ma, 15.1±3.6 Ma, 94.1±10.5 Ma, and 82.7±4.2 Ma. Because of the microstructural site of these biotites within the pressure shadow of the K-feldspar clast and their ability to incorporate excess Ar released from the K-feldspar clast or a fluid during changing P_{Ar} (Reddy et al., 1996; Roddick et al., 1980; Warren et al., 2012), we argue that these four age values of biotite in the pressure shadow of the K-feldspar clast are affected by excess Ar. Clear evidence for inherited Ar was not observed in this study.

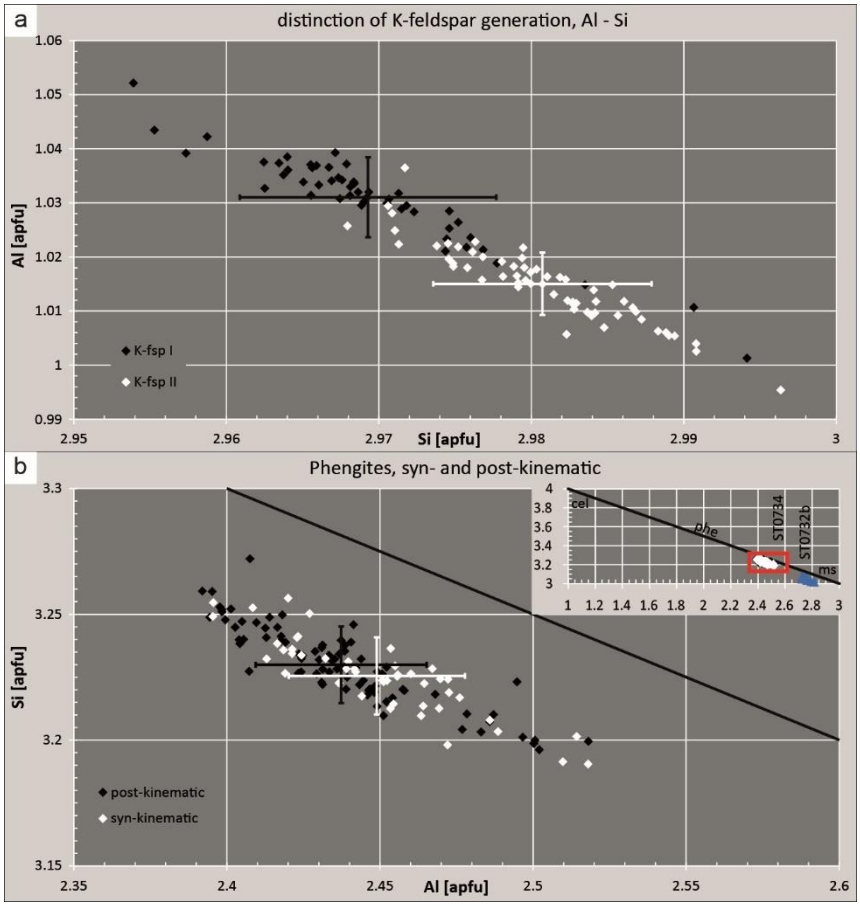

Figure 10a: *Diagram of Si versus Al atoms per formula unit [apfu] of K-feldspar clasts (K-fsp I=black diamonds) and recrystallized K-feldspar (K-fsp II=white diamonds) of sample ST0730 (Tuxer Shear Zones). Mean values and variability of the chemical composition are given as standard deviation (black bars=K-fsp I, white bars K-fsp II). Note the chemical difference between the two K-feldspar generations.* ***b:*** *Diagram of Al versus Si atoms per formula unit [apfu] of the syn-kinematic (white diamonds) and post-kinematic (black diamonds) phengites of ultramylonite sample ST0734 (Tuxer Shear Zones). Mean values and variability of the chemical composition are given as standard deviation (white bars=syn-kinematic phe, black bars=post-kinematic phe). Note the chemical similarity of syn- and post-kinematic phengites. Inlet in the upper right corner shows the data along a tie-line of phengite between the two end-members muscovite (ms; Al=3 and Si=3) and celadonite (cel; Al=1 and Si=4). In the lower right corner the chemical composition of muscovite of the protolith ST0732b are also shown as blue triangles.*

2.12.3 Pre-kinematic minerals

2.12.3.1 Muscovite

Large surface ablation performed on muscovite blasts of the protolith ST0732b (3 Fig. 2) yield age values between 33.8 and 21.9 Ma (*1, 6, 8, 14* Fig. 5d). These age values are slightly older than the ages obtained from syn-kinematic phengite of the ultramylonite ST0734 (3 Fig. 2) of the Tuxer Shear Zones. The muscovite blasts are clearly crosscut by and completely consumed in the ultramylonite which was observed in the outcrop of samples ST0732b and ST0734. Therefore, the muscovite reflects pre-kinematic age values which might indicate that ductile shear initiated after 21.9±1.2 Ma.

2.12.3.2 Biotite

Biotite analyses reveal scattering and ambiguous age values. Biotites of the Ahorn Shear Zone (ST0505, 2 Fig. 2) vary between 45.6 and 25.4 Ma, whereas biotites that are spatially closest to the phengite shear band (*4–8* Fig. 3b) yield age values overlapping with the phengite ages. The isochron of the latter biotites shows an atmospheric-like $^{40}Ar/^{36}Ar$ intercept (Tab. 2). A comparable spatial age younging of biotites was observed in the Tuxer Shear Zone sample FT0728 (6 Fig. 2; *9–11*, *13* Fig. 6c). Biotite ages pass from 15.2 to 6.9 Ma, when approaching syn-kinematic phengites. Analyses of biotite from a deformed amphibolite dyke of the Tuxer Shear Zones (ST0727, 5 Fig. 2) and from an undeformed mafic enclave of the same outcrop (ST0728, 5 Fig. 2) show large scatter of age values of 92.6 to 7.3 Ma (Tab. 2). These data lack any systematic trend and repeatability and are affected by extraneous Ar.

Biotite inclusions (7 Fig. 2) within an plagioclase clast of sample ST0706a yield 23.1±5.1 Ma and 15.8±2.4 Ma, overlapping with the syn-kinematic phengite ages, but the foliation-parallel biotites of this sample (Fig. 7b, Tab. 2) yield scattering and young age values varying from 15.8 to 7.9 Ma (Fig. 7b, Tab. 2). In the Greiner Shear Zone sample FT0719 (8 Fig. 2, Fig. 8b) comparable biotite age values of 13.9–4.4 Ma were observed. The small-scale age variation of these young biotites proscribes their interpretation as cooling ages. Since they overlap with ages of recrystallized K-feldspar they reflect rather formation ages.

2.12.3.3. K-feldspar

Analyses of a K-feldspar clasts yield ages of 53.9±4.5 Ma and 43.8±2.9 Ma (*3*, *5* Fig. 4b) for the Ahorn Shear Zone, and they vary between 49.4 and 33.5 Ma (*15–17* Fig. 9) for the Tuxer Shear Zones. In contrast, analysis of recrystallized K-feldspar of the Tuxer Shear Zones results in 22.4±3.8 Ma (8 Fig. 4b) and in an age range of 32.5 to 18.0 Ma (*10–14* Fig. 9), which overlaps with the ages of the syn-kinematic phengite of from samples of the same shear zone. K-feldspar analyses of the protolith sample ST0732b (Fig. 5d) yield scattering age values between 185.3 and 19.6 Ma (Tab. 2). Therefore, analyses of K-feldspar clasts in the protolith and the mylonites are interpreted as reflect partial resetting.

2.12.4 Rb/Sr methodology

Rb/Sr analyses of two samples (ST0505 and ST0734, Fig. 2) were carried out at the Freie Universität Berlin. Microsampling was performed using a microscope stage mounted micro mill gadget (Müller et al., 2000). Mono-mineral cores of albite and phengite (Ø=100–600 µm) were drilled out of 200 µm thick sections. Masses of the cores were calculated using the volume equation of a cylinder, the section thickness, the measured radii and typical mineral densities of albite and phengite. Enriched ^{87}Rb and ^{84}Sr spike solutions were added to the mineral cores and solved in a mixture (1:4) of concentrated nitric acid and hydrofluoric acid. The rubidium and strontium ions were separated in 2.5 M HCl chemistry using ion-chromatographic columns. Rb and Sr were loaded on double Re-filaments. Sample ST0505 was measured on a Finnigan MAT 261, where $^{87}Sr/^{86}Sr$ ratio of the measured standard NBS 987 yield 0.710246±30 (2 SE; standard error). Sample ST0734 was measured on a Thermo Scientific TRITON, where $^{87}Sr/^{86}Sr$ ratio of the measured standard NBS 987 yield 0.710245±10 (2 SE; standard error). The results of the Rb/Sr analyses are given in Table 3 (supplement).

Table 3. Rb/Sr in situ mineral ages of syn-kinematic phengite, albite and calcite out of thick sections

Mineral	Weight (µg)	Rb (ppm)	Sr (ppm)	$^{87}Rb/^{86}Sr \pm \sigma$	$^{87}Sr/^{86}Sr \pm \sigma$	Mineral 1	Mineral 2	Mineral 3	Mineral 4	Age (Ma) ± σ
ST0505 in situ drilling localities I, II and III										
Ib phe	13	556	82	19.702 ± 0.084	0.72036 ± 0.00040	Ib phe	Ic ab	-	-	24.4 ± 4.2
Ic ab	13	362	1052	0.9966 ± 0.0042	0.71388 ± 0.00041	Ib phe	Id ab	-	-	22.4 ± 3.9
Id ab	47	354	961	1.0670 ± 0.0045	0.71442 ± 0.00034	IIa phe	IIIb ab	-	-	21.1 ± 4.3
IIa phe	22	182	21	24.54 ± 0.10	0.71832 ± 0.00050					
IIIb ab	35	80	538	0.4283 ± 0.0018	0.71109 ± 0.00056					
ST0734 in situ drilling locality I										
Ia phe	38	476	91	15.225 ± 0.065	0.72038 ± 0.00015	Ia phe	Ib phe	Ic phe	If ab	16.28 ± 0.62
Ib phe	19	589	132	12.932 ± 0.055	0.71916 ± 0.00033					
Ic phe	30	497	95	15.159 ± 0.064	0.720403 ± 0.000063					
If ab	46	59	206	0.8358 ± 0.0035	0.717067 ± 0.000026					

Notes: per locality with a size of ≤ 1cm^2 monomieralic aggregates of ab, phe and cc were seperated using a microscope stage mounted micro mill gadet
localities within one thicksection of 200 µm are given in roman numerals
in situ drilling cores (80 - 300 µm in diameter)of one locality are given in small roman letters
drilled mineral phases: phe = phengite, ab = albite
minerals used for isochron calculation are given in arabic numerals
isochron calculation was performed using the Microsoft Excel Add-In 3.41 (Ludwig, 2008)

2.13 Supplement references

Giogris D., Cosca, M., Li, S., 2000. Distribution and significance of extraneous argon in UHP eclogite (Sulu terrain, China): insight from in situ $^{40}Ar/^{39}Ar$ UV-laser ablation analysis, Earth Planet. Sc. Lett. 181 (2000) 605–615.

McDougall, I., Harrison, M.T., 1999. Geochronology and Thermochronology by the $^{40}Ar/^{39}Ar$ Method, Oxford University Press, Oxford, 269 p.

Müller, W., Aerden, D., Halliday, A.N., 2000. Isotopic Dating of Strain Fringe Increments: Duration and Rates of Deformation in Shear Zones, Science 288, pp. 2195–2198.

Mulch, A., Cosca, M.A., Andresen, A., Fiebig, J., 2005. Time scales of deformation and exhumation in extensional detachment systems determined by high-spatial resolution in situ UV-laser $^{40}Ar/^{39}Ar$ dating, Earth Planet. Sc. Lett. 233, pp. 275–390.

Reddy, S.M., Kelly, S.P. and Wheeler, J., 1996. A $^{40}Ar/^{39}Ar$ laser probe study of micas from the Sesia Zone, Italian Alps: implications for metamorphic and deformation histories, J. metamorphic Geol., 1996, 14, pp.

Roddick, J.C., Cliff, R.A. and Rex, D.C., 1980. The evolution of excess argon in Alpine biotites $^{40}Ar/^{39}Ar$ analyses, Earth Planet. Sc. Lett. 48, pp. 185-208.

Singer, B. S., Wijbrans, J. R., Nelson, S. T., Pringle, M. S., Feeley, T. C., Dungan, M., 1998. Inherited argon in a Pleistocene andesite lava: $^{40}Ar/^{39}Ar$ incremental-heating and laser-fusion analyses of plagioclase, Geology 26, 427–430.

Warren, C.L., Smye, A.J., Kelley, S.P., 2012. Using white mica $^{40}Ar/^{39}Ar$ data as a tracer for fluid flow and permeability under high-P conditions: Tauern Window, Eastern Alps. J. Metamorph. Geol. 30, pp. 63–80. doi: 10.1111/j.1525-1314.2011.00956.x

3. Translation of indentation into lateral extrusion across a restraining bend: The western Tauern Window, Eastern Alps

3.1 Keywords

Eastern Alps; Tauern Window; Dolomites indentation; lateral extrusion; transpression; restraining bend

3.2 Abstract

The western Tauern Window accommodated shortening comparable to a crumble zone generated by convergence between the Dolomites indenter and the European foreland in the Oligo-Miocene time and translated this deformation into lateral extrusion. Our structural results point to a zone of localized deformation on the scale of the orogen consisting of tight, upright folds associated with a network of sinistral shear zones striking from southwest of the Indenter tip through the western Tauern Window and finally terminating in the SEMP Fault. Hence, the western Tauern Window links the sinistral NNE-striking Giudicarie Belt with the sinistral east-striking SEMP Fault, forming a large-scale restraining bend between them. The relationship between folds, shear zones and fabrics of the western Tauern Window (fold axial planes (AP_2), axial-plane foliations (S_2), and sinistral shear zones (C_{sin})) indicate an overall transpressional strain field.

North-directed Dolomites indentation of ~58 km resulted in upright ENE-striking folds accommodating ~38 km of shortening and a spatially associated, coeval network of sinistral shear zones accommodating the remaining ~20 km of shortening, causing ~26–31 km sinistral displacement. The kinematic continuity of the SEMP Fault with the Giudicarie Belt reinforces the idea that extensional displacement along the Brenner Fault is modest, hence exhumation of the western Tauern Window occurred mainly by folding and erosion, and extensional unroofing was of minor importance.

3.3 Introduction

The Tauern Window (Figure 1a) is the largest tectonic window of the Eastern Alps, where lower plate rocks once buried to depths >35 km were exhumed to ground level in Cenozoic time (e.g., Selverstone and Spear, 1985; Spear and Franz, 1986; Kurz et al., 2008). This east-west elongate window is a structural and metamorphic dome, whose arcuate axis coincides with the areas of Cenozoic, high-grade Barrovian metamorphism (Grundmann and Morteani, 1985; Selverstone, 1985) and with the youngest cooling ages (Most, 2003; Luth and Willingshofer, 2008; Rosenberg and Berger, 2009; Bertrand, 2013). The Tauern Window can be subdivided into an eastern and a western sub-dome, both characterized by elongate, concentric, metamorphic isograds (Grundmann and Morteani, 1985) and by intersecting and bordering shear zones (e.g., Neubauer et al., 1999; Linzer et al., 2002; Rosenberg et al., 2004; Scharf et al., 2013; Schneider et al., 2013). The central area between the two sub-domes is devoid of shear zones and characterized by the presence of higher tectonostratigraphic nappes that are mainly eroded within the adjacent sub-domes (Bousquet et al., 2012a; Schmid et al., 2013). The current debate on the exhumation mechanisms of the Tauern Window can be illustrated by two opposite models. One emphasizes orogen-parallel, large-scale extension, exhuming the eastern and western margins of the Tauern Window along low-angle

normal faults (e.g., Neubauer et al., 1999; Frisch et al., 2000). The other model emphasizes upright folding associated with erosional denudation (e.g., Cornelius, 1940; Laubscher, 1990). In spite of these differences, most authors agree on two points. First, exhumation of the Tauern Window is mainly caused by the northward displacement of the Dolomites Indenter (Figure 1a) (e.g., Cornelius, 1940). Second, Dolomites indentation caused an eastward, lateral extrusion of the Eastern Alps, associated with orogen-parallel extension (Figure 1a) (Ratschbacher et al., 1991a). However, the timing of Dolomites indentation, the absolute amounts of shortening, displacement and extension remain controversial (Neubauer et al., 1999; Frisch et al., 2000; Linzer et al., 2002; Rosenberg and Berger, 2009; Pomella et al., 2011, 2012; Rosenberg and Garcia, 2011, 2012; Fügenschuh et al., 2012; Luth et al., 2013; Scharf et al., 2013; Schmid et al., 2013).

We present new structural data from the western Tauern Window that we combine with a compilation of existing foliation data from the Tauern Window (Figure 2) (Angel and Staber, 1950; Exner, 1956; 1962a; 1962b; 1979; 1980; 1983; 1989; Karl et al., 1979; Frank et al., 1987; Becker, 1993; Höck et al., 1994; Giese, 2004; Lichtenheld, 2004; Moser, 2006; Frank and Pestal, 2008; Rockenschaub et al., 2009; 2011) to highlight the structural differences between the eastern and western sub-domes. We discuss these differences with respect to the kinematics of the Eastern Alps, and show that they reflect a large-scale transition from indentation to lateral extrusion that is consistent with our re-estimates of the amounts of shortening, displacement and extension in the western Tauern Window.

3.4 Geological setting of the western Tauern Window

3.4.1 Tectonometamorphic frame

The deepest structural units of the Tauern Window (Figure 1a) consist of Variscan basement, Permo-Carboniferous intrusives and their parautochtoneous host rocks covered by Post-Variscan meta-sediments, all forming the Venediger Duplex (Schmid et al., 2013). Rock units of the European distal Margin, the Matreier Zone (Piemont-Liguria Ocean), and the Glockner Nappe (Valais Ocean) were thrust on top of the Venediger Duplex (Figure 1a) (Schmid et al., 2013). The Austroalpine nappes surrounding the Tauern Window (Figure 1a) are Adria-derived and were thrust over Europe in the Cretaceous (Schmid et al., 2013).

The European distal margin consists of felsic and carbonate rocks, Triassic and Jurassic marbles (e.g. Hochstegenkalk) and bodies of Cenozoic eclogites (Schmid et al., 2013). The Matreier Zone is considered as a fossil accretionary prism formed during the subduction of the Piemont-Liguria Ocean in the Late Cretaceous (Schmid et al., 2013). It consists of an imbrication or mélange zone with m- to km-scale blocks of sedimentary to metamorphic rocks (Schmid et al., 2013) embedded in calcareous micaschists and subordinate ophiolitic lithologies.

The Glockner Nappe (Valais Ocean) consists mainly of calcareous micaschists and meta-pelites of Cretaceous age (Höck et al., 2006). It underwent the main stage of Barrovian metamorphism in the upper greenschist to amphibolite facies (0.53 GPa, 530 °C), with an early, poorly preserved blueschist and eclogite stage and prior to the amphibolite-facies metamorphism (Dachs and Proyer, 2001).

The timing of high-P (blueschist-facies) metamorphism is controversially debated. Some authors argue for Eocene (36 Ma, Zimmermann et al., 1994; 42-39 Ma, Ratschbacher et al., 2004; 39-38 Ma, Kurz et al., 2008) others for Oligocene (32 Ma, Glodny et al., 2005; 33 Ma, Smye et al., 2011; 33 Ma, Nagel et al., 2013). Kurz et al., (2008) argue for deformation-induces resetting during eclogite-facies metamorphism at 32 Ma. All units inside the Tauern Window were affected by Barrovian metamorphism (amphibolite-facies) subsequent ore coeval to the high-P event eclogite zone (Frank et al., 1987; Selverstone, 1993), in the Oligocene (32 Ma, von Blanckenburg et al.,

1989; 30-28, Inger and Cliff, 1994; ca. 30 Ma, Smye et al., 2011). The isograds of the Barrow metamorphism are concentric, cross-cut the nappe contacts and are sub-parallel to the upright folds that fold the nappes (e.g., Rosenberg and Garcia, 2011).

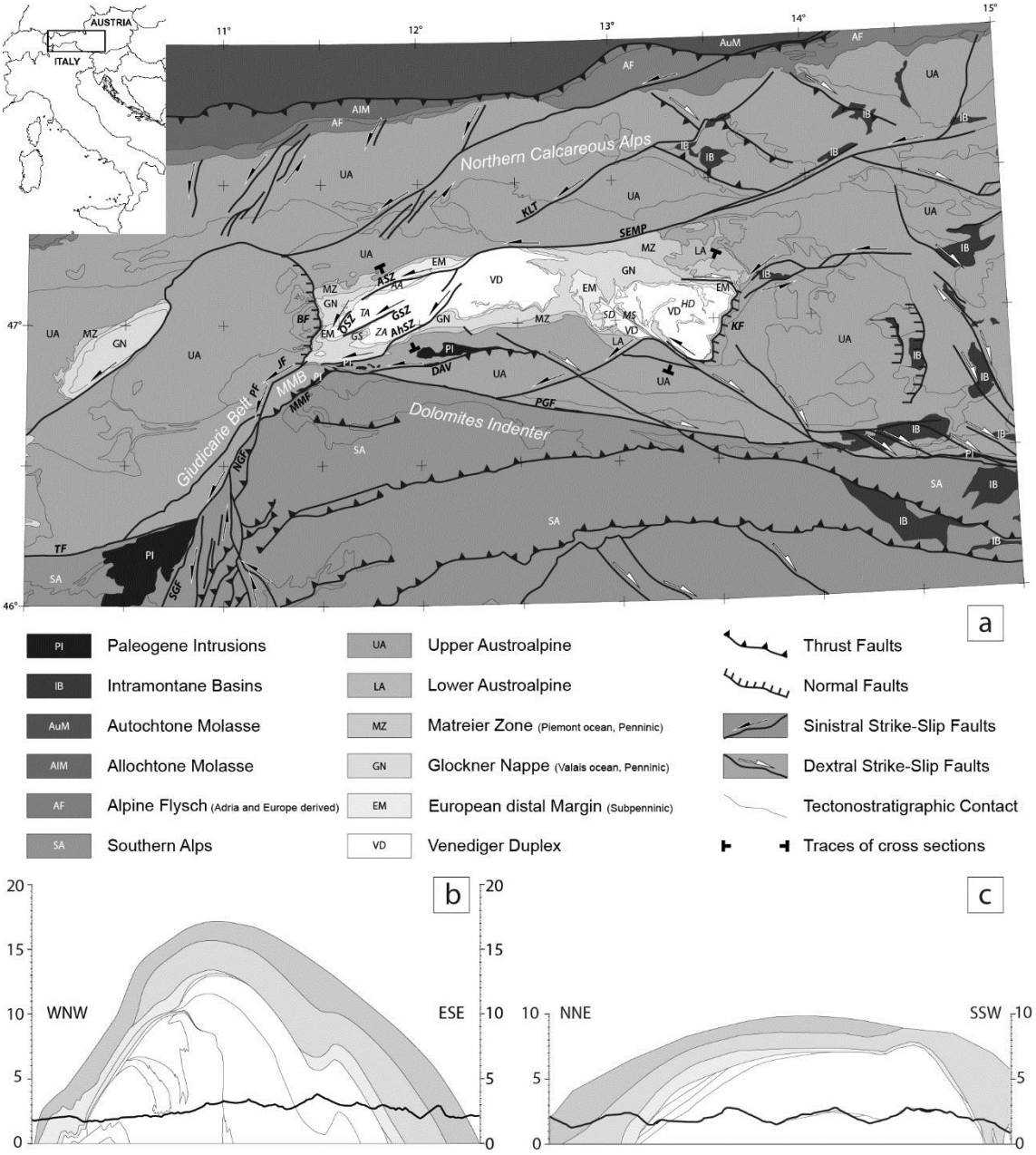

Figure 1a: *Simplified tectonostratigraphic map of the Tauern Window and surrounding units, modified after (Bousquet et al., 2012b). Highlighted are the discussed fault systems active in Cenozoic time. AhSZ=Ahrntal Shear Zone, ASZ=Ahorn Shear Zone, BF=Brenner Fault, DAV=Defereggen-Antholz-Vals Fault, GSZ=Greiner Shear Zone, JF=Jaufen Fault, KLT=Königssee-Lammertal-Traunsee Fault, KF=Katschberg Fault, MM=Meran-Mauls Fault, MMB=Meran-Mauls Basement, NFG=North Giudicarie Fault, OSZ=Olperer Shear Zone, PF=Passeier Fault, PGF=Pustertal-Gailtal Fault, SEMP=Salzach-Ennstal-Mariazell-Puchberg Fault, SGF=South Giudicarie Fault, TF=Tonale Fault. Fold structures are AA=Ahorn Antiform, GS=Greiner Synform, HD=Hochalm Dome, MS=Mallnitz Synform, SD=Sonnblick Dome, TA=Tuxer Antiform, ZA=Zillertaler Antiform* ***b:*** *Structural section crossing the western Tauern Window, simplified after Schmid et al. (2013).* ***c:*** *Structural section crossing the eastern Tauern Window, simplified after Schmid et al. (2013).*

The Austroalpine Units south of the Tauern Window are delimited by the Southern Alps. Because the latter were shortened less than the orogenic wedge described above, they are considered to have acted as indenters during collision (Ratschbacher et al., 1991; Rosenberg et al., 2004).

3.4.2 Structural frame

The western sub-dome consists of three upright antiforms (Ahorn-, Tuxer-, and Zillertaler Antiform; Figure 1a) that refold Early Alpine foliations generated by north-vergent nappe stacking during Adria-Europe collision (Schmid et al., 2013). Two-dimensional line-length balancing of the upright folds in the western sub-dome yields shortening amounts of 49 km for the entire dome structure (Rosenberg and Berger, 2009), or 32 km Schmid et al. (2013), for the Venediger Duplex above the present see-level. The upright folds are tight, strike ENE, have sub-horizontal doubly plunging fold axes, sub-vertical axial planes often associated with axial-plane foliations. The projected top of the antiform has a height of ~17 km (Figure 1b), from which an amplitude >20 km was inferred. In contrast, in the central and eastern Tauern Window upright folds strike east to ESE, have a lower top of the antiform (~10 km, Figure 1c), and no axial-plane foliation (Figure 2). These differences point to an eastward, along strike decrease in the amount of shortening.

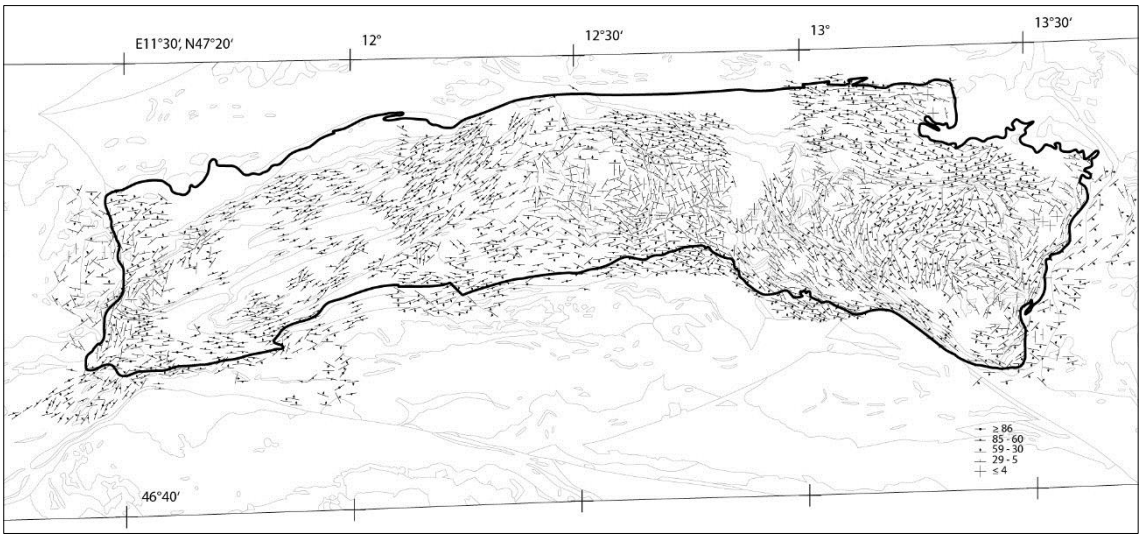

Figure 2: *Foliation map of the Tauern Window shows the main foliation (undifferentiated). Compiled literature data and own data (see paragraph 3.3 Introduction for references).*

The western margin of the Tauern Window is overprinted by the extensional Brenner Fault (Behrmann, 1988; Selverstone, 1988); the northern and southern margins of the western sub-dome and the tight, central Greiner Synform (Figure 1a) are overprinted by sinistral shear zones, striking sub-parallel to the axial planes of the upright folds. The major shear zones from north to south are the Ahorn (e.g., Rosenberg and Schneider, 2008), the Greiner (e.g., Steffen et al., 2001) and the Ahrntal shear zones (e.g., Reicherter et al., 1993), each of them being 1-3 km wide and several tens of kilometers long (Figure 1a). In addition, several small-scale sinistral shear zones in the range of 10s to 100s of meters width occur in and around the western Tauern Window (Figure 1a, and see paragraph 3.5.2 Shear zones of the western Tauern Window).

3.4.3 Timing of sinistral and extensional shear

Dating of fabric forming minerals of the major shear zones (Ahorn, Greiner, and Ahrntal shear zones) points to the inception of sinistral shear in the Lower Oligocene (~33 Ma) that continued until Upper Miocene time (Figure 3) (Barnes et al., 2004; Cole et al., 2007; Glodny et al., 2008; Schneider and Hammerschmidt, 2009; Kurz et al., 2008; Kitzig, 2010; Pollington and Baxter, 2010; Schneider et al., 2013). Miocene deformation ages also resulted from dating of minor shear zones in and around the western Tauern Window (Rinderkar, Tuxer, Olperer, Speikboden shear zones and Jaufen Fault) (Mancktelow et al., 2001, Müller et al., 2001; Cole et al., 2007; Frisch, 2010; Schneider et al., 2013). Sinistral shear terminated at 12-10 Ma inside the western Tauern Window (Schneider et al., 2013) and at 15-19 at the northern and southern margins (Schneider et al., 2013, Schneider et al., (in prep.)). Age data of fabric forming minerals and zircon fission tack (ZFT) cooling ages of the folded footwall of the Brenner Fault suggest a longevitiy of 15 Myr (21-7 Ma, Figure 3) (Fügenschuh et al., 1997; Glodny et al., 2008).

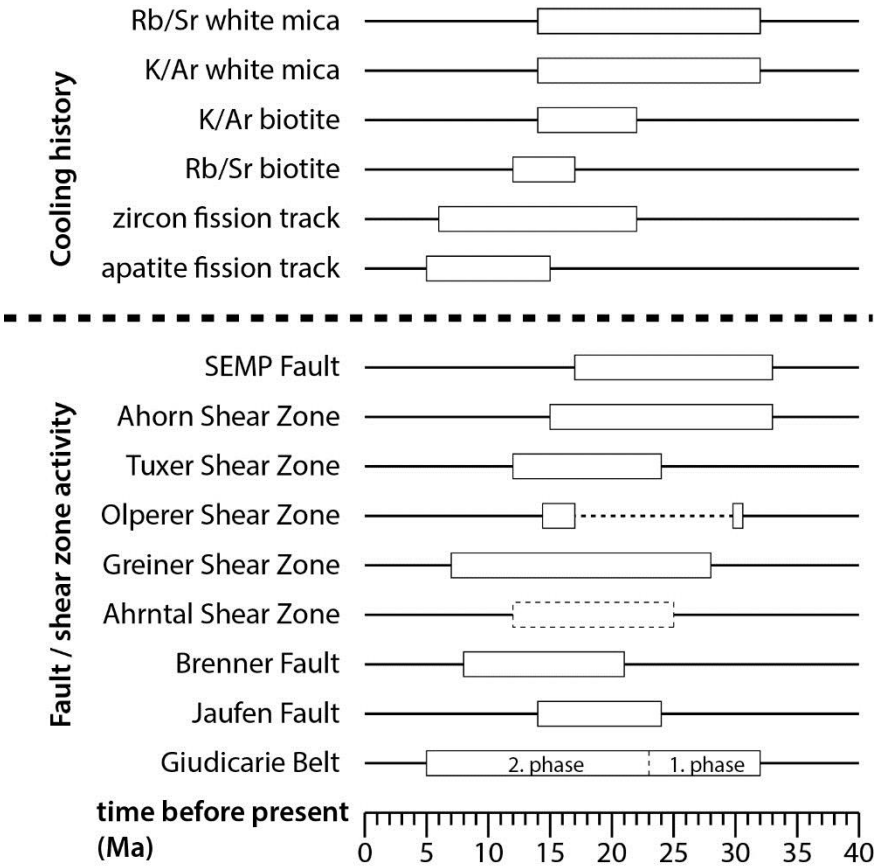

Figure 3: *Time ranges of cooling ages from the western Tauern Window (upper third). Rb/Sr white mica (Satir, 1975; Satir and Morteani, 1982; von Blanckenburg et al., 1989); K/Ar white mica (Satir, 1975; Raith et al., 1978; Thöni, 1980; von Blanckenburg et al., 1989); K/Ar biotite (Satir, 1975; Raith et al., 1978; von Blanckenburg et al., 1989; Most, 2003); Rb/Sr biotite (Satir, 1975; Borsi et al., 1978; von Blanckenburg et al., 1989); ZFT (Fügenschuh et al., 1997; Most, 2003; Bertrand, 2013); AFT (Grundmann and Morteani, 1985; Fügenschuh et al., 1997; Most, 2003; Bertrand, 2013). Longevities of ductile shear zones inside and transpressive faults outside the western Tauern Window (lower two third). North Giudicarie Fault (Müller et al., 2001); Jaufen Fault (Müller et al., 2001; Viola et al., 2001; Pomella et al., 2012; Bertrand, 2013 Schneider et al., (in prep.)); Brenner Fault (Fügenschuh et al., 1997; Glodny et al., 2008); Ahrntal Shear Zone (Cole et al., 2007; Glodny et al., 2008; Schneider and Hammerschmidt, 2009; Kitzig, 2010); Greiner Shear Zone (Barnes et al., 2004; Cole et al., 2007; Glodny et al., 2008; Pollington and Baxter, 2010;*

Schneider et al., 2013); Olperer Shear Zone (Glodny et al., 2008), Tuxer shear zones (Frisch, 2010; Schneider et al., 2013); Ahorn Shear Zone (Cole et al., 2007; Glodny et al., 2008; Schneider et al., 2013).

3.4.4. Cooling history

Cenozoic cooling ages characterize the Tauern Window (Figure 3) and Austroalpine rocks in the area adjacent to the indenter corner (Borsi et al., 1978; Spiess, 1995; Pomella et al., 2012), in contrast to the remaining Austroalpine rocks of the Eastern Alps, which typically show Cretaceous cooling ages. Isochron contours of different chronometers within the Tauern Window show a concentric elongate pattern that strikes sub-parallel to the trace of the upright folds and of the metamorphic isograds (Luth and Willingshofer, 2008; Rosenberg and Berger, 2009; Bertrand, 2013). The spatial distribution of cooling ages is characterized by older ages in the eastern and central Tauern Window compared to the western sub-dome, by a concentric isochron pattern with younger cooling ages in the center and older ones (up to 32 Ma) at the northern and southern margins (Satir, 1975; Borsi et al., 1975; Thöni, 1981) indicating a dome structure (Luth and Willingshofer, 2008; Rosenberg and Berger, 2009). Bertrand (2013) recently indicating that the youngest apatite fission track (AFT) and ZFT cooling ages coincide mainly with the fold culmination of the western sub-dome but also with its western margin.

ZFT cooling ages of the Austroalpine rocks in the Hanging wall of the Meran-Mauls Fault of the Dolomites indenter (Figure 1a) vary between 20 and 14 Ma (Viola et al., 2001; Pomella et al., 2012; Bertrand, 2013), hence being in the same cooling-age range as ZFT ages in the western Tauern Window (Most, 2003; Bertrand, 2013). Therefore, rocks north of the Meran-Mauls Fault cooled below the ZFT closure temperature coevally with the western Tauern Window (Rosenberg and Berger, 2009). North of the North Giudicarie Fault ZFT cooling ages are up to 35 Ma (Pomella et al., 2012).

3.4.5. Surrounding faults

3.4.5.1 Giudicarie Belt and Meran-Mauls basement

The sinistral transpressive Giudicarie Belt (Figure 1a) consists of several faults forming the western margin of the Dolomites Indenter, a ~77 km long NNE-striking segment of the otherwise mainly east-striking Periadriatic Line. The initial structure, the timing and the absolute displacement of the Giudicarie Belt are still debated. Some models assume an early Alpine jog of the Periadriatic Line around the corner of the future Dolomites indenter, hence a smaller Cenozoic sinistral displacement along the Giudicarie Belt amounting to 15 to 30 km (e.g., Picotti et al., 1995; Müller et al., 2001; Viola et al., 2001). Other models favor an originally straight Periadriatic Line, hence a Cenozoic sinistral displacement of ~70 km along the Giudicarie Belt caused by Dolomites indentation (e.g., Laubscher, 1988; Ratschbacher et al., 1991b; Werling, 1992). Following Laubscher (1988), and estimating an increase of ~50 km of Miocene north-south shortening from East to West of the Giudicarie Belt based in the Southern Alps on both sides of the Giudicarie belt (Schönborn, 1992; Nussbaum, 2000), we assume an originally straight Periadriatic Line and therefore a total of ~77 km apparent displacement between the Tonale and Pustertal-Gailtal faults corresponding to ~58 km of north-directed shortening (Figure 1a).

Assuming a northward movement of the Dolomites Indenter (e.g., Ratschbacher et al., 1991a), the eastern end of the Tonale Fault was located ~49 km west of the western end of the Pustertal-Gailtal Fault. These two faults were connected by an East-West segment of the Periadriatic Line which was progressively rotated into the Giudicarie Belt. Therefore less than ~77 km, the present-day length of the Giudicarie Belt, corresponds to a true sinistral displacement.

To the north, the Giudicarie Belt terminates in the Jaufen, the Meran-Mauls, and the Passeier faults, that together with the southwestern corner of the Tauern Window delimit the so-called Meran-Mauls basement (Figure 1a) (Pomella et al., 2011, 2012). The Passeier Fault is a late-stage structure of the Giudicarie Belt, since it crosscuts and postdates the Jaufen and the Meran-Mauls fault (Müller et al., 2001; Pomella et al., 2011).

Deformation age data of faults from the Giudicarie Belt cover the Oligo-Miocene time range. Thrust-related mylonites and pseudotachylites along the North Giudicarie and Meran-Mauls faults reveal Oligocene deformation ages (32-29 Ma and 26.9±0.8 Ma, respectively) (Müller et al., 2001). Pre-kinematic zircons of sinistrally and dextrally sheared dykes along the Jaufen Fault predated shearing at 32-30 Ma (Müller et al., 2001), whereas pseudotachylites and syn-kinematic minerals of mylonites from the Jaufen Fault reveal Oligo-Miocene deformation ages (21-17 Ma and 24-14 Ma, respectively) (Müller et al., 2001; Schneider et al., (in prep.)). Analyses of a pseudotachylite from the Passeier Fault revealed Miocene deformation age of 17.3±1.1 Ma (Müller et al., 2001).

Pomella et al. (2011, 2012), based on paleomagnetic and magnetic fabric, and on geochronological and structural data suggested that the activity of the Giudicarie Belt including the Meran-Mauls Fault started in Late Oligocene after emplacement of the Periadriatic intrusions (42-30 Ma). The first phase of the sinistral Giudicarie Belt bent the Periadriatic Line and terminated in the thrust of the Meran-Mauls Fault (Figures, 1a and 3), where deformation continued along the Naif Fault (Pomella et al., 2011). A second phase, during ongoing indentation, led to the formation of the Passeier- and the North Giudicarie faults, crosscutting the Meran-Mauls and Jaufen faults in their later stager, and to the exhumation of the Meran-Mauls basement at 17 Ma (Figures, 1a and 3).

Scharf et al. (2013) and Schmid et al. (2013) argue for initiation of Dolomites indentation not earlier than in Miocene time using local stratigraphic age constraints from the Monte Brione formation (Luciani and Silvestrina, 1996; Sciunnach, 2010), located close to the South Giudicarie Fault and from "thermal modelling" of the exhumation of the western Tauern Window (Fügenschuh et al., 1997), (see paragraph 5.5 for discussion).

3.4.5.2. Salzach-Ennstal-Mariazell-Puchberg (SEMP) Fault

The sinistral transpressive SEMP Fault (Figure 1a) strikes ENE, starting from the northern central margin of the Tauern Window, along 400 km until the Vienna Basin (Frost et al., 2009). This fault was active in the Oligo-Miocene, as suggested from $^{40}Ar/^{39}Ar$ ages of syn-kinematic white micas (Urbanek, 2002) and by deformed Miocene sediments in the Hieflau and Vienna basins (Peresson and Decker, 1997). Deformation of quaternary stalactites suggests that the SEMP Fault is still active at least along its eastern segment (Plan et al., 2010). Balancing the displacement accommodated by the SEMP Fault yield ~60 km of left-lateral motion (Linzer et al., 2002). Analogue models (Ratschbacher et al., 1991a; Rosenberg et al., 2004; 2007) designed to simulate indentation into the Eastern Alps suggest that the activation of sinistral analogue faults forming the northern boundary of the extruding wedge, as the SEMP Fault, may initiate in the earliest stages of indentation being approximately parallel to the western indenter margin, and rotate clockwise towards the northern margin of the Dolomites indenter.

3.4.5.3 Pustertal-Gailtal Fault

The Pustertal-Gailtal Fault (Figure 1a) formed along a segment of the pre-existing Periadriatic Line that has a prolonged tectonic history starting in Cretaceous (Schmid et al., 2013). Estimates on the Oligo-Miocene displacement are missing (Bistacchi et al., 2010). K/Ar formation ages of illite fractions of the brittle Sprechenstein-Mauls fault gouge, the westernmost segment of the Pustertal-Gailtal Fault vary between 13 and 16 Ma (Zwingmann and Mancktelow, 2004).

3.4.5.4 Defereggen-Antholz-Vals (DAV) and Speikboden faults

The 90 km long DAV Fault within the Austroalpine rocks (Figure 1a) coincides with the southern limit of Alpine metamorphism (Hoinkes et al., 1999) separating Cenozoic and partly reset Rb/Sr biotite cooling ages in the north from pre-Alpine Rb/Sr biotite cooling ages in the south (Borsi et al., 1973, 1978). $^{40}Ar/^{39}Ar$ dating of pseudotachylites from the DAV Fault yield 25.5±0.9 Ma, whereas a pseudotachylite from the Speikboden shear zone yields an apparent age of ~20 Ma (Mancktelow et al., 2001; Müller et al., 2001). Syn-kinematic micas of sinistral mylonites (Rb/Sr microsampling), and zircons (U/Pb) from sinistrally deformed dykes, yield, deformation and intrusion ages of ~30 Ma suggesting that sinistral shear terminated at 30 Ma (Müller et al., 2000).

The Speikboden Fault (Figure 4d) was interpreted as antithetic Riedel to the Pustertal-Gailtal Fault (Mancktelow et al., 2001; Müller et al., 2001). Considering its parallel orientation to some of the sinistral shear zones inside of the western Tauern Window (Figure 4d), and its Miocene deformation age (Mancktelow et al., 2001), we suggest that this and other NE-directed sinistral shear zones in the Austroalpine are related to the sinistral shear zones inside the western Tauern Window, which also have Miocene deformation ages (Glodny et al., 2008; Pollington and Baxter, 2010; Schneider et al., 2013).

3.4.5.5 Brenner Fault

First estimates on the amount of east-west extension vary between 9 and 14 km (Behrmann, 1988), or "several to tens" of kilometers (Selverstone, 1988). Recent estimates vary between 70 km (Fügenschuh et al., 1997), 4-12 km (Rosenberg and Garcia, 2011, 2012) and 44 km (Fügenschuh et al., 2012). The vertical offset (stratigraphic omission) of the Brenner Fault varies continuously along strike (Rosenberg and Garcia, 2011, 2012) and attains a maximum of ~17 km in the area of the Brenner Pass, along the hinge of the Tuxer Antiform (Figure 1a), where the Brenner Mylonites have their maximum thickness (Behrmann, 1988; Selverstone, 1988; Axen et al., 1995).

Recent re-assessment (Rosenberg and Garcia, 2011, 2012; Fügenschuh et al., 2012) showed that east-west extension along the Brenner Fault was overestimated in previous studies (Axen et al., 1995; Selverstone et al., 1995; Fügenschuh et al., 1997) because vertical displacements from both normal faulting and upright folding was entirely attributed to normal faulting. Following the structural arguments of (Rosenberg and Garcia, 2011, 2012) and using the average dip angle of the Brenner Mylonites obtained in this study we estimate that east-west extension accommodated by the Brenner Fault is ≤10 km.

3.5 Results

3.5.1 Deformation fabrics

Based on their orientation and shear sense, we subdivided all structural data into five distinct structural domains (Figure 4a) and three main foliations. Foliations that formed prior to upright folding were summarized as S_1 foliations (Figure 4b), although they may not have the same age. In the Austroalpine rocks S_1 foliations are Cretaceous (Bousquet et al., 2012b). In the European distal Margin and ocean-derived units, S_1 foliations formed during nappe-stacking and/or high-pressure metamorphism in the Eocene (Bousquet et al., 2012b). In the Venediger Duplex S_1 foliations formed during north-vergent imbrication in the Eocene/Oligocene (Schmid et al., 2013) or in the Oligocene (Glodny et al., 2005; Nagel et al., 2013). In addition, pre-alpine foliations e.g. of igneous rocks or migmatites, do exist in the Venediger Duplex and in the Austroalpine rocks.

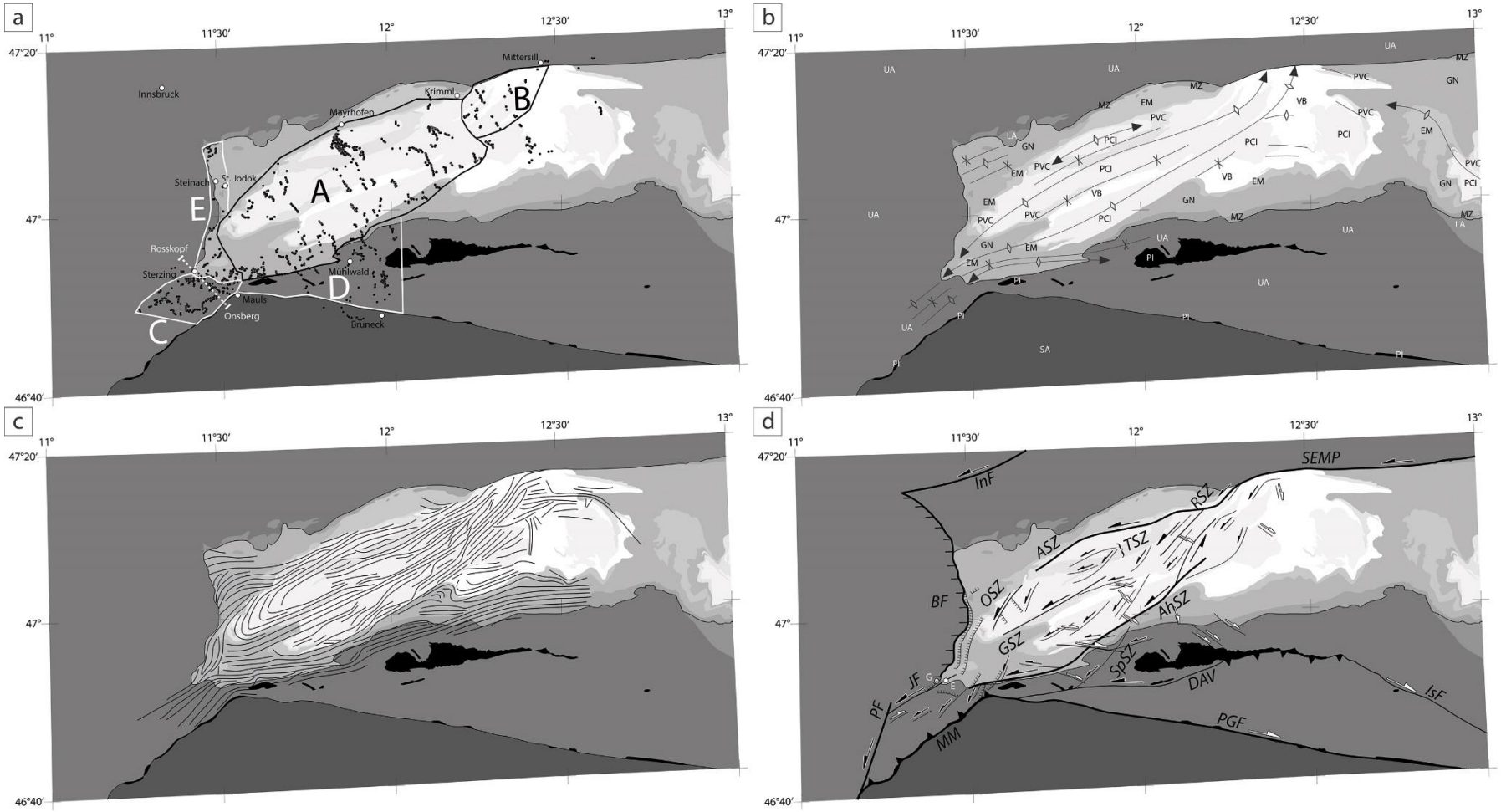

PI Paleogene Intrusions
SA Southern Alps
UA Upper Autroalpine
LA Lower Austroalpine
MZ Matreier Zone (Piemont ocean, Penninic)
GN Glockner Nappe (Valais ocean, Penninic)
EM European distal Margin (Subpenninic)
PVC Post-Variscian Cover
PCI Permo-Carboniferous Intrusions
VB Variscian Basement
Thrust Faults
Normal Faults
Sinistral Strike-Slip Faults
Dextral Strike-Slip Faults
Antiforms
Synforms
Innsbruck Towns and Villages
Onsberg Local Summits

AhSZ=Ahrntal Shear Zone, *ASZ*=Ahorn Shear Zone,
BF=Brenner Fault, *DAV*=Deferggen-Antholz-Vals Fault,
GSZ=Greiner Shear Zone, *InF*=Inntal Fault, *IsF*=Iseltal Fault, JSZ=Jaufen Shear Zone, *MM*=Meran-Maules Fault, *OSZ*=Olperer Shear Zone,
PF=Passeier Fault, *PGF*=Pustertal Fault, *SEMP*=Salzach-Ennstal-Puchberg-Mariazell Fault, *SpSZ*=Speikboden Shear Zone, *TSZ*=Tuxer shear zones

Figure 4: *Different close up's of the western Tauern Window based on (Bigi et al., 1994) showing* ***a:*** *the outcrop distribution of this study and the five domains (A-E) in which the structural data were grouped. In domain C the trace of the structural section between Rosskopf and Onsberg (Figure 5) is given;* ***b:*** *the interpreted traces of the D_2 upright folds and the abbreviations of the tectonostratigraphic units;* ***c:*** *the interpreted traces of the S_{2a} axial-plane foliation;* ***d:*** *the traces of the macro-scale sinistral shear zones and their names are shown. In domains C and E top-to-the-west extensional displacement occurs along the Brenner Mylonites and in minor shear zones. In domains A and D minor dextral displacement is associated with sinistral one. Localities of the different Jaufen Fault branches: G=Gasteig, E=Elzenbaum.*

Upright F_2 folds with steep to vertical axial planes and sub-horizontal fold axes overprinted and folded the S_1 foliations (Figure 4c). Widespread axial-plane foliations (S_{2a}) of the tight, upright F_2 folds crosscut the folded nappe contacts. Along the western margin, where the hinge of the western sub-dome plunges consistently west, doming caused moderately to gently westward dipping S_{2b} extensional foliations overprinting the pre-existing S_1 foliations (Figure 4c). Both S_2 foliations are related to doming but spatially separated and further eastwards e.g., along the tight Greiner Synform, afar from the westward plunging hinge of the sub-dome, the S_{2b} extensional foliations progressively turn into the S_{2a} axial-plane foliations (Figure 2).

Locally a third, mylonitic foliation formed (Figure 4d) along major NNE- to ENE-striking, sinistral (C_{sin}) and minor ESE- to ENE-striking, dextral (C_{dex}) shear zones (Reicherter et al., 1993; Lammerer and Weger, 1998; Cole et al., 2007; Rosenberg and Schneider, 2008; Schneider et al., 2013). West-dipping foliations related to predominant top-to-the-west and minor top-to-the-east normal shear zones (C_{nor}) along the western margin of the Tauern Window, the Brenner Mylonites, (Figure 4d) (Behrmann, 1988; Selverstone, 1988) are interpreted to be contemporaneous with the transcurrent shear zones. All shear foliations are tight, penetrative, mylonitic foliations, showing higher mica contents (Selverstone, 1993), smaller grain sizes compared to the S_2 foliations, and are associated with shear indicators.

3.5.2. Shear zones of the western Tauern Window

Previous mapping and descriptions of map-scale sinistral shear zones of the western Tauern Window differ significantly between each other e.g., (Figure 2, Behrmann and Frisch, 1990), (Figures 1 and 2, Selverstone, 1985), (Figure 1, Selverstone et al., 1991), (Figures 1 and 2, Reicherter et al., 1993), (Figure 3a, Lammerer and Weger, 1996), (Figure 1, Linzer et al., 2002), (Figure 1, Rosenberg et al., 2004), (Figure 1, Rosenberg et al., 2007), (Figures 2 and 3, Glodny et al., 2008), (Figure 1, Schmid et al., 2013). In the following we present a short kinematic and petrologic summary and a new map (Figure 4) of the major ductile shear zones of the western Tauern Window and its adjacent Austroalpine rocks, based on our new mapping of these structures. A simplified structural section is draw crossing the Meran-Mauls basement (Figure 5).

3.5.2.1 Ahorn Shear Zone

The Ahorn Shear Zone is a 2.5 km wide and ~50 km long transpressive mylonitic belt located at the northern limb of the western sub-dome, showing sinistral and south-side-up kinematic indicators (Figure 4d) (Rosenberg and Schneider, 2008). It strikes ENE and dips sub-vertically. The transition from the brittle SEMP Fault to the easternmost Ahorn Shear Zone occurs in the area of Mittersill and Krimml (Figure 4a) where overall sinistral brittle-ductile and ductile faults of the Rinderkar Shear Zone strike nearly north and turn suddenly into the eastward striking SEMP Fault (Figure 4d) (Cole et al., 2007).

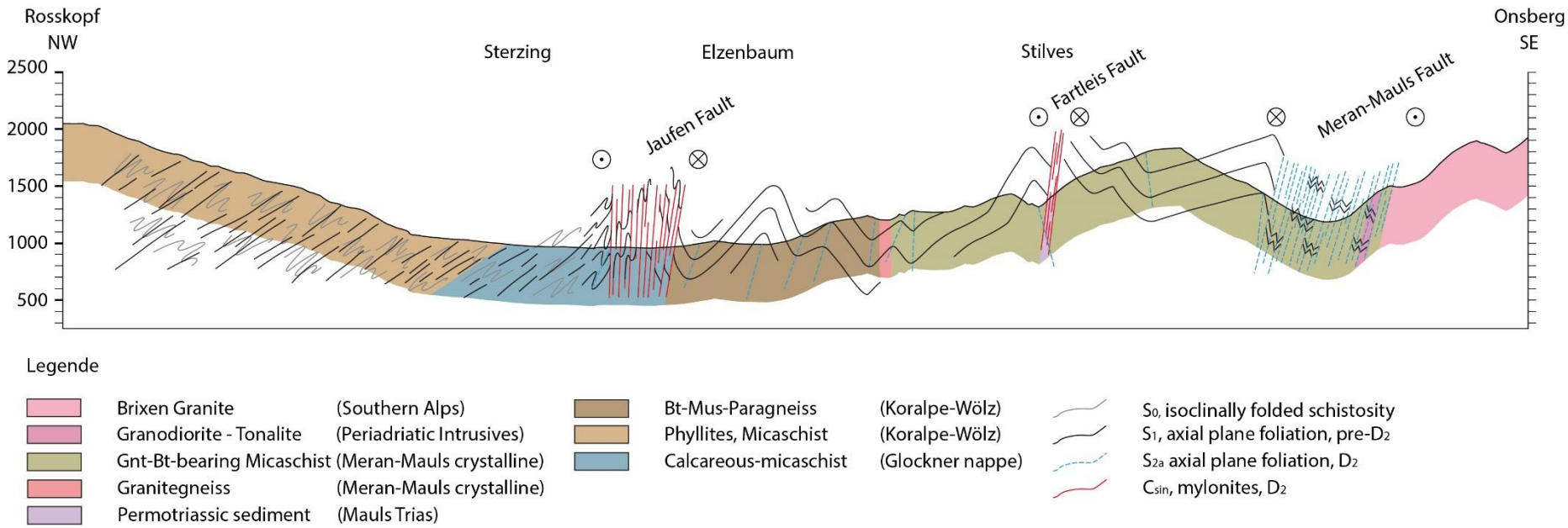

Figure 5: *SE trending structural cross section running from Rosskopf to Onsberg (see Figure 4a for map view). Lithological units were taken from the GK50 175 Sterzing. Jaufen-, Fartleis- and Meran-Mauls faults are indicated.*

3.5.2.2. Tuxer Shear Zones

A large number of outcrop-scale sinistral shear zones (1 to 10 m thickness) formed under lower amphibolite-facies conditions affected the central area of the western sub-dome suggesting the existence of an interconnected network that was termed Tuxer Shear Zones (Figure 4d) (Schneider et al., 2013). These shear zones strike NE- to east and dip sub-vertically to steeply south. To the ENE all these shear zones merge into the SEMP Fault (Figure 4d).

3.5.2.3 Greiner Shear Zone

The Greiner Shear Zone is situated within a first order tight syncline (Greiner Synform) between two large-scale antiforms (Tuxer and Zillertaler antiforms) in the center of the western sub-dome (Figures 1a and 4d) and affects all tectonostratigraphic units of the western Tauern Window (Selverstone, 1993; Steffen et al., 2001). It strikes east to ENE, dips steeply south, and was formed under amphibolite-facies conditions (e.g., Selverstone and Spear, 1985). Kinematic indicators show both sinistral (De Vecchi and Baggio, 1982; Behrmann and Frisch, 1990) and dextral (Barnes et al., 2004) senses of shear. Deformation temperatures increase eastwards and P estimates from syn-kinematic garnet at the eastern end of the Greiner Shear Zone (Figure 4d) suggest that deformation occurred at depths 35-40 km (Selverstone et al., 1991; Selverstone, 1993).

3.5.2.4 Olperer Shear Zone

Two sinistral shear zones (Lammerer and Weger, 1998, their Figure 3a), each of >40 km length, were inferred to connect and enter the SEMP Fault near Krimml (Figure 4a). Own investigations show that these structures are rather 10 to 15 km long (Figure 4d), strike NNE- to north and dip moderately to sub-vertically WNW to west. Deformation occurred within a 300 m thick zone under amphibolite-facies conditions, by combined sinistral and top-to-the-west extensional shear at the western end of the Olperer Shear Zone (Ebner et al., 2004).

3.5.2.5. Ahrntal Shear Zone

The Ahrntal Shear Zone (Figure 4d) is a 1.7 km wide and 70 km long (Schneider et al., 2009) transpressive mylonitic zone with predominant sinistral, minor dextral and north-side-up shear sense indicators, which strikes NE- to ENE and dips steeply to sub-vertically south. The Ahrntal Shear Zone formed under lower amphibolite- to greenschist-facies conditions (Kitzig, 2010; Wollnik, 2012). Key outcrops from north to south in the Vals Valley show south-directed and progressive transition from upright, tight folds (Figure 6a) in the north, to isoclinal folds with an axial-plane foliation (S_2; Figure 6b), finally overprinted by sinistral shear zones, also showing north-side-up kinematic indicators in the south (Figures 6c and 6d).

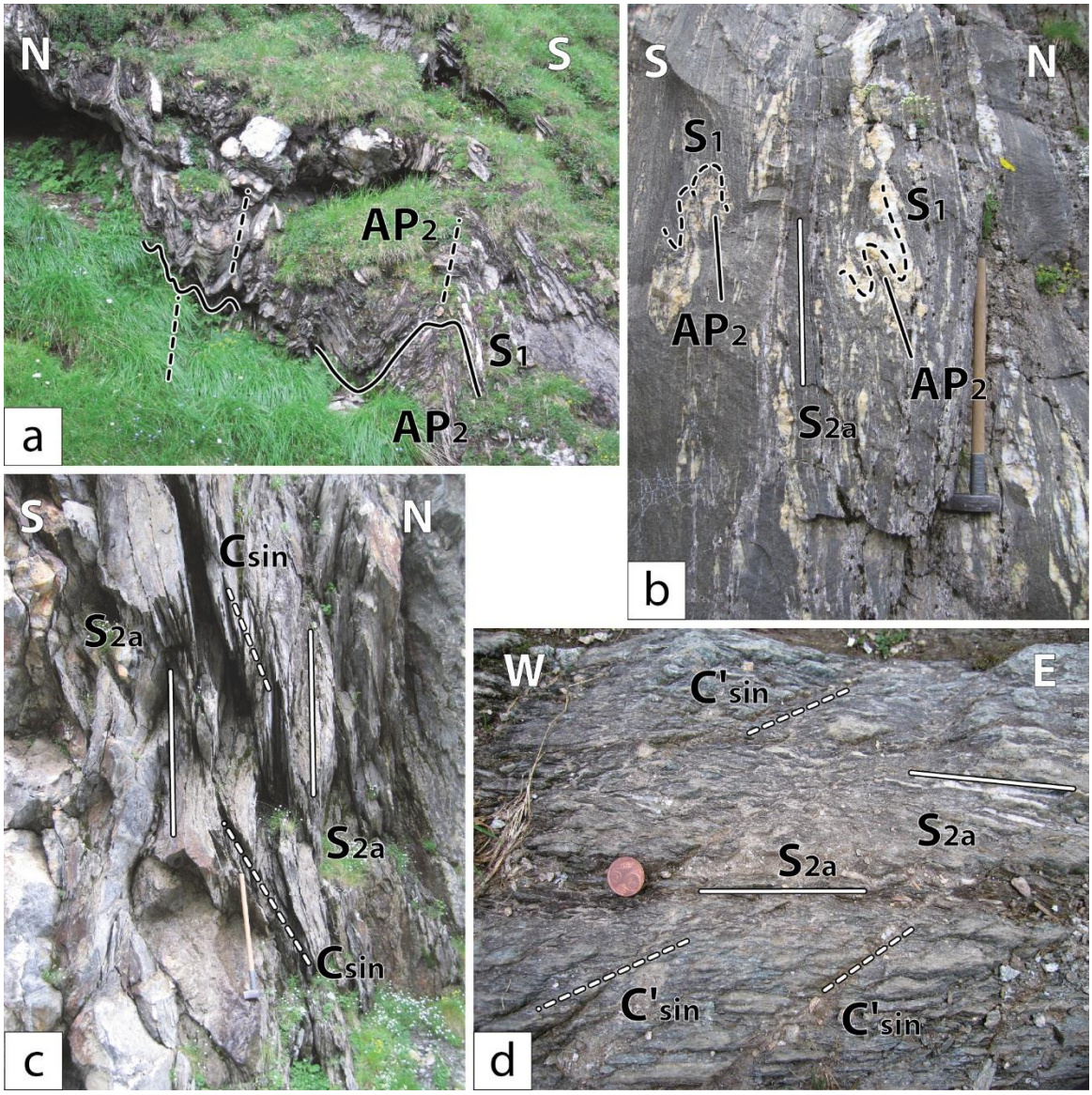

Figure 6: *Field photographs along the Vals valley from north to south.* ***a:*** *folded S_1 upright tight folds,* ***b:*** *tightly folded S_1 foliations, rootless folds, and newly formed sub-vertical S_{2a} axial-plane foliations,* ***c:*** *sub-vertical S_{2a} axial-plane foliations and localized sinistral shear zones C_{sin} having an additional north-side-up component, d. top view on sub-vertical S_{2a} axial-plane foliations and localized sinistral shear bands C'_{sin}.*

3.5.2.6 Meran-Mauls basement and Jaufen Fault

Our new structural data show that the Meran-Mauls basement between the Jaufen and the Meran-Mauls faults is folded by upright folds (F2) that are continuous with those of the western Tauern Window (Figures 4b, 4c, and 5). Since its first descriptions, the formation of the Jaufen Fault (Figure 4d) was related to the motion of the Dolomites Indenter (Spiess, 1995, 2001). Similar to the Olperer Shear Zone, field observations along the Jaufen Fault indicate that there are at least two branches of the Jaufen Fault. One branch accommodating top-to-the-west extensional shear in the area of Gasteig SW of Sterzing (Figure 4d) (Viola et al., 2001) and another branch affected by upright folding and mainly sinistral shear outcropping on the road to Pensenjoch NW of Elzenbaum (Figures 4d and 5) (Müller et al., 2001).

3.5.3 Structures of the western Tauern Window

3.5.3.1 S_1 foliation

In domains A, B and C (Figure 4a) folded S_1 foliations strike ENE and dip moderately to steeply NNW but also SSE indicating a south-vergence of the sub-dome (Figures 7a, 7b, and 7c). The sub-vertical pi-circle of domain A indicates a sub-horizontal WSW-ENE oriented fold axis (Figure 7a). The pi-circles indicate gently ENE-ward plunging fold axis (Figure 7b) in domain B, and WSW-ward plunging in domain C (Figure 7c). Along the northern and southern margins as well as in the tight synclines of the western Tauern Window, S_1 and S_2 form a composite foliation. On the outcrop scale regularly distributed crenulation cleavages and the occurrence of two distinct schistosities, corresponding to folded S_1 foliations crosscut by S_{2a} axial-plane foliations are observed (Figure 4b).

3.5.3.2 F_2 fold axes and axial planes

F_2 fold axes (FA_2) of domain A are sub-horizontal and oriented ENE-WSW (Figures 7a and 7f). The corresponding sub-vertical F_2 axial planes (AP_2) strike ENE (Figure 7k). In domain B the majority of the F_2 fold axes plunge moderately ENE-ward (Figure 7b), whereas in domain C they plunge SW-ward (Figure 7c). This change in plunge direction goes together with a similar change in orientation of the sub-vertical F_2 axial planes (Figures 7k, 7l, and 7m). The mean values of domain A and B strike consistently ENE, in contrast to the one of domain C, which strikes sub-parallel to the Meran-Mauls Fault and to the northwestern margin of the Dolomites Indenter (Figures 1a, 4b, and 4d).

3.5.3.3 S_2 foliations and L_2 stretching lineations

In domain A the sub-vertical S_{2a} axial-plane foliations strike consistently ENE (Figure 8a), slightly more northward than the corresponding F_2 axial planes (Figure 7k). The associated L_2 lineations plunge gently to sub-horizontally WSW, but also ENE. In domain B and C the mean values of the steep to sub-vertical S_{2a} axial-plane foliations strike ENE to NE (Figures 8b and 8c), which are slightly more northward directed than in domain A. The mean value of domain B predominantly dips SE-wards opposite to the one of domain C. The associated L_2 lineations are oriented sub-horizontally in domain B (Figure 8b) and plunge shallowly WSW in domain C (Figure 8c), hence L_2 lineations show a monotonous increase in plunge angle from NE to SW along strike (Figures 8a, 8b, and 8c). In domain E and at its transition to domain A shallowly, WNW-ward dipping S_{2b} extensional foliations dominate the structural grain. These foliations are composite foliations of the folded and westward-dipping S_1 foliations and top-to-the-west extensional shear planes.

Figure 7: *Stereo32 version 0.9 was used to plot Schmidt nets (Röller and Trepmann, 2008). All plots are equal area, lower hemisphere plots. Contouring using a cosine exponential equation was applied when the data show a preferred orientation and their absolute number was higher than fifteen, in the remaining few cases the raw data are shown. Mean values were deduced graphically in Stereo32 by the maxima of data culminations.* ***a, b, c, d, e:*** *Stereoplots of contoured S_1 foliations measurements in domains A-E. Great circles indicate pi-circles. Number of data, contouring intervals and parameters, and pi-circle value are given in the respective left columns.* ***f, g, h, i, j:*** *Stereoplots of contoured F_2 fold axes (FA_2) measurements in domains A-E. Number of data, contouring intervals and parameters, and mean values are given in the respective left columns.* ***k, l, m, n, o:*** *Stereoplots of contoured F_2 axial planes (AP_2) measurements in domains A-E. Great circles indicate AP_2 mean values. Number of data, contouring intervals and parameters, and mean values are given in the respective left columns.*

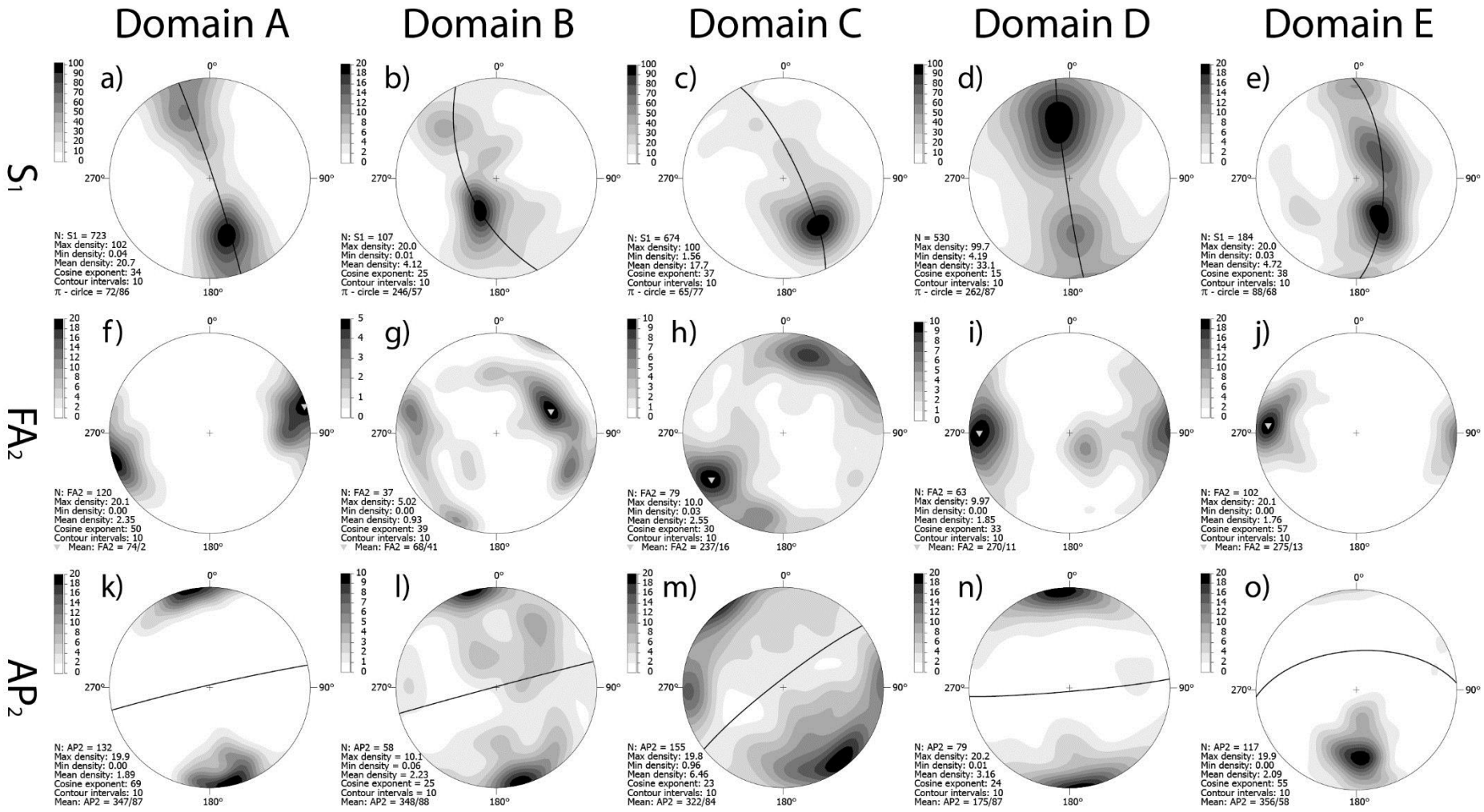
Domain A
Domain B
Domain C
Domain D
Domain E
S1
FA2
AP2
a)
N: S1 = 723
Max density: 102
Min density: 0.04
Mean density: 20.7
Cosine exponent: 34
Contour intervals: 10
π - cirlce = 72/86
b)
N: S1 = 107
Max density: 20.0
Min density: 0.01
Mean density: 4.12
Cosine exponent: 25
Contour intervals: 10
π - circle = 246/57
c)
N: S1 = 674
Max density: 100
Min density: 1.56
Mean density: 17.7
Cosine exponent: 37
Contour intervals: 10
π - circle = 65/77
d)
N = 530
Max density: 99.7
Min density: 4.19
Mean density: 33.1
Cosine exponent: 15
Contour intervals: 10
π - circle = 262/87
e)
N: S1 = 184
Max density: 20.0
Min density: 0.03
Mean density: 4.72
Cosine exponent: 38
Contour intervals: 10
π - circle = 88/68
f)
N: FA2 = 120
Max density: 20.1
Min density: 0.00
Mean density: 2.35
Cosine exponent: 50
Contour intervals: 10
Mean: FA2 = 74/2
g)
N: FA2 = 37
Max density: 5.02
Min density: 0.00
Mean density: 0.93
Cosine exponent: 39
Contour intervals: 10
Mean: FA2 = 68/41
h)
N: FA2 = 79
Max density: 10.0
Min density: 0.03
Mean density: 2.55
Cosine exponent: 30
Contour intervals: 10
Mean: FA2 = 237/16
i)
N: FA2 = 63
Max density: 9.97
Min density: 0.00
Mean density: 1.85
Cosine exponent: 33
Contour intervals: 10
Mean: FA2 = 270/11
j)
N: FA2 = 102
Max density: 20.1
Min density: 0.00
Mean density: 1.76
Cosine exponent: 57
Contour intervals: 10
Mean: FA2 = 275/13
k)
N: AP2 = 132
Max density: 19.9
Min density: 0.00
Mean density: 1.89
Cosine exponent: 69
Contour intervals: 10
Mean: AP2 = 347/87
l)
N: AP2 = 58
Max density = 10.1
Min density = 0.06
Mean density = 2.23
Cosine exponent = 25
Contour intervals = 10
Mean: AP2 = 348/88
m)
N: AP2 = 155
Max density: 19.8
Min density: 0.96
Mean density: 6.46
Cosine exponent: 23
Contour intervals: 10
Mean: AP2 = 322/84
n)
N: AP2 = 79
Max density: 20.2
Min density: 0.01
Mean density: 3.16
Cosine exponent: 24
Contour intervals: 10
Mean: AP2 = 175/87
o)
N: AP2 = 117
Max density: 19.9
Min density: 0.00
Mean density: 2.09
Cosine exponent: 55
Contour intervals: 10
Mean: AP2 = 356/58

3.5.3.4 Shear zones

Where the steep to sub-vertical NE- to ENE-ward striking S_{2a} axial-plane foliations are continuous and tightly spaced, shear zones (C_{sin} and C_{dex}) often occur, suggesting a control of deformation localization by the pre-existing S_{2a} axial-plane foliations. S_{2a} axial-plane foliations together with majoritarian sinistral shear zones form S-C-fabrics from cm- to km-scale. Similarly, extensional shear zones (C_{nor}) occur predominantly along that part of the Brenner Fault (domain E, Figure 4a), where the pre-existing S_{2b} extensional foliations follow the arcuate strike of the westward plunging hinge of the Tuxer Antiform (Figures 2 and 4c). S_{2b} extensional foliations together with extensional shear zones form S-C-fabrics of the Brenner Mylonites.

Transcurrent shear zones In domain A the sub-vertical sinistral shear zones (C_{sin}) strike ENE similar to, but slightly more northward than the corresponding S_{2a} axial-plane foliations (Figures 8a and 8f). The associated L_{sin} lineations are sub-horizontal to gently NE-plunging (Figure 8f). Some dextral shear zones inferred to be conjugated to the above mentioned sinistral ones, strike east and are associated with variously plunging lineations (L_{dex}, Figure 9a). In domain B, sinistral shear zones (C_{sin}) strike NE and mainly dip steeply SE (Figure 8g). Sub-horizontal L_{sin} lineations of these shear zones are NE-ward oriented (Figure 8g) but dips towards the NW. In domain C sub-vertical sinistral shear zones (C_{sin}) strike NE (Figure 8h), as in domain B (Figure 8g). The L_{sin} lineations plunge moderately SW to WNW opposite to those on domain B. The strike of the dextral shear zones within domain C is random (Figure 9e). In both domains B and C the mean values of the C_{sin} shear zones (Figures 8b and 8c) show a characteristic angle of 15 ° to the S_{2a} axial-plane foliation (Figures 8g and 8h).

Extensional shear zones In the area of the Olperer Shear Zone and the Jaufen Fault (Figure 4d) outcrop-scale shear zones show sinistral and top-to-the-west normal sense of shear, therefore they are interpreted as transtensive structures connecting the Brenner Mylonites with the sinistral shear zones of the western Tauern Window. The C_{nor} shear zones dip moderately NW in domain A (Figure 9c) and gently NNE in domain C, where they are associated with shallowly NW plunging L_{nor} lineations (Figure 9g).

Figure 8: *Stereo32 version 0.9 was used to plot Schmidt nets (Röller and Trepmann, 2008). All plots are equal area, lower hemisphere plots. Contouring using a cosine exponential equation was applied when the data show a preferred orientation and their absolute number was higher than twenty, in the remaining few cases the raw data are shown. If lineation and foliations are shown together in one plot, only foliations are contoured. Mean values were deduced graphically in Stereo32 by the maxima of data culminations.* ***a, b, c, d, e:*** *Stereoplots of contoured S_{2a} axial-plane foliations measurements and L_2 lineation measurements in the domains A-E. Great circles indicate S_{2a} mean values. Number of data, contouring intervals and parameters, and mean values are given in the respective left columns and the lower right corners.* ***f, g, h, i, j:*** *Stereoplots of contoured sinistral shear zones (C_{sin}) measurements and L_{sin} lineation measurements in domains A-E. Great circles indicate C_{sin} mean values. Number of data, contouring intervals and parameters, and mean values are given in the respective left columns and the lower right corners.* ***k, l, m, n, o:*** *Stereoplots of contoured sinistral shear zones (C'_{sin}) measurements in domains A-E. Great circles indicate C'_{sin} mean values. Number of data, contouring intervals and parameters, and mean values are given in the respective left columns.*

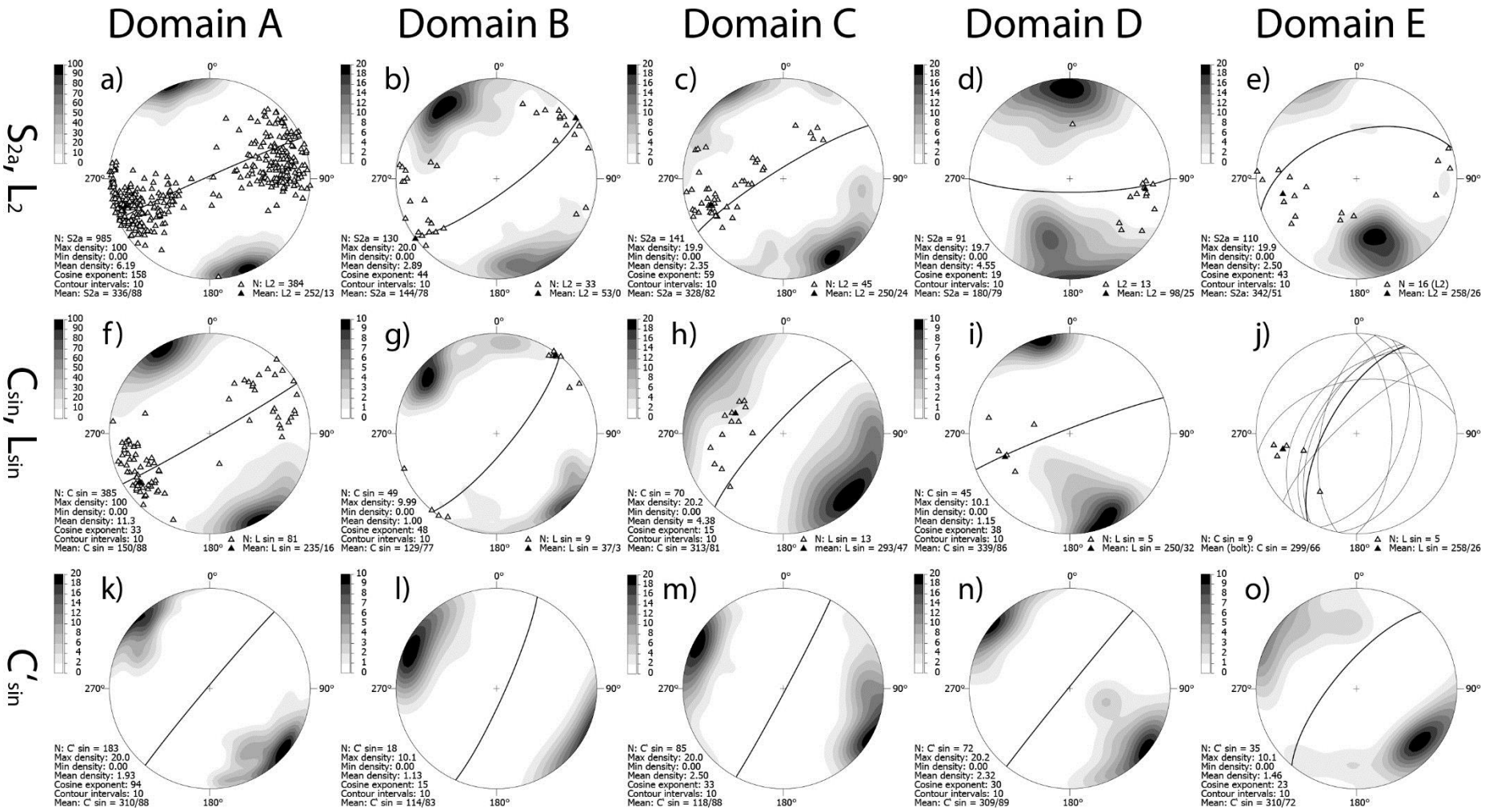
Domain A
Domain B
Domain C
Domain D
Domain E
S2a, L2
Csin, Lsin
C′sin
a)
N: S2a = 985
Max density: 100
Min density: 0.00
Mean density: 6.19
Cosine exponent: 158
Contour intervals: 10
Mean: S2a = 336/88
N: L2 = 384
Mean: L2 = 252/13
b)
N: S2a = 130
Max density: 20.0
Min density: 0.00
Mean density: 2.89
Cosine exponent: 44
Contour intervals: 10
Mean: S2a = 144/78
N: L2 = 33
Mean: L2 = 53/0
c)
N: S2a = 141
Max density: 19.9
Min density: 0.00
Mean density: 2.35
Cosine exponent: 59
Contour intervals: 10
Mean: S2a = 328/82
N: L2 = 45
Mean: L2 = 250/24
d)
N: S2a = 91
Max density: 19.7
Min density: 0.00
Mean density: 4.55
Cosine exponent: 19
Contour intervals: 10
Mean: S2a = 180/79
L2 = 13
Mean: L2 = 98/25
e)
N: S2a = 110
Max density: 19.9
Min density: 0.00
Mean density: 2.50
Cosine exponent: 43
Contour intervals: 10
Mean: S2a: 342/51
N = 16 (L2)
Mean: L2 = 258/26
f)
N: C sin = 385
Max density: 100
Min density: 0.00
Mean density: 11.3
Cosine exponent: 33
Contour intervals: 10
Mean: C sin = 150/88
N: L sin = 81
Mean: L sin = 235/16
g)
N: C sin = 49
Max density: 9.99
Min density: 0.00
Mean density: 1.00
Cosine exponent: 48
Contour intervals: 10
Mean: C sin = 129/77
N: L sin = 9
Mean: L sin = 37/3
h)
N: C sin = 70
Max density: 20.2
Min density: 0.00
Mean density = 4.38
Cosine exponent: 15
Contour intervals: 10
Mean: C sin = 313/81
N: L sin = 13
mean: L sin = 293/47
i)
N: C sin = 45
Max density: 10.1
Min density: 0.00
Mean density: 1.15
Cosine exponent: 38
Contour intervals: 10
Mean: C sin = 339/86
N: L sin = 5
Mean: L sin = 250/32
j)
N: C sin = 9
Mean (bolt): C sin = 299/66
N: L sin = 5
Mean: L sin = 258/26
k)
N: C′ sin = 183
Max density: 20.0
Min density: 0.00
Mean density: 1.93
Cosine exponent: 94
Contour intervals: 10
Mean: C′ sin = 310/88
l)
N: C′ sin= 18
Max density: 10.1
Min density: 0.00
Mean density: 1.13
Cosine exponent: 15
Contour intervals: 10
Mean: C′ sin = 114/83
m)
N: C′ sin = 85
Max density: 20.0
Min density: 0.00
Mean density: 2.50
Cosine exponent: 33
Contour intervals: 10
Mean: C′ sin = 118/88
n)
N: C′ sin = 72
Max density: 20.2
Min density: 0.00
Mean density: 2.32
Cosine exponent: 30
Contour intervals: 10
Mean: C′ sin = 309/89
o)
N: C′ sin = 35
Max density: 10.1
Min density: 0.00
Mean density: 1.46
Cosine exponent: 23
Contour intervals: 10
Mean: C′ sin = 310/72

3.5.4 Periphery of the western sub-dome

3.5.4.1 Domain D

In contrast to domains A, B and C (Figure 4d) the structural elements in domain D, strike predominantly east, and D_2 structures like S_2 foliations and shear zones are less developed. The most common structural feature of this domain are folded S_1 foliations, which strike east and predominantly dip gently to steeply south (Figure 7d), hence the opposite direction compared to domains A, B and C (Figures 7a, 7b, and 7c). The F_2 fold axes are sub-horizontally east-west oriented (Figures 7d and 7i). F_2 axial planes are sub-vertical and strike east (Figure 7n). Towards the west F_2 folds tighten and S_{2a} axial-plane foliations become more common.

The rarely observed sub-vertical S_{2a} axial-plane foliations of domain D strike east and the related L_2 lineations consistently plunge gently east (Figure 8d), i.e., in the opposite direction of L_2 in domain C (Figure 8c). Sub-vertical sinistral shear zones (C_{sin}) strike ENE showing gently westward plunging L_{sin} lineations (Figure 8i) and sub-vertical dextral shear zones strike east (Figure 9j), both being more eastward oriented than the ones in domains A, B, and C.

3.5.4.2 Domain E

The major difference between domain E and the remaining domains is that none of the D_2 structural elements AP_2, S_{2a}, C_{sin}, and C_{dex} are sub-vertical. All these elements dip NW to NE indicating a south-vergent fold (Brandner et al., 2008; Rosenberg and Garcia, 2011). The folded S_1 foliations of domain E strike NE to east and the F_2 fold axes plunge gently west (Figures 7e and 7j). The F_2 axial planes (AP_2) dip moderately north (Figure 7o), similar to those of domain D (Figure 7n). The S_{2a} axial-plane foliations strike ENE and mainly dip moderately NNW (Figure 8e), whereas the S_{2b} extensional foliations, following the westward plunging hinge, strike consistently NNE and dip gently WNW (Figure 8o). Since the S_{2b} extensional foliations are spatially restricted to the area NW of the Indenter tip, we suggest that the oblique geometry of the indenter caused the S_{2b} extensional foliations. The associated L_2 lineations plunge gently west (Figure 8e), as in domain C (Figure 8c). Only few NE-striking sinistral (Figure 8j) and ESE-striking dextral shear zones (Figure 9k) were observed. Numerous, top-to-the-west normal shear zones (C_{nor}), the Brenner Mylonites, occur (e.g., Axen et al., 1995). The gently SW-ward dipping extensional shear zones strike SE and the related L_{nor} consistently plunge gently WSW (Figure 9m).

A key outcrop, where overprinting relations can be assessed is located at the main road in St. Jodok (Figure 4a), where rocks of the Glockner nappe (Figure 10a) show northward dipping extensional shear zones (C_{nor}, Figures 10a and 10c) overprinting tight north-vergent folds along their limbs and synforms. C_{nor} are associated with collapse folds (F_3) (Froitzheim, 1992) that refold the F_2 folds and have flat axial planes (AP_3) with similar orientation to the C_{nor} planes (Figures 10a, 10b and 10c), and vertical, NW-SE opening tension gashes (Figure 10d).

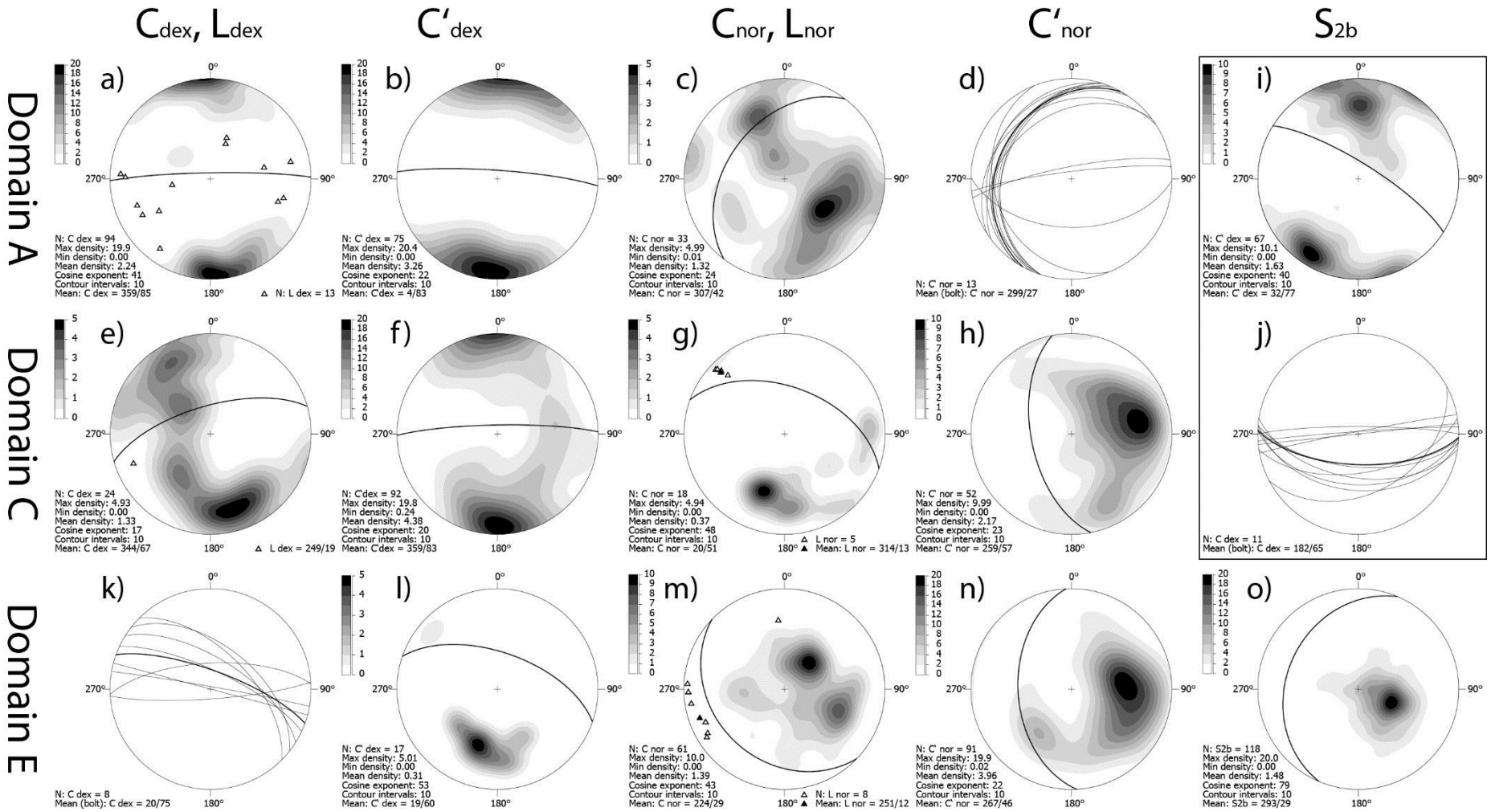
Cdex, Ldex
C′dex
Cnor, Lnor
C′nor
S2b
Domain A
Domain C
Domain E
a)
N: C dex = 94
Max density: 19.9
Min density: 0.00
Mean density: 2.24
Cosine exponent: 41
Contour intervals: 10
Mean: C dex = 359/85
N: L dex = 13
b)
N: C′ dex = 75
Max density: 20.4
Min density: 0.00
Mean density: 3.26
Cosine exponent: 22
Contour intervals: 10
Mean: C′dex = 4/83
c)
N: C nor = 33
Max density: 4.99
Min density: 0.01
Mean density: 1.32
Cosine exponent: 24
Contour intervals: 10
Mean: C nor = 307/42
d)
N: C′ nor = 13
Mean (bolt): C′ nor = 299/27
i)
N: C′ dex = 67
Max density: 10.1
Min density: 0.00
Mean density: 1.63
Cosine exponent: 40
Contour intervals: 10
Mean: C′ dex = 32/77
e)
N: C dex = 24
Max density: 4.93
Min density: 0.00
Mean density: 1.33
Cosine exponent: 17
Contour intervals: 10
Mean: C dex = 344/67
L dex = 249/19
f)
N: C′dex = 92
Max density: 19.8
Min density: 0.24
Mean density: 4.38
Cosine exponent: 20
Contour intervals: 10
Mean: C′dex = 359/83
g)
N: C nor = 18
Max density: 4.94
Min density: 0.00
Mean density: 0.37
Cosine exponent: 48
Contour intervals: 10
Mean: C nor = 20/51
L nor = 5
Mean: L nor = 314/13
h)
N: C′ nor = 52
Max density: 9.99
Min density: 0.00
Mean density: 2.17
Cosine exponent: 23
Contour intervals: 10
Mean: C′ nor = 259/57
j)
N: C dex = 11
Mean (bolt): C dex = 182/65
k)
N: C dex = 8
Mean (bolt): C dex = 20/75
l)
N: C′ dex = 17
Max density: 5.01
Min density: 0.00
Mean density: 0.31
Cosine exponent: 53
Contour intervals: 10
Mean: C′ dex = 19/60
m)
N: C nor = 61
Max density: 10.0
Min density: 0.00
Mean density: 1.39
Cosine exponent: 43
Contour intervals: 10
Mean: C nor = 224/29
N: L nor = 8
Mean: L nor = 251/12
n)
N: C′ nor = 91
Max density: 19.9
Min density: 0.02
Mean density: 3.96
Cosine exponent: 22
Contour intervals: 10
Mean: C′ nor = 267/46
o)
N: S2b = 118
Max density: 20.0
Min density: 0.00
Mean density: 1.48
Cosine exponent: 79
Contour intervals: 10
Mean: S2b = 293/29

Figure 9: *Stereo32 version 0.9 was used to plot Schmidt nets (Röller and Trepmann, 2008). All plots are equal area, lower hemisphere plots. Contouring using a cosine exponential equation was applied when the data show a preferred orientation and their absolute number was higher than twenty, in the remaining few cases the raw data are shown. If lineation and foliations are shown together in one plot, only foliations are contoured. Mean values were deduced graphically in Stereo32 by the maxima of data culminations.* ***a, e, k, j:*** *Stereoplots of contoured C_{dex} foliations measurements and L_{dex} lineation measurements in domains A, C, E and D. Great circles indicate C_{dex} mean values. Number of data, contouring intervals and parameters, and mean value are given in the respective left columns and the lower right corners.* ***b, f, l, i:*** *Stereoplots of contoured C'_{dex} foliations measurements in domains A, C, E and D. Great circles indicate C'_{dex} mean values. Number of data, contouring intervals and parameters, and mean values are given in the respective left columns.* ***c, g, m:*** *Stereoplots of contoured C_{nor} foliations measurements and Lnor lineation measurements in the domains A, C and E. Great circles indicate C_{nor} mean values. Number of data, contouring intervals and parameters, and mean values are given in the respective left columns and the lower right corners.* ***d, h, n:*** *Stereoplots of contoured C'_{nor} foliations measurements in domains A, C and E. Great circles indicate C'_{nor} mean values. Number of data, contouring intervals and parameters, and mean values are given in the respective left columns.* ***o:*** *Stereoplot of contoured S_{2b} extensional foliations measurements in domain E. Great circles indicate S_{2b} mean value. Number of data, contouring intervals and parameters, and mean value are given in the respective left columns.*

The structures of this outcrop indicate that extensional shear along the western margin of the western sub-dome formed syn- to post-D_2 upright folds. In addition, the northward dipping C_{nor} shear planes and AP_3 axial planes of the collapse folds follow the arcuate strike of the pre-existing S_1 foliations along the northern limb of the Tuxer Antiform (Figure 1a). Therefore, they delimit the Brenner Mylonites to the north and the otherwise northward striking Brenner Mylonites become parallel to the ENE-ward striking sinistral transtensive Olperer Shear Zone. To the south the Brenner Mylonites are delimited by the sinistral transtensive Jaufen Fault.

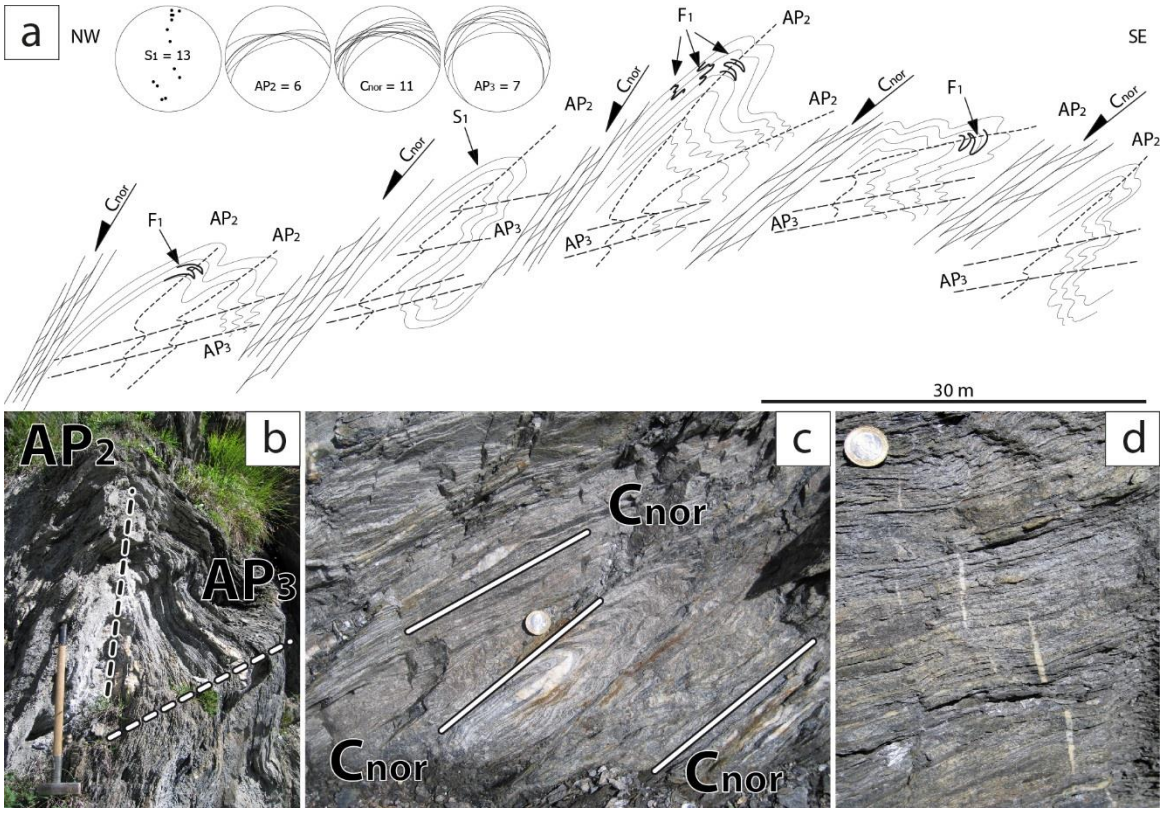

Figure 10a: *Sketch of an outcrop along the road in St. Jodok. The outcrop is ~100 m long.* ***b:*** *north-vergent tight folds (F_2) are* ***c:*** *sheared by extensional shear zones along their limbs.* ***d:*** *tension gashes are also present indicating NW-SE extension. Collapse folds (F_3) are developed, refolding the steep F_2 folds. Stereoplots: (from left to right) S_1 foliations, AP_2 axial planes, C_{nor} extensional shear zones and AP_3 collapse folds.*

3.5.5 Shear bands

The mean values of sinistral shear bands (C'_{sin}) within all five domains show remarkably similar orientations. All mean values strike NE to NNE and are sub-vertical (Figures 8k, 8l, 8m, 8n, and 8o), or steeply NW dipping in domain E. The dextral shear bands C'_{dex} in the domains A and C strike east (Figures 9b and 9f), unlike in the peripheral domains D and E where the dextral shear bands C'_{dex} strike ESE (Figures 9i and 9l). Moderately westward dipping extensional shear bands C'_{nor} are a common feature of domain E and C and are related to the C_{nor} extensional shear zones (Figures 9d, 9h and 9n) but are rarely observed in domain A (Figure 9d).

3.5.6 Structural summary

The structures of domains A, B, and C are similar with respect to the orientations of upright folds and sinistral shear zones. In general, the mean values of the axial-plane foliations (S_{2a}, Figures 8a, 8b, and 8c) show orientations that are slightly more north-directed than those of the axial planes (AP_2, Figures 7k, 7l, and 7m). The mean values of the sinistral shear zones (C_{sin}, Figures 8f, 8g, and 8h) show orientations that are slightly more north-directed than the mean values of the axial-plane foliations (S_{2a}, Figures 8a, 8b, and 8c) of those domains. Hence, a successive formation of these structures within an overall left-lateral system can be inferred. Along strike from the northeastern to the southwestern termination the mean values of S_{2a}, C_{sin} and C'_{sin} planes indicate a change in dip direction from steeply NW-dipping in domain B (Figures 8b, 8g, and 8l) to sub-vertical in domain A (Figures 8a, 8f, and 8k) to steeply SE-dipping in domain C (Figures 8c, 8h, and 8m). In addition, the structural planes show an along strike change in strike direction from NE-striking in domain B (Figures 8b, 8g, and 8l) to ENE-striking in domain A (Figures 8a, 8f, and 8k) and again to NE-striking in domain C (Figures 8c, 8h, and 8m). These trends point to a large-scale sigmoidal structure centered within domain A having its northeastern and southwestern terminations in domains B and C.

3.5.7 Shortening accommodated by upright folding

To compare the amounts of shortening accommodated in the western and eastern sub-domes, we performed line-length balancing of the base of the Austroalpine assuming a horizontal orientation before upright folding (Figures 1b and 1c). Well aware of the fact that this can only be an first-order estimate due the fact that orogen-parallel extension occurred perpendicular to the section and that folding under high-temperature conditions may have lengthen the folded surface, we note that these two effects may partly balance each other. The result suggest ~38 km of shortening for the westernmost part of the dome on the base of structural sections of Schmid et al. (2013). This shortening amount is larger than the one estimated by Schmid et al. (2013) because it also includes the Austroalpine units, which are folded together with the ones of the Tauern Window. Therefore, 20 km of the 58 km of indentation estimated above must have been accommodated by other processes than folding. In the eastern part of the Tauern Window ~20 km of shortening are estimated by line-length balancing. This eastward decrease of shortening points to a clockwise rotation of the Southern Alps, during indentation, or it might indicate the eastward decreasing differential shortening by the obliquity of the Dolomites indenter.

3.6 Discussion

3.6.1 Comparison with earlier studies

Conceptual models claiming exhumation of the western Tauern Window by extensional unroofing, require, that extensional displacements along the Brenner Fault are transferred to transcurrent strike-slip faults located at the northern and southern terminations of the Brenner Fault (Fügenschuh et al., 1997; Scharf et al., 2013; Schmid et al., 2013). Our fieldwork (Figure 4d) shows that neither a sinistral strike-slip fault at the northern termination, nor a km-scale, dextral strike-slip fault at the southern termination of the Brenner Fault are present. In spite of the widespread occurrence of sinistral shear zones throughout the western Tauern Window and its surrounding area (Figures 4d, 8f, 8g, 8h, and 8i), the northern part of the Brenner Mylonites is devoid of such structures (Figures 4d, and 8j). The northwestern margin of the Tauern Window is characterized by south-vergent F_2 folds and S_1 foliations (Figures 7e, 7j, 7o), reactivated by both S_2 foliations (Figures 8e and 9o). North of the locality St. Jodok (Figure 4a) no ductile shear zone affecting the northwestern margin was found. The transtensive Olperer Shear Zone (Lammerer and Wegner, 1998; Ebner et al., 2004) and the transtensive Jaufen Fault (Müller et al., 2001; Viola et al., 2001) are the only structure that could have transferred sinistral strike-slip into top-to-the-west extensional displacement along the Brenner Fault. However, these structures are connected to the southernmost part of the Brenner Fault, hence they cannot have accommodated the amount of extension that affected most of the Brenner Fault, in contrast to previous interpretations (Axen et al., 1995; Fügenschuh et al., 1997, 2011). A similar contradiction is shown by our structural data in the southwestern margin of the Tauern Window, where extensional unroofing models claim a transition from the Brenner Mylonites into the dextral Pustertal-Gailtal Fault. We observed that the Austroalpine and ocean-derived units in Domain C, are largely overprinted by sinistral (Figures 5, 8c, 8h, 8m) and only minor dextral and extensional shear zones (Figures 9e, 9f, 9g, and 9h). Therefore, from a kinematic point of view, tectonic unroofing models are in conflict with the structural evidence of the western sub-dome.

3.6.2 Corner effect of the Dolomites Indenter

Upright folding affected all units of the Tauern Window and the Austroalpine nappes north of the Dolomites Indenter (Figures 1b and 1c) (Schmid et al., 2013). The structures in domains C and E form a bow tie around its northernmost tip. The traces of the folded S_1 foliations, the axial planes, and axial-plane foliations in domains C and E in the west and the corresponding traces in domains A and D in the east converge to each other (Figures 7a, 7c, 7d, 7e, 7k, 7m, 7n, 7o, 8a, 8c, 8d, and 8e). The knot of this bow tie lies north of Mauls (Figure 4a) and coincides with the indenter tip, where the Brenner Mylonites separate the two areas. Therefore, this structural bow tie is suggested to result from indentation.

3.6.3 Deformation fabrics and crustal level

The style of deformation appears to be correlated to the structural level of the nappe stack exposed at the surface. Domains C and D consist of Austroalpine rocks) that show predominantly open to tight F_2 folds with well-preserved S_1 foliations (Figures 7c and 9d) rotated into a nearly parallel orientation to the respective indenter margins. S_{2a} axial-plane foliations or transcurrent shear zones are rare (Figures 8c and 9d) and, if present, they only occur on the small scale, whereas, brittle deformation is widespread in these rocks (Viola et al., 2001; Bertrand, 2013). On the contrary, rocks of the Venediger Duplex, European distal Margin, and the ocean-derived units of domains A and

E, which represent the deeper structural level, are characterized by tight F_2 folds and the widespread occurrence of S_{2a} axial-plane foliations (Figures 8a and 9d). Numerous meso- and macro-scale C_{sin} shear zones, or top-to-the-west extensional C_{nor} shear zones (domain E) are common in domains A and E (Figures 8f, 8i, 9a, 9c, 9k, and 9m). Although the domains C and D are adjacent to the margins of the Dolomites Indenter, these domains show less intense ductile deformation, except for the area of Mauls north of the indenter tip, compared to domains A and E. These observations show that metamorphic temperature, which reached greenschist- to amphibolite-facies conditions in the lower plate during Cenozoic time, enhanced the localization of ductile deformation in these areas. On the other hand, the higher content of carbonates and sheet silicates in the European distal Margin and the ocean-derived units probably promoted the localization of ductile deformation inside the Tauern Window. These observations suggest that the difference in the style of deformation between the Austroalpine units in domain C and those inside the Tauern Window, are not in conflict with the observed continuity and parallelism of the structures between these domains. These differences merely reflect the transition from a lower to a higher crustal level, both affected by the same shortening event.

3.6.4 From upright folding to localized shearing

Sinistral shear zones in the western sub-dome preferentially occur along the steep limbs and within the tight synclines of F_2 folds (Figure 4d), nucleating sub-parallel to the S_{2a} axial-plane foliations (Figure 4b), e.g., the Ahorn, Greiner and Ahrntal shear zones. Similarly extensional and transtensive shear zones as the Jaufen Fault, the Brenner Mylonites, the Olperer Shear Zone, or outcrop-scale shear zones in St. Jodok (Figure 10), occur along the south-vergent limbs, marked by arcuate-striking pre-existing S_1, overprinted by S_{2b} extensional foliations, of the westward-plunging hinge of the Tuxer Antiform (Figures 3 and 4c).

A succession from broad doming, to tight folding with axial-plane foliation development, to localized shear can be inferred from the following arguments. The eastern sub-dome, which is not shortened as much as the western one, consists of folds of larger wavelength and smaller amplitude, and does not show the formation of an axial-plane foliation, nor of widespread strike-slip shear zones (Figure 2). Therefore, the structure of the eastern sub-dome may be considered to reflect a state of shortening of the western sub-dome in an earlier stage of its evolution. Another argument is based on the observed spatial succession of open fold without axial-plane foliation to tight and isoclinal folds with incipient axial-plane foliation, and finally to rootless folds with intense axial-plane foliation and sub-parallel sinistral shear zones. This structural, spatial evolution was observed at the southern (Figure 5) and northern (Rosenberg and Schneider, 2008) boundaries of the Venediger Duplex. The presence of sinistral shear zones where the shortening gradient attains a maximum, suggests a temporal evolution from open to tight folds and from tight folds to isoclinal ones associated with sinistral shear zones. In addition, the orientation of the fabrics (from AP_2, to S_{2a}, to C_{sin}) of the western sub-dome commonly nucleated along pre-existing structures that form suitable anisotropies. The angles between the mean values of the distinct structures (AP_2, S_{2a}, C_{sin}, and C'_{sin}) in domains A, B, and C are low, (6-20 °), mostly ~15 ° (Figures 7k, 7l, 7m, 8a, 8b, 8c, 8f, 8g, 8h, 8k, 8l, and 8m), which are characteristic for strike-slip regimes (Woodcock and Fischer, 1986; Dewey et al., 1998). By analogy with indentation experiments, designed to simulate shortening in the Eastern Alps, it can be assumed, that the main fabric orientation rotates towards parallelism with the northern indenter margin although the convergence direction remains constant (Ratschbacher et al., 1991a, 1991b; Rosenberg et al., 2004, 2007). The strike of the C'_{sin} mean values (024-040 °) is remarkably consistent in all five domains, sub-parallel to the strike of the North Giudicarie Fault (Martin et al., 1993), suggesting it to be the overall shear plane.

3.6.5 The western Tauern Window: a restraining bend

Upright folds, accommodating ~38 km of north-oriented shortening, dominate the structural grain of the western Tauern Window (Figures 1b and 1c). Clear crosscutting relationships between structural elements (AP_2, S_{2a}, C_{sin}, and C'_{sin}) are rare, however, the systematic low angles (mostly ~15 °) between the mean strike directions of sinistral shear zones, axial-plane foliations and axial planes of upright folds, suggests that these structures all formed within the same deformation field characterized by a ~N-oriented maximum shortening direction. This orientation is also compatible with the orientation of the dextral shear zones. Therefore, we suggest that upright folds and shear zones are coeval. The overwhelming majority of shear zones both on the outcrop- as on the map-scale is sinistral, which indicates that deformation took place in a sinistral transpressional field. This result is in agreement with the map-scale pattern of folds and shear zones, showing that the NNE-striking, sinistral Giudicarie Belt turns into the NNE- to ENE-striking folds and sinistral shear zone network of the western Tauern Window, before entering the sinistral SEMP Fault. Hence, the latter orientation corresponds to that of a restraining bend.

The mean orientation of the structural elements show two along-strike trends passing the domains C, A, and B from SW to NE (Figures 4b, 4c, and 4d). First, the foliations strike NE at the terminations of the western sub-dome (domains B and C) and ENE in its center (domain A, Figures 7k, 7l, 7m, 8a, 8b, 8c, 8f, 8g, and 8h). The fold axes are doubly plunging at the terminations (domains B and C, Figures 7b, 7c, 7g, and 7h) and sub-horizontal in the center (domain A, Figures 7a and 7f). This sigmoidal pattern resembles the foliation pattern of transpressive areas e.g. positive flower structure (Sanderson and Marchini, 1984; Dewey et al., 1998), strike-slip duplexes (Woodcock and Fischer, 1986). Second, all foliations show an inward steepening of the average dip angle from the terminations (domain B and C), to the center (domain A) of the restraining bend (Figures 7k, 7l, 7m, 8a, 8b, 8c, 8f, 8g, and 8h). This trend indicates a vortex of the foliations located in the central domain A.

3.6.6. Age of doming in the Tauern Window

From a geochronological point of view, the concentric, elliptical distribution of cooling ages of several chronometers (see compilations of Most, 2003; Luth and Willingshofer, 2008; Rosenberg and Berger, 2009; Bertrand, 2013) in the western sub-dome, passing from ≥32 Ma (Rb/Sr and K/Ar of white mica) in the outer regions (Satir, 1975; Borsi et al., 1975; Thöni, 1981) to ≥5 Ma (AFT) in the center of the Tauern Window (Grundmann and Morteani, 1985; Fügenschuh et al., 1997; Most, 2003; Bertrand, 2013), is a strong argument in favor of an Oligocene age for the initiation of folding (doming), hence of indentation.

Structures in the Meran-Mauls basement (domain C) resemble those of the western Tauern Window, since these rocks are deformed by upright folds striking sub-parallel to the northwestern margin of the Dolomites Indenter (Figures 4, 6, 7c, 7h, and 7m), which are associated in their late stage with steep to sub-vertical, sinistral transtensive, NE-striking faults (Figure 4d; e.g., Jaufen and Fartleis faults). The Meran-Mauls Fault may have acted as “snowplow” accommodating first dextral and later on reverse displacements (Prosser, 1998; Viola et al., 2001; Pomella et al., 2011; Luth et al., 2013). The Miocene cooling ages of the Austroalpine units within the Meran-Mauls basement, contrasting with the otherwise Cretaceous cooling ages shows that Miocene exhumation occurred everywhere around the Dolomites indenter, inferring that shortening was accommodated by upright folds, hence by doming. Therefore, from a structural and temporal point of view the Meran-Mauls basement can be treated as part of the western Tauern Window (Rosenberg and Berger, 2009; Pomella et al., 2012), which links the sinistral the Passeier and North Giudicarie faults with the restraining bend in the western Tauern Window.

Following the unanimously accepted interpretation that doming of the Tauern Window is related to the convergent displacement of the Dolomites Indenter (Cornelius, 1940), bordered by the Giudicarie Fault along its western margin, the age of activity of the Giudicarie Fault is the key to assess the age of doming of the Tauern Window. Recent interpretations (Schmid et al., 2013) argued that Dolomites indentation initiated not before Miocene (23-21 Ma). The first argument supporting this conclusion are stratigraphic constraints based on the observation that pelagic sediments were being deposited until 21.5 Ma, close to the South Giudicarie Fault (Luciani and Silvestrina, 1996). However, cross sections perpendicular to the Giudicarie Belt (Leloup et al., 1988) show that shortening was modest, probably insufficient to severely modify the regional depth of the submarine surface in the realm of the Giudicarie Belt. Moreover, several pre-Miocene hiati were observed and interpreted as possible "transgressive onlaps" in Monte Brione formation, to argue for sea level changes, although it was conceded that "a tectonic component (causing those hiati) cannot be excluded" (Luciani, 1989). Deformation age data of the North Giudicarie and the Meran-Mauls faults point to Lower Oligocene and Upper Oligocene activity, respectively (Müller et al., 2001) whereas ZFT data point to Miocene activation of the North Giudicarie Fault (Pomella et al., 2011, 2012).

The second argument claiming inception of Dolomites indentation not earlier than 23-21 Ma (Schmid et al., 2013) is a thermal model (Fügenschuh et al., 1997), which determines the onset of "rapid exhumation" in the footwall of the Brenner Fault at ~20 Ma (Scharf et al., 2013; Schmid et al., 2013). However samples used to construct the T-t path stem from areas with different structural and metamorphic history, being situated either in the high-metamorphic site of the tight Greiner Synform (footwall of the Brenner Fault) (Christensen et al., 1994) or within the low-metamorphic site of the Brenner Mylonites (Fügenschuh et al., 1997). Both these major structural elements, normal faulting and upright folding, affected the isotherms, having different a priori metamorphic grades, participated in exhumation of the western sub-dome, but were not differentiated in the thermal model of Fügenschuh et al. (1997) and Scharf et al. (2013), making the T-t path questionable.

3.6.7 Decoupling along the western margin

Sinistral shear zones of the restraining bend (domains A, B, and C) described in this study clearly shows a southward rotation in strike direction in domains C and E (Figures 8h, and 8j) where the belt enters the Meran-Mauls basement (Figure 4d). The transtensive Olperer Shear Zone (Ebner et al., 2004) as well as the transtensive Jaufen Fault (Müller et al., 2001; Viola et al., 2001), are suitable structures to translate sinistral displacement of the western Tauern Window into top-to-the-west extension along the Brenner Fault (Figure 4d). In domain E all structural planes dip gently to steeply north to WSW (Figures 7o, 8e, 8j, 9k, 9m, and 9o) and no sub-vertical, ductile structures occur. Upright folding (Figures 7e and 7o) enabled the formation of S_{2a} axial-plane foliation (Figure 8e) and S_{2b} extensional foliations (Figure 9o) which formed around the westward plunging hinge of the Tuxer Antiform. The S_{2b} extensional foliations on their part are associated with top-to-the-west extensional shear zones and the Brenner Mylonites (C_{nor}).

The structures found at St. Jodok (Figures 4d and 10) demonstrate two main points. First, extensional shear zones in the area of Steinach (Figure 4a) strike east, dip north, and indicate an arcuate strike of the Brenner Mylonites as proposed by Fügenschuh et al., (1997) and Töchterle et al. (2011) further south. Therefore, the eastward striking extensional shear zones in the area of St. Jodok, following the arcuate-strike of S_1 foliations around the hinge of the Tuxer Antiform, mark the northern termination of the Brenner Mylonites which separate the thick occurrences of extensional mylonites southward and their absence in the north, as described earlier (Behrmann, 1988; Selverstone, 1988; Axen et al., 1995). Second, since the extensional shear zones C_{nor} associated with the formation of F_3 collapse folds overprint the steep limbs, tight synclines and axial planes of the F_2 folds (Figure 10), the onset of the Brenner Fault postdates, at least locally, the

upright folds related to doming. However, because the Brenner Mylonites are folded themselves by open folds (Rosenberg and Garcia, 2011) the Brenner Fault must have been active during D_2, in agreement with its Miocene deformation age data (Figure 3).

Domain E marks a structural boundary between the western Tauern Window that was shortened due to Dolomites indentation and the flat-lying Mesozoic cover of the uppermost Austroalpine nappes, the Ötztal basement, which was unaffected by indentation. The reason for such a sharp boundary is the geometry of the Dolomites Indenter. Rocks north of the Meran-Mauls basement, were shortened less due to a more oblique convergence of the Dolomites Indenter that was strongly partitioned into top-to-the-west extensional shear. In contrast, north of the Pustertal-Gailtal Fault (Figure 1a) the more perpendicular convergence was mainly accommodated by folding and by sinistral shear within the Tauern Window. Hence, in domain E a lateral change of the amount of vertical displacement occurred (Selverstone, 1988; Selverstone et al., 1991) by several processes. First, material paths were vertically stretched to attain their present structural level in the folded area (western Tauern Window), compared to their initial level before folding below the Austroalpine, the Ötztal basement (Figure 2) (Rosenberg and Garcia, 2011; 2012). Second, a clockwise rotation of the Dolomites indenter would cause an eastward component of motion, which results in maximum east-west extension in front of the tip of Dolomites Indenter i.e., the Brenner Fault. Third, partitioning of deformation into strike-slip and shortening, respectively parallel and perpendicular to the indenter margins, causes a divergence of material paths away from the indenter tip, resulting in an east-west extensional component (e.g. Reiter et al., 2011). Fourth, the western margin of the western sub-dome is marked by first order westward plunging fold axes of the Tuxer and Zillertaler antiforms, causing a progressive eastward increase of exhumation.

3.6.8 Decoupling to the east, transition to lateral extrusion

The central Tauern Window was neither affected by transcurrent shear zones nor by folds of high-amplitude (Figures 2 and 4d). Accordingly, the level of exhumation is less deep and large areas are still covered by rocks of the European distal Margin and ocean-derived units. Therefore, exhumation of the central Tauern Window differs from that of the western Tauern Window.

During the second phase of Dolomites indentation (Pomella et al., 2011; 2012) the transpressive motion of the western Tauern Window was transferred out of it along the sinistral shear zones in the realm of Mittersill that yield Miocene deformation ages (e.g., Rinderkar Shear Zone: Cole et al., 2007; Schneider et al., 2013). Hence, north-south shortening was largely translated into E-directed strike-slip motion along the transpressive to transtensive SEMP Fault (Peresson and Decker, 1997; Linzer et al., 2002). The sinistral transpressive belt (domains A, B, and C) described in this study shows a major northward rotation in strike direction of all structural elements in domain B (Figures 8b, 8g and 8l) where the belt turns into the SEMP Fault (Figure 4d) (Cole et al., 2007; Rosenberg and Schneider, 2008). South and SW of this area, numerous sinistral shear zones with a NNE-strike crosscut the Venediger Duplex (Figures 1a and 4) and delimit the sinistral transpressive belt to the west from an area to the east, devoid of sub-vertical foliations (Figure 2) and delimited to the north by the SEMP Fault. Hence, this NNE-striking belt, forms the boundary between an area to the east that is translated eastward by the SEMP and an area to the west that is intensely shortened, sheared, and uplifted.

Two conceptual models may explain the change from tight folding and distributed sinistral shear zone networks in the western Tauern Window to open folds and localized strike-slip faults (SEMP Fault) in the central Tauern Window. F_2 folds north of the indenter tip are tight, nearly isoclinal (Rosenberg and Garcia, 2011, their Figure 4), hence accommodation of additional shortening may have needed a processes other than folding, i.e. sinistral strike-slip. Crustal thickening due to upright folds of the western sub-dome was larger than in the central and eastern Tauern Window (Figures 1b and 1c), in agreement with earlier termination of cooling in the central and eastern Tauern Window (compilation by Luth and Willingshofer, 2008; Rosenberg and Berger, 2009;

Bertrand, 2013; Scharf et al., 2013). Therefore, this model, favoring the onset of sinistral strike-slip in a late-stage of folding, would explain the presence of numerous strike-slip shear zones in the west, but not in the east. However, the SEMP Fault existed already at 35-28 Ma (Figure 3) (Urbanek et al., 2002), and could have accommodated sinistral strike-slip of the western Tauern Window (Cole et al., 2007; Rosenberg and Schneider, 2008). As a consequence, the kinematic continuity between the Giudicarie and the SEMP Fault may have existed since the inception of doming, decoupling the central and eastern Tauern Window from the western and enabling their escape eastward (Ratschbacher et al., 1991b).

3.6.9 Estimates of shortening, displacement and extension

Several investigations proposed to link indentation and exhumation of the Tauern Window, relating displacements of the major Faults surrounding the Tauern Window (Fig. 11). Neubauer et al. (1999) proposed an exhumation model by extension of a previously thickened crust within a pull-apart structure (Figure 11a) during orogen-parallel strike-slip and oblique convergence. Linzer et al. (2002) described the along-strike changes of the SEMP Fault from predominantly transpressive in the west to predominant transtensive in the east, suggesting that the western Tauern Window formed a restraining bend connecting to the SEMP Fault during orogen-parallel extension of 120 km in the central Eastern Alps (Figure 11b). On the other hand they interpreted the SEMP Fault as the lateral ramp of the Brenner normal Fault, suggesting a kinematic link between these structures, and stating that exhumation of the Tauern Window occurred along the Brenner and Katschberg faults (Figure 1a). Fügenschuh et al., (2012) considered that 44 km of extension along the Brenner normal fault were transformed into the "Tauern North Boundary Fault" (Töchterle et al., 2011) and the dextral Periadriatic Fault, at the northern and southern ends of the Brenner Fault, respectively. Hence, the largest part of the western Tauern Window would be exhumed by extensional unroofing, laterally accommodated by strike-slip faulting. Scharf et al. (2013) interpreted exhumation of the western Tauern Window in terms of stretching faults accommodating ~70 km of extension along the "Brenner Shear Zone System" (Figure 11c).

In spite of some differences in the way faults are linked, the left-lateral displacement of the SEMP Fault in all these models is absorbed along the Brenner Fault, resulting in very significant extensional denudation of its footwall (Fügenschuh et al., 1997, 2012; Neubauer et al., 1999; Scharf et al., 2013). As a consequence, Dolomites indentation needs to be accommodated by structures other than the SEMP and the Brenner faults, being kinematically unrelated to indentation; it would be entirely accommodated by upright folds in the western Tauern Window. Hence, exhumation of the western Tauern Window would result from ~70 km of east-west extension in addition to erosion of upright folds of >20 km amplitude. If 44 km of extension explain exhumation of the footwall from 17 km depth (Fügenschuh et al., 2012) and upright folds explain a differential uplift and exhumation of ~10 km, adjacent to the Brenner Fault, where the fold amplitude plunge west, the combined activity of folding and extension in the western Tauern Window would lead to an amount of exhumation corresponding to >27 km exceeding by far the one inferred from both stratigraphic (Schmid et al., 2013) and petrologic (Selverstone, 1993) constraints.

None of the models above presented structural data from the western Tauern Window, in order to assess the kinematic and temporal links between the faults accommodating collision. Therefore, different conceptual kinematic models were suggested, showing different links and even different traces of the major faults in map view. Some studies consider the SEMP Fault to be the lateral ramp of the Brenner Fault (Fügenschuh et al., 1997; Neubauer et al., 1999; Linzer et al., 2002; Scharf et al., 2013). Although Linzer et al. (2002) showed the splitting of the SEMP Fault into several sinistral splays terminating in the western Tauern Window, they proposed a kinematic continuity between the SEMP and the Giudicarie Faults. Other investigations (Rosenberg and Schneider, 2008) pointed out that the major left-lateral shear zones of the western Tauern Window show an "en échelon" pattern, which transfers sinistral displacements from SW to NE. The structural data and

interpretations presented in this work allow us to discriminate between these models. Sinistral shear zones of the western Tauern Window, do not terminate in the northern Brenner Fault, but strike across the southwestern end of the Tauern Window, from where they continue into the Meran-Mauls basement (Figures 2 and 4d). Hence, the boundary between Tauern Window and Austroalpine Units here does not represent a structural boundary, but the transition from a deeper to a higher structural level, both affected by the same structures and deformation events. These are manifested by the upright folds and sinistral shear zones accommodating vertical and lateral extension, respectively.

Figure 11: *Sketch of tectonic models of the western Tauern Window: BF=Brenner Fault, BSZS=Brenner Shear Zone System, GB=Giudicarie Belt, KLT=Königsee-Lammertal-Traunsee Fault, SEMP=Salzach-Ennstal-Mariazell-Puchberg Fault, wTW=western Tauern Window.* ***a:*** *Simplified model after Neubauer et al. (1999), exhumation of the Tauern Window in two stages, first stage (red lines) is a sinistral extensive step-over structure (pull-apart) under NW directed shortening, second stage (blue lines) is a dextral transpressive system under NE directed shortening* ***b:*** *Simplified model after Linzer et al. (2002) shows a connection between the SEMP Fault and the Giudicarie Belt via the sinistral shear zones of the western Tauern Window. The SEMP Fault was interpreted as lateral ramp of the Brenner Fault* ***c:*** *Exhumation model after Scharf et al. (2013) shows that sinistral displacement of ~66 km along the SEMP and the KTL faults is entirely accommodated in the western Tauern Window by ~70 km of lateral stretching that decreases to zero displacement westwards. Along the Brenner Shear Zone System, that envelopes the western Tauern Window, a similar amount of east-west extension of ~70 km was discussed. These three regions (BSZS, wTW, SEMP+KLT) are balanced out in east-west direction. As a consequence shortening caused by Dolomites indentation would be solely accommodated by upright folding in the western Tauern Window.* ***d:*** *~58 km of shortening caused by the Dolomites Indenter was accommodated by upright folds (~38 km) and partly translated into sinistral shear zones casing a displacement of ~26-31 km. These three regions (GB, wTW, SEMP) are interconnected and Dolomites indentation would be the driving force for lateral extrusion and the transpression inside the western Tauern Window.*

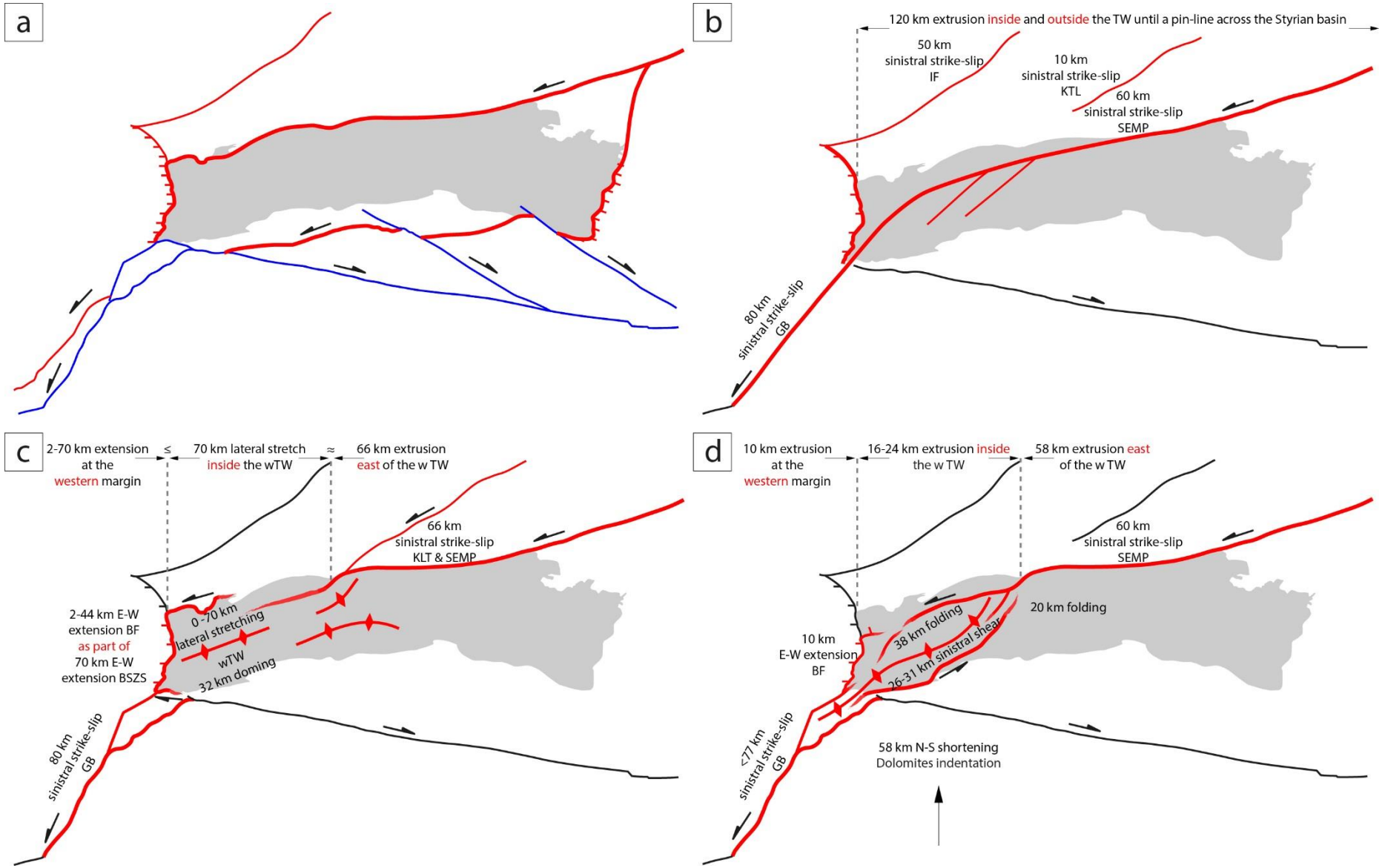
a
b
120 km extrusion inside and outside the TW until a pin-line across the Styrian basin
50 km
sinistral strike-slip
IF
10 km
sinistral strike-slip
KTL
60 km
sinistral strike-slip
SEMP
80 km
sinistral strike-slip
GB
c
2-70 km extension
at the
western margin
≤
70 km lateral stretch
inside the wTW
≈
66 km extrusion
east of the w TW
66 km
sinistral strike-slip
KLT & SEMP
2-44 km E-W
extension BF
as part of
70 km E-W
extension BSZS
0 -70 km
lateral stretching
wTW
32 km doming
80 km
sinistral strike-slip
GB
d
10 km extrusion
at the
western margin
16-24 km extrusion inside
the w TW
58 km extrusion east
of the w TW
60 km
sinistral strike-slip
SEMP
20 km folding
38 km folding
26-31 km sinistral shear
10 km
E-W extension
BF
<77 km
sinistral strike-slip
GB
58 km N-S shortening
Dolomites indentation

Using the known amounts of displacement accommodated by the first-order structures in the area, we estimate orogen-perpendicular shortening, and orogen-parallel extension to test if the field-based kinematic links inferred above offer a plausible model to explain the kinematics and exhumation in front of the Dolomites indenter. In order to do so, we summarize the known amounts of displacement related to the first order structures discussed above (Figure 11d). If a northward convergence is assumed (Rosenberg et al., 2007, for discussion) the Dolomites indenter was displaced northward by ~58 km along the NE-striking, ~77 km long Giudicarie belt. Shortening accommodated by upright folds in the western Tauern Window, including the Austroalpine basement to the south amounts to ~38 km, based on line-length balancing of the antiformal structure. Hence, the remaining ~20 km of shortening must be accommodated by left-lateral displacements along the Ahorn, Tuxer, Greiner, Olperer, and Ahrntal shear zones (Figure 4d). Taking the present-day orientation of these shear zones as a reference, using their mean strike directions of domains A, B, and C, their left-lateral displacement necessary to accommodate ~20 km of north-south shortening corresponds to ~26-31 km. These shear zones contribute ~14-26 km to east-west lateral extrusion. Left-lateral displacement along the SEMP Fault is inferred to be ~60 km (Linzer et al., 2002) having an east-west extrusion component of ~58 km. It is important to note that the amount of extension of the Brenner Fault does not affect directly the estimates above, because north-south shortening cannot be accommodated by north-south striking normal faults. However the degree of kinematic linkage between the SEMP and the Brenner Fault is important, in that it connects or disconnects the Giudicarie Belt from the SEMP faults. Displacement markers for the sinistral shear zones in the western Tauern Window are missing, however, the values above are qualitatively consistent, with the structural data, showing that both folding and sinistral strike-slip continue west of the indenter corner and do not connect to the Brenner Fault.

Therefore, we conclude that the majority of the displacement of the SEMP Fault is not transformed into extension along the Brenner Fault (Figures 1a, 4d, and 11d) but rather to the Giudicarie Belt. This structural link is also consistent with the time constraints from deformation age data.

3.7 Conclusion

Based on new structural mapping of the western Tauern Window and on a structural compilation covering the entire window, we reassessed the position and the links between Cenozoic faults and shear zones, to discriminate between different kinematic models and to propose a new one.

The western Tauern Window shows a different structural evolution compared to the central and eastern Tauern Window. In the former, the widespread association of high-amplitude, tight upright folds and sinistral shear zones, testifies a larger amount of orogen-perpendicular shortening and a peculiar position linking the Giudicarie Belt, hence indentation to the SEMP Fault, hence lateral extrusion.

Against previous interpretations suggesting that exhumation of the western Tauern Window results from tectonic unroofing, emphasizing extensional tectonics, we showed that the fault pattern and the relative displacements on the faults required by such models do not match with the structures of the western Tauern Window. In contrast this fault pattern and the inferred displacements are consistent with exhumation dominated by erosional denudation during upright folding.

The western Tauern Window forms a restraining bend linking the sinistral, transpressive Giudicarie Belt, with the sinistral SEMP Fault. ~58 km of north-directed shortening caused by the Dolomites Indenter were accommodated by upright folds (~38 km) and partly by sinistral shear zones attaining ~26-31 km of bulk sinistral displacement, i.e. ~16-24 km east-west extrusion. North-south shortening in the central area decreases, as seen from the lower amplitude of folds, the absence of interconnected networks of shear zones, and preserved, higher tectonostratigraphic units. These

observations are consistent with the larger exposure of Austroalpine Units south of the Tauern Window and the more southerly position of the indenter margin.

3.8 Acknowledgement

Data supporting Figures 7, 8, and 9 are available as in Supplementary material Table S1. This study was funded by the DFG grant Ro2177/4. We acknowledge family Schwärzer, especially M. Schwärzer, G. Fankhauser and R. Emberger for field support and accommodation. For helpful discussions we thank A. Bertrand, S. Favaro, S. Garcia, M.R. Handy, L. Ratschbacher, D. Rutte, and R. Schuster. For critical and constructive reviews of the manuscript in a very final stage we thank H. Pomella and S.M. Schmid and finally we thank C. Teyssier and one anonymous journal reviewers for improving the manuscript substantially.

3.9 References

Angel F., and R. Staber (1950), Geologische Karte des Ankogel-Hochalm-Gebiets, 1:50.000. In: Angel, F., and R. Staber, Wien (Freytag & Berndt).

Axen, G. J., J. M. Bartley, and J. Selverstone (1995), Structural expression of a rolling hinge in the footwall of the Brenner Line normal fault, eastern Alps, Tectonics, 14(6), 1380–1392, doi:10.1029/95TC02406.

Axen, G.J., J. Selverstone, T. Byrne, and J.M. Fletcher (1998), If the strong crust leads, will the weak crust follow, GSA today, 8(12), 1–8.

Barnes, J.D., J. Selverstone, Z.D. and Sharp (2004), Interaction between serpentinite devolatization, metasomatism and strike-slip strain localization during deep-crustal shearing in the Eastern Alps, J. Metamorph. Geol., 22, 283–300.

Becker, B. (1993), The structural evolution of the Radstadt Thrust System, Eastern Alps, Austria – Kinematics, Thrust Geometries, Strain Analysis -, Tübinger Geowissenschaftliche Arbeiten, 14.

Behrmann, J.H. (1988), Crustal scale extension in a convergent orogen: The Sterzing-Steinach mylonite zone in the eastern Alps, Geodinamica Acta, 2, 63–73.

Behrmann, J.H., and W. Frisch (1990), Sinistral Ductile Shearing Associated with Metamorphic Decompression in the Tauern Window, Eastern Alps, Jb. Geol. B.-A., 133 (2), 135–146.

Bertrand, A., (2013), Chapter II: Cooling history and late exhumation of the Tauern Window (Eastern Alps) inferred from apatite and zircon fission track thermochronology, PhD thesis, Freie Universität Berlin, p. 196.

Bigi, G., D. Cosentino, M. Parotto, and R. Sartori (1992), Structural model of Italy, 1:500000, CNR, Progetto Finalizzato Geodinamica.

Bistacchi, A., M. Massiron, and L. Menegon (2010). Three-dimensional characterization of a crustal-scale fault zone: The Pusteria and Sprechenstein fault system (Eastern Alps), J. Struc. Geol., 32(12), 2022–2041.

Borsi, S., A. Del Morro, F.P. Sassi, and G. Zirpoli (1973), Metamorphic evolution of the Austridic rocks to the south of the Tauern Window (Eastern Alps): radiometric and geopetrologic data, Mem. Soc. geol. ital. (Pisa), 12, 549–571.

Borsi, S., A. Del Moro, F.P. Sassi, A. Zanferrari, and G. Zirpoli (1978), New geopetrologic and radiometric data on the alpine history of the Austridic continental margin south of the Tauern Window, Mem. Sci. Geol. (Padova), 32, 1–17.

Bousquet, R., S.M. Schmid, G. Zeilinger, R. Oberhänsli, C.L. Rosenberg, G. Molli, C. Robert, M. Wiederkehr, and P. Rossi (2012a), Tectonic framework of the Alps, CCGM/CGMW

Bousquet, R., R. Oberhänsli, S.M. Schmid, A. Berger, M. Wiederkehr, C. Robert, C.L. Rosenberg, F. Koller, G. Molli, and G. Zeilinger (2012b), Metamorphic framework of the Alps, CCGM/CGMW

Brandner, R., A. Töchterle, and F. Reiter (2008), Überblick zu den Ergebnissen der geologischen Vorerkundung für den Brenner-Basistunnel, Geo. Alp, 5, 165–174.

Christensen, J. N., J. Selverstone, J.L. Rosenfeld, and D.J. DePaolo (1994), Correlation by Rb-Sr geochronology of garnet growth histories from different structural levels within the Tauern Window, Eastern Alps, Contrib. Mineral. Petr., 118(1), 1–12.

Cole, J., B. Hacker, L. Ratschbacher, J. Dolan, G. Seward, E. Frost, and W. Frank (2007), Localized ductile shear below the seismogenic zone: Structural analysis of an exhumed strike-slip fault, Austrian Alps, J. Geophys. Res., 112, doi:10.1029/2007JB004975.

Cornelius, H.P. (1940), Zur Auffassung der Ostalpen im Sinne der Deckenlehre, Ger. J. Geosci., 92, 271–312.

Dachs, E. and A. Proyer (2001), Relics of high-pressure metamorphism from the Grossglockner region, Hohe Tauern, Austria: paragenetic evolution and PT-paths of retrogressed eclogites, Eur. J. Mineral., 13, 67–86.

Davis, J.H., and F. von Blanckenburg (1994), Slab breakoff: A model of lithosphere detachment and its test in the magmatism and deformation of collisional orogens, Earth Panet. Sc. Lett. 129, 85–102

De Vecchi, G., and P. Baggio (1982), The Pennine zone of the Vizze region in the western Tauern Window (Italian Eastern Alps). - Boll. Soc. Geol. ital., 101, 89–116.

Dewey, J.F., R.E. Holdsworth, and R.A. Strachan (1998), Transpression and transtension zones, Geol. Soc. (London) Spec. Publ., 135, 1–14, doi: 10.1144/GSL.SP.1998.135.01.01.

Ebner, M., K. Decker, and B. Grasemann (2004), Normal versus Strike-Slip Faulting–Deformation Mechanisms During Exhumation in the Footwall of the Brenner Normal Fault (Tyrol, Austria), ISSN 1608–8166, PanGeo Austria 2004, abstract volume.

Exner, C. (1956). Geologische Karte der Umgebung von Gastein, 1:50.000, Wien: Geol. B–A.

Exner, C. (1962a), Sonnblicklamelle und Mölltallinie, Jb. Geol. B–A., 105, 272–286.

Exner, C. (1962b), Geologische Karte der Sonnblickgruppe, 1:50.000, Geologische Bundesanstalt, Wien.

Exner, C. (1979), Geologische Karte des Salzachtales zwischen Taxenbach und Lend, 1:25.000. In: Exner, C., Geologie des Salzachtales zwischen Taxenbach und Lend, Jb. Geol. B–A., 122, p. 73.

Exner, C. (1980), Geologie der Hohen Tauern bei Gmünd in Kärnten, Jb. Geol. B–A., 123, 343–410.

Exner, C. (1983), Geologische Karte der Hafnergruppe, 1:25.000. Mitt. D. Ges. Geol. U. Bergbaustudenten in Österreich, 29, 1983.

Exner, C. (1989), Geologie des mittleren Lungaus, Jb. Geol. B–A., 132, 7–103.

Frank, W. and G. Pestal (2008), Geologische Karte – Umgebung von Wagrain, Nachrug auf C. Exner, 1:25.000. Jb. Geol. B–A., p. 148.

Frank, W., C. Miller, G. Pestal, H.P. Cornelius, G. Fuchs, G. Grundmann, L. Hoke, G. Malecki, F. Popp, O. Schmidegg, H.P. Steyrer (1987), Geological map sheet 152 Matrei 1:50.000. Wien: Geol. B–A.

Frisch, W., I. Dunkl, and J. Kuhlemann (2000), Postcollisional orogen-parallel large-scale extension in the Eastern Alps, Tectonophysics, 327, 239–265.

Frisch, O. (2010), Altersbestimmungen an Hellglimmer und Biotit aus dem Tuxer Gneiskerns, westliches Tauernfenster, Ostalpen: Ein methodischer Vergleich zur Datierung von Scherzonen, Diploma-Thesis, Freie Universität Berlin, p. 74.

Froitzheim, N. (1992), Formation of recumbent folds during synorogenic crustal extension (Austroalpine nappes, Switzerland), Geology, 20, 923–926, doi:10.1130/0091-7613.

Frost, E., J. Dolan, C. Sammis, B. Hacker, J. Cole, and L. Ratschbacher (2009), Progressive strain localization in a major strike-slip fault exhumed from midseismogenic depths: Structural observations from the Salzach-Ennstal-Mariazell-Puchberg fault system, Austria, J. Geophys. Res., 114, B04406, doi:10.1029/2008JB005763.

Fügenschuh, B., D. Seward, and N.S. Mancktelow (1997), Exhumation in a convergent orogen: the western Tauern Window, Terra Nova, 9, 213–217.

Fügenschuh B., N.S. Mancktelow, and S.M. Schmid (2012), Comment on ‘‘Estimating displacement along the Brenner Fault and orogenparallel extension in the Eastern Alps’’ by Rosenberg and Garcia. Int. J. Earth. Sci., 101, 1451–1455, doi: 10.1007/s00531-011-0725-4

Giese, J. (2004), Geologie der südwestlichen Grenze des Tauernfensters (Mühlwalder Kamm, Italien) und die Analyse von Quarztexturen und Mikrogefügen in L-Tektoniten, Diploma-Thesis, Freie Universität Berlin, p. 134.

Glodny, J., U. Ring, A. Kühn, P. Gleissner, and G. Franz (2005), Crystallization and very rapid exhumation of the youngest Alpine eclogites (Tauern Window, Eastern Alps) from Rb/Sr mineral assemblage analysis, Contrib. Mineral. Petr., 149(6), 699–712.

Glodny, J., U. Ring, and A. Kühn (2008), Coeval high-pressure metamorphism, thrusting, strike-slip, and extensional shearing in the Tauern Window, Eastern Alps, Tectonics 27, TC4004, doi:10.1029/2007TC002193.

Grundmann, G. and G. Morteani (1985), The young uplift and thermal history of the central Eastern Alps (Austria/Italy), evidence from apatite fission track ages, Jb. Geol. B–A., 128, 197–216.

Hoernes, S. and H. Friedrichsen (1974), Oxygen isotope studies on metamorphic rocks of the Western Hohe Tauern area (Austria). Schweiz. Mineral. Petrog., 54, 769–788.

Höck, V., G. Pestal, P. Brandmeier, E. Clar, H.P. Cornelius, W. Frank, H. Matl, P. Neumayr, K. Petrakakis, T. Stadlmann, und H.P. Steyrer (1994), Geological map sheet 153 Großglockner 1:50.000. Wien: Geol. B–A.

Höck, V., A. Slaczka, and, A. Uchmann (2006), New biostratigraphic and palaeoenvironmental data on metamorphosed limestones from the northern margin of the Tauern Window (Eastern Alps, Austria). Austrian J. Earth Sci., 99, 42–56.

Hoinkes, G., F. Koller, G. Rantitsch, E. Dachs, V. Hock, F. Neubauer, and R. Schuster (1999), Alpine metamorphism of the Eastern Alps, Schweiz. Mineral. Petrog., 79 (1), 155–181.l

Inger, S., and R.A. Cliff (1994), Timing of metamorphism in the Tauern Window, Eastern Alps: Rb-Sr ages and fabric formation, J. Metamorph. Geol., 12(5), 695–707.

Karl, F., O. Schmidegg, H.P. Cornelius, A. Bianchi, and G.V. Dal Piaz (1979), Geological map sheet 151 Krimml 1:50.000. Wien: Geol. B.–A.

Kitzig, C.M. (2010), Structural analyses and dating of deformation of the Ahrntal fault, Diploma-Thesis, Freie Universität Berlin, p. 114.

Kurz, W., R. Handler, and C. Bertoldi (2008), Tracing the exhumation of the Eclogite Zone (Tauern Window, Eastern Alps) by $^{40}Ar/^{39}Ar$ dating of white mica in eclogites, Swiss J. Geosci., doi:10.1007/s00015-008-1281-1.

Lammerer, B. and M. Weger (1998), Footwall uplift in an orogenic wedge: the Tauern Window in the Eastern Alps of Europe, Tectonophysics, 285, 213–230.

Laubscher, H. (1988), Material balance in Alpine orogeny, Geol. Soc. Am. Bull., 100(9), 1313–1328.

Laubscher, H.P. (1990), The problem of the deep structure of the Southern Alps: 3-D material balance considerations and regional consequences, Tectonophysics, 176, 103–121.

Lichtenheld, T. (2004), Diplomkartierung zwischen Nevesstausee und Weissenbachtal Südtirol, Italien, Diploma-Mapping, Freie Universität Berlin, p. 75.

Linzer, H.G., K. Decker, H. Peresson, R. Dell'Mour, and W. Frisch (2002), Balancing lateral orogenic float of the Eastern Alps, Tectonophysics, 354(3), 211–237.

Luciani, V. (1989), Stratigrafia Sequenziale del Terziaro Nelle Catena del Monte Baldo (Provincie di Verona a Trento), Mem. Sci. Geol. (Padova), 41, 263–351.

Luciani, V., & Silvestrini, A. (1996), Planktonic foraminiferal biostratigraphy and paleoclimatology of the Oligocene/Miocene transition from the Monte Brione Formation (Northern Italy, Lake Garda), Memorie di Scienze Geologiche, 48, 155–169.

Luth, S., E. Willingshofer, M. ter Borgh, D. Sokoutis, J. van Otterloo, and A. Versteeg (2013), Kinematic analysis and analogue modelling of the Passeier-and Jaufen faults: implications for crustal indentation in the Eastern Alps, Int. J. Earth Sci., 1–20.

Luth, S.W. and E. Willingshofer (2008), Mapping of the Post-Collisional Cooling History of the Eastern Alps, Swiss J. Geosci., 101, 207–223.

Mancktelow, N.S., D.F. Stöckli, B. Grollimung, W. Müller, B. Fügenschuh, G. Viola, D. Seward, I.M. Villa (2001), The DAV and Periadriatic fault system in the Eastern Alps south of the Tauern window. Int. J. Earth Sci., 90, 593–622.

Martin, S., G. Bigazzi, M. Zattin, G. Viola, and M.L. Balestrieri (1998), Neogene kinematics of the Giudicarie fault (Central-Eastern Alps, Italy): new apatite fission-track data, Terra Nova, 10(4), 217–221.

Moser, M. (2006), Geological map sheet 177 St. Jacob in Defereggen 1:50.000. Wien: Geol. B–A.

Most, P. (2003), Late Alpine cooling histories of tectonic blocks along the central part of the Transalp-Traverse (Inntal – Gadertal): constraints from geochronology, PhD-thesis Eberhardt-Karls-Universität Tübingen, 151.

Müller, W., N.S. Mancktelow, and M. Meier (2000), Rb–Sr microchrons of synkinematic mica in mylonites: an example from the DAV fault of the Eastern Alps, Earth Panet. Sc. Lett., 180, 385–397.

Müller, W., G. Prosser, N.S. Mancktelow, I.M. Villa, S.P. Kelley, G. Viola, and F. Oberli (2001), Geochronological constraints on the evolution of the Periadriatic Fault System (Alps), Int. J. Earth Sci., 90, 623–653.

Nagel, T.J., D. Herwartz, S. Rexroth, C. Münker, N. Froitzheim, and W. Kurz (2013). Lu-Hf dating, petrography, and tectonic implications of the youngest Alpine eclogites (Tauern Window, Austria), Lithos, 170-171, 179–190.

Neubauer F., J. Genser, W. Kurz, and X. Wang (1999), Exhumation of the Tauern Window, Eastern Alps, Phys. Chem. Earth 24, No. 8, 675–680.

Nussbaum, C. 2000, Neogene Tectonics and Thermal Maturity of Sediments of the Easternmost Southern Alps (Friuli Area, Italy), PhD Thesis, Institut de Géologie Université de Neuchâtel

Peresson, H. and K. Decker (1997), The Tertiary dynamics of the northern Eastern Alps (Austria): changing palaeostresses in a collisional plate boundary, Tectonophysics, 272(2), 125–157.

Picotti, V., G. Prosser, A. Castellarin (1995), Structures and kinematics of the Giudicarie–Val Trompia fold and thrust belt (Central Southern Alps Northern Italy), Mem. Sc. Geol., 47, 95–109.

Plan, L., B. Grasemann, C. Spötl, K. Decker, R. Boch, and J. Kramers (2010), Neotectonic extrusion of the Eastern Alps: Constraints from U/Th dating of tectonically damaged speleothems, Geology, 38(6), 483–486.

Pollington, A.D. and E.F. Baxter (2010), High resolution Sm-Nd garnet geochronology reveals the uneven pace of tectonometamorphic processes, Earth Planet. Sc. Lett., 293, 63–71.

Pomella, H., U. Klötzli, R. Scholger, M. Stipp, and B. Fügenschuh (2011), The Northern Giudicarie and the Meran-Mauls fault (Alps, Northern Italy) in the light of new paleomagnetic and geochronological data from boudinaged Eo-/Oligocene tonalities, Int. J. Earth Sci., 100(8), 1827–1850.

Pomella, H., M. Stipp, and B. Fügenschuh (2012), Thermochronological record of thrusting and strike-slip faulting along the Giudicarie fault system (Alps, Northern Italy), Tectonophysics, 579, 118–130.

Prosser, G. (1998), Strike-slip movements and thrusting along a transpressive fault zone: The North Giudicarie line (Insubric line, northern Italy), Tectonics, 17(6), 921-937.

Raith, M., P. Raase, H. Kreuzer, and P. Müller (1978), The age of the Alpidic metamorphism in the western Tauern Window. Austrian Alps, according to radiometric dating, In: Closs, H, D. Röder, and K. Schmidt, Alps, Apennines, Hellenides; Inter-Union Commission on Geodynamics, Schweizerbart'sche Verlagsbuchhandlung (Stuttgart), Scientific Report No. 38, p. 140–148.

Ratschbacher, L., O. Merle, P. Davy, and P. Cobbold (1991a), Lateral extrusion in the eastern Alps: Part 1. Boundary conditions and experiments scaled for gravity, Tectonics 10, 245–256.

Ratschbacher, L., W. Frisch, H.G. Linzer, and O. Merle (1991b), Lateral extrusion in the Eastern Alps, part 2: structural analysis, Tectonics, 10(2), 257–271.

Ratschbacher, L., C. Dingeldey, C. Miller, B.R. Hacker, and M.O. McWilliams (2004), Formation, subduction, and exhumation of Penninic oceanic crust in the Eastern Alps: time constraints from $^{40}Ar/^{39}Ar$ geochronology, Tectonophysics, 394, 155–170.

Reicherter, K., R. Fimmel, and W. Frisch (1993), Sinistral strike-slip faults in the central Tauern window (Eastern Alps, Austria) Jb. Geol. B–A., 136, 495–502.

Reiter, K., N. Kukowski, and L. Ratschbacher (2011), The interaction of two indenters in analogue experiments and implications for curved fold-and-thrust belts, Earth Planet. Sc. Lett., 302(1), 132-146.

Röller, K. and C. Trepmann (2008), Stereo32 Version 0.09. http://www.ruhr-uni-bochum.de/hardrock/downloads.htm2008.

Rockenschaub, M., A. Nowotny, K. Decker, J. Feijth, D. Frieling, W. Frisch, A. Gruber, B. Kolenprat, J. Magiera, G. Poscher, F. Reiter, F. Riedl, T. Scheibner, und J. Zasadny (2009), Geological map sheet 149 Brenner 1:50.000. Wien: Geol. B–A.

Rockenschaub, M., A. Nowotny, R. Brandner, V. Fenti, W. Frisch, C. Friz, P. Frizzo, B. Kolenprat, J. Magiera, C. Prager, M. Reiser, T. Scheiber, A. Bistacchi, G.V. Dal Piaz, G. Dal Piaz, M. Massironi, B. Monoppoli, A. Schiavo, and G. Toffolon (2011), Geological map sheet 175 Sterzing 1:50.000. Wien: Geol. B–A.

Rosenberg, C.L. and A. Berger (2009), On the causes and modes of exhumation and lateral growth of the Alps, Tectonics 28, doi:10.1029/2008TC002442

Rosenberg, C.L. and S. Garcia (2011), Estimating displacement along the Brenner Fault and orogen-parallel extension in the Eastern Alps, Int. J. Earth Sci., 100, 1129–1145.

Rosenberg, C.L. and S. Garcia (2012), Reply to the comment of Fügenschuh et al. on the paper 'Estimating displacement along the Brenner Fault and orogen-parallel extension in the Eastern Alps' by Rosenberg and Garcia, Int J Earth Sci (Geol Rundsch) (2011) 100:1129–1145, Int. J. Earth Sci. 101:1457–1464, doi:10.1007/s00531-011-0726-3.

Rosenberg, C.L. and S. Schneider (2008), The western termination of the SEMP Fault (eastern Alps) and its bearing on the exhumation of the Tauern Window, In: Siegesmund, S., Fügenschuh, B., Froitzheim, N. (Eds) Tectonic Aspects of the Alpine-Dinaride-Carpathian System, Geol. Soc. (London) Spec. Publ., 298, 197–218.

Rosenberg, C.L., J.-P. Brun, and D. Gapais (2004), An indentation model of the Eastern Alps and the origin of the Tauern Window, Geology, 32, 997–1000.

Rosenberg, C.L., J.P. Brun, F. Cagnard, and D. Gapais (2007), Oblique indentation in the Eastern Alps: Insights from laboratory experiments, Tectonics, 26, doi:10.1029/2006TC001960.

Sanderson, D.J. and W.R.D. Marchini (1984), Transpression, J. Struct. Geol., 6, 449–458.

Satir, M. (1975), Die Entwicklungsgeschichte der westlichen Höhen Tauern und der südlichen Ötztalmasse aufgrund radiometrischer Altersbestimmungen, Mem. Ist. Geol. Mineral. Univ. (Padova), No. 31, p. 85.

Satir, M. and G. Morteani (1982), Petrological study and radiometric age determination of the migmatites in the Penninic rocks of the Zillertaler Alpen (Tyrol/Austria), Tscher. Miner. Petrogr., 30(1), 59–75.

Scharf, A., M.R. Handy, S. Favaro, S.M. Schmid, and A. Bertrand (2013), Modes of orogen-parallel stretching and extensional exhumation in response to microplate indentation and roll- back subduction (Tauern Window, Eastern Alps), Int. J. Earth Sci., doi:10.1007/s00531-013-0894-4.

Schmid, S.M., A. Scharf, M.R. Handy, and C.L. Rosenberg (2013), The Tauern Window (Eastern Alps. Austria): a new tectonic map, with cross-sections and a tectonometamorphic synthesis, Swiss J. Geosci. 106(1), 1–32.

Schneider, S. and K. Hammerschmidt (2009), K-Ar dating of sinistral deformation in the upper Schieferhülle, south-western Tauern Window (Eastern Alps), In EGU General Assembly Conference Abstracts, 11, 13813.

Schneider, S., N. Bungies, F. Frütsch, C.M. Kitzig, C.L. Rosenberg, M. Spanka, C. von Nicolai, and M. Wanner, (2009), Extent and significance of sinistral shear along the southwestern border of the Tauern Window, Eastern Alps (Italy/Austria), In EGU General Assembly Conference Abstracts, 11, 11429.

Schneider, S., K. Hammerschmidt, and C.L. Rosenberg (2013), Dating the longevity of ductile shear zones: Insight from $^{40}Ar/^{39}Ar$ in situ analyses, Earth Planet. Sc. Lett., (369–370), 43–58.

Schneider, S., C.M. Kitzig, S. Wollnik, M. Spanka, K. Hammerschmidt, and C.L. Rosenberg (in prep.), Timing and kinematics of the Ahrntal shear zone, the southern border of the sinistral

transpressive belt localized in the western Tauern Window, Eastern Alps, In: Ductile Shear Zones: from Micro- to Meso-scales (Blackwell Publishers) edited by S. Mukherjee and K. Mulchrone

Schönborn, G. (1992), Alpine tectonics and kinematic models of the central Southern Alps, Mem. Sci. Geol., 44, 229–393.

Sciunnach, D., G. Scardia, F. Tremolada, and I.P. Silva (2010), The Monte Orfano Conglomerate revisited: stratigraphic constraints on Cenozoic tectonic uplift of the Southern Alps (Lombardy, northern Italy), Int. J. Earth Sci. 99, 1335–1355, doi:10.1007/s00531-009-0452-2.

Selverstone, J. (1985), Petrologic constraints on imbrication, metamorphism, and uplift in the SW Tauern Window, Eastern Alps, Tectonics, 4(7), 687–704.

Selverstone, J. (1988), Evidence for E-W crustal extension in the Eastern Alps: implications for the unroofing history of the Tauern Window, Tectonics, 7, 87–105.

Selverstone, J. (1993), Micro- to macroscale interactions between deformational and metamorphic processes, Tauern Window, Eastern Alps, Schweiz. Miner. Petrog. 73, 229–239.

Selverstone, J. and F.S. Spear (1985), Metamorphic P–T Paths from pelitic schists and greenstones from the south-west Tauern Window, Eastern Alps, J. Metamorp. Geol., 3(4), 439–465.

Selverstone, J., G. Morteani, and J.M. Staude (1991), Fluid channeling during ductile shearing: transformation of granodiorite into aluminous schist in the Tauern Window, Eastern Alps, J. Metamorph. Geol., 9, 419–431.

Selverstone, J., G.J. Axen, and J.M. Bartley (1995), Fluid inclusion constraints on the kinematics of footwall uplift beneath the Brenner Line normal fault, eastern Alps, Tectonics, 14(2), 264–278.

Smye, A.J., M.J. Bickle, T.J.B. Holland, R.R. Parrish, and D.J. Condon (2011), Rapid formation and exhumation of the youngest Alpine eclogites: A thermal conundrum to Barrovian metamorphism, Earth Planet. Sc. Lett., (306), 193–204.

Spear F.S. and G. Franz (1986), PT evolution of metasediments from the Eclogite Zone, south-central Tauern Window, Austria. Lithos, 19(3), 219–234.

Spiess, R. (1995), The Passeier- Jaufen Line: A tectonic boundary between Variscan and an eo-Alpine Meran-Mauls basement, Schweiz. Mineral. Petrog., 75, 413–425.

Spiess R., M. Marini, W. Frank, B. Marcolongo, and G. Cavazzini (2001), The kinematics of the Southern Passeier fault: radiometric and petrographic constraints, Schweiz. Mineral. Petrog., 81, 197–212.

Steffen, K., J. Selverstone, and A. Brearley (2001), Episodic weakening and strengthening during synmetamorphic deformation in a deep crustal shear zone in the Alps, Geol. Soc. (London) Spec. Publ., 186, 141–156.

Thöni, M. (1980), Distribution of pre-Alpine and Alpine metamorphism of the southern Ötztal Mass and the Scarl Unit, based on K/Ar age determinations, Mitt. österr. geol. G., 71(72), 139–165.

Töchterle, A., R. Brandner, and F. Reiter (2011), Strain partitioning on major fault zones in the northwestern Tauern Window—insights from the investigations of the Brenner base tunnel. Austrian J. Earth Sci., 104, 15–35.

Urbanek, C., W. Frank, B. Grasemann, and K. Decker (2002), Eoalpine versus Tertiary deformation: Dating of heterogeneously partitioned strain (Tauern Window, Austria), PanGeo Austria 2002, abstract volume.

Viola, G., N.S. Mancktelow, and D. Seward (2001), Late Oligocene-Neogene evolution of Europe-Adria collision: New structural and geochronological evidence from the Giudicarie fault system (Italian Eastern Alps), Tectonics, 20(6), 999–1020, doi:10.1029/2001TC900021.

von Blanckenburg, F., I.M. Villa, H. Baur, G. Morteani, and R.H. Steiger (1989), Time calibration of a PT-path from the Western Tauern Window, Eastern Alps: the problem of closure temperatures, Contrib. Mineral. Petr., 101, 1–11.

Werling, E. (1992), Tonale-, Pejo- und Judicarienlinie. Kinematik, Mikrostrukturen und Metamorphose von Tektoniten aus räumlich interferierenden aber verschiedenaltrigen Verwerfungszonen, PhD Thesis, ETH Zürich, p. 276.

Woodcock, N.H, and M. Fischer (1986), Strike-slip duplexes, J. Struct. Geol., 8, 725–735.

Wollnik, S. (2012), Änderungen der Mikrostrukturen und der Zusammensetzung entlang eines Verformungsgradienten in Gneisen aus dem Ahrntal (Tauernfenster), mit besonderem Augenmerk auf Granulares Fließen, Diploma-Thesis, Freie Universistät Berlin, p. 66.

Zimmermann, R., K. Hammerschmidt, G. Franz (1994), Eocene high pressure metamorphism in the Penninic units of the Tauern Window (Eastern Alps): evidence from ^{40}Ar-^{39}Ar dating and petrological investigations, Contrib. Mineral. Petr., 117, 175–186.

Zwingmann, H. and N.S. Mancktelow (2004), Timing of Alpine fault gouges, Earth Planet. Sc. Lett., 223(3), 415–425.

3.10 Supplementary material

Supporting Table 1: raw data of structural measurements

Domain A			Domain B			Domain C			Domain D			Domain E		
338	64	S1	350	30	S1	161	58	S1	350	42	S1	49	55	S0
165	75	S1	352	36	S1	132	70	S1	357	43	S1	62	64	S0
249	46	S1	303	54	S1	153	60	S1	342	44	S1	43	51	S0
315	65	S1	304	57	S1	163	65	S1	326	24	S1	186	88	S1
0	53	S1	330	60	S1	337	81	S1	120	78	S1	238	22	S1
353	30	S1	322	54	S1	343	70	S1	124	81	S1	243	37	S1
346	35	S1	39	34	S1	345	70	S1	144	54	S1	326	45	S1
325	36	S1	173	20	S1	347	35	S1	142	45	S1	174	19	S1
350	42	S1	338	13	S1	323	60	S1	142	44	S1	357	45	S1
11	48	S1	336	41	S1	319	60	S1	151	60	S1	180	48	S1
359	58	S1	188	39	S1	335	63	S1	143	64	S1	169	63	S1
0	54	S1	21	56	S1	327	62	S1	150	84	S1	169	58	S1
347	64	S1	16	55	S1	311	54	S1	124	38	S1	192	74	S1
169	35	S1	25	38	S1	306	69	S1	119	36	S1	181	60	S1
162	84	S1	20	42	S1	329	57	S1	229	35	S1	349	74	S1
143	39	S1	24	54	S1	355	52	S1	116	33	S1	351	79	S1
107	14	S1	22	52	S1	343	47	S1	127	57	S1	191	40	S1
241	70	S1	146	66	S1	359	39	S1	357	49	S1	186	44	S1
183	78	S1	124	61	S1	359	39	S1	152	10	S1	320	47	S1
181	62	S1	133	24	S1	346	53	S1	147	39	S1	315	64	S1
178	57	S1	183	24	S1	242	54	S1	68	44	S1	315	40	S1
352	88	S1	192	26	S1	317	68	S1	75	44	S1	344	57	S1
151	75	S1	173	88	S1	315	64	S1	32	48	S1	330	45	S1
171	69	S1	351	87	S1	336	64	S1	38	42	S1	334	71	S1
182	65	S1	157	72	S1	331	46	S1	115	9	S1	330	64	S1
181	71	S1	136	36	S1	148	64	S1	116	4	S1	324	67	S1
170	71	S1	154	30	S1	141	51	S1	45	72	S1	50	6	S1
339	67	S1	134	84	S1	129	50	S1	63	48	S1	355	79	S1
327	52	S1	152	55	S1	139	50	S1	34	66	S1	45	30	S1
168	79	S1	313	66	S1	288	50	S1	3	38	S1	277	47	S1
193	35	S1	19	74	S1	281	59	S1	9	23	S1	336	38	S1
352	62	S1	21	74	S1	275	74	S1	256	76	S1	338	49	S1
330	70	S1	198	78	S1	355	30	S1	288	77	S1	332	25	S1
340	60	S1	38	87	S1	331	27	S1	281	67	S1	315	33	S1
351	89	S1	33	53	S1	105	75	S1	284	60	S1	316	30	S1
177	87	S1	4	58	S1	332	74	S1	130	56	S1	335	64	S1
325	73	S1	21	75	S1	326	48	S1	112	57	S1	335	63	S1
347	87	S1	17	74	S1	302	38	S1	115	57	S1	337	76	S1
343	79	S1	349	69	S1	265	21	S1	144	63	S1	328	68	S1
318	65	S1	11	73	S1	260	21	S1	124	35	S1	336	32	S1
310	61	S1	29	28	S1	268	67	S1	163	41	S1	335	35	S1
165	78	S1	1	36	S1	305	35	S1	139	37	S1	300	19	S1
331	45	S1	24	45	S1	297	43	S1	130	76	S1	57	9	S1
148	57	S1	25	43	S1	323	68	S1	144	44	S1	359	20	S1
321	55	S1	20	70	S1	320	68	S1	142	48	S1	355	54	S1
325	37	S1	8	48	S1	325	70	S1	153	44	S1	330	56	S1
320	56	S1	341	74	S1	136	52	S1	148	48	S1	334	60	S1
337	80	S1	22	40	S1	123	63	S1	98	36	S1	328	52	S1
330	40	S1	10	51	S1	322	58	S1	163	25	S1	332	48	S1

Supporting Table 1: raw data of structural measurements

Domain A			Domain B			Domain C			Domain D			Domain E		
355	61	S1	30	40	S1	322	55	S1	139	64	S1	333	49	S1
339	34	S1	24	51	S1	321	46	S1	85	32	S1	280	33	S1
351	74	S1	21	45	S1	322	53	S1	129	85	S1	284	33	S1
172	65	S1	11	55	S1	342	34	S1	356	42	S1	315	46	S1
2	75	S1	181	33	S1	2	32	S1	3	45	S1	309	41	S1
158	72	S1	194	45	S1	356	34	S1	168	54	S1	297	35	S1
166	76	S1	209	45	S1	324	72	S1	185	64	S1	257	33	S1
155	57	S1	196	42	S1	338	60	S1	187	51	S1	290	35	S1
154	50	S1	142	52	S1	312	47	S1	181	59	S1	288	35	S1
316	62	S1	353	62	S1	313	41	S1	184	65	S1	56	48	S1
153	73	S1	168	68	S1	328	49	S1	156	65	S1	62	57	S1
334	65	S1	131	72	S1	321	54	S1	163	60	S1	57	49	S1
315	72	S1	340	32	S1	328	44	S1	160	45	S1	79	49	S1
331	64	S1	114	15	S1	316	38	S1	181	40	S1	72	53	S1
34	36	S1	11	13	S1	342	53	S1	171	85	S1	106	62	S1
11	44	S1	304	30	S1	334	57	S1	185	76	S1	120	67	S1
4	50	S1	329	22	S1	359	28	S1	181	71	S1	58	60	S1
159	81	S1	331	54	S1	359	25	S1	156	86	S1	85	61	S1
158	71	S1	2	65	S1	325	65	S1	347	88	S1	101	68	S1
168	67	S1	143	68	S1	332	49	S1	170	79	S1	97	68	S1
167	68	S1	129	67	S1	296	39	S1	27	65	S1	157	75	S1
351	86	S1	153	55	S1	316	33	S1	22	65	S1	157	62	S1
175	79	S1	157	56	S1	82	20	S1	14	76	S1	120	24	S1
175	81	S1	137	79	S1	194	28	S1	0	56	S1	149	75	S1
172	90	S1	132	80	S1	223	28	S1	2	74	S1	170	52	S1
346	79	S1	129	76	S1	348	35	S1	9	74	S1	162	86	S1
325	69	S1	130	77	S1	346	38	S1	165	78	S1	264	59	S1
341	80	S1	129	69	S1	344	48	S1	165	85	S1	247	75	S1
180	40	S1	30	19	S1	5	30	S1	140	82	S1	191	88	S1
168	83	S1	42	30	S1	345	35	S1	135	79	S1	218	43	S1
168	60	S1	30	22	S1	335	32	S1	154	84	S1	283	45	S1
175	41	S1	48	23	S1	348	35	S1	163	83	S1	176	85	S1
170	71	S1	31	40	S1	340	44	S1	350	83	S1	211	36	S1
170	65	S1	33	36	S1	338	61	S1	350	81	S1	198	73	S1
160	35	S1	59	37	S1	167	64	S1	334	65	S1	235	49	S1
148	35	S1	58	34	S1	177	40	S1	334	73	S1	184	79	S1
145	55	S1	48	29	S1	191	28	S1	320	54	S1	168	76	S1
230	34	S1	52	35	S1	211	27	S1	355	45	S1	164	41	S1
150	38	S1	64	48	S1	264	33	S1	315	49	S1	175	55	S1
150	56	S1	59	29	S1	303	68	S1	352	39	S1	198	41	S1
175	67	S1	85	23	S1	288	87	S1	10	49	S1	188	35	S1
73	35	S1	73	27	S1	277	74	S1	358	45	S1	104	87	S1
252	62	S1	96	26	S1	324	50	S1	353	42	S1	9	63	S1
315	34	S1	28	43	S1	21	25	S1	334	52	S1	19	70	S1
346	59	S1	71	39	S1	19	23	S1	354	79	S1	350	52	S1
322	48	S1	288	68	S1	25	25	S1	355	78	S1	17	58	S1
325	60	S1	300	48	S1	58	15	S1	16	48	S1	281	32	S1
342	75	S1	148	26	S1	267	4	S1	342	44	S1	317	42	S1
351	40	S1	338	81	S1	292	35	S1	11	66	S1	309	33	S1

Supporting Table 1: raw data of structural measurements

Domain A			Domain B			Domain C			Domain D			Domain E		
358	58	S1	39	35	S1	273	42	S1	338	56	S1	175	82	S1
328	62	S1	20	38	S1	7	20	S1	349	70	S1	173	88	S1
332	55	S1	142	26	S1	97	53	S1	351	81	S1	173	79	S1
340	60	S1	339	21	S1	289	38	S1	11	83	S1	176	37	S1
340	72	S1	316	24	S1	247	47	S1	359	84	S1	348	24	S1
340	84	S1	106	55	S1	277	47	S1	338	63	S1	347	31	S1
342	70	S1	108	61	S1	310	63	S1	320	70	S1	206	60	S1
170	89	S1	64	35	S1	272	52	S1	9	35	S1	240	35	S1
254	32	S1	75	39	S1	251	64	S1	62	45	S1	228	38	S1
336	38	S1	329	82	S2	270	19	S1	46	39	S1	339	60	S1
342	38	S1	330	67	S2	113	87	S1	33	34	S1	351	86	S1
159	75	S1	178	62	S2	272	67	S1	47	32	S1	191	69	S1
150	60	S1	216	65	S2	279	37	S1	24	43	S1	325	31	S1
335	38	S1	185	75	S2	291	69	S1	45	37	S1	167	72	S1
328	37	S1	192	33	S2	268	45	S1	44	34	S1	338	22	S1
1	58	S1	180	56	S2	266	45	S1	5	42	S1	350	47	S1
357	54	S1	184	77	S2	304	58	S1	69	34	S1	170	85	S1
346	53	S1	189	80	S2	282	40	S1	24	43	S1	336	55	S1
326	45	S1	216	56	S2	306	52	S1	179	49	S1	198	42	S1
340	35	S1	3	82	S2	312	53	S1	165	50	S1	190	88	S1
339	69	S1	10	84	S2	337	65	S1	225	66	S1	0	52	S1
331	35	S1	220	80	S2	311	82	S1	168	66	S1	215	45	S1
147	42	S1	211	86	S2	286	79	S1	164	30	S1	216	49	S1
165	59	S1	135	86	S2	321	65	S1	135	24	S1	246	25	S1
165	59	S1	325	68	S2	326	85	S1	175	48	S1	203	33	S1
322	48	S1	312	69	S2	321	56	S1	189	27	S1	202	39	S1
328	46	S1	359	79	S2	0	55	S1	177	42	S1	204	29	S1
340	46	S1	186	88	S2	321	41	S1	20	8	S1	247	22	S1
350	49	S1	346	85	S2	328	48	S1	208	33	S1	250	28	S1
325	68	S1	346	86	S2	348	57	S1	225	32	S1	197	14	S1
18	89	S1	351	85	S2	348	66	S1	346	18	S1	202	26	S1
10	61	S1	151	60	S2	331	82	S1	354	38	S1	246	18	S1
171	85	S1	159	63	S2	65	53	S1	220	36	S1	232	28	S1
162	83	S1	148	62	S2	354	64	S1	194	52	S1	235	29	S1
10	61	S1	155	67	S2	349	54	S1	177	28	S1	251	22	S1
11	41	S1	157	65	S2	348	49	S1	207	43	S1	263	28	S1
5	48	S1	153	67	S2	14	47	S1	214	27	S1	257	41	S1
31	17	S1	355	74	S2	342	80	S1	192	77	S1	240	35	S1
344	57	S1	360	73	S2	347	65	S1	207	77	S1	253	49	S1
355	69	S1	138	80	S2	162	59	S1	3	74	S1	266	59	S1
332	67	S1	150	72	S2	162	49	S1	167	44	S1	310	48	S1
336	79	S1	135	73	S2	308	48	S1	193	60	S1	316	52	S1
335	88	S1	168	78	S2	304	45	S1	159	52	S1	293	47	S1
157	64	S1	157	84	S2	34	28	S1	168	64	S1	265	35	S1
155	62	S1	329	83	S2	48	30	S1	171	66	S1	317	30	S1
155	62	S1	329	89	S2	123	66	S1	351	53	S1	335	33	S1
162	46	S1	317	84	S2	137	67	S1	305	55	S1	274	25	S1
166	52	S1	318	82	S2	120	11	S1	311	20	S1	267	27	S1
170	52	S1	122	79	S2	356	28	S1	340	42	S1	239	15	S1

Supporting Table 1: raw data of structural measurements

Domain A			Domain B			Domain C			Domain D			Domain E		
120	49	S1	131	70	S2	179	10	S1	347	45	S1	205	24	S1
144	35	S1	131	72	S2	348	45	S1	188	86	S1	191	28	S1
131	43	S1	145	62	S2	11	26	S1	3	88	S1	191	21	S1
165	82	S1	346	74	S2	32	25	S1	0	84	S1	208	9	S1
45	19	S1	348	71	S2	341	40	S1	342	43	S1	172	25	S1
35	23	S1	344	71	S2	345	35	S1	359	81	S1	202	19	S1
340	35	S1	342	75	S2	353	45	S1	174	65	S1	229	21	S1
176	82	S1	339	65	S2	356	38	S1	183	75	S1	219	30	S1
115	82	S1	339	72	S2	351	30	S1	151	34	S1	335	20	S1
191	5	S1	353	68	S2	324	28	S1	172	58	S1	326	32	S1
240	10	S1	355	68	S2	302	35	S1	158	30	S1	329	18	S1
342	72	S1	358	68	S2	106	25	S1	174	46	S1	195	63	S1
348	78	S1	6	72	S2	120	51	S1	169	70	S1	184	81	S1
166	78	S1	1	77	S2	233	83	S1	168	67	S1	329	34	S1
324	83	S1	346	85	S2	264	28	S1	174	64	S1	186	27	S1
177	64	S1	342	81	S2	325	30	S1	178	80	S1	13	89	S1
152	69	S1	350	84	S2	344	22	S1	170	64	S1	22	46	S1
185	87	S1	160	65	S2	296	31	S1	170	67	S1	4	64	S1
264	34	S1	322	83	S2	334	81	S1	165	43	S1	33	43	S1
284	45	S1	151	68	S2	246	77	S1	154	55	S1	9	67	S1
153	75	S1	336	64	S2	263	63	S1	162	57	S1	182	72	S1
152	88	S1	174	48	S2	277	82	S1	168	55	S1	178	46	S1
350	87	S1	168	50	S2	278	81	S1	171	61	S1	186	72	S1
336	90	S1	188	58	S2	186	28	S1	166	67	S1	330	55	S1
336	90	S1	181	47	S2	154	62	S1	180	56	S1	337	47	S1
355	38	S1	112	60	S2	172	47	S1	172	70	S1	169	39	S1
347	60	S1	114	57	S2	322	52	S1	142	15	S1	220	34	S1
349	87	S1	94	30	S2	324	50	S1	175	65	S1	344	36	S1
355	85	S1	97	63	S2	304	440	S1	161	41	S1	320	22	S1
6	56	S1	105	70	S2	336	87	S1	172	40	S1	15	25	S1
2	55	S1	259	37	S2	353	85	S1	155	24	S1	354	35	S1
355	76	S1	285	51	S2	315	48	S1	135	19	S1	337	44	S1
5	84	S1	125	46	S2	334	62	S1	175	35	S1	24	28	S1
172	87	S1	91	45	S2	297	34	S1	170	38	S1	5	40	S1
145	62	S1	316	65	S2	304	25	S1	165	68	S1	334	59	S1
116	46	S1	109	63	S2	329	48	S1	164	67	S1	330	21	S1
349	58	S1	119	63	S2	356	45	S1	164	63	S1	334	28	S1
33	27	S1	119	67	S2	345	47	S1	167	72	S1	355	81	S2
112	24	S1	128	80	S2	323	60	S1	172	78	S1	343	90	S2
21	29	S1	132	71	S2	321	48	S1	205	33	S1	342	88	S2
340	70	S1	131	80	S2	328	62	S1	206	30	S1	342	87	S2
332	70	S1	139	72	S2	303	60	S1	190	37	S1	357	78	S2
354	86	S1	133	72	S2	308	56	S1	190	45	S1	353	75	S2
357	72	S1	132	69	S2	300	85	S1	161	34	S1	359	60	S2
349	88	S1	137	84	S2	309	70	S1	174	45	S1	345	46	S2
346	65	S1	136	86	S2	269	58	S1	166	35	S1	144	80	S2
8	57	S1	138	74	S2	328	60	S1	173	35	S1	155	72	S2
324	43	S1	133	80	S2	314	59	S1	188	40	S1	325	86	S2
329	9	S1	150	90	S2	309	26	S1	196	37	S1	309	73	S2

Supporting Table 1: raw data of structural measurements

Domain A			Domain B			Domain C			Domain D			Domain E		
312	42	S1	158	87	S2	325	37	S1	19	24	S1	333	85	S2
145	81	S1	148	76	S2	332	48	S1	14	30	S1	318	83	S2
153	88	S1	142	78	S2	331	49	S1	10	20	S1	16	69	S2
5	86	S1	148	78	S2	272	22	S1	106	27	S1	15	79	S2
165	35	S1	158	68	S2	247	21	S1	13	67	S1	21	80	S2
146	27	S1	150	82	S2	303	51	S1	357	59	S1	22	76	S2
146	20	S1	146	84	S2	316	54	S1	18	80	S1	348	63	S2
347	53	S1	150	82	S2	331	39	S1	11	81	S1	349	74	S2
335	69	S1	142	82	S2	327	38	S1	167	36	S1	358	67	S2
329	65	S1	288	58	S2	339	55	S1	162	22	S1	344	46	S2
338	57	S1	290	73	S2	340	54	S1	180	54	S1	351	59	S2
335	50	S1	134	71	S2	292	75	S1	199	56	S1	353	70	S2
280	32	S1	293	76	S2	304	86	S1	210	45	S1	332	79	S2
344	54	S1	121	90	S2	251	37	S1	191	45	S1	345	71	S2
351	64	S1	310	67	S2	259	39	S1	224	38	S1	330	45	S2
334	55	S1	133	80	S2	152	26	S1	134	23	S1	334	71	S2
340	60	S1	129	63	S2	161	24	S1	121	24	S1	330	64	S2
342	72	S1	120	64	S2	98	35	S1	194	38	S1	324	67	S2
332	65	S1	162	82	S2	93	31	S1	203	53	S1	330	64	S2
341	72	S1	153	75	S2	130	83	S1	200	58	S1	330	64	S2
12	55	S1	162	82	S2	134	64	S1	136	78	S1	319	67	S2
10	58	S1	153	75	S2	291	48	S1	150	58	S1	330	69	S2
5	64	S1	356	39	S2	291	40	S1	147	63	S1	323	63	S2
253	8	S1	334	62	S2	301	46	S1	144	69	S1	319	81	S2
215	18	S1	45	30	S2	240	34	S1	160	67	S1	342	40	S2
160	65	S1	33	33	S2	256	35	S1	203	55	S1	332	35	S2
170	90	S1	347	46	S2	155	72	S1	192	64	S1	332	49	S2
156	60	S1	333	37	S2	141	45	S1	216	35	S1	333	53	S2
150	80	S1	150	80	S2	157	54	S1	170	65	S1	352	37	S2
334	74	S1	161	85	S2	308	50	S1	186	55	S1	342	48	S2
173	25	S1	145	88	S2	306	54	S1	196	37	S1	345	49	S2
115	3	S1	161	78	S2	306	46	S1	296	39	S1	352	52	S2
80	42	S1	149	62	S2	341	67	S1	186	73	S1	354	52	S2
350	84	S1	332	82	S2	331	58	S1	214	51	S1	359	52	S2
145	45	S1	326	86	S2	333	61	S1	198	13	S1	6	45	S2
120	52	S1	345	77	S2	331	50	S1	196	14	S1	328	52	S2
348	57	S1	28	73	S2	322	72	S1	2	40	S1	340	73	S2
194	83	S1	30	88	S2	318	48	S1	58	45	S1	44	54	S2
40	72	S1	271	20	S2	176	65	S1	290	15	S1	355	46	S2
7	61	S1	159	30	S2	188	69	S1	113	18	S1	343	48	S2
347	67	S1	135	36	S2	299	56	S1	172	63	S1	331	50	S2
347	37	S1	258	85	dex C	304	56	S1	179	43	S1	358	51	S2
356	39	S1	38	77	dex C	302	60	S1	182	80	S1	325	40	S2
172	55	S1	22	72	dex C	338	47	S1	168	46	S1	5	61	S2
184	57	S1	356	39	rev C	333	45	S1	174	53	S1	324	65	S2
358	70	S1	352	45	rev C	310	41	S1	172	65	S1	10	43	S2
344	65	S1	11	66	rev C	228	21	S1	186	71	S1	342	84	S2
350	55	S1	194	74	rev C	300	6	S1	189	80	S1	333	57	S2
355	68	S1	131	73	sin C	301	50	S1	343	46	S1	152	70	S2

Supporting Table 1: raw data of structural measurements

Domain A			Domain B			Domain C			Domain D			Domain E		
6	45	S1	124	72	sin C	288	58	S1	0	52	S1	168	71	S2
2	37	S1	140	70	sin C	280	43	S1	145	35	S1	332	85	S2
332	34	S1	296	75	sin C	174	21	S1	32	22	S1	143	80	S2
337	37	S1	304	85	sin C	325	25	S1	172	33	S1	308	88	S2
346	67	S1	112	82	sin C	269	18	S1	121	42	S1	343	66	S2
334	54	S1	210	78	sin C	177	23	S1	139	28	S1	343	52	S2
172	84	S1	11	63	sin C	291	37	S1	182	24	S1	244	90	S2
355	86	S1	39	78	sin C	200	24	S1	146	36	S1	244	90	S2
334	35	S1	5	65	sin C	281	49	S1	172	54	S1	337	72	S2
341	54	S1	186	80	sin C	273	48	S1	178	43	S1	348	87	S2
342	50	S1	17	86	sin C	333	54	S1	149	38	S1	331	70	S2
352	60	S1	139	79	sin C	325	42	S1	206	46	S1	334	86	S2
356	72	S1	135	85	sin C	303	33	S1	178	87	S1	329	42	S2
348	70	S1	129	72	sin C	16	29	S1	187	82	S1	327	54	S2
324	27	S1	323	86	sin C	309	49	S1	9	68	S1	343	53	S2
329	26	S1	125	60	sin C	19	90	S1	359	62	S1	340	57	S2
331	44	S1	152	61	sin C	2	70	S1	342	72	S1	318	51	S2
349	59	S1	162	70	sin C	318	52	S1	341	42	S1	176	40	S2
342	70	S1	126	74	sin C	343	74	S1	327	60	S1	156	68	S2
345	55	S1	128	79	sin C	314	56	S1	280	34	S1	170	47	S2
340	56	S1	126	82	sin C	344	38	S1	10	66	S1	292	90	S2
346	35	S1	137	90	sin C	276	48	S1	37	30	S1	140	80	S2
344	50	S1	135	84	sin C	326	46	S1	353	78	S1	134	80	S2
345	23	S1	137	75	sin C	317	48	S1	339	84	S1	300	82	S2
149	37	S1	122	78	sin C	334	81	S1	338	49	S1	334	36	S2
5	71	S1	118	70	sin C	353	81	S1	118	18	S1	339	21	S2
338	40	S1	122	70	sin C	5	67	S1	146	54	S1	264	79	S2
310	62	S1	330	85	sin C	24	77	S1	158	82	S1	273	76	S2
345	60	S1	335	88	sin C	343	54	S1	152	65	S1	167	85	S2
331	73	S1	350	87	sin C	189	46	S1	163	68	S1	166	78	S2
320	75	S1	348	85	sin C	289	29	S1	328	86	S1	357	67	S2
350	81	S1	126	60	sin C	202	58	S1	156	80	S1	11	64	S2
295	45	S1	311	78	sin C	231	32	S1	156	32	S1	285	10	S3
338	55	S1	296	75	sin C	207	20	S1	158	30	S1	220	28	S3
353	80	S1	304	85	sin C	258	52	S1	140	24	S1	306	7	S3
153	76	S1	112	82	sin C	340	52	S1	121	20	S1	353	19	S3
130	68	S1	291	65	sin C	2	44	S1	144	23	S1	100	36	S3
143	62	S1	164	66	sin C	173	5	S1	188	23	S1	319	16	S3
136	70	S1	298	68	sin C	67	29	S1	337	85	S1	289	45	S3
144	75	S1	320	85	sin C	305	21	S1	357	82	S1	248	46	S3
138	66	S1	178	82	sin C	173	15	S1	1	84	S1	277	53	S3
140	74	S1	191	78	sin C	81	54	S1	168	30	S1	197	30	S3
142	79	S1	181	74	sin C	214	35	S1	137	28	S1	308	59	S3
137	40	S1	192	84	sin C	44	20	S1	168	35	S1	226	19	S3
161	51	S1	30	53	sin C	24	16	S1	178	42	S1	253	32	S3
154	69	S1	321	78	sin C	4	20	S1	190	56	S1	263	30	S3
316	33	S1	317	90	sin C	26	56	S1	175	62	S1	315	28	S3
144	84	S1	322	82	sin C	48	31	S1	174	30	S1	300	30	S3
140	75	S1	157	51	dex C	78	79	S1	112	36	S1	339	60	S3

Supporting Table 1: raw data of structural measurements

Domain A			Domain B			Domain C			Domain D			Domain E		
141	56	S1	4	79	dex C	65	79	S1	66	45	S1	335	50	S3
176	48	S1	174	73	dex C	52	37	S1	30	39	S1	266	18	S3
170	67	S1	96	46	norm C	33	46	S1	118	25	S1	284	27	S3
299	50	S1	133	43	norm C	15	39	S1	170	65	S1	338	18	S3
289	52	S1	102	49	norm C	340	53	S1	357	68	S1	344	16	S3
262	24	S1	83	55	norm C	257	39	S1	152	63	S1	118	20	S3
238	15	S1	66	51	norm C	337	44	S1	17	72	S1	286	24	S3
183	39	S1	68	25	norm C	347	42	S1	174	85	S1	286	26	S3
312	67	S1	60	54	norm C	341	50	S1	148	78	S1	333	39	S3
310	67	S1	80	45	norm C	335	65	S1	170	66	S1	357	65	S3
324	80	S1	91	71	norm C	331	58	S1	338	84	S1	341	56	S3
326	78	S1	141	67	norm C	326	67	S1	176	84	S1	259	59	S3
288	59	S1	99	74	norm C	331	45	S1	333	79	S1	294	54	S3
308	66	S1	64	50	norm C	321	40	S1	178	22	S1	280	47	S3
176	56	S1	139	45	sin C	338	40	S1	320	24	S1	285	57	S3
164	62	S1	119	86	sin C	356	45	S1	114	40	S1	305	55	S3
145	66	S1	113	75	sin C	320	43	S1	113	24	S1	110	25	S3
153	66	S1	97	81	sin C	353	51	S1	6	14	S1	87	32	S3
170	53	S1	129	74	sin C	338	41	S1	143	37	S1	292	38	S3
169	57	S1	132	90	sin C	308	34	S1	307	36	S1	100	23	S3
140	62	S1	316	82	sin C	329	33	S1	148	73	S1	305	30	S3
140	67	S1	320	88	sin C	358	36	S1	138	68	S1	311	28	S3
183	63	S1	141	78	sin C	11	26	S1	336	68	S1	336	38	S3
301	87	S1	149	80	sin C	16	36	S1	333	71	S1	316	36	S3
321	61	S1	101	76	sin C	329	9	S1	328	61	S1	336	31	S3
166	39	S1	102	80	sin C	307	14	S1	81	10	S1	262	28	S3
164	70	S1	104	80	sin C	65	24	S1	321	32	S1	216	35	S3
153	70	S1	124	83	sin C	350	28	S1	174	20	S1	14	25	S3
168	56	S1	108	82	sin C	288	25	S1	307	38	S1	326	36	S3
244	22	S1	296	84	sin C	294	39	S1	311	47	S1	326	46	S3
150	77	S1	110	85	sin C	338	40	S1	353	69	S1	314	40	S3
287	23	S1	106	81	sin C	335	39	S1	216	58	S1	285	32	S3
164	24	S1	33	17	AE1	328	30	S1	298	30	S1	287	28	S3
58	33	S1	6	30	AE1	18	30	S1	181	26	S1	293	41	S3
319	44	S1	31	41	AE1	21	20	S1	174	41	S1	283	44	S3
326	51	S1	31	40	AE1	324	27	S1	166	50	S1	282	38	S3
354	21	S1	33	36	AE1	341	33	S1	109	28	S1	292	39	S3
225	14	S1	59	37	AE1	332	50	S1	136	31	S1	282	37	S3
57	21	S1	58	34	AE1	339	39	S1	77	22	S1	286	32	S3
289	17	S1	48	29	AE1	296	41	S1	154	47	S1	309	30	S3
130	27	S1	52	35	AE1	312	40	S1	185	48	S1	325	30	S3
193	18	S1	64	48	AE1	315	37	S1	121	55	S1	298	26	S3
154	4	S1	59	29	AE1	323	33	S1	128	34	S1	301	27	S3
255	20	S1	85	23	AE1	304	40	S1	112	32	S1	285	29	S3
226	19	S1	73	27	AE1	313	38	S1	125	30	S1	204	14	S3
339	19	S1	96	26	AE1	322	58	S1	140	41	S1	214	7	S3
215	21	S1	28	43	AE1	315	70	S1	166	22	S1	259	12	S3
337	42	S1	71	39	AE1	316	59	S1	163	34	S1	317	11	S3
305	15	S1	320	76	AE2	308	40	S1	218	32	S1	160	17	S3

Supporting Table 1: raw data of structural measurements

Domain A			Domain B			Domain C			Domain D			Domain E		
294	10	S1	30	53	AE2	301	56	S1	188	26	S1	230	45	S3
311	31	S1	209	72	AE2	304	49	S1	172	35	S1	6	41	S3
172	23	S1	205	61	AE2	306	55	S1	166	62	S1	262	13	S3
181	35	S1	214	66	AE2	329	68	S1	218	30	S1	209	34	S3
335	50	S1	216	56	AE2	331	58	S1	206	25	S1	0	0	S3
44	21	S1	202	62	AE2	325	59	S1	192	10	S1	270	27	S3
326	36	S1	234	36	AE2	313	77	S1	357	43	S1	269	24	S3
168	38	S1	259	78	AE2	335	52	S1	276	35	S1	254	11	S3
208	11	S1	268	82	AE2	323	63	S1	285	38	S1	256	6	S3
244	11	S1	191	82	AE2	325	71	S1	301	55	S1	323	21	S3
336	26	S1	356	82	AE2	328	79	S1	222	66	S1	236	20	S3
321	44	S1	171	85	AE2	333	68	S1	198	75	S1	292	34	S3
289	23	S1	180	90	AE2	347	48	S1	359	61	S1	300	33	S3
127	25	S1	166	82	AE2	347	48	S1	348	36	S1	309	48	S3
131	16	S1	344	80	AE2	334	71	S1	352	67	S1	53	11	S3
190	3	S1	167	86	AE2	337	60	S1	357	42	S1	299	25	S3
146	39	S1	167	87	AE2	341	64	S1	348	63	S1	96	15	S3
201	10	S1	352	47	AE2	335	77	S1	354	60	S1	300	30	S3
188	44	S1	355	48	AE2	344	69	S1	350	57	S1	286	34	S3
166	58	S1	346	76	AE2	326	57	S1	159	24	S1	281	40	S3
183	42	S1	11	45	AE2	153	62	S1	168	18	S1	267	47	S3
178	79	S1	349	66	AE2	154	42	S1	164	23	S1	273	34	S3
158	51	S1	92	74	AE2	161	39	S1	148	25	S1	300	37	S3
209	34	S1	83	70	AE2	150	62	S1	176	25	S1	302	40	S3
186	42	S1	315	75	AE2	357	88	S1	166	9	S1	320	58	S3
165	55	S1	296	58	AE2	199	60	S1	170	37	S1	320	52	S3
152	79	S1	272	22	AE2	196	53	S1	130	11	S1	323	56	S3
147	82	S1	204	30	AE2	198	66	S1	254	15	S1	299	40	S3
149	58	S1	153	50	AE2	169	90	S1	258	6	S1	320	40	S3
174	48	S1	125	16	AE2	325	47	S1	136	45	S1	306	29	S3
151	45	S1	251	50	AE2	307	51	S1	120	36	S1	251	41	S3
173	53	S1	234	58	AE2	303	47	S1	116	28	S1	222	62	S3
152	59	S1	109	81	AE2	28	15	S1	172	56	S1	286	27	S3
172	37	S1	225	80	AE2	296	29	S1	156	75	S1	314	14	S3
147	26	S1	345	35	AE2	156	51	S1	170	65	S1	255	26	S3
165	38	S1	227	47	AE2	126	45	S1	153	57	S1	2	26	S3
269	19	S1	291	48	AE2	139	44	S1	172	49	S1	338	39	S3
131	17	S1	311	62	AE2	103	40	S1	188	52	S1	330	21	S3
311	16	S1	249	43	AE2	327	67	S1	148	26	S1	296	50	S3
212	45	S1	312	70	AE2	116	72	S1	162	25	S1	268	35	S3
194	63	S1	185	25	AE2	91	38	S1	173	49	S1	254	7	S3
333	74	S1	280	15	AE2	110	25	S1	183	63	S1	307	23	S3
338	66	S1	148	24	AE2	141	35	S1	190	42	S1	281	23	S3
331	15	S1	160	90	AE2	153	45	S1	157	55	S1	265	23	S3
0	0	S1	350	80	AE2	148	51	S1	172	50	S1	78	8	S3
349	37	S1	162	82	AE2	325	78	S1	171	60	S1	66	10	S3
342	24	S1	271	20	AE2	180	58	S1	166	39	S1	91	2	S3
263	16	S1	159	30	AE2	137	54	S1	178	40	S1	231	19	S3
332	62	S1	135	36	AE2	128	58	S1	174	38	S1	285	12	S3

Supporting Table 1: raw data of structural measurements

Domain A			Domain B			Domain C			Domain D			Domain E		
347	45	S1	28	73	AE2	129	33	S1	211	27	S1	288	22	S3
317	30	S1	30	88	AE2	101	41	S1	185	19	S1	2	67	AE1
312	63	S1	152	68	AE2	250	27	S1	203	44	S1	6	64	AE1
316	63	S1	163	82	AE2	247	16	S1	183	63	S1	17	67	AE1
302	57	S1	159	51	AE2	50	52	S1	200	67	S1	62	22	AE1
117	30	S1	332	82	AE2	72	55	S1	194	22	S1	188	40	AE1
156	55	S1	326	86	AE2	331	15	S1	323	33	S1	220	14	AE1
146	65	S1	345	77	AE2	266	24	S1	302	21	S1	244	18	AE1
194	25	S1	100	9	FA1	265	35	S1	273	23	S1	256	25	AE1
300	29	S1	132	3	FA1	355	25	S1	158	30	S1	280	28	AE1
324	42	S1	328	22	FA1	47	26	S1	168	27	S1	291	24	AE1
244	8	S1	124	4	FA1	69	22	S1	243	21	S1	300	30	AE1
324	58	S1	312	3	FA1	52	24	S1	165	44	S1	320	45	AE1
323	54	S1	310	3	FA1	69	32	S1	203	17	S1	321	57	AE1
289	40	S1	272	42	FA2	63	13	S1	230	13	S1	332	40	AE1
304	45	S1	262	24	FA2	359	49	S1	212	58	S1	335	38	AE1
334	80	S1	280	23	FA2	328	54	S1	207	68	S1	336	34	AE1
342	82	S1	278	22	FA2	337	54	S1	200	83	S1	337	45	AE1
319	72	S1	288	12	FA2	340	46	S1	238	64	S1	354	40	AE1
342	35	S1	288	8	FA2	341	38	S1	234	62	S1	357	67	AE1
327	50	S1	320	30	FA2	341	58	S1	211	70	S1	357	59	AE1
315	36	S1	283	2	FA2	336	64	S1	216	76	S1	341	78	AE2
340	52	S1	72	40	FA2	328	68	S1	200	81	S1	342	84	AE2
332	56	S1	85	19	FA2	99	66	S1	210	70	S1	0	25	AE2
334	46	S1	83	22	FA2	101	67	S1	222	68	S1	0	63	AE2
190	21	S1	53	42	FA2	115	66	S1	217	68	S1	2	76	AE2
307	37	S1	83	47	FA2	54	87	S1	222	76	S1	2	88	AE2
328	48	S1	73	32	FA2	232	75	S1	210	65	S1	2	79	AE2
352	62	S1	53	24	FA2	11	67	S1	198	66	S1	2	67	AE2
349	60	S1	67	40	FA2	32	69	S1	168	50	S1	2	67	AE2
354	61	S1	74	42	FA2	23	65	S1	167	71	S1	3	67	AE2
346	56	S1	55	45	FA2	16	62	S1	172	84	S1	3	50	AE2
346	60	S1	349	43	FA2	44	60	S1	169	62	S1	5	55	AE2
193	14	S1	359	37	FA2	34	65	S1	188	73	S1	5	77	AE2
188	16	S1	36	33	FA2	37	58	S1	180	78	S1	5	44	AE2
191	13	S1	21	39	FA2	297	72	S1	171	66	S1	6	44	AE2
335	67	S1	114	20	FA2	344	66	S1	202	75	S1	6	56	AE2
335	77	S1	121	20	FA2	322	82	S1	188	64	S1	7	87	AE2
330	88	S1	125	16	FA2	288	42	S1	189	54	S1	7	58	AE2
2	33	S1	44	44	FA2	309	47	S1	192	64	S1	8	59	AE2
32	17	S1	22	0	FA2	304	74	S1	204	80	S1	8	18	AE2
30	14	S1	235	60	FA2	310	45	S1	217	81	S1	10	54	AE2
6	44	S1	225	15	FA2	319	50	S1	16	78	S1	10	64	AE2
256	36	S1	202	10	FA2	334	50	S1	45	72	S1	11	53	AE2
12	45	S1	208	5	FA2	326	47	S1	158	14	S1	12	34	AE2
11	66	S1	256	17	FA2	348	60	S1	162	57	S1	12	33	AE2
9	48	S1	71	70	FA2	314	58	S1	173	62	S1	12	65	AE2
316	40	S1	210	48	FA2	337	68	S1	182	59	S1	13	48	AE2
313	38	S1	240	20	FA2	150	82	S1	121	88	S1	14	45	AE2

Supporting Table 1: raw data of structural measurements

Domain A			Domain B			Domain C			Domain D			Domain E		
321	26	S1	98	26	FA2	198	42	S1	62	58	S1	16	57	AE2
325	36	S1	110	21	FA2	111	72	S1	60	63	S1	16	50	AE2
158	72	S1	300	10	L1	150	60	S1	61	57	S1	17	50	AE2
156	79	S1	297	22	L1	144	70	S1	89	65	S1	18	65	AE2
137	27	S1	253	17	L1	308	72	S1	61	723	S1	19	52	AE2
216	34	S1	231	16	L2	162	82	S1	100	73	S1	21	57	AE2
353	25	S1	108	6	L2	188	77	S1	103	64	S1	21	17	AE2
357	28	S1	284	34	L2	171	58	S1	100	74	S1	21	87	AE2
344	62	S1	114	13	L2	157	41	S1	155	80	S1	22	76	AE2
358	63	S1	282	40	L2	152	46	S1	5	45	S1	26	80	AE2
178	38	S1	278	4	L2	160	47	S1	346	31	S1	28	67	AE2
181	46	S1	226	4	L2	156	38	S1	353	54	S1	29	54	AE2
154	15	S1	232	8	L2	135	40	S1	357	45	S1	30	46	AE2
183	37	S1	268	8	L2	195	24	S1	342	54	S1	32	62	AE2
183	34	S1	277	7	L2	185	15	S1	9	18	S1	34	42	AE2
168	33	S1	275	11	L2	195	18	S1	0	42	S1	34	50	AE2
161	32	S1	253	27	L2	315	45	S1	336	17	S1	41	47	AE2
121	21	S1	246	2	L2	333	52	S1	4	35	S1	42	87	AE2
147	14	S1	226	29	L2	308	78	S1	344	22	S1	61	88	AE2
165	16	S1	228	21	L2	318	78	S1	358	34	S1	70	64	AE2
146	22	S1	255	13	L2	320	72	S1	346	48	S1	74	83	AE2
164	33	S1	235	23	L2	17	31	S1	337	14	S1	92	53	AE2
352	54	S1	238	22	L2	34	42	S1	325	55	S1	95	74	AE2
350	73	S1	270	13	L2	57	35	S1	312	53	S1	154	58	AE2
354	72	S1	268	10	L2	80	60	S1	336	72	S1	160	71	AE2
358	54	S1	32	24	L2	6	28	S1	322	64	S1	175	82	AE2
11	48	S1	20	22	L2	335	38	S1	39	80	S1	187	75	AE2
338	68	S1	36	17	L2	112	38	S1	72	65	S1	190	52	AE2
348	36	S1	61	11	L2	150	50	S1	42	75	S1	219	70	AE2
351	73	S1	235	7	L2	22	49	S1	296	80	S1	221	40	AE2
351	63	S1	58	2	L2	22	62	S1	148	82	S1	229	49	AE2
337	63	S1	43	8	L2	44	40	S1	137	79	S1	239	85	AE2
347	54	S1	48	9	L2	349	12	S1	138	86	S1	246	78	AE2
350	57	S1	47	13	L2	291	35	S1	288	80	S1	257	68	AE2
355	62	S1	46	12	L2	193	24	S1	332	86	S1	258	68	AE2
351	62	S1	53	13	L2	198	24	S1	103	84	S1	289	19	AE2
349	70	S1	72	3	L2	185	21	S1	137	90	S1	304	22	AE2
349	67	S1	58	30	L2	160	28	S1	150	80	S1	309	14	AE2
349	71	S1	40	0	L sin	192	16	S1	100	81	S1	313	44	AE2
359	75	S1	38	3	L sin	164	39	S1	102	81	S1	317	90	AE2
0	83	S1	210	4	L sin	160	26	S1	158	82	S1	318	56	AE2
355	90	S1	36	5	L sin	228	10	S1	119	73	S1	327	46	AE2
350	60	S1	34	7	L sin	245	9	S1	128	66	S1	333	23	AE2
350	61	S1	35	0	L sin	266	13	S1	109	65	S1	334	90	AE2
359	69	S1	59	4	L sin	281	31	S1	138	61	S1	335	38	AE2
349	60	S1	249	2	L sin	256	36	S1	91	87	S1	337	20	AE2
350	50	S1	58	15	L sin	348	54	S1	276	80	S1	338	35	AE2
219	9	S1	58	15	L norm	342	36	S1	138	82	S1	339	90	AE2
226	26	S1	220	23	L dex	322	36	S1	257	85	S1	340	35	AE2

Supporting Table 1: raw data of structural measurements

Domain A			Domain B			Domain C			Domain D			Domain E		
195	30	S1	227	12	L dex	294	55	S1	233	81	S1	342	60	AE2
194	53	S1				296	50	S1	147	82	S1	342	47	AE2
198	48	S1				291	56	S1	113	81	S1	342	28	AE2
194	51	S1				316	41	S1	134	80	S1	343	65	AE2
192	53	S1				298	41	S1	190	80	S1	344	83	AE2
56	61	S1				313	39	S1	186	78	S1	344	25	AE2
56	64	S1				331	37	S1	142	68	S1	345	55	AE2
60	84	S1				326	33	S1	130	78	S1	345	49	AE2
277	39	S1				325	37	S1	115	49	S1	345	19	AE2
351	77	S1				312	55	S1	6	41	S1	346	86	AE2
351	78	S1				303	54	S1	0	45	S1	346	60	AE2
359	72	S1				309	45	S1	330	38	S1	346	58	AE2
8	74	S1				312	53	S1	328	38	S1	346	38	AE2
6	67	S1				318	58	S1	10	33	S1	347	61	AE2
0	70	S1				312	48	S1	3	26	S1	347	52	AE2
2	71	S1				310	86	S1	1	41	S1	348	64	AE2
186	72	S1				139	84	S1	342	45	S1	349	84	AE2
351	80	S1				144	87	S1	2	58	S1	350	50	AE2
357	78	S1				324	90	S1	356	52	S1	351	61	AE2
156	42	S1				148	88	S1	334	30	S1	351	76	AE2
159	37	S1				200	23	S1	353	30	S1	352	47	AE2
156	78	S1				172	28	S1	105	38	S1	352	66	AE2
159	76	S1				181	24	S1	121	45	S1	353	50	AE2
152	45	S1				189	18	S1	116	33	S1	353	70	AE2
146	30	S1				184	12	S1	359	53	S1	353	79	AE2
150	32	S1				205	60	S1	16	56	S1	353	19	AE2
156	82	S1				202	61	S1	8	62	S1	353	53	AE2
153	83	S1				196	65	S1	2	73	S1	353	51	AE2
142	38	S1				197	50	S1	2	62	S1	355	57	AE2
152	45	S1				184	72	S1	353	47	S1	355	58	AE2
146	60	S1				210	68	S1	355	50	S1	356	65	AE2
142	58	S1				204	50	S1	345	51	S1	357	60	AE2
139	51	S1				218	42	S1	353	48	S1	358	26	AE2
150	69	S1				206	65	S1	354	46	S1	359	87	AE2
181	35	S1				195	50	S1	163	90	S1	359	65	AE2
162	82	S1				202	51	S1	166	75	S1	359	38	AE2
157	82	S1				196	55	S1	165	67	S1	348	61	AE2
162	76	S1				196	45	S1	157	60	S1	351	78	AE2
345	84	S1				20	88	S1	142	67	S1	355	72	AE2
321	78	S1				197	88	S1	143	72	S1	359	49	AE2
336	72	S1				183	51	S1	2	61	S2	350	32	AE3
352	66	S1				210	65	S1	23	79	S2	343	40	AE3
16	57	S1				198	72	S1	22	82	S2	3	20	AE3
9	58	S1				327	23	S1	124	68	S2	3	21	AE3
152	60	S1				17	33	S1	311	86	S2	4	64	AE3
169	55	S1				149	60	S1	133	88	S2	6	30	AE3
352	56	S1				301	31	S1	136	60	S2	10	64	AE3
350	50	S1				159	90	S1	356	88	S2	15	78	AE3
351	74	S1				167	56	S1	331	89	S2	17	87	AE3

Supporting Table 1: raw data of structural measurements

Domain A			Domain A			Domain C			Domain D			Domain E		
345	75	S1	164	90	S2	194	39	S1	166	52	S2	21	20	AE3
347	67	S1	338	77	S2	198	54	S1	177	70	S2	28	38	AE3
338	54	S1	138	62	S2	202	23	S1	173	59	S2	34	85	AE3
341	65	S1	139	65	S2	192	35	S1	178	62	S2	34	31	AE3
341	52	S1	346	65	S2	308	30	S1	194	70	S2	56	23	AE3
340	55	S1	342	68	S2	341	46	S1	192	77	S2	70	90	AE3
331	74	S1	8	74	S2	343	45	S1	196	80	S2	164	53	AE3
345	85	S1	317	75	S2	342	45	S1	194	84	S2	166	75	AE3
352	66	S1	320	72	S2	157	45	S1	188	83	S2	172	67	AE3
336	62	S1	102	52	S2	347	60	S1	188	85	S2	179	72	AE3
342	50	S1	128	75	S2	348	60	S1	186	89	S2	191	70	AE3
233	36	S1	319	82	S2	351	54	S1	188	82	S2	195	8	AE3
154	65	S1	342	90	S2	219	40	S1	180	74	S2	196	82	AE3
153	50	S1	342	72	S2	235	33	S1	172	78	S2	200	80	AE3
56	25	S1	357	78	S2	220	46	S1	170	75	S2	207	71	AE3
74	45	S1	189	63	S2	239	18	S1	174	80	S2	213	4	AE3
30	34	S1	173	53	S2	208	30	S1	191	64	S2	218	57	AE3
98	25	S1	199	52	S2	234	11	S1	207	66	S2	222	62	AE3
88	41	S1	9	73	S2	218	18	S1	202	63	S2	229	28	AE3
312	35	S1	352	71	S2	27	60	S1	212	72	S2	236	76	AE3
316	41	S1	351	57	S2	219	37	S1	176	60	S2	251	18	AE3
329	75	S1	354	61	S2	191	18	S1	205	55	S2	256	88	AE3
324	69	S1	345	80	S2	153	25	S1	194	62	S2	257	72	AE3
212	24	S1	324	83	S2	198	23	S1	185	54	S2	264	24	AE3
165	38	S1	139	82	S2	181	26	S1	188	63	S2	281	25	AE3
328	54	S1	156	60	S2	309	25	S1	161	73	S2	284	26	AE3
332	54	S1	159	80	S2	288	74	S1	175	82	S2	303	20	AE3
329	76	S1	13	50	S2	268	78	S1	170	84	S2	313	23	AE3
334	64	S1	22	52	S2	108	82	S1	343	85	S2	337	34	AE3
330	61	S1	11	43	S2	280	71	S1	149	88	S2	351	54	AE3
351	50	S1	351	50	S2	122	86	S1	157	83	S2	353	13	AE3
355	51	S1	331	48	S2	109	75	S1	328	86	S2	1	57	AES3
331	59	S1	342	58	S2	113	72	S1	340	82	S2	351	55	AES3
328	56	S1	347	58	S2	114	69	S1	159	81	S2	353	49	AES3
328	70	S1	345	45	S2	261	41	S1	162	71	S2	355	56	AES3
341	45	S1	34	63	S2	240	20	S1	147	90	S2	207	16	AE3
342	49	S1	342	80	S2	254	31	S1	145	80	S2	345	64	AE3
316	80	S1	356	87	S2	298	17	S1	149	75	S2	240	29	norm C
326	74	S1	176	85	S2	357	36	S1	5	62	S2	236	34	norm C
321	81	S1	174	81	S2	307	12	S1	38	48	S2	299	58	norm C
197	41	S1	168	81	S2	3	19	S1	15	52	S2	290	55	norm C
195	30	S1	176	84	S2	22	21	S1	38	46	S2	313	55	norm C
169	24	S1	6	83	S2	10	26	S1	9	39	S2	304	56	norm C
171	27	S1	355	86	S2	19	21	S1	16	46	S2	283	49	norm C
151	75	S1	359	86	S2	41	29	S1	338	39	S2	276	44	norm C
151	73	S1	178	88	S2	346	32	S1	18	62	S2	211	32	norm C
170	90	S1	170	84	S2	330	24	S1	344	51	S2	221	36	norm C
169	89	S1	176	86	S2	334	32	S1	345	56	S2	205	48	norm C
157	63	S1	182	77	S2	304	66	S1	14	52	S2	235	38	norm C

Supporting Table 1: raw data of structural measurements

Domain A			Domain A			Domain C			Domain D			Domain E		
149	75	S1	180	77	S2	94	78	S1	19	49	S2	207	22	norm C
177	34	S1	178	69	S2	301	65	S1	49	30	S2	213	25	norm C
157	60	S1	173	88	S2	297	67	S1	325	53	S2	169	43	norm C
169	38	S1	347	87	S2	319	59	S1	10	57	S2	192	24	norm C
179	39	S1	350	90	S2	316	64	S1	330	45	S2	177	38	norm C
168	64	S1	13	87	S2	316	65	S1	10	46	S2	57	29	norm C
164	65	S1	359	87	S2	294	45	S1	30	51	S2	82	48	norm C
166	69	S1	180	89	S2	285	47	S1	330	69	S2	244	18	norm C
292	27	S1	1	86	S2	275	52	S1	353	75	S2	1	53	norm C
315	42	S1	179	89	S2	281	48	S1	25	50	S2	25	16	norm C
317	37	S1	5	87	S2	291	62	S1	326	55	S2	348	38	norm C
326	42	S1	190	88	S2	332	61	S1	339	81	S2	81	36	norm C
328	67	S1	7	87	S2	332	68	S1	30	69	S2	108	27	norm C
336	64	S1	359	86	S2	328	67	S1	16	63	S2	84	30	norm C
137	48	S1	5	86	S2	310	65	S1	27	70	S2	98	42	norm C
119	64	S1	3	88	S2	311	42	S1	179	78	S2	140	32	norm C
140	62	S1	0	83	S2	310	54	S1	19	70	S2	176	22	norm C
174	75	S1	186	83	S2	314	65	S1	4	75	S2	188	17	norm C
166	84	S1	181	86	S2	337	77	S1	186	86	S2	56	19	norm C
136	58	S1	352	86	S2	299	61	S1	355	79	S2	291	42	norm C
196	84	S1	355	83	S2	316	78	S1	352	90	S2	290	40	norm C
27	89	S1	1	85	S2	322	55	S1	180	87	S2	171	13	norm C
151	69	S1	358	82	S2	324	61	S1	18	76	S2	300	34	norm C
134	66	S1	356	87	S2	308	54	S1	159	35	S2	259	34	norm C
177	50	S1	5	88	S2	313	37	S1	170	49	S2	296	52	norm C
169	67	S1	173	88	S2	321	62	S1	177	35	S2	271	61	norm C
164	47	S1	180	90	S2	311	56	S1	158	38	S2	307	42	norm C
159	61	S1	2	87	S2	321	59	S1	134	24	S2	354	68	norm C
356	80	S1	151	85	S2	307	62	S1	128	38	S2	325	72	norm C
23	44	S1	149	86	S2	315	40	S1	43	43	S2	290	58	norm C
40	46	S1	151	88	S2	303	39	S1	36	36	S2	319	26	norm C
321	66	S1	142	75	S2	291	49	S1	38	35	S2	331	20	norm C
329	70	S1	148	64	S2	307	59	S1	23	44	S2	265	58	norm C
273	22	S1	150	70	S2	299	52	S1	189	54	dex C	264	65	norm C
302	20	S1	1	78	S2	306	72	S1	185	43	dex C	283	31	norm C
188	39	S1	159	82	S2	307	70	S1	182	48	dex C	294	48	norm C
196	40	S1	160	75	S2	318	43	S1	185	63	dex C	226	27	norm C
198	40	S1	168	65	S2	337	47	S1	183	65	dex C	217	38	norm C
195	48	S1	134	73	S2	308	41	S1	356	88	dex C	226	33	norm C
222	26	S1	152	90	S2	315	48	S1	174	90	dex C	226	28	norm C
195	36	S1	338	80	S2	281	64	S1	349	88	dex C	209	38	norm C
168	38	S1	165	84	S2	54	64	S1	0	84	dex C	274	52	norm C
330	47	S1	311	13	S3	319	54	S1	171	58	dex C	278	16	norm C
332	54	S1	339	59	S3	317	50	S1	152	40	dex C	320	50	norm C
332	50	S1	339	59	S3	329	45	S1	31	58	norm C	337	43	norm C
356	40	S1	324	28	S3	315	53	S1	20	58	norm C	231	28	norm C
8	40	S1	322	30	S3	313	55	S1	7	35	norm C	34	48	norm C
330	57	S1	347	48	S3	334	65	S1	286	65	norm C	330	21	norm C
345	54	S1	357	67	dex C	332	41	S1	321	42	rev C	269	14	norm C

Supporting Table 1: raw data of structural measurements

Domain A			Domain A			Domain C			Domain D			Domain E		
11	42	S1	333	85	dex C	326	53	S1	331	33	rev C	343	74	sin C
329	30	S1	350	85	dex C	334	36	S1	38	46	rev C	339	79	sin C
344	39	S1	183	88	dex C	239	11	S1	358	71	sin C	346	74	sin C
4	32	S1	130	90	dex C	1	26	S1	163	77	sin C	337	88	sin C
355	32	S1	341	85	dex C	353	15	S1	161	90	sin C	8	48	sin C
12	24	S1	161	81	dex C	274	29	S1	169	80	sin C	3	40	sin C
342	49	S1	161	78	dex C	290	61	S1	160	80	sin C	10	56	sin C
0	77	S1	188	58	dex C	296	55	S1	335	83	sin C	353	50	sin C
351	70	S1	196	63	dex C	220	70	S1	157	75	sin C	353	48	sin C
353	82	S1	8	76	dex C	229	68	S1	145	82	sin C	356	64	sin C
0	75	S1	12	60	dex C	226	60	S1	327	82	sin C	330	60	sin C
9	52	S1	11	83	dex C	316	37	S1	328	80	sin C	322	32	sin C
346	67	S1	7	78	dex C	315	36	S1	318	73	sin C	325	41	sin C
333	86	S1	22	88	dex C	321	81	S1	319	66	sin C	347	38	sin C
334	54	S1	185	87	dex C	314	81	S1	329	77	sin C	278	75	sin C
353	75	S1	188	65	dex C	321	89	S1	327	67	sin C	201	42	sin C
333	47	S1	195	73	dex C	156	85	S1	328	83	sin C	199	45	sin C
329	54	S1	199	69	dex C	119	68	S1	164	76	sin C	308	45	sin C
147	31	S1	182	63	dex C	115	65	S1	351	88	sin C	297	58	sin C
3	77	S1	333	76	dex C	107	74	S1	333	77	sin C	317	77	sin C
145	75	S1	174	67	dex C	138	67	S1	346	85	sin C	301	55	sin C
180	72	S1	5	74	dex C	119	62	S1	130	89	sin C	349	46	sin C
161	73	S1	102	58	dex C	160	70	S1	55	27	sin C	100	36	sin C
121	73	S1	1	78	dex C	195	10	S1	340	34	sin C	111	52	sin C
340	60	S1	1	83	dex C	164	17	S1	324	48	sin C	90	61	sin C
129	68	S1	341	79	dex C	224	14	S1	335	50	sin C	281	61	sin C
129	67	S1	4	88	dex C	184	86	S1	340	54	sin C	15	90	dex C
322	54	S1	355	87	dex C	15	72	S1	352	34	sin C	10	88	dex C
322	44	S1	7	77	dex C	162	45	S1	13	26	sin C	38	54	dex C
336	75	S1	183	87	dex C	331	57	S1	26	32	sin C	45	59	dex C
330	86	S1	339	63	dex C	324	51	S1	356	67	sin C	32	65	dex C
345	43	S1	343	55	dex C	204	87	S1	351	58	sin C	357	69	dex C
351	60	S1	162	82	dex C	203	83	S1	2	57	sin C	25	75	dex C
150	75	S1	354	83	dex C	201	88	S1	352	84	sin C	176	82	dex C
152	75	S1	321	57	dex C	170	88	S1	174	88	sin C	305	80	norm C
152	74	S1	329	69	dex C	160	80	S1	350	87	sin C	293	31	norm C
299	50	S1	9	67	dex C	149	83	S1	336	87	sin C	359	60	norm C
280	44	S1	356	72	dex C	359	76	S2	162	87	sin C	356	58	norm C
295	40	S1	182	80	dex C	345	70	S2	358	45	sin C	338	57	norm C
307	42	S1	192	72	dex C	349	87	S2	12	50	sin C	337	55	norm C
200	62	S1	182	85	dex C	352	72	S2	336	68	sin C	333	55	norm C
213	61	S1	330	68	dex C	352	58	S2	333	65	sin C	314	57	norm C
201	55	S1	5	76	dex C	335	55	S2	340	75	sin C	303	68	norm C
206	58	S1	182	83	dex C	257	70	S2	340	68	sin C	281	71	norm C
355	88	S1	305	69	dex C	233	78	S2	38	46	sin C	278	75	norm C
202	70	S1	136	88	dex C	228	78	S2	166	77	sin C	344	61	norm C
208	64	S1	131	87	dex C	211	84	S2	175	77	sin C	312	83	norm C
330	33	S1	247	52	dex C	208	86	S2	42	68	dex C	305	54	norm C
144	64	S1	4	34	dex C	184	86	S2	36	28	dex C	304	49	norm C

Supporting Table 1: raw data of structural measurements

Domain A			Domain A			Domain C			Domain D			Domain E		
168	69	S1	314	65	dex C	77	72	S2	22	65	dex C	299	70	norm C
218	41	S1	321	62	dex C	49	55	S2	333	88	dex C	298	58	norm C
133	74	S1	339	76	dex C	47	54	S2	173	77	dex C	291	45	norm C
21	34	S1	337	57	dex C	23	86	S2	154	86	dex C	283	55	norm C
31	40	S1	4	66	dex C	16	87	S2	336	85	dex C	276	43	norm C
159	39	S1	12	62	dex C	15	58	S2	337	79	dex C	273	40	norm C
161	38	S1	32	30	dex C	15	70	S2	165	85	dex C	267	44	norm C
11	72	S1	112	40	dex C	15	80	S2	175	67	dex C	233	23	norm C
358	76	S1	357	86	dex C	14	50	S2	191	69	dex C	322	50	norm C
156	58	S1	167	83	dex C	13	75	S2	5	90	dex C	318	32	norm C
332	90	S1	8	76	dex C	12	65	S2	352	72	dex C	317	29	norm C
4	65	S1	350	82	dex C	10	54	S2	12	54	dex C	311	64	norm C
191	51	S1	334	77	dex C	10	81	S2	148	64	dex C	299	55	norm C
62	3	S1	345	79	dex C	6	66	S2	157	54	dex C	295	46	norm C
350	75	S1	340	84	dex C	2	86	S2	149	54	dex C	289	68	norm C
8	54	S1	355	83	dex C	165	52	S2	41	84	dex C	284	75	norm C
1	54	S1	350	85	dex C	165	88	S2	28	84	dex C	284	55	norm C
16	77	S1	142	90	dex C	167	76	S2	80	45	dex C	282	41	norm C
165	90	S1	172	88	dex C	170	77	S2	20	52	dex C	282	61	norm C
342	67	S1	359	74	dex C	176	83	S2	50	67	dex C	280	65	norm C
330	83	S1	324	71	dex C	246	25	S2	46	53	dex C	276	64	norm C
163	81	S1	326	75	dex C	239	29	S2	70	84	dex C	274	78	norm C
176	87	S1	165	88	dex C	226	24	S2	50	75	dex C	270	64	norm C
183	83	S1	174	80	dex C	226	25	S2	163	88	dex C	268	58	norm C
187	87	S1	180	88	dex C	210	20	S2	165	84	dex C	266	38	norm C
342	67	S1	178	82	dex C	203	29	S2	188	85	dex C	266	46	norm C
333	78	S1	338	90	dex C	199	42	S2	163	89	dex C	265	38	norm C
325	42	S1	340	88	dex C	193	29	S2	172	87	dex C	264	46	norm C
163	63	S1	215	74	dex C	191	49	S2	174	64	dex C	264	29	norm C
172	85	S1	216	81	dex C	11	48	S2	178	60	dex C	264	65	norm C
176	84	S1	215	52	dex C	317	46	S2	177	56	dex C	263	44	norm C
351	85	S1	180	50	dex C	297	46	S2	175	64	dex C	260	42	norm C
349	82	S1	133	24	dex C	295	40	S2	185	67	dex C	260	68	norm C
165	87	S1	126	30	dex C	302	38	S2	195	70	dex C	259	61	norm C
325	84	S1	132	32	dex C	349	59	S2	202	68	dex C	259	82	norm C
166	64	S1	229	68	dex C	349	65	S2	39	69	dex C	256	28	norm C
145	80	S1	214	82	dex C	341	67	S2	40	77	dex C	250	38	norm C
318	75	S2	302	73	dex C	338	66	S2	24	72	dex C	250	43	norm C
330	76	S2	337	74	dex C	334	64	S2	212	86	dex C	250	42	norm C
357	87	S2	168	86	dex C	333	50	S2	187	90	dex C	250	46	norm C
359	90	S2	5	75	dex C	332	54	S2	6	81	dex C	246	41	norm C
170	88	S2	5	83	dex C	331	60	S2	16	75	dex C	244	55	norm C
331	68	S2	10	87	dex C	321	55	S2	29	84	dex C	238	35	norm C
356	79	S2	335	90	dex C	294	76	S2	31	74	dex C	235	54	norm C
356	82	S2	27	72	dex C	292	21	S2	192	43	dex C	216	48	norm C
330	84	S2	32	66	dex C	291	51	S2	196	49	dex C	212	44	norm C
343	76	S2	158	78	dex C	290	48	S2	234	33	dex C	211	58	norm C
188	82	S2	159	76	dex C	290	75	S2	247	33	dex C	201	64	norm C
344	84	S2	14	75	dex C	289	55	S2	263	25	dex C	116	24	norm C

Supporting Table 1: raw data of structural measurements

Domain A			Domain A			Domain C			Domain D			Domain E		
337	72	S2	184	78	dex C	289	64	S2	210	39	dex C	267	58	norm C
340	86	S2	35	89	dex C	289	24	S2	198	25	dex C	259	64	norm C
345	90	S2	225	87	dex C	288	23	S2	187	20	dex C	247	38	norm C
168	84	S2	225	84	dex C	287	72	S2	189	54	dex C	239	59	norm C
172	88	S2	7	73	dex C	280	75	S2	185	43	dex C	232	39	norm C
333	87	S2	18	80	dex C	276	63	S2	182	48	dex C	184	64	norm C
324	86	S2	346	84	dex C	276	77	S2	185	63	dex C	220	27	norm C
335	89	S2	198	90	dex C	276	64	S2	183	65	dex C	201	26	norm C
351	76	S2	336	81	dex C	275	68	S2	24	80	dex C	323	39	norm C
350	74	S2	336	86	dex C	274	53	S2	32	85	dex C	319	37	norm C
337	75	S2	172	71	dex C	274	64	S2	32	80	dex C	318	54	norm C
310	78	S2	161	72	dex C	268	23	S2	31	81	dex C	314	60	norm C
354	84	S2	17	46	dex C	266	38	S2	32	70	dex C	304	59	norm C
325	81	S2	357	58	dex C	266	24	S2	220	81	dex C	283	38	norm C
327	88	S2	5	89	dex C	264	34	S2	237	89	dex C	42	44	norm C
338	84	S2	184	84	dex C	250	39	S2	40	66	dex C	37	48	norm C
340	80	S2	329	69	dex C	246	44	S2	179	38	norm C	40	40	norm C
344	85	S2	339	65	dex C	245	30	S2	178	36	norm C	24	51	norm C
166	82	S2	356	80	dex C	89	84	S2	124	24	norm C	19	54	norm C
165	85	S2	341	85	dex C	98	84	S2	254	42	norm C	94	37	norm C
358	78	S2	20	75	dex C	103	44	S2	244	54	norm C	76	45	norm C
338	85	S2	20	56	dex C	107	87	S2	224	52	norm C	45	45	norm C
0	80	S2	14	68	dex C	108	49	S2	223	69	norm C	46	43	norm C
345	79	S2	208	89	dex C	109	85	S2	96	65	norm C	36	46	norm C
335	84	S2	208	80	dex C	112	72	S2	349	74	rev C	23	60	norm C
340	86	S2	210	88	dex C	114	71	S2	348	77	rev C	52	43	norm C
350	80	S2	358	72	dex C	115	75	S2	44	68	rev C	18	44	norm C
345	76	S2	358	80	dex C	118	68	S2	51	74	rev C	352	68	rev C
335	82	S2	7	89	dex C	119	85	S2	41	69	rev C	337	45	rev C
344	87	S2	212	80	dex C	120	82	S2	40	67	rev C	329	45	rev C
0	84	S2	171	76	dex C	124	55	S2	0	46	sin C	157	48	rev C
358	79	S2	175	55	dex C	126	86	S2	7	58	sin C	83	43	rev C
163	86	S2	29	56	dex C	128	90	S2	301	65	sin C	332	76	sin C
169	84	S2	45	69	dex C	129	55	S2	106	87	sin C	327	72	sin C
167	82	S2	27	87	dex C	135	89	S2	107	77	sin C	327	63	sin C
352	88	S2	212	63	dex C	140	78	S2	28	50	sin C	321	67	sin C
340	77	S2	234	72	dex C	141	75	S2	101	68	sin C	317	64	sin C
355	84	S2	207	60	dex C	142	85	S2	107	67	sin C	316	90	sin C
358	75	S2	229	83	dex C	146	88	S2	337	85	sin C	314	70	sin C
155	86	S2	234	79	dex C	150	86	S2	346	90	sin C	314	66	sin C
344	85	S2	193	78	dex C	151	72	S2	74	52	sin C	312	75	sin C
160	89	S2	185	76	dex C	152	79	S2	141	76	sin C	308	74	sin C
6	74	S2	342	68	dex C	155	87	S2	129	78	sin C	304	68	sin C
175	88	S2	343	86	dex C	162	87	S2	137	89	sin C	304	67	sin C
337	88	S2	172	76	dex C	163	86	S2	300	74	sin C	301	85	sin C
167	82	S2	187	86	dex C	265	88	S2	132	87	sin C	300	70	sin C
355	73	S2	357	80	dex C	272	72	S2	128	80	sin C	298	75	sin C
338	75	S2	348	80	dex C	295	40	S2	291	82	sin C	288	80	sin C
336	86	S2	343	81	dex C	297	76	S2	298	75	sin C	286	85	sin C

Supporting Table 1: raw data of structural measurements

Domain A			Domain A			Domain C			Domain D			Domain E		
345	81	S2	220	78	dex C	297	46	S2	283	53	sin C	286	81	sin C
2	82	S2	13	74	dex C	299	85	S2	284	64	sin C	178	52	sin C
335	72	S2	14	70	dex C	300	64	S2	308	90	sin C	175	57	sin C
342	65	S2	141	84	dex C	302	38	S2	309	87	sin C	174	82	sin C
341	82	S2	172	88	dex C	306	83	S2	127	88	sin C	165	55	sin C
351	81	S2	8	55	dex C	306	80	S2	131	89	sin C	147	87	sin C
349	66	S2	9	67	dex C	308	73	S2	133	86	sin C	139	72	sin C
346	77	S2	18	63	dex C	308	34	S2	302	78	sin C	139	70	sin C
358	88	S2	12	90	dex C	308	81	S2	303	90	sin C	135	57	sin C
342	80	S2	180	77	dex C	308	70	S2	342	85	sin C	118	78	sin C
134	86	S2	4	81	dex C	308	80	S2	2	86	sin C	114	81	sin C
0	82	S2	343	85	dex C	309	88	S2	346	79	sin C	105	75	sin C
347	89	S2	2	86	dex C	310	66	S2	148	89	sin C	96	84	sin C
355	83	S2	198	76	dex C	310	86	S2	76	43	sin C	87	77	sin C
3	90	S2	2	82	dex C	310	78	S2	317	55	sin C	40	82	sin C
334	84	S2	205	84	dex C	311	88	S2	327	81	sin C	32	75	sin C
341	76	S2	41	81	dex C	312	72	S2	341	82	sin C	5	63	sin C
315	65	S2	29	74	dex C	312	86	S2	326	76	sin C	2	67	sin C
357	72	S2	31	70	dex C	313	72	S2	305	72	sin C	46	43	dex C
335	82	S2	3	78	dex C	317	52	S2	298	87	sin C	36	46	dex C
166	86	S2	358	70	dex C	317	46	S2	144	87	sin C	23	60	dex C
167	89	S2	326	42	norm C	318	62	S2	148	90	sin C	52	43	dex C
351	82	S2	308	34	norm C	318	74	S2	139	74	sin C	18	44	dex C
175	89	S2	307	41	norm C	321	71	S2	288	90	sin C	352	68	dex C
162	85	S2	305	37	norm C	321	80	S2	125	80	sin C	337	45	dex C
337	90	S2	161	61	norm C	322	73	S2	103	90	sin C	329	45	dex C
166	87	S2	161	65	norm C	323	78	S2	136	72	sin C	357	50	dex C
336	75	S2	105	88	norm C	325	78	S2	137	68	sin C	349	61	dex C
162	82	S2	322	72	norm C	325	78	S2	126	78	sin C	131	75	dex C
170	82	S2	100	81	norm C	325	71	S2	305	83	sin C	21	52	dex C
355	75	S2	155	49	norm C	326	77	S2	307	88	sin C	21	47	dex C
358	77	S2	245	14	norm C	326	86	S2	304	84	sin C	17	42	dex C
342	82	S2	224	35	norm C	326	88	S2	326	62	sin C	15	54	dex C
324	86	S2	294	64	norm C	326	75	S2	318	56	sin C	10	64	dex C
337	83	S2	268	41	norm C	326	86	S2	302	75	sin C	2	60	dex C
156	83	S2	70	49	norm C	328	80	S2	310	77	sin C	273	17	L1
166	87	S2	44	55	norm C	329	85	S2	288	75	sin C	93	6	L1
342	89	S2	276	72	norm C	329	54	S2	307	70	sin C	236	9	L1
345	80	S2	296	57	norm C	330	90	S2	274	38	sin C	62	5	L1
343	75	S2	279	53	norm C	330	86	S2	295	31	sin C	50	3	L1
350	90	S2	263	53	norm C	330	84	S2	292	31	sin C	73	35	L1
348	84	S2	254	65	norm C	330	89	S2	291	34	sin C	222	32	L1
162	85	S2	140	15	norm C	332	69	S2	286	25	sin C	235	43	L1
334	78	S2	152	19	norm C	332	84	S2	294	30	sin C	254	35	L1
155	83	S2	164	31	norm C	334	69	S2	296	32	sin C	253	37	L1
350	88	S2	310	42	norm C	334	82	S2	320	57	sin C	233	47	L1
175	84	S2	354	46	norm C	335	82	S2	312	57	sin C	230	46	L1
165	83	S2	333	61	norm C	335	79	S2	330	73	sin C	289	3	L1
341	90	S2	6	79	norm C	337	74	S2	139	89	sin C	264	24	L1

Supporting Table 1: raw data of structural measurements

Domain A			Domain A			Domain C			Domain D			Domain E		
343	75	S2	160	55	norm C	342	74	S2	309	80	sin C	253	34	L1
155	85	S2	140	58	norm C	342	87	S2	328	86	sin C	254	45	L1
0	90	S2	346	66	norm C	150	75	C dex	309	88	sin C	236	18	L1
151	88	S2	175	85	norm C	153	71	C dex	308	90	sin C	245	24	L1
152	85	S2	345	76	norm C	178	68	C dex	344	77	AE1	239	15	L1
358	86	S2	349	80	norm C	156	68	C dex	12	55	AE1	229	21	L1
358	90	S2	353	84	norm C	355	70	C dex	39	45	AE1	219	30	L1
0	79	S2	292	33	norm C	338	68	C dex	32	22	AE1	279	7	L1
330	84	S2	304	27	norm C	131	67	C dex	245	46	AE1	109	7	L1
334	81	S2	294	28	norm C	123	52	C dex	222	50	AE1	285	47	L1
334	81	S2	288	32	norm C	138	30	C dex	322	28	AE1	97	24	L1
350	83	S2	288	21	norm C	141	28	C dex	27	15	AE1	282	11	L1
354	89	S2	327	25	norm C	135	34	C dex	39	22	AE1	262	12	L1
150	79	S2	288	30	norm C	105	76	C dex	42	25	AE1	252	19	L1
325	90	S2	302	20	norm C	288	86	C dex	164	30	AE1	263	6	L1
170	84	S2	323	35	norm C	324	68	C dex	134	39	AE1	277	39	L1
154	88	S2	248	24	norm C	326	60	C dex	341	29	AE1	274	19	L1
342	75	S2	181	50	norm C	319	58	C dex	32	75	AE2	271	23	L1
325	88	S2	343	34	rev C	345	70	C dex	38	73	AE2	268	10	L1
170	71	S2	347	47	rev C	353	73	C dex	175	82	AE2	285	25	L1
349	87	S2	357	38	rev C	36	36	C dex	356	82	AE2	329	27	L1
178	77	S2	326	87	rev C	76	25	C dex	132	78	AE2	87	1	L1
157	87	S2	337	85	rev C	5	65	C dex	148	60	AE2	252	25	L2
349	80	S2	335	81	rev C	16	53	C dex	298	70	AE2	269	7	L2
342	88	S2	138	98	rev C	50	42	C dex	319	32	AE2	102	20	L2
346	84	S2	142	81	rev C	34	48	C dex	106	88	AE2	72	4	L2
166	84	S2	320	85	rev C	289	70	C norm	105	81	AE2	84	7	L2
158	85	S2	349	85	rev C	1	64	C norm	124	84	AE2	276	23	L2
175	84	S2	351	85	rev C	359	69	C norm	309	87	AE2	271	34	L2
175	56	S2	346	71	rev C	22	55	C norm	146	77	AE2	201	53	L2
333	84	S2	334	65	rev C	18	45	C norm	145	42	AE2	184	59	L2
2	83	S2	135	48	rev C	19	54	C norm	319	78	AE2	203	59	L2
353	80	S2	153	36	rev C	22	66	C norm	7	47	AE2	235	22	L2
315	66	S2	326	81	rev C	329	75	C norm	15	27	AE2	238	29	L2
348	78	S2	355	85	rev C	317	86	C norm	347	64	AE2	78	18	L2
320	71	S2	353	72	rev C	30	53	C norm	168	85	AE2	274	1	L2
356	89	S2	337	72	rev C	20	45	C norm	166	62	AE2	260	48	L2
358	85	S2	335	75	rev C	305	45	C norm	328	70	AE2	254	36	L2
315	64	S2	304	67	rev C	267	72	C norm	335	78	AE2	262	18	L sin
8	89	S2	311	45	rev C	265	75	C norm	157	89	AE2	254	19	L sin
350	74	S2	314	45	rev C	13	48	C norm	343	83	AE2	260	30	L sin
164	85	S2	334	51	rev C	347	37	C norm	7	84	AE2	252	44	L sin
337	89	S2	334	52	rev C	348	65	C norm	171	76	AE2	212	32	L sin
5	89	S2	302	55	rev C	350	55	C norm	344	90	AE2	261	7	L norm
359	80	S2	303	52	rev C	138	83	C rev	346	81	AE2	247	16	L norm
180	80	S2	9	67	rev C	355	77	C rev	194	76	AE2	240	13	L norm
348	83	S2	12	63	rev C	108	88	C rev	11	89	AE2	247	16	L norm
345	80	S2	18	53	rev C	296	86	C rev	219	85	AE2	238	10	L norm
165	80	S2	157	70	sin C	223	73	C rev	203	73	AE2	268	5	L norm

Supporting Table 1: raw data of structural measurements

Domain A			Domain A			Domain C			Domain D			Domain E		
335	80	S2	167	63	sin C	308	85	C rev	199	74	AE2	273	4	L norm
186	78	S2	343	82	sin C	333	89	C rev	211	74	AE2	355	32	L norm
350	88	S2	345	88	sin C	119	77	C rev	189	85	AE2	261	3	FA1
355	85	S2	342	72	sin C	117	80	C rev	330	78	AE2	276	2	FA1
344	90	S2	354	84	sin C	305	87	C rev	169	74	AE2	270	3	FA1
335	89	S2	188	88	sin C	135	82	C rev	343	79	AE2	270	2	FA1
161	89	S2	2	90	sin C	318	88	C rev	352	82	AE2	276	29	FA1
350	86	S2	139	89	sin C	324	86	C rev	6	60	AE2	284	9	FA1
167	79	S2	338	89	sin C	211	90	C rev	13	38	AE2	254	3	FA1
149	80	S2	332	89	sin C	186	70	C rev	352	46	AE2	86	17	FA1
146	88	S2	333	82	sin C	183	66	C rev	358	51	AE2	269	6	FA1
158	75	S2	333	79	sin C	348	75	C rev	182	86	AE2	255	19	FA1
144	67	S2	335	81	sin C	181	85	C rev	164	87	AE2	257	19	FA1
355	88	S2	145	87	sin C	123	68	C rev	179	86	AE2	267	44	FA1
159	88	S2	144	88	sin C	111	84	C rev	61	89	AE2	272	27	FA1
152	82	S2	172	79	sin C	295	15	C rev	208	82	AE2	260	11	FA1
165	71	S2	152	74	sin C	303	31	C rev	196	74	AE2	247	18	FA1
336	81	S2	152	77	sin C	292	81	C sin	170	88	AE2	285	14	FA1
176	87	S2	154	84	sin C	304	86	C sin	180	90	AE2	260	11	FA1
347	73	S2	148	85	sin C	296	79	C sin	10	84	AE2	247	18	FA1
151	80	S2	151	85	sin C	335	48	C sin	178	80	AE2	253	19	FA2
180	72	S2	137	71	sin C	318	50	C sin	170	78	AE2	265	8	FA2
174	87	S2	139	75	sin C	327	50	C sin	175	73	AE2	291	14	FA2
162	88	S2	149	80	sin C	334	90	C sin	180	75	AE2	277	15	FA2
354	71	S2	148	74	sin C	315	75	C sin	355	88	AE2	254	22	FA2
180	72	S2	168	86	sin C	157	80	C sin	171	80	AE2	278	3	FA2
344	70	S2	325	81	sin C	164	89	C sin	342	88	AE2	276	4	FA2
153	70	S2	329	81	sin C	140	85	C sin	175	90	AE2	252	38	FA2
152	67	S2	324	83	sin C	274	51	C sin	47	64	AE2	84	14	FA2
168	69	S2	155	77	sin C	250	30	C sin	162	80	AE2	266	7	FA2
168	82	S2	170	84	sin C	279	71	C sin	190	90	AE2	85	2	FA2
335	86	S2	148	86	sin C	306	39	C sin	10	90	AE2	270	11	FA2
337	85	S2	339	84	sin C	293	45	C sin	330	90	AE2	270	7	FA2
344	79	S2	340	80	sin C	287	50	C sin	148	84	AE2	265	7	FA2
346	78	S2	340	84	sin C	251	60	C sin	323	90	AE2	276	4	FA2
342	80	S2	338	64	sin C	88	90	C sin	183	45	AE2	72	5	FA2
342	82	S2	339	74	sin C	260	79	C sin	191	89	AE2	94	4	FA2
340	87	S2	338	76	sin C	266	85	C sin	220	88	AE2	80	6	FA2
355	88	S2	328	62	sin C	264	73	C sin	252	76	AE2	117	7	FA2
178	87	S2	345	85	sin C	268	78	C sin	263	52	AE2	278	10	FA2
312	85	S2	18	85	sin C	262	74	C sin	261	64	AE2	276	23	FA2
156	85	S2	11	85	sin C	132	48	C sin	14	79	AE2	86	7	FA2
320	60	S2	9	83	sin C	133	54	C sin	357	55	AE2	110	8	FA2
350	81	S2	4	82	sin C	146	60	C sin	346	58	AE2	115	12	FA2
345	84	S2	8	79	sin C	119	51	C sin	232	32	AE2	87	18	FA2
338	86	S2	6	87	sin C	121	49	C sin	242	48	AE2	105	19	FA2
323	87	S2	7	58	sin C	334	82	C sin	268	55	AE2	95	14	FA2
340	86	S2	357	43	sin C	325	90	C sin	86	78	AE4	299	24	FA2
164	80	S2	26	40	sin C	337	55	C sin	91	69	AE4	122	21	FA2

Supporting Table 1: raw data of structural measurements

Domain A			Domain A			Domain C			Domain D			Domain E		
142	75	S2	345	55	sin C	346	76	C sin	281	90	AE4	301	27	FA2
165	90	S2	338	46	sin C	331	72	C sin	94	82	AE4	91	2	FA2
358	83	S2	339	69	sin C	342	76	C sin	92	79	AE4	262	11	FA2
302	75	S2	323	68	sin C	334	80	C sin	308	84	AE4	267	12	FA2
160	90	S2	326	42	sin C	158	88	C sin	132	82	AE4	277	13	FA2
331	70	S2	308	34	sin C	311	86	C sin	158	77	AE4	274	18	FA2
338	80	S2	307	41	sin C	326	73	C sin	231	58	AE4	266	18	FA2
341	85	S2	305	37	sin C	314	72	C sin	108	74	AE4	272	7	FA2
333	55	S2	152	80	sin C	318	58	C sin	79	82	AE4	108	13	FA2
332	50	S2	156	80	sin C	155	77	C sin	252	74	AE4	101	23	FA2
337	65	S2	322	90	sin C	130	72	C sin	111	78	AE4	245	35	FA2
357	88	S2	148	84	sin C	142	69	C sin	93	85	AE4	97	9	FA2
158	90	S2	158	81	sin C	266	74	C sin	112	90	AE4	94	6	FA2
334	89	S2	140	80	sin C	260	75	C sin	126	83	AE4	323	30	FA2
338	83	S2	150	70	sin C	274	80	C sin	116	88	AE4	321	25	FA2
0	85	S2	330	88	sin C	114	71	C sin	133	88	AE4	78	23	FA2
155	86	S2	338	70	sin C	125	78	C sin	142	84	AE4	113	17	FA2
152	87	S2	340	90	sin C	117	84	C sin	324	65	AE4	250	5	FA2
154	90	S2	340	75	sin C	100	86	C sin	103	82	AE4	260	28	FA2
171	69	S2	161	82	sin C	79	89	C sin	130	32	FA1	320	52	FA2
167	65	S2	148	87	sin C	303	62	C sin	103	32	FA1	279	22	FA2
136	81	S2	311	73	sin C	298	68	C sin	335	38	FA1	2	9	FA2
332	86	S2	168	68	sin C	312	77	C sin	349	36	FA1	279	21	FA2
337	87	S2	154	67	sin C	312	77	C sin	71	14	FA1	280	21	FA2
344	68	S2	154	72	sin C	298	82	C sin	65	11	FA1	307	43	FA2
171	56	S2	155	73	sin C	332	59	C sin	74	20	FA1	307	18	FA2
160	61	S2	154	78	sin C	322	38	C sin	100	20	FA1	301	26	FA2
172	69	S2	144	80	sin C	293	70	C sin	124	1	FA2	306	33	FA2
328	82	S2	134	88	sin C	303	77	C sin	303	7	FA2	300	38	FA2
333	82	S2	139	87	sin C	324	76	C sin	91	46	FA2	292	16	FA2
340	82	S2	133	77	sin C	320	75	C sin	88	50	FA2	294	30	FA2
180	90	S2	176	77	sin C	316	84	C sin	226	1	FA2	285	17	FA2
135	88	S2	169	82	sin C	300	85	C sin	225	2	FA2	296	17	FA2
142	56	S2	164	75	sin C	272	84	C sin	48	25	FA2	307	22	FA2
139	74	S2	156	73	sin C	318	83	C sin	110	29	FA2	298	26	FA2
161	76	S2	322	86	sin C	316	85	C sin	56	18	FA2	357	28	FA2
155	71	S2	172	90	sin C	108	90	C sin	38	21	FA2	4	9	FA2
153	62	S2	140	81	sin C	296	86	C sin	74	28	FA2	278	17	FA2
168	68	S2	132	80	sin C	5	52	C' dex	264	5	FA2	269	24	FA2
153	83	S2	165	85	sin C	29	45	C' dex	254	3	FA2	271	18	FA2
349	72	S2	137	75	sin C	37	60	C' dex	252	7	FA2	233	44	FA2
169	82	S2	311	85	sin C	57	53	C' dex	79	8	FA2	274	42	FA2
358	90	S2	137	68	sin C	226	77	C' dex	167	22	FA2	269	53	FA2
1	88	S2	149	72	sin C	17	83	C' dex	62	73	FA2	256	9	FA2
155	89	S2	138	73	sin C	216	63	C' dex	84	74	FA2	256	33	FA2
351	87	S2	153	62	sin C	195	64	C' dex	281	37	FA2	240	47	FA2
347	79	S2	150	49	sin C	0	80	C' dex	270	38	FA2	254	35	FA2
351	83	S2	140	76	sin C	357	85	C' dex	135	74	FA2	244	39	FA2
350	80	S2	131	77	sin C	349	48	C' dex	146	66	FA2	206	43	FA2

Supporting Table 1: raw data of structural measurements

Domain A			Domain A			Domain C			Domain D			Domain E		
355	85	S2	142	84	sin C	41	55	C' dex	132	74	FA2	85	12	FA2
188	58	S2	142	77	sin C	22	55	C' dex	188	77	FA2	286	4	FA2
346	87	S2	142	75	sin C	258	48	C' dex	260	7	FA2	294	27	FA2
355	75	S2	154	83	sin C	183	78	C' dex	86	10	FA2	304	22	FA2
353	79	S2	148	83	sin C	176	76	C' dex	287	14	FA2	267	41	FA2
352	80	S2	135	72	sin C	208	68	C' dex	118	0	FA2	263	28	FA2
3	69	S2	135	65	sin C	191	70	C' dex	270	10	FA2	272	13	FA2
357	75	S2	147	90	sin C	14	65	C' dex	275	7	FA2	280	6	FA2
4	67	S2	331	88	sin C	7	72	C' dex	265	30	FA2	287	11	FA2
3	74	S2	335	70	sin C	139	74	C' dex	262	27	FA2	269	5	FA2
6	81	S2	339	74	sin C	146	81	C' dex	267	20	FA2	288	32	FA2
357	71	S2	326	80	sin C	294	53	C' dex	223	31	FA2	276	13	FA2
357	77	S2	148	85	sin C	292	47	C' dex	247	10	FA2	270	19	FA2
353	77	S2	336	87	sin C	299	45	C' dex	240	15	FA2	286	6	FA2
355	80	S2	159	77	sin C	25	15	C' dex	145	8	FA2	288	19	FA2
3	78	S2	174	74	sin C	345	45	C' dex	244	32	FA2	276	8	FA2
356	77	S2	159	72	sin C	167	69	C' dex	106	16	FA2	290	5	FA2
6	64	S2	354	74	sin C	99	54	C' dex	93	0	FA2	228	20	FA2
7	90	S2	345	75	sin C	151	55	C' dex	100	20	FA2	283	22	FA2
7	81	S2	185	85	sin C	170	53	C' dex	287	14	FA2	319	55	FA2
166	88	S2	0	74	sin C	181	34	C' dex	127	74	FA2	94	6	FA2
357	88	S2	2	72	sin C	182	32	C' dex	132	54	FA2	269	30	FA2
358	88	S2	4	82	sin C	139	68	C' dex	144	64	FA2	282	25	FA2
178	84	S2	164	87	sin C	6	64	C' dex	153	48	FA2	277	24	FA2
3	89	S2	151	87	sin C	350	75	C' dex	96	42	FA2	244	3	FA3
161	75	S2	149	73	sin C	329	77	C' dex	275	22	FA2	325	10	FA3
182	84	S2	151	90	sin C	340	72	C' dex	272	12	FA2	80	3	FA3
191	78	S2	144	86	sin C	4	82	C' dex	262	29	FA2	259	15	FA3
176	69	S2	325	82	sin C	7	88	C' dex	275	10	FA2	284	7	FA3
343	74	S2	330	85	sin C	172	76	C' dex	285	14	FA2	267	4	FA3
188	85	S2	331	85	sin C	350	89	C' dex	87	12	FA2	244	22	FA3
194	88	S2	349	81	sin C	0	65	C' dex	112	7	FA2	114	14	FA3
199	72	S2	324	85	sin C	21	69	C' dex	94	18	FA2	285	24	FA3
336	87	S2	342	70	sin C	354	73	C' dex	99	15	FA2	274	5	FA3
152	84	S2	341	77	sin C	3	67	C' dex	88	10	FA2	274	13	FA3
150	80	S2	336	76	sin C	356	64	C' dex	279	28	FA2	272	13	FA3
332	89	S2	343	84	sin C	347	88	C' dex	250	20	FA2	282	17	FA3
140	84	S2	165	86	sin C	343	78	C' dex	75	25	FA2	122	12	FA3
314	80	S2	331	82	sin C	319	55	C' dex	266	9	FA2	270	8	FA3
331	87	S2	322	74	sin C	320	61	C' dex	285	27	FA2	260	1	FA3
142	84	S2	320	72	sin C	24	27	C' dex	242	51	FA2	273	24	FA3
321	78	S2	345	72	sin C	31	36	C' dex	151	60	FA4	263	31	FA3
351	85	S2	344	77	sin C	45	36	C' dex	69	56	FA4	267	23	FA3
353	82	S2	157	83	sin C	222	58	C' dex	260	87	FA4	341	28	FA3
173	89	S2	153	90	sin C	203	71	C' dex	80	81	FA4	285	32	FA3
358	84	S2	334	83	sin C	325	43	C' dex	76	76	FA4	319	31	FA3
355	85	S2	155	83	sin C	256	44	C' dex	240	54	FA4	299	30	FA3
161	86	S2	152	90	sin C	230	50	C' dex	72	76	FA4	290	20	FA3
6	85	S2	156	77	sin C	200	37	C' dex	214	77	FA4	321	15	FA3

Supporting Table 1: raw data of structural measurements

Domain A			Domain A			Domain C			Domain D			Domain E		
6	84	S2	153	78	sin C	260	55	C' dex	156	85	FA4	325	13	FA3
349	84	S2	168	87	sin C	264	52	C' dex	113	69	FA4	282	15	FA3
340	87	S2	158	68	sin C	255	39	C' dex	155	64	FA4	280	12	FA3
160	79	S2	161	67	sin C	288	79	C' dex	320	60	FA4	277	7	FA3
162	76	S2	139	76	sin C	284	77	C' dex	212	40	FA4	290	10	FA3
331	60	S2	131	79	sin C	274	88	C' dex	62	85	FA4	279	21	FA3
335	57	S2	134	65	sin C	357	87	C' dex	259	88	FA4	291	32	FA3
341	70	S2	340	86	sin C	185	86	C' dex	126	83	FA4	278	12	FA3
152	86	S2	155	87	sin C	353	84	C' dex	194	42	FA4	274	16	FA3
332	90	S2	335	75	sin C	164	64	C' dex	286	53	FA4	294	0	FA3
144	89	S2	333	76	sin C	157	72	C' dex	39	14	L1	300	4	FA3
140	89	S2	339	67	sin C	347	86	C' dex	29	6	L1	286	11	FA3
147	70	S2	333	75	sin C	339	87	C' dex	271	8	L1	286	10	FA3
0	69	S2	340	80	sin C	158	82	C' dex	272	9	L1			
333	80	S2	334	86	sin C	164	68	C' dex	272	4	L1			
343	75	S2	155	20	sin C	171	80	C' dex	111	35	L1			
333	90	S2	312	82	sin C	330	84	C' dex	105	37	L1			
338	81	S2	163	64	sin C	0	75	C' dex	267	22	L1			
165	90	S2	333	70	sin C	17	83	C' dex	246	29	L1			
162	87	S2	332	61	sin C	186	89	C' dex	254	14	L1			
142	74	S2	324	55	sin C	354	82	C' dex	257	37	L1			
138	80	S2	326	65	sin C	8	80	C' dex	247	11	L1			
326	90	S2	124	66	sin C	9	70	C' dex	246	20	L1			
339	89	S2	298	84	sin C	294	42	C' dex	250	22	L1			
328	80	S2	294	88	sin C	311	36	C' dex	257	37	L1			
160	89	S2	284	76	sin C	333	55	C' dex	264	28	L1			
321	87	S2	108	71	sin C	334	50	C' dex	74	49	L1			
325	85	S2	88	84	sin C	27	65	C' dex	106	51	L1			
335	88	S2	104	74	sin C	20	70	C' dex	98	39	L1			
157	80	S2	134	86	sin C	24	66	C' dex	274	36	L1			
153	81	S2	281	69	sin C	5	90	C' dex	74	27	L1			
330	90	S2	289	69	sin C	258	58	C' dex	82	11	L1			
325	77	S2	291	53	sin C	306	45	C' norm	66	27	L1			
138	85	S2	340	64	sin C	317	55	C' norm	73	28	L1			
336	85	S2	311	45	sin C	224	52	C' norm	76	18	L1			
341	80	S2	160	88	sin C	230	48	C' norm	148	40	L1			
326	83	S2	134	72	sin C	295	78	C' norm	90	34	L1			
326	86	S2	122	65	sin C	268	70	C' norm	69	24	L1			
330	83	S2	318	87	sin C	264	16	C' norm	72	9	L1			
324	82	S2	308	84	sin C	321	16	C' norm	73	74	L1			
324	81	S2	328	90	sin C	297	36	C' norm	58	74	L1			
154	82	S2	142	87	sin C	247	21	C' norm	75	61	L1			
162	88	S2	315	77	sin C	151	55	C' norm	284	7	L1			
351	75	S2	154	63	sin C	170	53	C' norm	108	2	L1			
353	71	S2	142	83	sin C	181	34	C' norm	272	8	L1			
328	65	S2	159	59	sin C	182	32	C' norm	97	26	L2			
348	85	S2	146	68	sin C	139	68	C' norm	103	23	L2			
163	72	S2	147	69	sin C	332	52	C' norm	101	23	L2			
356	63	S2	94	84	sin C	329	64	C' norm	92	25	L2			

Supporting Table 1: raw data of structural measurements

Domain A			Domain A			Domain C			Domain D			Domain A		
181	40	S2	76	65	sin C	198	43	C' norm	94	28	L2	318	32	AE3
183	43	S2	246	79	sin C	216	36	C' norm	103	32	L2	300	22	AE3
161	88	S2	286	56	sin C	4	21	C' norm	94	18	L2	314	29	AE3
175	73	S2	147	72	sin C	293	53	C' norm	107	37	L2	285	45	AE3
171	79	S2	333	83	sin C	273	43	C' norm	110	11	L2	288	33	AE3
163	45	S2	326	81	sin C	276	45	C' norm	126	12	L2	246	52	AE3
335	80	S2	307	85	sin C	226	22	C' norm	132	34	L2	272	45	AE3
152	50	S2	347	43	sin C	244	28	C' norm	135	28	L2	283	41	AE3
150	89	S2	351	85	sin C	252	43	C' norm	3	45	L2	92	60	AE3
147	77	S2	271	49	sin C	334	80	C' norm	281	19	L sin	268	69	AE3
150	86	S2	303	56	sin C	332	78	C' norm	284	60	L sin	253	65	AE3
146	71	S2	280	88	sin C	270	57	C' norm	235	34	L sin	274	72	AE3
350	75	S2	101	77	sin C	260	70	C' norm	256	28	L sin	89	87	AE3
337	63	S2	116	80	sin C	208	40	C' norm	251	34	L sin	310	24	AE3
341	62	S2	18	82	sin C	219	53	C' norm				312	24	AE3
189	79	S2	17	74	sin C	228	53	C' norm				241	28	AE3
349	81	S2	337	47	sin C	344	70	C' norm				236	44	AE3
337	61	S2	331	52	sin C	333	66	C' norm				222	49	AE3
353	68	S2	314	49	sin C	283	64	C' norm				321	17	AE3
329	50	S2	321	36	sin C	263	38	C' norm				314	15	AE3
322	68	S2	300	50	sin C	248	54	C' norm				342	25	AE3
351	49	S2	295	66	sin C	250	63	C' norm				338	35	AE3
335	55	S2	287	68	sin C	271	38	C' norm				302	10	AE3
322	45	S2	298	72	sin C	239	45	C' norm				37	30	FA1
326	70	S2	288	70	sin C	264	74	C' norm				51	22	FA1
134	87	S2	278	69	sin C	9	70	C' norm				78	37	FA1
326	83	S2	280	58	sin C	305	65	C' norm				86	24	FA1
333	74	S2	307	77	sin C	239	75	C' norm				242	7	FA1
154	88	S2	294	74	sin C	247	63	C' norm				224	31	FA1
144	67	S2	299	73	sin C	267	67	C' norm				242	28	FA1
329	70	S2	299	72	sin C	266	61	C' norm				224	31	FA1
331	85	S2	286	78	sin C	257	61	C' norm				250	10	FA1
162	85	S2	278	67	sin C	24	66	C' norm				254	14	FA1
330	80	S2	110	67	sin C	5	90	C' norm				274	2	FA1
344	66	S2	118	67	sin C	258	58	C' norm				277	11	FA1
331	90	S2	84	75	sin C	117	72	C' rev				71	4	FA1
338	86	S2	133	90	sin C	118	69	C' rev				245	5	FA1
149	84	S2	149	82	sin C	72	42	C' rev				85	7	FA1
334	89	S2	153	73	sin C	67	42	C' rev				74	4	FA1
160	85	S2	155	82	sin C	301	60	C' rev				96	7	FA1
150	81	S2	154	76	sin C	307	57	C' rev				92	5	FA1
332	69	S2	148	80	sin C	303	50	C' rev				254	7	FA1
349	84	S2	110	77	sin C	320	30	C' rev				259	0	FA1
347	82	S2	126	84	sin C	325	75	C' rev				110	24	FA1
166	85	S2	312	85	sin C	304	70	C' rev				102	18	FA1
173	83	S2	304	83	sin C	292	65	C' rev				100	15	FA1
351	68	S2	141	75	sin C	271	51	C' rev				69	7	FA2
166	86	S2	141	76	sin C	68	77	C' rev				251	3	FA2
350	88	S2	149	84	sin C	58	64	C' rev				227	26	FA2

Supporting Table 1: raw data of structural measurements

Domain A			Domain A			Domain C			Domain A			Domain A		
355	80	S2	263	53	sin C	201	69	C' rev	71	59	L2	240	14	FA2
329	71	S2	254	65	sin C	224	77	C' rev	74	69	L2	255	4	FA2
329	61	S2	304	80	sin C	205	70	C' rev	73	67	L2	249	2	FA2
328	72	S2	149	82	sin C	184	73	C' rev	70	24	L2	72	16	FA2
357	73	S2	121	83	sin C	240	90	C' rev	64	48	L2	84	24	FA2
355	77	S2	129	73	sin C	306	88	C' rev	72	41	L2	250	5	FA2
344	62	S2	307	77	sin C	305	75	C' rev	68	46	L2	78	6	FA2
340	78	S2	287	89	sin C	294	42	C' rev	84	45	L2	228	8	FA2
175	75	S2	304	40	sin C	311	36	C' rev	90	36	L2	81	12	FA2
183	85	S2	304	69	sin C	333	55	C' rev	90	34	L2	264	24	FA2
7	67	S2	271	76	sin C	334	50	C' rev	93	51	L2	254	30	FA2
2	59	S2	308	54	sin C	27	65	C' rev	79	55	L2	254	16	FA2
334	60	S2	306	59	sin C	20	70	C' rev	98	57	L2	256	19	FA2
348	64	S2	302	76	sin C	18	67	C' sin	275	45	L2	255	16	FA2
0	59	S2	295	65	sin C	119	72	C' sin	270	35	L2	93	29	FA2
332	87	S2	304	54	sin C	114	71	C' sin	256	23	L2	93	30	FA2
341	81	S2	320	66	sin C	126	85	C' sin	254	46	L2	251	5	FA2
332	80	S2	295	65	sin C	113	77	C' sin	262	62	L2	71	1	FA2
332	85	S2	311	64	sin C	277	89	C' sin	96	34	L2	63	10	FA2
0	70	S2	328	62	sin C	298	85	C' sin	68	39	L2	72	20	FA2
359	71	S2	345	85	sin C	316	55	C' sin	89	45	L2	74	20	FA2
344	52	S2	156	81	sin C	122	75	C' sin	96	47	L2	65	26	FA2
347	56	S2	140	76	sin C	306	78	C' sin	50	45	L2	72	20	FA2
1	70	S2	348	52	sin C	324	70	C' sin	52	43	L2	69	28	FA2
358	65	S2	348	42	sin C	254	82	C' sin	58	40	L2	14	66	FA2
181	84	S2	297	80	sin C	270	69	C' sin	54	30	L2	16	50	FA2
337	86	S2	132	83	sin C	257	70	C' sin	78	35	L2	66	20	FA2
343	65	S2	143	80	sin C	292	77	C' sin	64	29	L2	85	13	FA2
184	71	S2	309	87	sin C	124	70	C' sin	60	52	L2	272	32	FA2
1	89	S2	324	85	sin C	117	76	C' sin	72	5	L2	253	5	FA2
167	82	S2	153	89	sin C	302	90	C' sin	12	64	L2	245	12	FA2
169	88	S2	156	90	sin C	300	72	C' sin	251	47	L2	245	15	FA2
9	90	S2	146	85	sin C	274	77	C' sin	237	39	L2	79	5	FA2
171	75	S2	149	84	sin C	77	88	C' sin	225	37	L2	69	4	FA2
178	82	S2	340	81	sin C	261	87	C' sin	233	38	L2	76	0	FA2
191	86	S2	328	82	sin C	126	80	C' sin	249	25	L2	234	10	FA2
8	84	S2	336	86	sin C	123	84	C' sin	247	25	L2	242	9	FA2
188	83	S2	342	85	sin C	136	81	C' sin	242	19	L2	269	24	FA2
345	69	S2	113	70	sin C	121	79	C' sin	243	22	L2	244	22	FA2
341	75	S2	100	80	sin C	283	83	C' sin	244	24	L2	244	11	FA2
178	79	S2	333	85	sin C	284	57	C' sin	247	24	L2	222	59	FA2
178	83	S2	327	88	sin C	260	77	C' sin	31	43	L2	240	80	FA2
336	64	S2	286	55	sin C	265	77	C' sin	51	29	L2	257	1	FA2
334	72	S2	328	82	sin C	110	45	C' sin	50	16	L2	256	2	FA2
342	82	S2	331	90	sin C	112	44	C' sin	242	26	L2	244	3	FA2
357	58	S2	154	73	sin C	106	89	C' sin	243	25	L2	90	11	FA2
351	81	S2	142	72	sin C	105	90	C' sin	247	52	L2	240	9	FA2
346	77	S2	332	76	sin C	237	83	C' sin	248	47	L2	55	3	FA2
346	67	S2	312	82	sin C	149	74	C' sin	93	28	L2	62	1	FA2

Supporting Table 1: raw data of structural measurements

Domain A			Domain A			Domain C			Domain A			Domain A		
335	90	S2	313	84	sin C	105	76	C' sin	97	27	L2	40	14	FA2
334	90	S2	148	65	sin C	108	75	C' sin	98	38	L2	219	11	FA2
334	78	S2	139	58	sin C	107	74	C' sin	234	38	L2	218	19	FA2
333	76	S2	163	72	sin C	100	86	C' sin	231	46	L2	225	26	FA2
339	80	S2	166	65	sin C	301	84	C' sin	237	18	L2	70	15	FA2
349	73	S2	343	86	sin C	277	65	C' sin	234	20	L2	70	21	FA2
342	55	S2	158	80	sin C	275	72	C' sin	235	17	L2	239	22	FA2
349	80	S2	346	89	sin C	90	85	C' sin	39	15	L2	75	16	FA2
334	50	S2	167	88	sin C	86	73	C' sin	55	10	L2	56	1	FA2
345	69	S2	339	86	sin C	306	68	C' sin	62	3	L2	237	5	FA2
324	78	S2	345	86	sin C	306	80	C' sin	61	9	L2	265	20	FA2
161	78	S2	139	80	sin C	233	90	C' sin	81	34	L2	254	5	FA2
335	88	S2	148	70	sin C	42	89	C' sin	67	22	L2	266	2	FA2
159	82	S2	130	67	sin C	246	85	C' sin	74	22	L2	265	4	FA2
159	74	S2	146	55	sin C	225	78	C' sin	88	23	L2	257	17	FA2
339	87	S2	152	75	sin C	306	82	C' sin	94	38	L2	264	21	FA2
333	80	S2	155	87	sin C	309	90	C' sin	152	74	L2	260	7	FA2
342	72	S2	147	74	sin C	129	86	C' sin	86	59	L2	263	11	FA2
339	71	S2	313	77	sin C	280	58	C' sin	55	27	L2	281	54	FA2
344	79	S2	310	74	sin C	271	68	C' sin	87	27	L2	285	3	FA2
349	89	S2	314	72	sin C	106	81	C' sin	56	36	L2	84	26	FA2
334	69	S2	304	90	sin C	116	84	C' sin	62	32	L2	95	17	FA2
338	74	S2	301	80	sin C	114	81	C' sin	88	25	L2	88	32	FA2
336	85	S2	289	89	sin C	99	75	C' sin	84	28	L2	89	31	FA2
329	80	S2	111	88	sin C	115	77	C' sin	83	48	L2	90	35	FA2
330	85	S2	334	81	sin C	298	88	C' sin	77	33	L2	90	12	FA2
299	69	S2	331	77	sin C	310	80	C' sin	85	12	L2	89	18	FA2
332	76	S2	161	86	sin C	118	85	C' sin	82	8	L2	263	33	FA2
332	77	S2	316	90	sin C	305	87	C' sin	168	77	L2	245	20	FA2
346	88	S2	315	84	sin C	141	78	C' sin	222	58	L2	112	5	FA2
336	88	S2	321	66	sin C	82	68	C' sin	232	42	L2	111	1	FA2
152	70	S2	122	78	sin C	93	80	C' sin	107	63	L2	102	32	FA2
153	81	S2	315	86	sin C	289	70	C' sin	73	53	L2	94	23	FA2
160	81	S2	150	90	sin C	98	86	C' sin	81	31	L2	84	18	FA2
150	83	S2	140	84	sin C	90	89	C' sin	83	28	L2	86	22	FA2
156	80	S2	321	83	sin C	96	80	C' sin	84	46	L2	281	5	FA2
156	81	S2	305	78	sin C	291	81	C' sin	89	44	L2	340	14	FA2
146	82	S2	304	77	sin C	286	87	C' sin	246	42	L2	330	24	FA2
322	88	S2	349	67	sin C	315	77	C' sin	243	58	L2	329	32	FA2
333	80	S2	352	62	sin C	308	82	C' sin	240	52	L2	285	10	FA2
3387	80	S2	145	75	sin C	319	87	C' sin	246	56	L2	270	1	FA2
159	75	S2	140	77	sin C	274	77	C' sin	235	52	L2	71	10	FA2
160	74	S2	310	42	sin C	283	79	C' sin	250	49	L2	70	16	FA2
325	84	S2	295	72	sin C	247	63	C' sin	252	55	L2	94	23	FA2
326	87	S2	139	84	sin C	267	67	C' sin	263	56	L2	89	29	FA2
157	79	S2	329	84	sin C	266	61	C' sin	253	56	L2	77	34	FA2
157	66	S2	332	85	sin C	257	61	C' sin	262	55	L2	287	8	FA2
295	65	S2	332	89	sin C	306	88	C' sin	237	55	L2	284	2	FA2
298	67	S2	246	78	sin C	305	75	C' sin	239	54	L2	91	5	FA2

Supporting Table 1: raw data of structural measurements

Domain A			Domain A			Domain C			Domain A			Domain A		
144	83	S2	264	85	sin C	147	20	AE1	247	36	L2	96	15	FA2
331	90	S2	312	62	sin C	195	56	AE1	242	47	L2	78	4	FA2
335	90	S2	347	66	sin C	204	54	AE1	269	75	L2	79	9	FA2
144	69	S2	349	63	sin C	286	44	AE1	248	63	L2	268	6	FA2
146	76	S2	110	74	sin C	305	34	AE1	241	61	L2	92	32	FA2
327	87	S2	307	88	sin C	306	38	AE1	75	37	L2	45	45	FA2
149	88	S2	303	78	sin C	37	67	AE1	91	42	L2	89	22	FA2
142	88	S2	91	72	sin C	123	27	AE1	75	52	L2	65	34	FA2
153	89	S2	320	75	sin C	172	45	AE1	75	28	L2	230	39	FA2
144	90	S2	305	90	sin C	210	29	AE1	252	4	L2	236	18	FA2
148	90	S2	308	87	sin C	153	30	AE1	251	19	L2	275	62	FA2
151	90	S2	342	68	sin C	140	63	AE1	250	27	L2	64	17	FA2
142	90	S2	141	88	sin C	97	14	AE1	68	13	L2	72	8	FA2
330	85	S2	332	84	sin C	73	52	AE1	65	15	L2	53	12	FA2
336	80	S2	167	88	sin C	70	50	AE1	53	9	L2	52	29	FA2
154	86	S2	329	84	sin C	291	16	AE1	59	20	L2	95	12	FA2
141	84	S2	335	82	sin C	265	18	AE1	59	11	L2	99	22	FA2
155	87	S2	129	83	sin C	303	10	AE1	47	20	L2	59	32	FA2
330	70	S2	134	85	sin C	216	23	AE1	15	38	L2	92	4	FA2
332	78	S2	167	86	sin C	197	45	AE1	40	27	L2	248	13	FA3
153	80	S2	171	86	sin C	89	0	AE1	34	28	L2	250	13	FA3
149	85	S2	134	40	sin C	228	14	AE1	81	28	L2	253	2	FA3
336	83	S2	132	60	sin C	279	28	AE1	81	20	L2	243	54	FA3
334	75	S2	155	75	sin C	274	54	AE1	89	10	L2	251	32	FA3
333	75	S2	325	79	sin C	22	26	AE1	68	24	L2	256	42	FA3
333	75	S2	149	83	sin C	33	29	AE1	78	14	L2	252	12	FA3
335	84	S2	328	86	sin C	334	36	AE1	75	25	L2	85	36	FA3
336	75	S2	149	86	sin C	239	11	AE1	85	24	L2	266	35	FA3
336	85	S2	313	81	sin C	1	26	AE1	77	19	L2	264	28	FA3
156	87	S2	165	82	sin C	353	15	AE1	68	24	L2	242	43	FA3
161	89	S2	356	88	sin C	274	29	AE1	71	20	L2	235	31	FA3
157	87	S2	166	70	sin C	308	85	AE2	69	27	L2	25	35	FA3
331	90	S2	165	71	sin C	300	86	AE2	71	29	L2	82	47	FA3
334	86	S2	345	82	sin C	351	48	AE2	80	23	L2	212	52	FA3
335	86	S2	346	78	sin C	24	64	AE2	67	32	L2	217	60	FA3
333	88	S2	350	87	sin C	323	67	AE2	78	18	L2	231	59	FA3
336	89	S2	343	73	sin C	341	82	AE2	76	33	L2	153	85	FA3
325	70	S2	353	80	sin C	144	52	AE2	76	22	L2	271	17	FA3
339	82	S2	0	80	sin C	130	57	AE2	256	15	L2	274	15	FA3
339	82	S2	181	89	sin C	90	90	AE2	257	8	L2	298	18	FA3
161	88	S2	170	86	sin C	329	65	AE2	248	4	L2	252	4	FA3
357	79	S2	161	68	sin C	326	84	AE2	256	21	L2	258	11	FA3
126	47	S2	116	64	sin C	312	73	AE2	266	22	L2	267	8	FA3
135	58	S2	127	78	sin C	302	72	AE2	252	39	L2	82	11	L1
160	69	S2	119	52	sin C	309	65	AE2	253	14	L2	285	7	L1
156	73	S2	285	82	sin C	204	73	AE2	261	33	L2	272	3	L1
135	50	S2	125	62	sin C	166	69	AE2	253	11	L2	258	18	L1
150	57	S2	112	65	sin C	171	69	AE2	254	18	L2	259	20	L1
137	78	S2	314	80	sin C	17	9	AE2	242	8	L2	265	13	L1

Supporting Table 1: raw data of structural measurements

Domain A			Domain A			Domain C			Domain A			Domain A		
139	76	S2	318	67	sin C	330	15	AE2	263	5	L2	263	20	L1
144	64	S2	306	66	sin C	95	37	AE2	220	30	L2	65	4	L1
145	57	S2	331	71	sin C	68	22	AE2	232	10	L2	252	8	L1
132	51	S2	333	84	sin C	110	74	AE2	237	20	L2	261	11	L1
142	55	S2	343	88	sin C	93	85	AE2	249	27	L2	239	34	L1
133	68	S2	324	84	sin C	280	75	AE2	234	4	L2	255	21	L1
137	64	S2	336	83	sin C	258	86	AE2	229	15	L2	255	32	L1
157	77	S2	324	80	sin C	266	83	AE2	230	20	L2	260	32	L1
156	72	S2	330	60	sin C	294	79	AE2	241	8	L2	248	21	L1
344	58	S2	310	90	sin C	299	72	AE2	243	5	L2	262	19	L1
328	52	S2	286	89	sin C	284	64	AE2	250	21	L2	261	6	L1
160	88	S2	138	88	sin C	282	67	AE2	236	17	L2	249	21	L1
336	88	S2	330	52	sin C	277	45	AE2	229	29	L2	246	2	L1
332	86	S2	316	56	sin C	317	50	AE2	42	18	L2	254	15	L1
148	86	S2	313	67	sin C	320	70	AE2	52	10	L2	249	46	L1
0	72	S2	123	55	sin C	333	52	AE2	232	10	L2	235	41	L1
345	85	S2	267	83	sin C	333	69	AE2	224	8	L2	221	24	L1
352	64	S2	295	81	sin C	325	82	AE2	60	7	L2	55	8	L1
21	65	S2	330	51	sin C	343	90	AE2	51	5	L2	60	4	L1
10	68	S2	332	84	sin C	131	37	AE2	250	14	L2	254	4	L1
172	60	S2	330	82	sin C	133	34	AE2	242	9	L2	235	18	L1
173	60	S2	308	60	sin C	117	60	AE2	236	12	L2	232	11	L1
315	80	S2	309	66	sin C	243	72	AE2	228	4	L2	83	20	L1
323	73	S2	314	51	sin C	270	88	AE2	238	6	L2	88	21	L1
326	90	S2	335	62	sin C	276	76	AE2	90	13	L2	245	6	L1
137	90	S2	318	58	sin C	90	70	AE2	275	5	L2	255	14	L1
158	84	S2	326	64	sin C	80	70	AE2	82	16	L2	257	12	L1
160	82	S2	358	46	sin C	91	70	AE2	82	5	L2	232	2	L1
157	82	S2	334	39	sin C	345	73	AE2	267	5	L2	208	52	L1
162	87	S2	319	81	sin C	345	73	AE2	246	46	L3	226	25	L1
159	82	S2	297	69	sin C	326	87	AE2	242	44	L3	232	24	L1
185	83	S2	142	78	sin C	324	82	AE2	242	39	L3	236	24	L1
340	90	S2	132	86	sin C	329	80	AE2	235	44	L3	236	28	L1
349	86	S2	154	78	sin C	146	84	AE2	273	3	L3	264	19	L1
339	86	S2	151	77	sin C	330	78	AE2	250	23	L dex	264	22	L1
340	87	S2	128	72	sin C	93	80	AE2	271	16	L dex	273	32	L1
344	89	S2	132	76	sin C	321	88	AE2	261	58	L dex	251	19	L1
159	83	S2	139	72	sin C	145	89	AE2	109	30	L dex	255	17	L1
340	82	S2	124	60	sin C	146	87	AE2	242	24	L dex	62	4	L1
337	84	S2	121	79	sin C	37	76	AE2	216	15	L dex	241	17	L1
171	80	S2	115	80	sin C	312	45	AE2	238	39	L dex	250	14	L1
169	86	S2	127	77	sin C	345	52	AE2	78	45	L dex	246	10	L1
169	88	S2	118	70	sin C	260	86	AE2	78	20	L dex	248	19	L1
172	85	S2	303	85	sin C	311	74	AE2	105	26	L dex	57	4	L1
164	87	S2	307	90	sin C	312	72	AE2	273	11	L dex	262	20	L1
166	86	S2	312	90	sin C	308	70	AE2	21	54	L dex	89	20	L1
335	84	S2	309	78	sin C	316	75	AE2	23	59	L dex	218	10	L1
338	65	S2	313	83	sin C	356	86	AE2	262	30	L rev	85	28	L1
335	58	S2	337	67	sin C	180	34	AE2	268	35	L rev	265	23	L1

Supporting Table 1: raw data of structural measurements

Domain A			Domain A			Domain C			Domain A			Domain A		
317	63	S2	344	70	sin C	167	26	AE2	66	6	L rev	109	11	L1
326	70	S2	356	74	sin C	305	78	AE2	230	25	L rev	271	5	L1
343	82	S2	107	61	sin C	321	85	AE2	49	5	L rev	76	5	L1
335	80	S2	300	78	sin C	357	76	AE2	48	14	L rev	251	9	L1
332	79	S2	304	85	sin C	352	62	AE2	245	10	L rev	82	8	L1
324	78	S2	332	67	sin C	218	58	AE2	265	19	L sin	264	1	L1
168	66	S2	322	67	sin C	252	82	AE2	259	14	L sin	272	5	L1
161	63	S2	319	55	sin C	269	73	AE2	264	17	L sin	106	3	L1
154	70	S2	321	71	sin C	267	72	AE2	260	28	L sin	72	4	L1
145	65	S2	323	67	sin C	246	88	AE2	265	20	L sin	82	5	L1
180	70	S2	168	72	sin C	245	90	AE2	163	64	L sin	261	7	L1
176	78	S2	324	48	sin C	75	83	AE2	247	32	L sin	258	8	L1
162	86	S2	309	35	sin C	83	68	AE2	243	32	L sin	76	4	L1
323	83	S2	336	60	sin C	72	73	AE2	234	17	L sin	243	3	L1
345	87	S2	338	65	sin C	284	36	AE2	236	8	L sin	70	1	L1
140	87	S2	342	45	sin C	293	44	AE2	226	10	L sin	72	4	L1
133	88	S2	355	78	sin C	290	40	AE2	223	3	L sin	261	21	L1
131	84	S2	349	82	sin C	353	70	AE2	252	17	L sin	267	24	L1
0	82	S2	353	85	sin C	150	76	AE2	251	21	L sin	243	8	L1
153	74	S2	349	84	sin C	357	68	AE2	228	18	L sin	224	14	L1
152	67	S2	339	86	sin C	12	53	AE2	231	15	L sin	59	8	L1
355	80	S2	353	85	sin C	282	50	AE2	228	27	L sin	38	24	L1
331	86	S2	354	87	sin C	273	46	AE2	228	22	L sin	232	1	L1
340	80	S2	343	84	sin C	213	60	AE2	230	21	L sin	248	5	L1
350	80	S2	342	77	sin C	208	56	AE2	222	22	L sin	270	14	L1
159	90	S2	325	63	sin C	337	28	AE2	236	12	L sin	218	38	L1
148	89	S2	326	57	sin C	23	46	AE2	233	37	L sin	160	67	L1
335	81	S2	339	50	sin C	2	85	AE2	234	37	L sin	220	49	L1
343	74	S2	342	77	sin C	346	77	AE2	244	12	L sin	215	13	L1
336	89	S2	329	66	sin C	111	33	AE2	243	17	L sin	219	21	L1
339	78	S2	294	80	sin C	233	56	AE2	240	18	L sin	233	20	L1
152	84	S2	300	68	sin C	223	78	AE2	232	8	L sin	234	12	L1
173	78	S2	286	62	sin C	194	71	AE2	232	8	L sin	250	38	L1
142	83	S2	292	60	sin C	298	84	AE2	233	9	L sin	256	12	L1
314	85	S2	320	87	sin C	139	78	AE2	230	10	L sin	76	11	L1
330	69	S2	145	86	sin C	299	75	AE2	235	14	L sin	250	9	L1
341	37	S2	346	84	sin C	129	65	AE2	226	12	L sin	222	3	L1
331	67	S2	308	86	sin C	117	75	AE2	251	7	L sin	266	7	L1
339	62	S2	351	82	sin C	104	72	AE2	260	24	L sin	260	6	L1
341	54	S2	156	90	sin C	171	42	AE2	77	14	L sin	248	18	L1
298	65	S2	321	86	sin C	343	51	AE2	42	1	L sin	226	4	L1
346	62	S2	331	89	sin C	338	49	AE2	42	15	L sin	269	14	L1
323	74	S2	312	83	sin C	32	55	AE2	229	29	L sin	248	17	L1
320	77	S2	310	80	sin C	45	61	AE2	222	24	L sin	329	22	L1
312	81	S2	316	83	sin C	279	10	AE2	239	16	L sin	240	22	L1
323	85	S2	301	77	sin C	279	32	AE2	217	26	L sin	330	24	L1
319	70	S2	306	79	sin C	338	28	AE2	203	7	L sin	264	10	L1
324	73	S2	317	77	sin C	332	32	AE2	262	28	L sin	261	3	L1
321	60	S2	309	85	sin C	340	22	AE2	244	24	L sin	82	2	L1

Supporting Table 1: raw data of structural measurements

Domain A			Domain A			Domain C			Domain A			Domain A		
323	78	S2	317	86	sin C	326	40	AE2	262	21	L sin	81	24	L1
169	72	S2	313	80	sin C	131	78	AE2	42	37	L sin	96	28	L1
141	90	S2	317	76	sin C	111	75	AE2	249	12	L sin	85	32	L1
149	84	S2	318	70	sin C	133	74	AE2	253	5	L sin	76	36	L1
141	89	S2	288	88	sin C	116	67	AE2	256	11	L sin	43	20	L1
313	74	S2	303	86	sin C	101	90	AE2	58	2	L sin	44	17	L1
327	63	S2	306	88	sin C	310	90	AE2	79	19	L sin	64	7	L1
332	63	S2	304	86	sin C	319	90	AE2	82	22	L sin	58	4	L1
325	68	S2	301	85	sin C	151	68	AE2	261	15	L sin	252	24	L1
319	65	S2	301	90	sin C	150	76	AE2	256	17	L sin	248	22	L1
306	61	S2	125	85	sin C	326	46	AE2	66	6	L sin	252	12	L1
267	74	S2	114	88	sin C	349	39	AE2	230	25	L sin	275	22	L1
295	65	S2	321	90	sin C	175	45	AE2	49	5	L sin	275	26	L1
302	67	S2	140	78	sin C	181	61	AE2	48	14	L sin	264	17	L1
294	66	S2	106	80	sin C	175	59	AE2	245	10	L sin	256	4	L1
305	53	S2	114	69	sin C	202	84	AE2	69	32	L sin	260	3	L1
314	73	S2	124	90	sin C	340	82	AE2	86	30	L sin	259	8	L1
288	50	S2	136	87	sin C	359	70	AE2	83	31	L sin	256	12	L1
310	62	S2	305	78	sin C	5	87	AE2	254	24	L sin	240	45	L1
137	62	S2	317	75	sin C	5	72	AE2	46	38	L sin	238	32	L1
143	63	S2	149	84	sin C	348	69	AE2	29	58	L sin	222	52	L1
137	54	S2	150	84	sin C	200	32	AE2	247	37	L sin	242	40	L1
141	55	S2	145	80	sin C	220	32	AE2	242	37	L sin	228	38	L1
143	50	S2	144	78	sin C	210	88	AE2	93	29	L sin	241	20	L1
149	74	S2	130	61	sin C	197	5	AE2	234	12	L sin	239	21	L1
141	68	S2	94	64	sin C	11	64	AE2	26	44	L sin	240	28	L1
121	90	S2	114	72	sin C	13	66	AE2	37	36	L sin	107	11	L1
149	61	S2	117	70	sin C	24	48	AE2	41	35	L sin	267	13	L1
138	70	S2	129	68	sin C	21	65	AE2	40	25	L sin	267	7	L1
155	67	S2	108	54	sin C	29	86	AE2	33	37	L sin	100	29	L1
151	75	S2	115	64	sin C	323	87	AE2	71	34	L sin	105	8	L1
142	75	S2	136	82	sin C	340	84	AE2	72	56	L sin	0	76	L1
145	80	S2	130	75	sin C	304	40	AE2	75	14	L sin	72	7	L1
142	80	S2	140	80	sin C	77	75	AE3	77	31	L sin	232	18	L1
150	54	S2	148	90	sin C	88	81	AE3	264	13	L sin	4	90	L1
129	53	S2	135	79	sin C	86	77	AE3	277	3	L sin	209	40	L1
81	50	S2	133	75	sin C	90	90	AE3	287	33	L sin	257	10	L1
337	75	S2	325	89	sin C	80	79	AE3				255	24	L2
347	88	S2	330	87	sin C	95	78	AE3				252	16	L2
342	82	S2	150	89	sin C	251	49	L1				254	12	L2
353	86	S2	338	64	sin C	263	48	L1				259	6	L2
341	88	S2	277	90	sin C	290	41	L1				214	15	L2
347	87	S2	122	82	sin C	345	17	L1				239	12	L2
321	84	S2	292	83	sin C	341	39	L1				265	3	L2
172	90	S2	282	72	sin C	8	47	L1				260	7	L2
333	75	S2	276	67	sin C	357	43	L1				255	13	L2
3	82	S2	275	70	sin C	320	58	L1				260	6	L2
336	84	S2	130	72	sin C	232	24	L1				262	3	L2
357	80	S2	135	70	sin C	42	1	L1				80	18	L2

Supporting Table 1: raw data of structural measurements

Domain A			Domain A			Domain C			Domain A		
339	84	S2	132	85	sin C	25	17	L1	254	4	L2
171	84	S2	297	83	sin C	29	32	L1	265	1	L2
171	87	S2	299	80	sin C	36	27	L1	260	26	L2
167	86	S2	304	82	sin C	10	16	L1	254	23	L2
354	86	S2	113	80	sin C	240	6	L1	276	24	L2
170	86	S2	133	71	sin C	56	20	L1	251	14	L2
155	81	S2	306	74	sin C	58	13	L1	251	16	L2
161	75	S2	104	87	sin C	63	2	L1	64	6	L2
162	75	S2	289	74	sin C	62	13	L1	264	21	L2
150	73	S2	296	84	sin C	112	40	L1	241	13	L2
151	73	S2	297	68	sin C	109	14	L1	256	5	L2
159	76	S2	319	85	sin C	108	24	L1	258	1	L2
163	82	S2	139	82	sin C	268	35	L1	262	17	L2
149	74	S2	305	72	sin C	279	24	L1	102	6	L2
152	72	S2	127	81	sin C	289	28	L1	258	23	L2
165	84	S2	294	89	sin C	195	36	L1	240	16	L2
162	83	S2	241	71	sin C	196	31	L1	258	19	L2
171	79	S2	106	69	sin C	3	9	L1	256	17	L2
163	81	S2	150	83	sin C	18	25	L1	260	7	L2
158	81	S2	144	90	sin C	355	9	L1	251	8	L2
176	85	S2	118	72	sin C	248	22	L2	60	11	L2
168	83	S2	135	83	sin C	248	10	L2	276	6	L2
180	81	S2	136	82	sin C	243	37	L2	269	3	L2
178	79	S2	314	88	sin C	252	32	L2	231	17	L2
191	75	S2	143	78	sin C	251	5	L2	254	29	L2
310	75	S2	143	89	sin C	245	21	L2	252	14	L2
320	81	S2	308	84	sin C	250	22	L2	262	10	L2
320	76	S2	137	82	sin C	244	25	L2	240	6	L2
176	67	S2	78	37	AE1	255	23	L2	261	5	L2
170	87	S2	359	64	AE1	231	23	L2	252	4	L2
168	86	S2	22	70	AE1	241	24	L2	75	2	L2
156	90	S2	131	36	AE1	299	72	L2	253	24	L2
152	83	S2	45	26	AE1	292	72	L2	258	24	L2
152	87	S2	104	42	AE1	240	25	L2	81	24	L2
156	81	S2	155	43	AE1	244	22	L2	249	9	L2
158	82	S2	146	34	AE1	238	45	L2	238	16	L2
144	87	S2	73	56	AE1	260	64	L2	258	13	L2
152	71	S2	83	29	AE1	266	58	L2	250	8	L2
159	74	S2	10	54	AE1	260	61	L2	264	22	L2
149	72	S2	353	61	AE1	266	56	L2	264	16	L2
336	84	S2	277	32	AE1	304	60	L2	253	11	L2
335	88	S2	198	58	AE1	300	64	L2	75	1	L2
169	83	S2	177	44	AE1	306	64	L2	79	14	L2
159	83	S2	173	82	AE1	262	50	L2	64	12	L2
149	88	S2	166	72	AE1	262	24	L2	272	55	L2
346	85	S2	351	56	AE1	250	28	L2	252	25	L2
328	85	S2	328	24	AE1	253	29	L2	253	30	L2
156	81	S2	327	28	AE1	262	26	L2	260	41	L2
148	85	S2	298	24	AE1	249	25	L2	266	43	L2

Supporting Table 1: raw data of structural measurements

Domain A			Domain A			Domain C			Domain A		
340	75	S2	166	15	AE1	257	31	L2	226	35	L2
340	78	S2	12	33	AE1	232	36	L2	244	20	L2
326	84	S2	321	45	AE1	274	17	L2	253	16	L2
315	80	S2	335	45	AE1	262	3	L2	228	22	L2
351	72	S2	146	9	AE1	250	7	L2	253	28	L2
343	84	S2	173	33	AE1	34	39	L2	51	9	L2
146	84	S2	165	43	AE1	13	45	L2	256	9	L2
150	87	S2	188	38	AE1	31	46	L2	251	6	L2
323	85	S2	169	28	AE1	46	44	L2	245	5	L2
168	76	S2	153	60	AE1	37	49	L2	246	2	L2
158	80	S2	168	64	AE1	247	3	L2	242	0	L2
163	77	S2	170	37	AE1	253	16	L2	247	4	L2
170	80	S2	22	71	AE1	263	9	L2	249	19	L2
152	78	S2	133	18	AE1	292	18	L2	255	20	L2
148	75	S2	338	72	AE2	288	9	L2	248	6	L2
152	75	S2	332	74	AE2	289	11	L2	254	14	L2
140	90	S2	344	80	AE2	249	19	L dex	260	18	L2
148	90	S2	335	89	AE2	266	0	L dex	252	14	L2
146	90	S2	346	83	AE2	313	7	L norm	246	8	L2
314	49	S2	169	89	AE2	315	12	L norm	243	7	L2
328	47	S2	11	69	AE2	314	8	L norm	242	11	L2
330	46	S2	11	60	AE2	316	20	L norm	233	37	L2
340	84	S2	153	80	AE2	310	16	L norm	258	4	L2
161	90	S2	160	82	AE2	240	30	L sin	261	11	L2
337	65	S2	331	70	AE2	246	26	L sin	90	29	L2
344	73	S2	338	65	AE2	306	45	L sin	92	22	L2
129	76	S2	344	80	AE2	292	44	L sin	279	2	L2
145	78	S2	335	79	AE2	310	48	L sin	87	11	L2
177	81	S2	6	77	AE2	283	46	L sin	266	4	L2
151	71	S2	354	83	AE2	225	26	L sin	175	2	L2
160	69	S2	160	88	AE2	287	39	L sin	85	3	L2
163	80	S2	342	65	AE2	285	52	L sin	94	0	L2
152	75	S2	157	68	AE2	305	52	L sin	269	4	L2
165	84	S2	165	72	AE2	271	65	L sin	275	6	L2
163	81	S2	345	84	AE2	269	39	L sin	270	4	L2
153	77	S2	340	75	AE2	259	27	L sin	266	5	L2
160	86	S2	325	86	AE2	266	3	FA1	268	4	L2
157	85	S2	339	77	AE2	275	19	FA1	265	4	L2
150	75	S2	332	71	AE2	343	10	FA1	88	28	L2
348	74	S2	190	71	AE2	33	16	FA1	90	44	L2
343	67	S2	335	90	AE2	37	11	FA1	91	32	L2
346	69	S2	156	75	AE2	130	12	FA1	91	25	L2
339	79	S2	164	78	AE2	108	22	FA1	83	22	L2
343	76	S2	337	81	AE2	107	26	FA1	94	34	L2
341	80	S2	187	50	AE2	195	23	FA1	100	27	L2
350	75	S2	167	82	AE2	68	24	FA1	92	21	L2
356	77	S2	339	80	AE2	125	54	FA1	67	27	L2
354	75	S2	131	88	AE2	175	7	FA1	278	6	L2
348	90	S2	135	80	AE2	293	8	FA1	62	12	L2

Supporting Table 1: raw data of structural measurements

Domain A			Domain A			Domain C			Domain A		
353	90	S2	159	81	AE2	250	10	FA1	69	12	L2
349	87	S2	342	62	AE2	274	15	FA1	75	20	L2
349	85	S2	4	62	AE2	91	4	FA1	64	2	L2
344	87	S2	176	74	AE2	158	15	FA1	45	7	L2
352	84	S2	5	81	AE2	254	6	FA1	61	17	L2
343	85	S2	342	73	AE2	203	4	FA1	74	5	L2
342	72	S2	344	43	AE2	285	22	FA1	62	28	L2
350	74	S2	341	41	AE2	96	15	FA1	234	3	L2
174	83	S2	170	53	AE2	267	20	FA1	93	28	L2
308	78	S2	145	82	AE2	265	12	FA1	76	35	L2
348	86	S2	298	78	AE2	261	24	FA1	70	26	L2
324	59	S2	147	48	AE2	258	13	FA1	90	25	L2
330	72	S2	163	71	AE2	9	65	FA2	262	28	L2
334	65	S2	155	80	AE2	30	60	FA2	258	25	L2
345	64	S2	329	77	AE2	225	26	FA2	232	12	L2
351	60	S2	333	63	AE2	214	23	FA2	49	11	L2
306	87	S2	317	80	AE2	226	41	FA2	226	24	L2
127	67	S2	135	75	AE2	205	13	FA2	235	10	L2
332	70	S2	136	84	AE2	51	4	FA2	251	30	L2
339	76	S2	327	73	AE2	264	13	FA2	176	68	L2
322	83	S2	156	87	AE2	76	2	FA2	244	16	L2
323	90	S2	159	90	AE2	77	7	FA2	242	37	L2
320	90	S2	332	84	AE2	29	0	FA2	236	30	L2
153	84	S2	332	54	AE2	34	14	FA2	237	48	L2
151	78	S2	349	56	AE2	40	23	FA2	241	30	L2
328	72	S2	13	46	AE2	26	18	FA2	252	14	L2
324	78	S2	140	75	AE2	26	10	FA2	254	12	L2
328	75	S2	144	66	AE2	28	32	FA2	254	14	L2
311	81	S2	356	51	AE2	13	33	FA2	261	20	L2
127	53	S2	343	63	AE2	357	12	FA2	242	12	L2
129	62	S2	343	53	AE2	2	13	FA2	242	4	L2
147	75	S2	352	35	AE2	189	13	FA2	274	2	L2
144	82	S2	348	55	AE2	190	20	FA2	94	14	L2
155	61	S2	358	62	AE2	13	17	FA2	58	53	L2
153	61	S2	342	54	AE2	12	14	FA2	250	7	L2
316	87	S2	348	52	AE2	237	4	FA2	252	13	L2
134	85	S2	346	59	AE2	258	40	FA2	242	8	L2
316	87	S2	19	76	AE2	80	15	FA2	254	9	L2
134	85	S2	10	76	AE2	227	16	FA2	254	0	L2
126	69	S2	10	80	AE2	238	20	FA2	250	0	L2
127	69	S2	9	89	AE2	190	20	FA2	245	1	L2
133	80	S2	11	90	AE2	194	15	FA2	76	15	L2
135	62	S2	181	81	AE2	164	8	FA2	82	18	L2
132	58	S2	181	82	AE2	164	8	FA2	280	6	L2
149	77	S2	163	81	AE2	56	8	FA2	78	39	L2
150	80	S2	178	74	AE2	242	29	FA2	51	41	L2
324	75	S2	348	89	AE2	241	40	FA2	98	26	L2
332	75	S2	348	90	AE2	241	30	FA2	91	27	L2
314	79	S2	26	25	AE2	243	13	FA2	88	25	L2

Supporting Table 1: raw data of structural measurements

Domain A			Domain A			Domain C			Domain A		
313	84	S2	80	38	AE2	72	29	FA2	83	23	L2
154	88	S2	46	39	AE2	318	40	FA2	272	2	L2
335	67	S2	12	86	AE2	243	13	FA2	83	34	L2
338	75	S2	6	82	AE2	333	36	FA2	87	30	L2
329	69	S2	1	67	AE2	230	9	FA2	96	26	L2
176	67	S2	357	73	AE2	243	9	FA2	98	27	L2
321	87	S2	336	65	AE2	230	60	FA2	92	35	L2
329	85	S2	349	86	AE2	240	45	FA2	69	87	L2
300	57	S2	349	62	AE2	225	18	FA2	94	25	L2
328	77	S2	159	82	AE2	240	14	FA2	90	34	L2
328	85	S2	163	78	AE2	293	42	FA2	94	24	L2
322	86	S2	342	84	AE2	339	28	FA2	96	9	L2
316	84	S2	154	76	AE2	351	20	FA2	101	14	L2
318	68	S2	340	88	AE2	329	5	FA2	92	30	L2
324	73	S2	328	67	AE2	346	21	FA2	87	14	L2
325	85	S2	344	84	AE2	77	34	FA2	119	34	L2
328	89	S2	186	84	AE2	269	68	FA2	81	24	L2
152	87	S2	182	78	AE2	267	60	FA2	87	7	L2
306	81	S2	149	80	AE2	295	14	FA2	94	35	L2
323	81	S2	167	82	AE2	101	8	FA2	92	17	L2
166	78	S2	348	86	AE2	290	53	FA2	92	35	L2
171	75	S2	346	80	AE2	101	43	FA2	95	17	L2
346	80	S2	354	79	AE2	238	30	FA2	94	41	L2
176	77	S2	8	81	AE2	47	17	FA2	91	17	L2
160	73	S2	13	86	AE2	194	8	FA2	92	26	L2
149	88	S2	13	85	AE2	194	59	FA2	96	3	L2
148	87	S2	9	66	AE2	197	27	FA2	112	29	L2
164	86	S2	344	72	AE2	237	21	FA2	86	16	L2
191	78	S2	181	86	AE2	122	18	FA2	86	26	L2
170	79	S2	352	86	AE2	124	23	FA2	88	12	L2
178	76	S2	355	83	AE2	19	12	FA2	87	12	L2
182	74	S2	1	85	AE2	13	26	FA2	250	21	L2
185	72	S2	5	88	AE2	20	4	FA2	251	21	L2
180	76	S2	173	88	AE2	19	28	FA2	240	40	L2
191	72	S2	180	90	AE2	8	31	FA2	234	35	L2
177	87	S2	2	87	AE2	47	14	FA2	237	41	L2
346	86	S2	134	73	AE2	59	18	FA2	243	38	L2
340	86	S2	356	87	AE2	35	25	FA2	41	18	L2
318	70	S2	176	85	AE2	57	4	FA2	40	11	L2
308	67	S2	174	81	AE2	126	2	FA2	235	28	L2
292	65	S2	168	81	AE2	248	7	FA2	234	35	L2
292	64	S2	176	84	AE2	11	24	FA2	45	8	L2
279	65	S2	6	83	AE2	90	71	FA3	90	47	L2
317	74	S2	355	86	AE2	129	74	FA3	84	55	L2
348	84	S2	170	84	AE2	87	70	FA3	82	40	L2
311	63	S2	176	86	AE2	86	85	FA3	251	16	L2
319	58	S2	359	70	AE2	120	75	FA3	88	65	L2
333	75	S2	4	76	AE2	93	78	FA3	67	31	L2
330	68	S2	313	13	AE3				68	29	L2

Note, AE corresponds to AP and S3 corresponds to S_{2b}.

4. U-Pb ages of apatite in the western Tauern Window (Eastern Alps): Tracing the onset of collision-related exhumation in the European plate

4.1 Highlights and article information

First U–Pb cooling ages of apatite obtained in the European Alps.

Elongate concentric cooling pattern indicates exhumation by folding and erosion.

Cooling pattern resembles those of geochronometers having lower closure temperatures.

Sample-specific cooling-rates yield 15.3±1.9 K/Myr in the western Tauern Window.

Thermal climax of the Barrovian metamorphism is inferred to occur between 37 and 34 Ma.

Article history: Received 20 November 2014

Received in revised form 2 February 2015

Accepted 12 February 2015

Available online 13 February 2015

Editor: A. Yin

doi:10.1016/j.epsl.2015.02.020

4.2 Keywords

LA-ICP-MS; U-Pb dating of apatite; median ages; student-t test; Tauerncrystallization

4.3 Abstract

We performed U-Pb analyses of zircons and apatites from eighteen samples distributed along three sections crossing the western Tauern Window (Eastern Alps). Zircon analyses yield concordant ages of ~295 Ma dating the Variscan emplacement of the Zentralgneiss batholith. Apatite analyses scatter over a wide age range and show two age clusters. A considerable number of apatite analyses for each sample reflect a relatively uniform cluster of age values varying between ~40-20 Ma. A second cluster reveals age values scattering between ~300-40 Ma. We applied an age extractor algorithm to all apatite analyses of each sample to calculate median ages from the younger age cluster and asymmetric 2σ errors as their uncertainties, which are mostly in the range of 10 %.

These median ages are interpreted to date cooling below ~450-500 °C during Alpine orogeny after the thermal climax of the western Tauern Window. The cooling ages give a consistent picture over the study area of ~31-29 Ma. Along each section younger cooling ages were obtained in the center compared to the margins. In addition, the eastern section shows older cooling ages of ~36-34 Ma whereas the western section younger cooling ages of ~26-25 Ma. Both age trends, (1) younging towards the centers of the sections and (2) younging towards the west across all three section are confirmed by six independent two-sample student-t-tests. Spatially the age pattern resembles those observed from geochronometers having lower closure temperatures (~375-110 °C), that are largely related to doming after Dolomites indentation. Cooling rates of five samples, where additional fission track ages are available, yield uniform result and could be averaged to 15.2±1.5 K/Myr (2σ). By linear extrapolation using the specific cooling rates and the estimated maximum temperature (T_{max}) we obtained a time range of ~38 to 34 Ma, interpreted to date the thermal climax of the Barrovian metamorphism in the western Tauern Window.

4.4 Introduction

Phosphorus is moderately incompatible and generally present in nature as the oxyanion PO_4^{3-}, which forms the common mineral apatite ($Ca_5(PO_4)_3(OH,F,Cl)$). Fluorapatite compared to Chlor- or Hydroxylapatite, is by far the most common member of the apatite family found as accessory phase in many rock types. In most igneous rocks it is a minor but ubiquitous mineral, where it might reach high concentrations in enclaves or cumulates (White, 2005). The presence of apatite in most rocks is due to its low solubility in naturally occurring melts and fluids, and to the restricted ability of common rock-forming minerals to incorporate the amount phosphorus that is present in most rocks into their crystal structure (Piccoli and Candela, 2002).

Apatite crystallization takes place over a wide temperature range in most felsic metaluminous magmatic systems because apatite saturation is achieved relatively early compared to other minerals and its reaction to other phosphate-bearing minerals is sluggish (Wolf and London, 1995). However, most igneous apatites crystallize over a restricted temperature interval of 60-100 °C around the apatite saturation temperature that is usually >680 °C in felsic rocks (Piccoli and Candela, 1994, 2002). The apatite crystal habitus might give some hints of its formation process. According to Höche et al., (2001) needles result from surface-controlled growth at high supersaturation whereas stubby crystals grow at lower degrees of supersaturation under conditions where growth is diffusion-controlled. Apatite needles can precipitate from experiments without a rapid quench, but the proportion of acicular to stubby apatite increases with increasing cooling rate (Wyllie et al., 1962).

Apatites contain a moderately high concentration of lattice-bound U (~5 to 50 ppm), hence they are suitable for U-Th-Pb chronology (e.g., Harrison et al., 2002; Willigers et al., 2002). Generally apatites show no compositional zoning, sometimes micro-inclusions are common, but the U-Pb systematics do not appear to be influenced significantly by these micro-inclusions (Chamberlain and Bowring, 2000).

Apatite is stable at epidote-amphibolite-facies conditions during metamorphism, i.e. at temperatures that are typically higher than the apatite closure temperature for Pb diffusion (Cherniak et al., 1991; Krogstad and Walker, 1994). During cooling apatite is inert to recrystallization and growth before Pb isotopic exchange by thermally enhanced diffusion has ceased. Therefore, apatite U-Pb systematics are controlled by diffusion rather than growth or recrystallization (Willigers et al., 2001). Closure temperatures for Pb diffusion in apatite are 400

°C to 500 °C for typical diffusive diameters and cooling rates based on both experimental and empirical estimates and are valid for both, rapidly and slow cooling regions (Willigers et al., 2001, 2002 and references therein). In hydrothermal systems, apatite growth can occur below its closure temperatures and apatite U-Pb ages may be used to date the timing of fluid flow directly (e.g., Corfu and Stone, 1998).

Willigers et al. (2001) showed that the formerly assumed closure temperature of ~620 °C for U-Pb apatite was overestimated, because K/Ar hornblende ages of the same samples and areas are consistently older. The authors calculated a closure temperature of ~500 °C for U-Pb apatite. Chamberlain and Bowring (2000) showed that apatite is a reliable, mid-range (~450 °C), diffusion-controlled system, suitable for constraining cooling and exhumation histories from both igneous and metamorphic rocks.

Large metamorphic sites, like orogenic domes and ranges, might be affected by poly-phase metamorphism and/or additional poly-phase localized deformation causing map-scale 3D-variations of the cooling pattern. Nowadays dating of metamorphic cooling is ideally achieved by applying multiple geochronometers covering a wide range of closure temperatures to a single sample (e.g., Willigers et al., 2002). If then multi-dating is applied to several samples covering the area of interest a refined picture of the cooling history might be obtained, from whose differential cooling- and exhumation rates might be calculated and structures like folds, shear zones and faults might be detected (e.g., Borsi et al., 1973). The major advantage of this multi-dating approach is to minimize the possibly complex cooling history to the dimension of the hand specimen and, therefore, to calculate sample-specific vertical cooling paths. Spatial corrections of horizontal temperature gradients might be avoided by this approach. Absolute closure temperatures of geochronometers, having large errors (10-20 %), are still debated, depending also on geological factors like fluid infiltration, grain size and cooling rates of the dated sample (Dodsen, 1973). On the contrary, the relative succession of different geochronometers seems to be uniform (e.g. U-Pb zircon, U-Pb monazite, U-Pb titanite, K/Ar amphibole, U-Pb apatite, Rb/Sr white mica, K/Ar white mica, K/Ar biotite, Rb/Sr biotite, K/Ar K-feldspar, ZFT, TFT, AFT). Hence, the relative closure temperatures seem to be consistent and robust (Villa, 1998; Willigers et al., 2001). This strongly suggests that there are consistent systematic differences in the rates at which volume diffusion of radiogenic nuclides occurs through specific mineral phases. In multi-approach studies where cooling from the high temperature range (>400 °C) was sustained, U-Pb cooling ages of monazites are followed by U-Pb cooling ages of apatites and K/Ar cooling ages of hornblendes (Willigers et al., 2001), therefore, the latter geochronometers are appropriate to date the onset of cooling from a Barrovian metamorphism.

There have been many studies dating U-Pb ages of apatite, e.g. based on the conventional TIMS analysis after chemical dissolution (e.g., Oosthuyzen and Burger, 1973), on ion-microprobe using SHRIMP (e.g., Kennedy and Dante, 1997), on non-destructive in situ dating using SIMS where the textural control matters (e.g., Sano et al., 1999), or by LA-ICPMS analyses (e.g., Thomson et al., 2012). These studies have exemplarily shown that U-Pb apatite cooling ages can be obtained by different analytical approaches. The present study applies the unconventional U-Pb apatite geochronometer, used for the first time in the Eastern Alps, to the western Tauern Window. Since the closure temperature of U-Pb apatite is generally higher compared to available cooling ages of the working area (cf. compilation of Luth and Willingshofer, 2008; Rosenberg and Berger, 2009; Bertrand et al., 2014) they might yield new time constraints for the reconstruction of the tectono-metamorphic evolution of the western Tauern Window.

4.5 Geological setting

The Tauern Window is a tectonic window exposing lower plate (European- and ocean-derived) units of the Alpine orogen surrounded by upper plate (Adria-derived) rocks (Fig. 1a). The European-derived rocks (Fig. 1a, Venediger Duplex) consist of granites to tonalities that are summarized as Zentralgneiss batholith (Finger et al., 1993, 1997) and its pre-magmatic country rocks. The formation, the shape and the structure of the Tauern Window is largely controlled by Dolomites indentation (Cornelius, 1940). The window coincides with an arcuate dome structure that can be subdivided into a western, a central and an eastern sub-dome (Schmid et al., 2013). These sub-domes have a common i.e., doming, and a different i.e., tight folding and shear zone localization, exhumation history. The central and eastern sub-domes are characterized by broad and open folds that refold an early Alpine foliation caused by nappe stacking (Schmid et al., 2013). There, the main foliations strike concentrically and are rather gently dipping (Schneider et al., 2014). Localized mylonitic deformation is rare in the eastern and central sub-domes and if present it only occurs marginally (Scharf et al., 2013). The western sub-dome is characterized by a NE-striking transpressive belt of tight, upright folds associated with a network of sinistral shear zones (Fig. 1a, Schneider et al., 2014). These structures connect two major Alpine fault systems, the Giudicarie Belt and the SEMP Fault, translating Dolomites indentation (Rosenberg et al., 2004) into lateral extrusion (Ratschbacher et al., 1991). Therefore, the western sub-dome was affected longer and more intensely by shortening compared to the eastern and central sub-domes which were decoupled by the restraining bend and escaped tectonically eastward (Schneider et al., 2014).

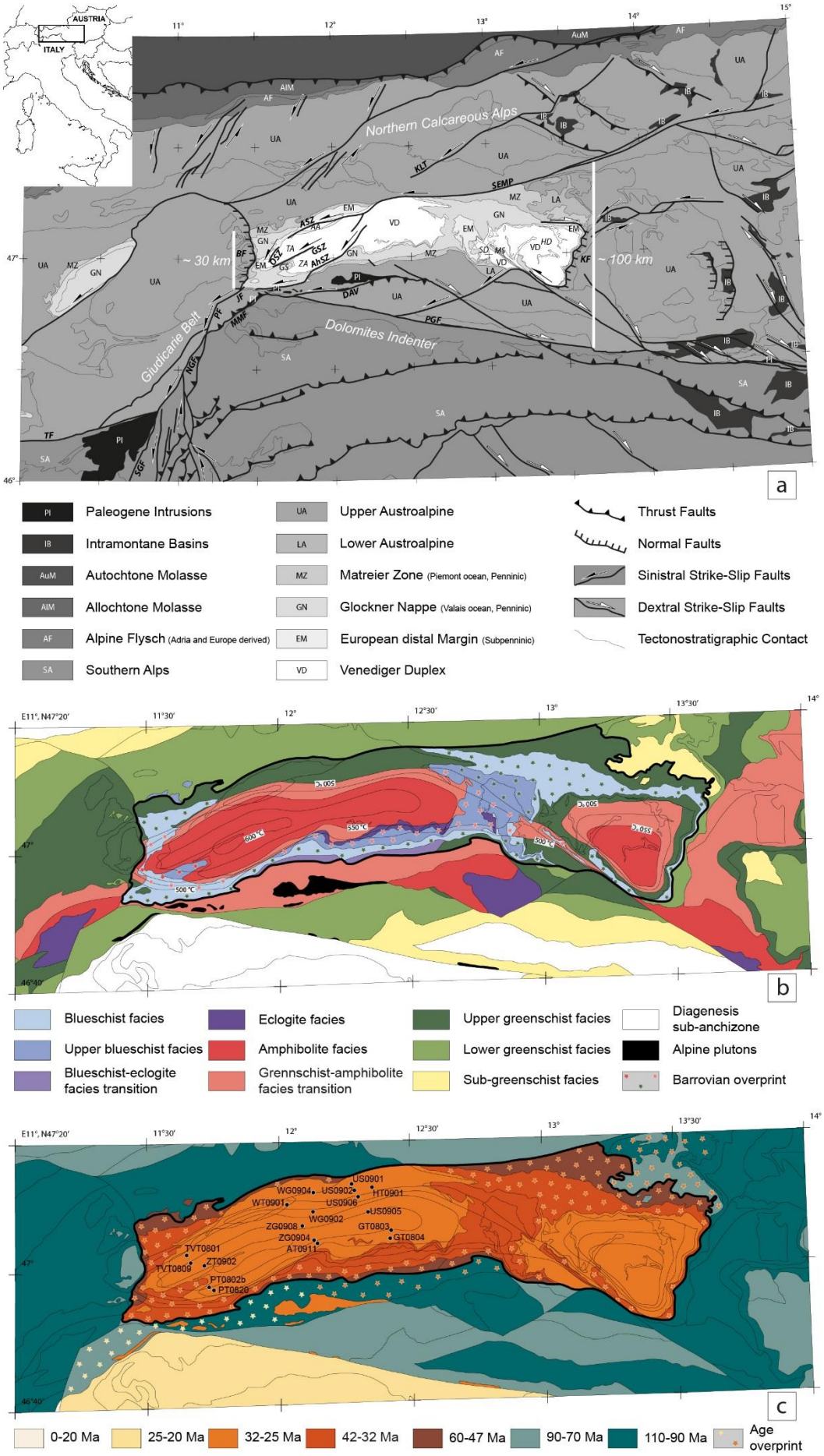
AUSTRIA
ITALY
Northern Calcareous Alps
Giudicarie Belt
Dolomites Indenter
~ 30 km
~ 100 km
a
Paleogene Intrusions
Intramontane Basins
Autochtone Molasse
Allochtone Molasse
Alpine Flysch (Adria and Europe derived)
Southern Alps
Upper Austroalpine
Lower Austroalpine
Matreier Zone (Piemont ocean, Penninic)
Glockner Nappe (Valais ocean, Penninic)
European distal Margin (Subpenninic)
Venediger Duplex
Thrust Faults
Normal Faults
Sinistral Strike-Slip Faults
Dextral Strike-Slip Faults
Tectonostratigraphic Contact
b
Blueschist facies
Upper blueschist facies
Blueschist-eclogite facies transition
Eclogite facies
Amphibolite facies
Grennschist-amphibolite facies transition
Upper greenschist facies
Lower greenschist facies
Sub-greenschist facies
Diagenesis sub-anchizone
Alpine plutons
Barrovian overprint
c
0-20 Ma
25-20 Ma
32-25 Ma
42-32 Ma
60-47 Ma
90-70 Ma
110-90 Ma
Age overprint

Figure 1a: *Simplified tectonostratigraphic map of the Tauern Window and surrounding units, modified after (Bousquet et al., 2012a). Highlighted are the discussed fault systems active in Cenozoic time. AhSZ=Ahrntal Shear Zone, ASZ=Ahorn Shear Zone, BF=Brenner Fault, DAV=Defereggen-Antholz-Vals Fault, GSZ=Greiner Shear Zone, JF=Jaufen Fault, KLT=Königssee-Lammertal-Traunsee Fault, KF=Katschberg Fault, MM=Meran-Mauls Fault, NFG=North Giudicarie Fault, OSZ=Olperer Shear Zone, PF=Passeier Fault, PGF=Pustertal-Gailtal Fault, SEMP=Salzach-Ennstal-Mariazell-Puchberg Fault, SGF=South Giudicarie, Fault TF=Tonale Fault. Fold structures are AA=Ahorn Antiform, GS=Greiner Synform, HD=Hochalm Dome, MS=Mallnitz Synform, SD=Sonnblick Dome, TA=Tuxer Antiform, ZA=Zillertaler Antiform.* ***b:*** *Simplified metamorphic map of the Tauern Window and surrounding Austroalpine units, modified after (Bousquet et al., 2012b).* ***c:*** *Simplified map showing the ages of the dominant metamorphic event in the Tauern Window and surrounding Austroalpine units, modified after (Bousquet et al., 2012b). Metamorphic isotherms of Fig. 1b are also included. Sample localities (black dots) and names are given.*

The eastward escaping orogenic wedge, located between the Pustertal-Gailtal and the SEMP faults (Fig. 1a), has its smallest width at the northern tip of the Dolomites Indenter (Ratschbacher et al., 1991). By assuming a laterally constant amount of shortening, the relative amount of shortening per crustal width is maximum in the west and decreases eastward (Ratschbacher et al., 1991, Fig. 1a). Some authors argue for clockwise rotation of the Dolomites Indenter (Laubscher et al., 1996) what would additionally increase the differential shortening in the west compared to the east.

The Zentralgneiss batholith has Early Permian, post-Variscan zircon U-Pb crystallization ages (Finger et al., 1993, 1997; Veselá et al., 2011) and are overprinted by two Alpine metamorphic events affecting the rocks of the Tauern Window (Fig. 1b). Prior to collision the ocean-derived rocks (Penninic) once separating Adria from Europe were subducted and underwent in parts blueschist- to eclogite-facies metamorphism. Subduction-related metamorphism in the ocean-derived rocks is mostly in the range of 0.9-1.3 GPa and 350-550 °C (Selverstone 1985, Bousquet at al., 2008). Remnants of the pressure climax (1.9-2.6 GPa, 550-590 °C) can be found in the Eclogite Zone in the southern central Tauern Window (Spear and Franz, 1986; Miller et al., 2007; Smye et al., 2011). Preservation and exhumation was enhanced by isothermal decompression, eclogite facies sinistral shear zones and by strong kinematic partitioning between eclogites and metasediments (Spear and Franz, 1986; Ratschbacher et al., 2004; Kurz et al., 2008; Neufeld et al., 2008; Smye et al., 2011).

During collision of Adria and Europe nappes stacked onto each other, imbrications of the Venediger duplex caused continental buckling (Schmid et al., 2013). Radioactive decay enhanced the heat production in the Venediger duplex, the so called "Tauerncrystallization" (Sander 1911, 1921) lead to greenschist- and amphibolite-facies (Barrovian) overprint of the entire dome, which is the dominant metamorphic feature in the Tauern Window (Bousquet et al., 2008). Metamorphic isograds (Fig. 1b) based on oxygen isotope thermometry in the western TW (Hoernes and Friedrichsen, 1974) show an ENE-WSW elongate, concentric pattern with decreasing temperatures from the core (630 °C) to the margins (405 °C). These isogrades strike sub-parallel to those deduced by mapping of garnet (Höck, 1980; Droop, 1981; Selverstone 1985) and biotite occurrences, and the anorthite component in plagioclase (Höck, 1980). The isogrades point to higher, amphibolite-facies conditions in the center, also supported by kyanite-, staurolite-, and silimanite occurrences, and lower, greenschist-facies conditions at the margins of the western sub-dome (Fig. 1b, Grundmann and Morteani, 1985). The peak metamorphic area coincides with the hinge of the Tauern Window that experienced a rather simple P-T evolution compared to the Lepontine dome in the western Alps (Bousquet et al., 2008).

The timing of high-pressure metamorphism is controversially, some authors argue for Eocene timing ~42-36 Ma (e.g. Zimmermann et al., 1994; Ratschbacher et al., 2004, Kurz et al., 2008, Smye et al., 2011 Fig. 1c) others for Oligocene timing (Glodny et al., 2005, Nagel et al., 2013). Kurz et al. 2008 argue for eclogite-facies strike-slip shear at ~32 Ma causing isotopic resetting, which is temporarily in agreement with the oldest deformation ages of strike-slip shear zones in the

western Tauern Window (Glodny et al., 2008; Pollington and Baxter, 2010; Schneider et al., 2013). The timing of Barrovian overprint is also debated, some authors argue for thermal climax at ~35 Ma (Lambert, 1970; Selverstone, 1985; Ratschbacher et al., 2004) others at 32-27 Ma (Cliff et al., 1985; Grundmann and Morteani, 1985; von Blanckenburg and Villa, 1988; von Blanckenburg et al., 1989; Christensen et al., 1994; Inger and Cliff, 1994; Zimmermann et al., 1994; Glodny et al., 2005; Gleißner et al., 2007). Several age data are available pointing to mineral formation (e.g. white mica, garnet, amphibole) at ~35 Ma (Lambert et al., 1970; Raith et al., 1987; von Blanckenburg and Villa 1988, Christensen et al., 1994; Dingledey et al., 1997) at different localities in the ocean-derived rocks, but the assignment of these age data to either high-pressure metamorphism or thermal climax of Barrovian metamorphism remains difficult for several reasons (e.g. excess argon, deformational resetting, formation vs. cooling ages). One phenomenological contradiction originates from P-T-t evolutions in the gneiss domes of the western Alps, where the high-pressure metamorphism can be temporarily differentiated from the thermal climax of the Barrovian metamorphism (cf. Bousquet at al., 2008). This differentiation is less pronounced in the Eastern Alps where the high-pressure metamorphism in the Eclogite zone might be contemporaneous to the thermal climax of the Barrovian metamorphism in the Venediger duplex (Bousquet at al., 2008; Glodny et al., 2008; Smye et al., 2011).

Timing of Dolomites indentation is based on deformation age data of faults from the Giudicarie Belt in Oligo-Miocene (~32-14 Ma) time. Deformation ages were obtained of thrust-related mylonites and pseudotachylites along the North Giudicarie and Meran-Mauls faults, of pre-kinematic zircons of sinistrally and dextrally sheared dykes along the Jaufen Fault predated shearing, of pseudotachylites and syn-kinematic minerals of mylonites from the Jaufen Fault, and of a pseudotachylite from the Passeier Fault (Müller et al., 2001). The longevity of sinistral shear zones forming a restraining bend in the western Tauern Window (Schneider et al., 2014) yield also Oligo-Miocene (~33-7 Ma) deformation ages from syn-kinematic minerals (Glodny et al., 2008; Pollington and Baxter, 2010; Schneider et al., 2013). The SEMP Fault as a main fault accommodating the lateral extrusion was also active in Oligo-Miocene time (~35-17 Ma) constrained by syn-kinematic mineral ages (Urbanek et al., 2002; Cole et al., 2007) and syn-tectonic sediments in the Hieflau basin (Peresson and Decker, 1997).

Oligo-Miocene cooling ages of the Tauern Window indicate high spatial variability for several geochronometers. Rb/Sr white mica ages vary between 32 and 16 Ma (Satir, 1975; Satir and Morteani, 1982; von Blanckenburg et al., 1989). K/Ar white mica ages vary between 32 and 14 Ma (Satir, 1975; Raith et al., 1978; Thöni, 1980; Satir and Friedrichsen, 1986; von Blanckenburg et al., 1989). K/Ar biotite ages vary between 22 and 14 Ma (Satir, 1975; Raith et al., 1978; von Blanckenburg et al., 1989; Most, 2003). Rb/Sr biotite ages vary between 17 and 12 Ma (Satir, 1975; Borsi et al., 1978; von Blanckenburg et al., 1989). ZFT ages vary between 22 and 6 Ma (Fügenschuh et al., 1997; Most, 2003; Bertrand et al., 2014). AFT ages vary between 14 and 5 Ma (Grundmann and Morteani, 1985; Fügenschuh et al., 1997; Most, 2003; Bertrand et al., 2014).

Cooling ages of the Tauern Window show isochron contours with similar trends as the metamorphic isograds, i.e. an ENE to SE striking, elongate concentric cooling pattern (see compilations of Luth and Willingshofer, 2008; Rosenberg and Berger, 2009; Bertrand et al., 2014). These data show that the eastern sub-dome cooled below 375 °C earlier than the western sub-dome, the isochrons of the eastern and western sub-domes follow a concentric, elongate trend, sub-parallel and symmetric about the hinge of the dome, respectively. All chronometers, indicate younger ages towards the hinge of the dome. Additionally, the western Tauern Window shows a westward younging trend of cooling ages. (Luth and Willingshofer, 2008). Recent, more data-rich studies indicate that for the low-temperature geochronometers (ZFT and AFT) a general westward younging trend affecting the entire western sub-dome is controversial (Bertrand et al., 2014). Instead the authors point to a

marginally younging along the extensional shear zones, the Brenner Fault, at the western and eastern ends of the Tauern Window.

The relationship between tectonic structures and age pattern for the higher temperature (>375 °C) history of the dome is more difficult to constrain because the too sparse age data derived from higher temperature geochronometers (e.g. Ar/Ar of amphibole ages, von Blanckenburg et al., 1989) do not allow the construction of isochrons and had to be corrected for excess argon, significantly. In addition, the interpretation of white mica ages is still controversial, recrystallization of white micas can occur even below its closure temperature (K/Ar and Rb/Sr). Numerous K/Ar and Rb/Sr white mica ages in the western sub-dome are younger than nearby K/Ar and Rb/Sr biotite ages, although the closure temperature of the former is generally regarded as higher (Raith et al. 1978). The map-scale restraining bend within the western sub-dome (Fig. 1a, Schneider et al., 2014) caused axial-plane foliations and shear zones that consist of phengite, whereas the undeformed Zentralgneiss is usually free of white mica (Schneider et al., 2013). Therefore, white mica cooling ages should be interpreted with caution. Hence, the high temperature history between the thermal climax (~630 °C, Hoernes and Friedrichsen, 1974) and the closure temperature (~375 °C) of the K/Ar muscovite and $^{40}Ar/^{39}Ar$ biotite chronometers is only punctually constrained yet (von Blanckenburg et al., 1989; Zimmermann et al., 1994; Ratschbacher et al., 2004; Kurz et al., 2008).

4.6 Sample description

Figure 2a: *Field photo of the granodioritic Zentralgneiss batholiths shows the typical magmatic paragenesis of qtz, K-fps, plg and bt also a small autolite is cognizable at the lower right corner. The rocks are not or weakly foliated. Coin for scale.* ***b:*** *Field photo of the Zentralgneiss batholiths shows parts of the magmatic inventory centimeter- to meter-scale xenolites are a common feature of the granodioritic gneisses. Hammer for scale.*

We collected eighteen gneiss-samples that were almost undeformed with respect to Alpine folding and shearing (Figs. 2a and b) for U-Th-Pb dating of apatites (e.g., Thomson et al., 2012) and zircons (e.g., Frei and Gerdes, 2009). Sixteen samples are orthogneisses, sample GT0803 is a paragneiss and GT0804 is an aplitic dike crosscutting these paragneisses. The Barrovian overprint of the Tauerncrystallization in these samples is manifested by amphibolite- to greenschist-facies mineral reactions and high-grade deformation fabrics (Figs. 3a-l). Observed amphibolite-facies minerals are staurolite, garnet, and epidote (Figs. 3a, h, i, j, k, and l). Common amphibolite- and greenschist-facies mineral reactions are saussuritization of plagioclase, sericitization of K-feldspar, plagioclase breakdown to clinozoizite, allanite breakdown to epidote, titanite formation along kinks and rims

of biotite, and biotite breakdown to chlorite (Figs. 3a, b, d, e, g, j, and l). Fabrics like chessboard sub-grains in quartz (Kruhl, 1996), myrmekite formation along rims of K-feldspar, and core-and-mantle-structures of K-feldspar (Figs. 3b, c, and f) point to high-grade deformation. Thin sections show that the apatites are mostly located within biotites (Figs. 4a, b, d, g, h, j, k, and l), within the matrix (Figs. 4c, e, and i) but also within plagioclase (Fig. 4f). In most cases the crystals are stubby (Figs. 4a, b, c, d, e, f, g, h, i, j, k, and l) and rarely acicular (Figs. 4a and l). In some cases the euhedral hexagonal shape of the crystals is cognizable (Figs. 4b, d, and i), but mostly apatites are subhedral and round having axial ratios of 1:1 to 1:3 (Figs. 4a, b, c, d, e, f, g, h, j, k, and l) sometimes forming clusters (Fig. 4c). Therefore, we argue apatites are magmatic minerals formed during Variscan pluton emplacement.

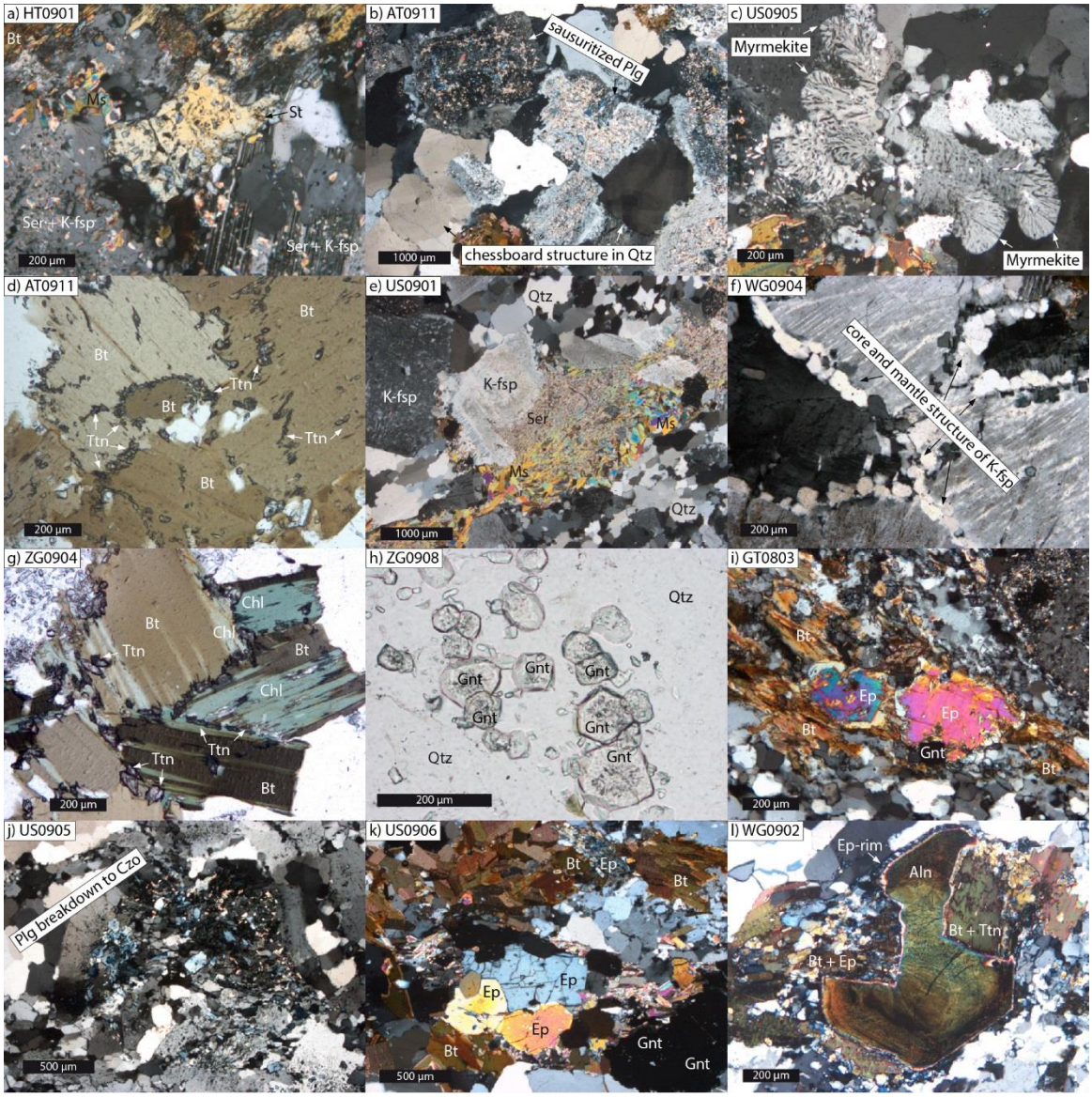

Figure 3: *Microscope photos showing different minerals and parageneses indicating amphibolite- and greenschist-facies metamorphism of some samples. Cross-polarized light if not indicated differently.* ***a:*** *In the center a stramineous staurolite grain having a poicilitic texture is shown. Also visible are sericitized K-feldspar, muscovite, and biotite.* ***b:*** *Three larger and one smaller saussuritized plagioclase grains are shown in the center. At the lower right and lower left margin large quartz grains show chess board structures.* ***c:*** *Dynamically recrystallized K-feldspar forming large myrmekites* ***d:*** *Plane-polarized light. Aggregate of biotite with titanite formed along its rims and fractures.* ***e:*** *Breakdown reaction of K-feldspar to sericite and*

muscovite is shown. ***f:*** *Large K-feldspar grains show sub-grain rotation recrystallization along their margins forming core-and-mantle-structures.* ***g:*** *Plane-polarized light. Aggregate of biotite intercalated with chlorite, also with titanite formed along its rims and fractures.* ***h:*** *Plane-polarized light. Aggregate of euhedral light pink garnet grains are shown that have inclusions in their cores.* ***i:*** *Paragenesis of biotite, epidote, and garnet is shown.* ***j:*** *Remnant of plagioclase grain that was replaced by clinozoizite is cognizable.* ***k:*** *Paragenesis of biotite, epidote, and garnet is shown.* ***l:*** *Large magmatic allanite grain that is partly replaced by biotite and epidote is shown.*

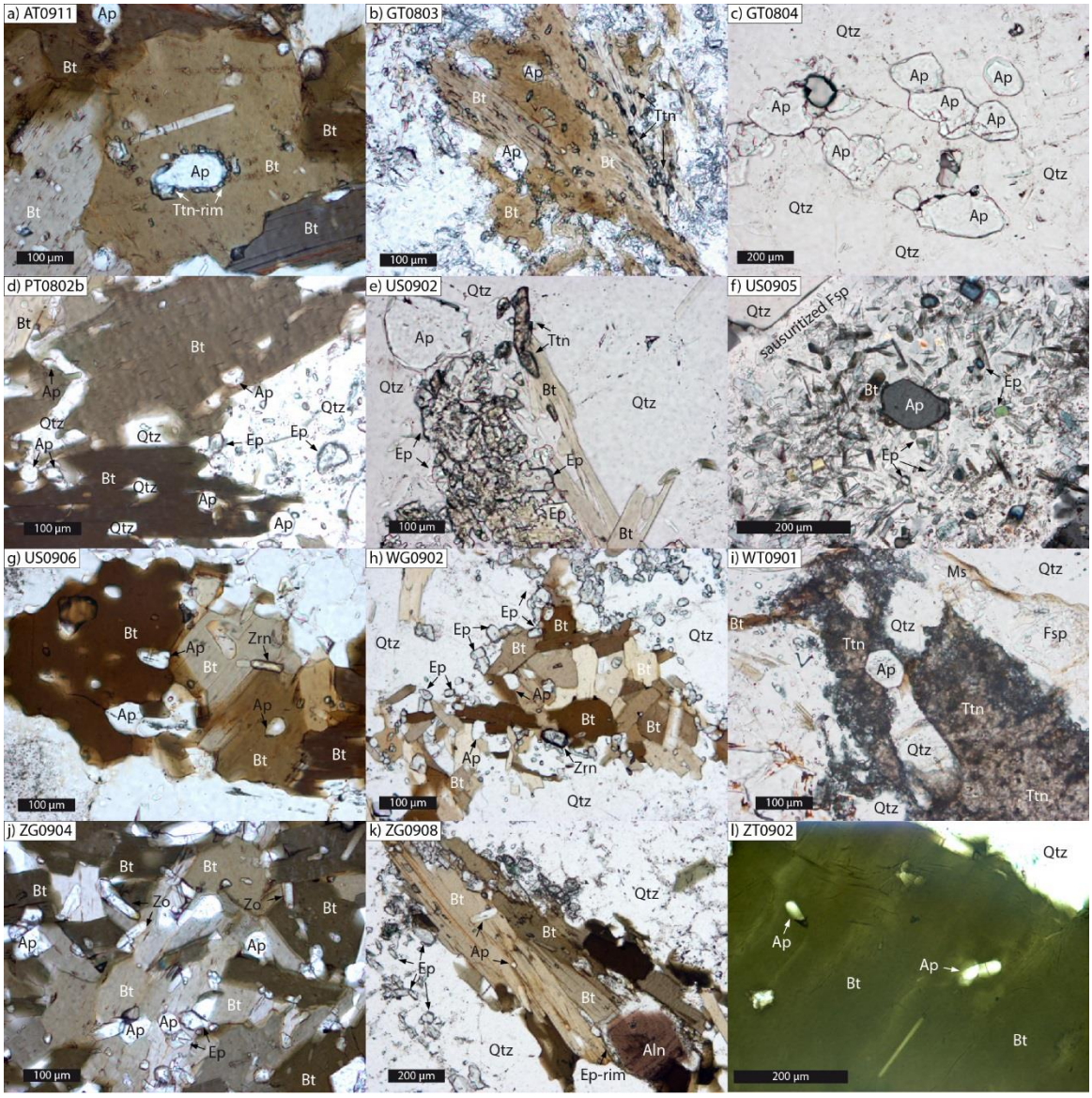

Figure 4: *Microscope photos showing plane-polarized light if not indicated differently,* ***a:*** *Rounded apatite inclusion in biotite with titanite crystals at the rim. Note acicular crystal in the center.* ***b, d, g, h, j, k, l:*** *Stubby apatite crystals within biotite.* ***a, j, l:*** *Note acicular crystals.* ***c:*** *Aggregate of stubby apatite grains within quartz matrix.* ***e:*** *Stubby apatite grains within quartz matrix.* ***f:*** *Crossed-polarized light. Stubby apatite within K-feldspar crystal.* ***i:*** *Euhedral apatite crystal within titanite aggregate.*

4.7 Methods

Apatites and zircons were extracted from fresh and crushed 2 to 4 kg gneiss-samples by means of standard grain-size, magnetic and density separation. Heavy minerals from the grain-size fraction 50-125 µm were concentrated using two heavy liquids (bromoform and diiodomethane). Suitable grains (zircons and apatites) for U-Th-Pb dating were cleaned, hand-picked, mounted in epoxy resin and polished for laser treatment.

Uranium, thorium and lead isotope analyses of zircons were performed by laser ablation (LA) at Central Analytical Facilities (CAF), Stellenbosch, South Africa using a New Wave ® 213 nm ultra-violet (UV) phase laser connected to a ThermoFischer Scientific ® Element 2 high-resolution sector-field inductively-coupled-plasma mass-spectrometer (HR-SF-ICP-MS). Uranium, thorium and lead isotope analyses of apatites were carried out at the Goethe University of Frankfurt, Germany (cf. Millionig et al., 2012). The LA-analyses were performed with a ThermoFischer Scientific ® Element 2 SF-ICP-MS coupled to a Resolution M-50 (Resonetics ®) 193 nm ArF excimer laser (ComprexPro 102, Coherent) system. Laser spot sizes for zircons, apatites, and for standard grains were kept relatively constant in the range of 50-80 µm to enhance comparability of the analyzed grains. Zircon data were acquired on five subsequent days and are listed in supplementary table 1. Apatite data were acquired on three subsequent days and are listed in supplementary table 2.

4.8 Theory and Calculations

We applied accurate and precise U–Pb age dating of zircons by LA-SF-ICP-MS following the method of Frei and Gerdes (2009), which involves: matrix-matched external standardization by standard-sample bracketing using the GJ-1 zircon reference standard (Jackson et al., 2004); careful matching of ablation conditions between standards and samples (e.g., Tiepolo, 2003); application of a purpose build low-volume ablation cell; use of He as carrier gas in order to stabilize the ablation signal and suppress U-Pb fractionation during ablation (e.g., Jackson et al., 2004); correction of the time-dependent within-analysis U-Pb fraction using the intercept method (e.g., Sylvester and Ghaderi, 1997; Košler and Sylvester, 2003).

To verify accuracy and reproducibility of zircon analyses we performed twenty-five analyses of the Plesovice standard, that yield a concordia age of 339.3±2.3 Ma, MSWD=0.057 and a probability=0.81 of concordance. Zircon U-Pb data are majoritarian concordant, therefore the metric applied in this study is the conventional 2D $^{206}Pb/^{238}U$ vs. $^{207}Pb/^{235}U$ Wetherill concordia using ISOPLOT (Ludwig, 1998) and the uncertainties of ^{235}U and ^{238}U decay constants (Steiger and Jäger, 1977) are acknowledged.

The raw data of the apatite analyses were corrected offline for background signal, common Pb, laser-induced element fractionation, instrument mass discrimination, and time-dependent elemental fractionation of Pb-U using an in-house MS Excel spreadsheet (Gerdes and Zeh, 2006, 2009). A common-Pb correction based on the interference and background-corrected ^{204}Pb signal and a model Pb composition (Stacy and Kramers, 1975) was carried out. The ^{204}Pb content for each ratio was determined in three different ways. Wherever possible it was estimated by subtracting the average mass 204 signal of the background, which mostly results from ^{204}Hg in the carrier gas (ca. 1000–1500 cps), from the mass 204 signal during sample ablation. Due to the high Hg background this method results in rather high detection limits (e.g., about 200 cps) for the ^{204}Pb and yields unsatisfactory results for analyses with lower radiogenic Pb (e.g., ^{206}Pb $<4\times10^5$ cps). For analysis

with Th/U <0.5 we therefore used the ^{208}Pb signal to determine the ^{204}Pb content by subtracting the radiogenic ^{208}Pb, estimated from the Th signal, and the $^{206}Pb/^{238}U$ age of the analysis. For minerals <100 Ma with high Th/U (>3) the ^{204}Pb content is estimated from the non-radiogenic ^{207}Pb, calculated from the $^{206}Pb/^{238}U$ (or $^{208}Pb/^{232}Th$) age and the ^{206}Pb signal assuming concordance of the U–Th–Pb system.

One in-house (Griedel) and two international (Plesovice and 91500) zircon age standards were analyzed during apatite analyses. Fifteen analyses of the Pleisovice standard yield a concordia age of 339.4±1.7 Ma, MSWD=2.0 (of concordance) and probability=0.16 (of concordance). Fifteen analyses of the Griedel standard yield a concordia age of 26.21±0.29 Ma, MSWD=2.5 (of concordance) and probability=0.11 (of concordance). Sixteen analyses of standard 91500 yield a concordia age of 1061.9±4.1 Ma, MSWD=4.9 (of concordance) and probability=0.027 (of concordance). Reported uncertainties (2σ) of the $^{206}Pb/^{238}U$ ratio during apatite analyses were propagated by quadratic addition of the external reproducibility (2 SE; standard error) obtained from the standard zircon GJ-1 (n=12; 2σ ~2.8 %) during the analytical session and the within-run precision of each analysis (2σ).

Apatite U-Pb data have commonly low U concentrations, in our samples too low to calculate proper $^{207}Pb/^{235}U$ ages and therefore concordia ages. Hence, the metric applied in this study is the TuffZirc age extractor, an ISOPLOT algorithm (originally based on the TuffZirc algorithm by Ludwig and Mundil, 2002). This algorithm implements a mathematically based approach on the loss and inheritance of Pb to reject age values affected by isotopic disturbance. It calculates a median age of the extracted age cluster that is characterized by a high-frequency age value, interpreted as true age, and its relatively conservative and asymmetric error as age uncertainty (Ludwig, 2009). It is suggested by Ludwig (2009) to include 10 or more grains within the process. This ISOPLOT algorithm is also applicable for minerals that show age variability influenced by Pb-loss and age resetting due to geological processes.

4.9 Results and Discussion

U-Pb results of zircons of sixteen samples are presented as eleven concordia age plots and five discordia plots in (Figs. 5a-p). Zircon ages are shown as light grey, open error ellipses and the calculated concordia ages are given as black and filled (dark gray) error ellipses. The sample names, the numbers of analyzed zircons and the numbers of analyses used for concordia age calculation are given in the upper left boxes of the diagrams (Figs. 5b, c, d, e, f, h, I, j, k, l, n, and o). The concordia ages, the MSWD and probabilities of concordance are given in the lower right boxes. The obtained discordiae were anchored to the origin since in all cases the discordia lower intercepts coincide with it. The age of the discordia upper intercepts and the MSWD are given in the lower right boxes (Figs. 5a, g, h, m, and p).

The concentrations of U (ppm), Pb (ppm), the element ratio Th/U, the percentage of common Pb on the base of ^{206}Pb, the isotopic ratios $^{207}Pb/^{235}U$, $^{206}Pb/^{238}U$, $^{207}Pb/^{206}Pb$, their percentage 2σ errors, the $^{207}Pb/^{235}U$-$^{206}Pb/^{238}U$ error correlation (rho), the $^{207}Pb/^{206}Pb$ ratio, its percentage error, and the $^{207}Pb/^{235}U$, $^{206}Pb/^{238}U$, $^{207}Pb/^{206}Pb$ ages plus their absolute 2σ error of each zircon analysis are given in supplementary table 1. For each rock sample several analyses (14-25) were performed that are given in one block and ordered in ascending $^{206}Pb/^{238}U$ age values. Those age values that were taken into account for concordia age calculation are indicated with an asterisk (*) in the supplementary table 2. For each sample block the calculated concordia age (or discordia upper intercept), its 2σ error, the MSWD and the probability of concordance for the coherent group is given in the heading. The $^{206}Pb/^{238}U$ and the $^{207}Pb/^{235}U$ ratios yield similar precisions of 4.7 % in average (1.3-26.0 %).

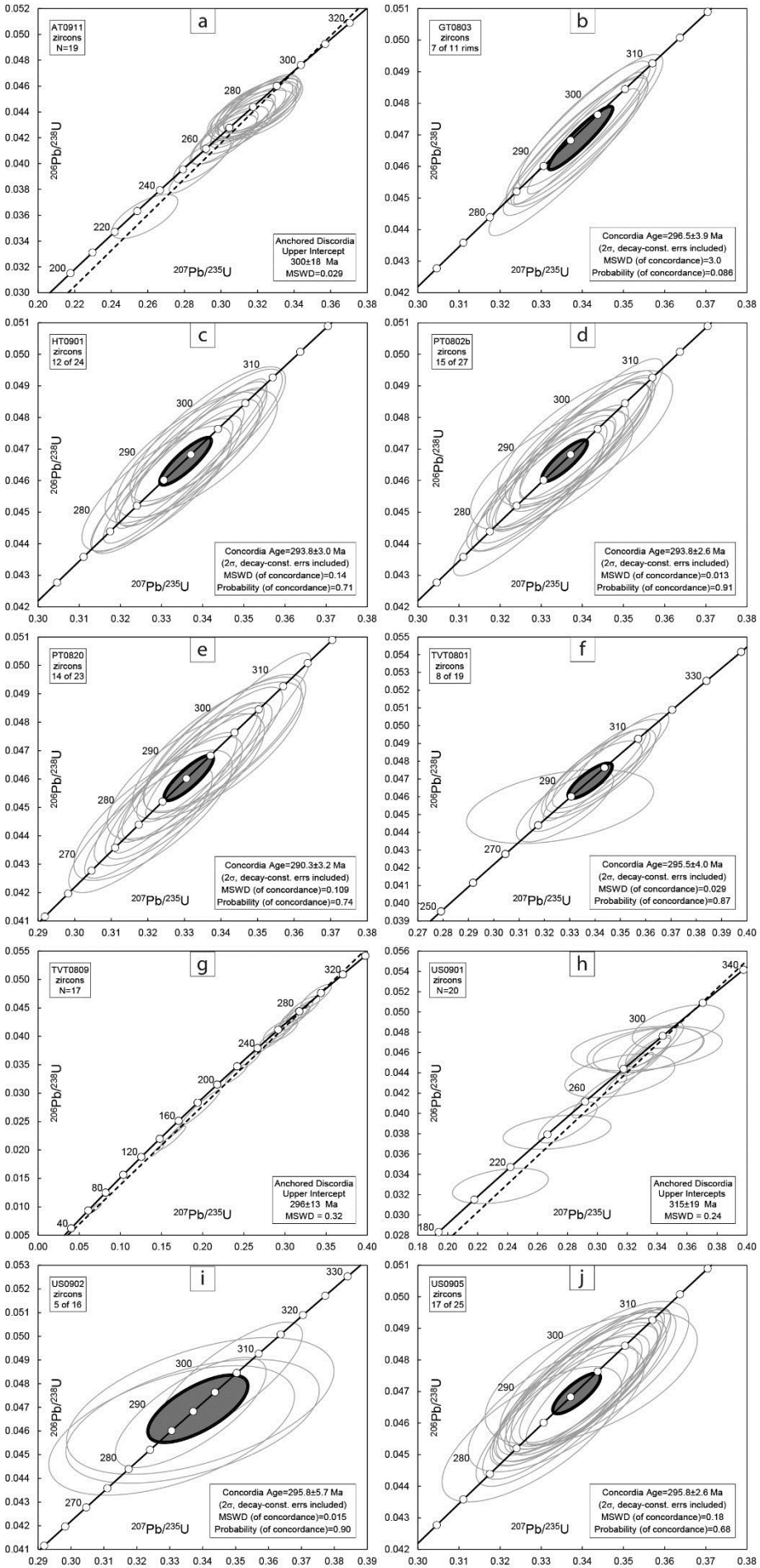
a
AT0911
zircons
N=19
Anchored Discordia
Upper Intercept
300±18 Ma
MSWD=0.029
b
GT0803
zircons
7 of 11 rims
Concordia Age=296.5±3.9 Ma
(2σ, decay-const. errs included)
MSWD (of concordance)=3.0
Probability (of concordance)=0.086
c
HT0901
zircons
12 of 24
Concordia Age=293.8±3.0 Ma
(2σ, decay-const. errs included)
MSWD (of concordance)=0.14
Probability (of concordance)=0.71
d
PT0802b
zircons
15 of 27
Concordia Age=293.8±2.6 Ma
(2σ, decay-const. errs included)
MSWD (of concordance)=0.013
Probability (of concordance)=0.91
e
PT0820
zircons
14 of 23
Concordia Age=290.3±3.2 Ma
(2σ, decay-const. errs included)
MSWD (of concordance)=0.109
Probability (of concordance)=0.74
f
TVT0801
zircons
8 of 19
Concordia Age=295.5±4.0 Ma
(2σ, decay-const. errs included)
MSWD (of concordance)=0.029
Probability (of concordance)=0.87
g
TVT0809
zircons
N=17
Anchored Discordia
Upper Intercept
296±13 Ma
MSWD = 0.32
h
US0901
zircons
N=20
Anchored Discordia
Upper Intercepts
315±19 Ma
MSWD = 0.24
i
US0902
zircons
5 of 16
Concordia Age=295.8±5.7 Ma
(2σ, decay-const. errs included)
MSWD (of concordance)=0.015
Probability (of concordance)=0.90
j
US0905
zircons
17 of 25
Concordia Age=295.8±2.6 Ma
(2σ, decay-const. errs included)
MSWD (of concordance)=0.18
Probability (of concordance)=0.68
206Pb/238U
207Pb/235U

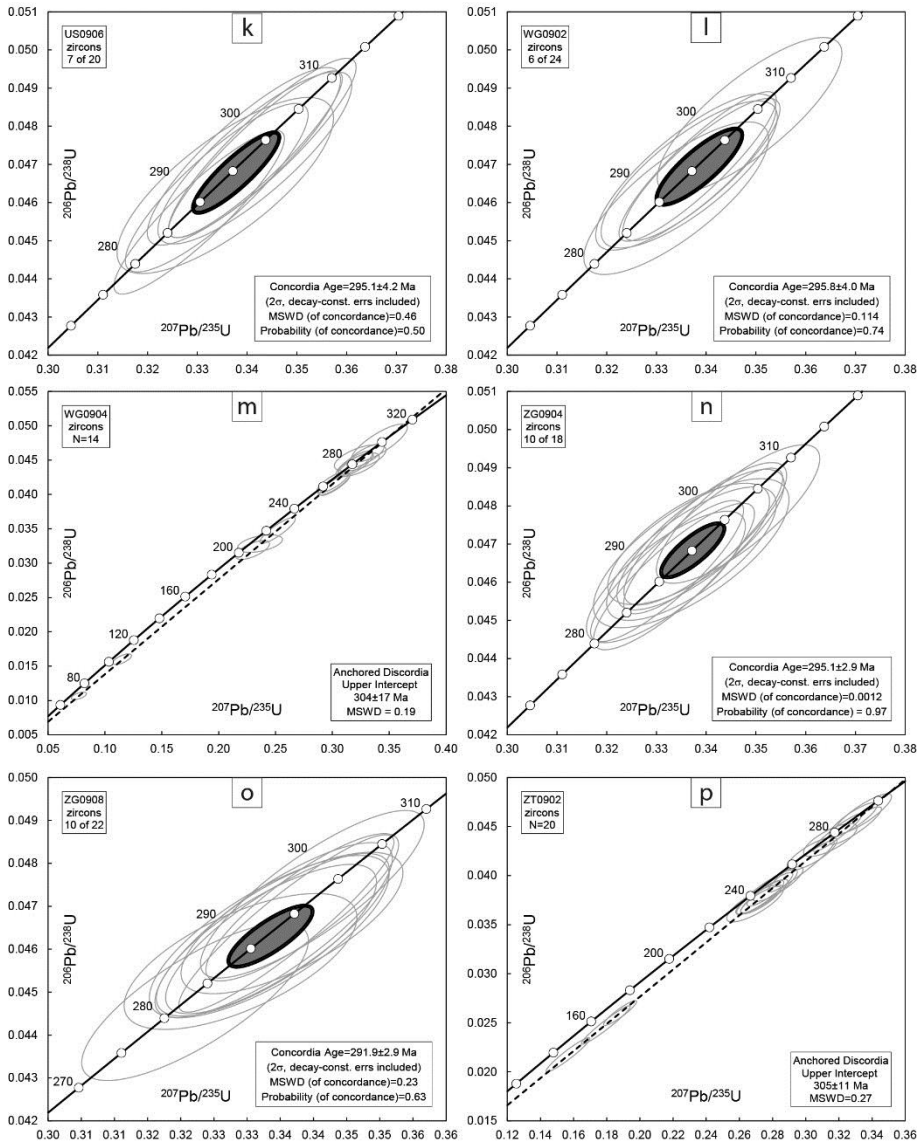

Figure 5a, g, h, m, p: *$^{206}Pb/^{238}U$ vs. $^{207}Pb/^{235}U$ discordia plots of zircon analyses showing the upper intercept, the lower intercept is anchored to the origin. Sample names and number of analyses are given in the upper left boxes. Discordia ages of the upper intercept and the MSWD are given in the lower right boxes.* ***b, c, d, e, f, h, i, j, k, l, n, o:*** *$^{206}Pb/^{238}U$ vs. $^{207}Pb/^{235}U$ concordia plots of zircon analyses, light grey and open circles indicate single measurements and dark grey filled circles indicate concordia ages. In the upper left box the names, the number of performed analyses, and the number of analyses used for the concordia plot is given. Excluded from concordia plots are analyses of zircon cores, analyses yielding inherited concordant age values or discordant age values. All the excluded analyses are listed in supplementary table 1. Concordia age together with its 2σ errors, the MSWDs and probabilities of concordance are given in the lower right boxes.*

U-Pb results of apatites of sixteen samples are presented as median age plots in (Figs. 6a-p). The vertical bars represent the 2σ errors of the apatite analyses ordered in descending age values. The black colored analyses were taken into account for median age calculation. Light gray and dark gray colored analyses were excluded by the ISOPLOT algorithm because of their large errors and the low frequency of their age values, respectively. In two cases (TVT0801 and ZG0804) the median age of the younger cluster was obtained in a second iterative stage. For both samples the five oldest apparent ages of single analyses were excluded during age calculation. Note that for sample PT0802b only the youngest age value was interpreted in the context of the two neighboring samples TVT0809 and ZT0902 to be representative (Fig. 6e). Therefore it is marked with an asterisk (*) in the text.

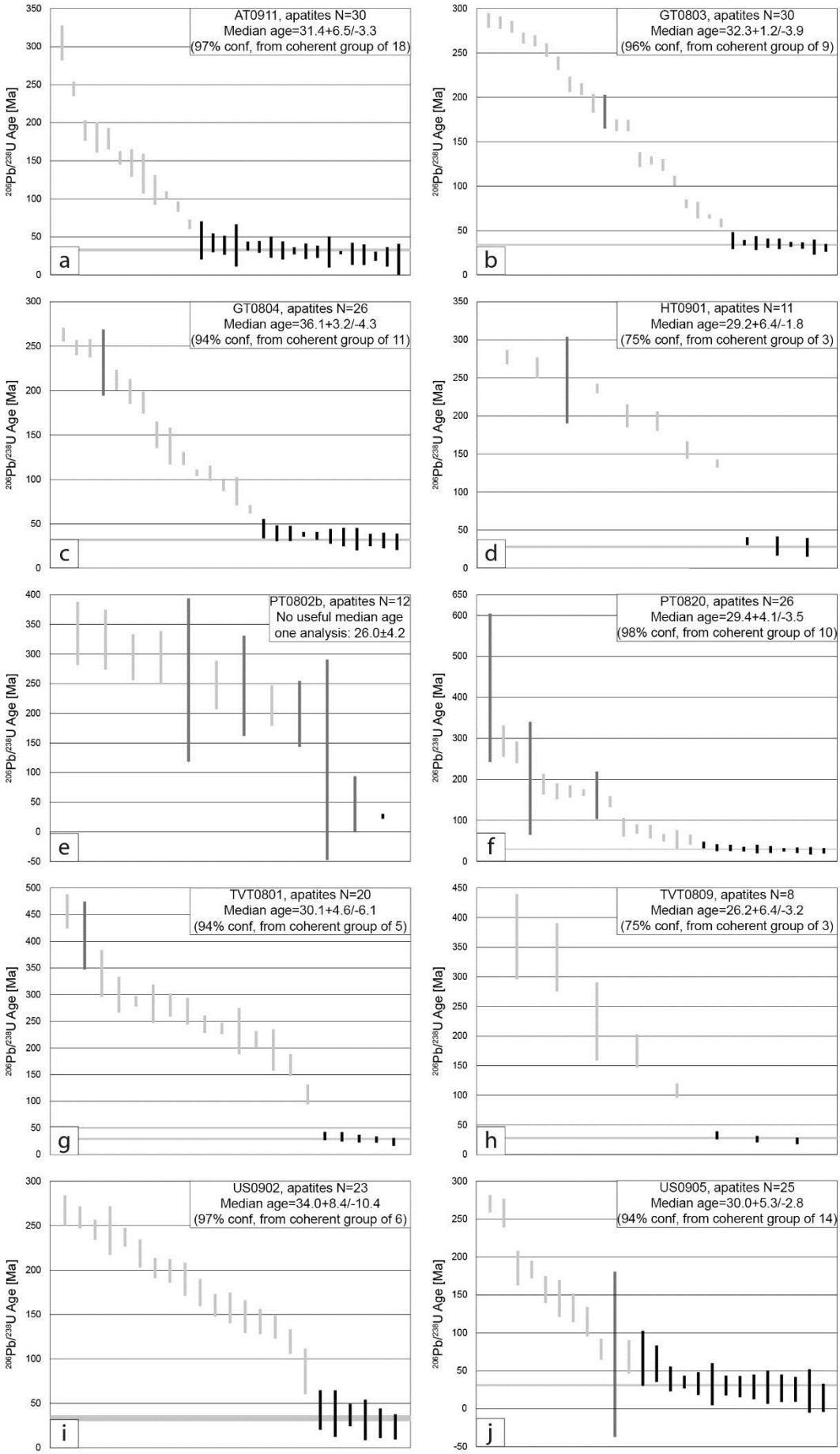
AT0911, apatites N=30
Median age=31.4+6.5/-3.3
(97% conf, from coherent group of 18)
a
GT0803, apatites N=30
Median age=32.3+1.2/-3.9
(96% conf, from coherent group of 9)
b
GT0804, apatites N=26
Median age=36.1+3.2/-4.3
(94% conf, from coherent group of 11)
c
HT0901, apatites N=11
Median age=29.2+6.4/-1.8
(75% conf, from coherent group of 3)
d
PT0802b, apatites N=12
No useful median age
one analysis: 26.0±4.2
e
PT0820, apatites N=26
Median age=29.4+4.1/-3.5
(98% conf, from coherent group of 10)
f
TVT0801, apatites N=20
Median age=30.1+4.6/-6.1
(94% conf, from coherent group of 5)
g
TVT0809, apatites N=8
Median age=26.2+6.4/-3.2
(75% conf, from coherent group of 3)
h
US0902, apatites N=23
Median age=34.0+8.4/-10.4
(97% conf, from coherent group of 6)
i
US0905, apatites N=25
Median age=30.0+5.3/-2.8
(94% conf, from coherent group of 14)
j
206Pb/238U Age [Ma]

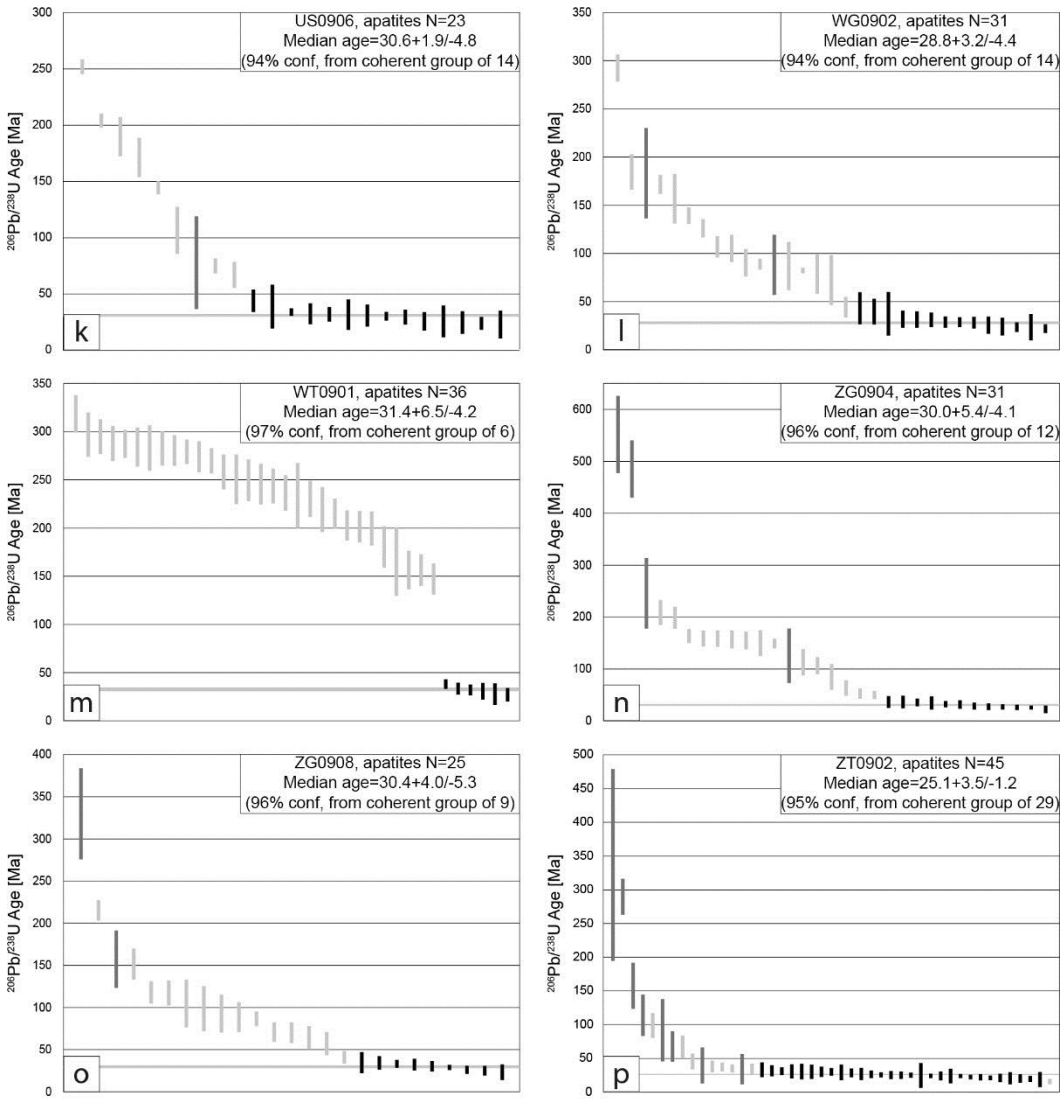

Figure 6a, b, c, d, e, f, g, h, i, j, k, l, m, n, o, p: *$^{206}Pb/^{238}U$ ages of apatite analyses ordered in descending age values. The vertical bars reflect the 2σ errors of the single grain analyses. The dark grey colored analyses were excluded by the ISOPLOT algorithm due to their high errors and the light grey colored analyses were excluded due to the low frequency of their age value, they reflect inherited and partly reset age values. The black colored analyses were taken into account for median age calculation. In two cases (TVT0801 and ZG0804) the median age of the younger cluster was obtained in a second iterative stage. For both samples the five oldest apparent ages of single analyses were excluded during calculation. Note that for sample PT0802b only the youngest age value was interpreted in the context to the two neighboring samples TVT0809 and ZT0902 to be representative for cooling after Alpine metamorphism. Therefore it is marked with an asterisk (*) in the text.*

The concentrations of Pb (cps), U (ppm), Pb (ppm), the element ratio Th/U, the percentage of common Pb (^{206}Pbc and ^{208}Pbc) on the base of ^{206}Pb and ^{208}Pb, the isotopic ratios $^{206}Pb/^{238}U$, $^{207}Pb/^{235}U$, their percentage 2σ error, the error correlation (rho) and the $^{207}Pb/^{235}U$, $^{206}Pb/^{238}U$ age values plus their absolute 2σ error of each apatite analyses are given in supplementary table 2. For each rock sample several analyses (8-45) were performed that are given in one block ordered in ascending $^{206}Pb/^{238}U$ age values. The $^{206}Pb/^{238}U$ ratio yield the highest precision, since ^{238}U is the most common uranium isotope, therefore the $^{206}Pb/^{238}U$ age values were used for median age extraction. Those age values that were taken into account for median age extraction are indicated with an asterisk (*) in supplementary table 2. For each sample block the extracted median age, its asymmetric 2σ error, and the confidence level for the coherent group is given in the heading.

4.9.1 Analytical and geological errors

The 2σ error of the $^{206}Pb/^{238}U$ zircon ages varies between 2.8 and 26 % with a mean value of 4.0 % and the 2σ error of the $^{207}Pb/^{235}U$ zircon ages varies between 3.5 and 26 % with a mean value of 5.4 %. Concordia-age errors are in the range of 1 to 2 % due to the data selection and statistical treatment, whereas the discordia-age errors (upper intercepts) are in the range of 4 to 6 %.

Some of the zircon data show concordance percentages between $^{206}Pb/^{238}U$ and the $^{207}Pb/^{235}U$ ages that are slightly higher than 100 % (supplementary table 1), the points plot slightly above the concordia but do overlap with it. Since these data are concordant within error it can be excluded that they are affected by U loss. Due to the high value of the $^{206}Pb/^{204}Pb$ ratio that scatters between 605 and 148,106 common Pb was excluded during data reduction. Therefore, in few cases, where the concordance percentage is 101 to 105 %, the disregard of common Pb might cause slightly older ages. These isolated data do not change the calculated concordia and discordia ages, therefore no common Pb correction was applied to the zircon analyses.

The 2σ error of the $^{206}Pb/^{238}U$ apatite ages varies between 6.9 and 130 % with a mean value of 32 %. These high errors are caused by the low U and Th concentrations (26 and 8 ppm in average, respectively; supplementary table 2) and the small accumulation of radiogenic Pb due to the young age values. Acceptable asymmetric 2σ errors of the apatite median ages vary between 3 and 31 %, being mostly in the range of 10 %. 9 out of 16 samples show that the positive errors of apatite median ages are larger than the negative errors indicating the data complexity caused by the large asymmetric age scatter of the apatite analyses (Figs. 6a-p).

The five samples of the western section yield median ages of 30.1 to 25.3 Ma, all overlapping in 2σ errors but indicating a spatially systematic distribution (Figs. 5e, f, g, h, p, and 7a). The northern- and southernmost samples yield the oldest median ages, towards the center samples median ages become younger, being youngest in the center of the section. The central section yields uniform median ages of 31.4 to 28.8 Ma, all overlapping in 2σ errors (Figs. 5a, l, m, n, o, and 7a). Although the two oldest median ages, like in the western section, lie at the northern and southern end of the section, this trend is less pronounced. Six samples along the eastern section yield median ages of 36.1 to 29.3 Ma, all overlapping in 2σ errors (Figs. 5b, c, d, i, j, and 7a). The two oldest median ages are located at the southern end of the section outside of the restraining bend (Schneider et al., 2014). The northernmost sample also shows an older median age, but due to its high error the trend is less convincing. The three samples in the center yield younger median ages comparable to the samples of the central section (Fig. 7b). Two age trends can be inferred, median ages in the centers of the section are younger than those at the margins and median ages in the east are older than those in the west.

Due to the high asymmetric 2σ error of ~10 % the spatial age trends of the apatite median ages are not significant, whereas they would be significant when accepting confidence levels of 68.2 % (1σ error). Therefore, we note that the 2σ errors might be too conservative or overestimated. This could be easily improved by analyzing a larger number of grains (≥100). As a rule, errors are smaller for those samples where more grains were analyzed (Figs 5b, i, and p).

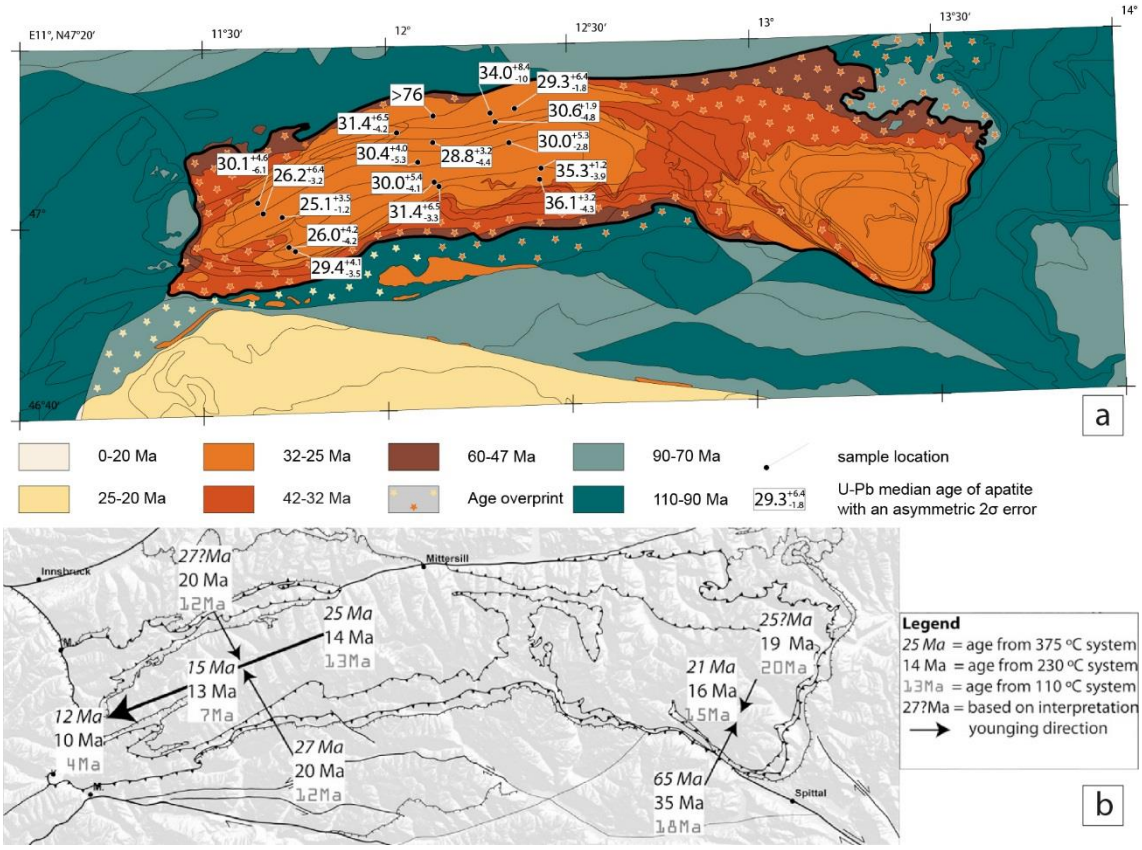

Figure 7a: *Simplified metamorphic map of the Tauern Window and surrounding Austroalpine units, modified after (Bousquet et al., 2012b). Median ages of apatite analyses and their asymmetric 2σ errors are shown in map view. The eastern and western sections show clearly a concentric pattern. The same trend is cognizable in the central section but less pronounced. A general westward younging trend can be inferred.* ***b:*** *Figure 11 of Luth and Willingshofer (2008) were the authors summarized the cooling trends in the Tauern Window that were obtained by a compilation of cooling ages from several geochronometers. The arrows indicate the younging direction for three different closure temperatures. The cooling trends in the western Tauern Window are identical to the U-Pb apatite cooling age trends in Fig. 7a.*

In order to discriminate the age values from the core and the margins of the Tauern Window in the three section we perform three two-tailed t-test on the age values. This test compares the mean of two populations (here, e.g. the U-Pb ages that were taken into account for median age calculation of apatite, marked with an asterisk in supplementary table 2 and black bars in Figs. 6a-p), from the core (population 1) and the cumulated margin (population 2) of the mentioned section and their variance at a given confidence level to decide whether the means are equal or different. The calculations show that for all three section the means of the centers differ from that of the cumulated margins. For the eastern section the mean (32.1 Ma) of the central samples (US0905, US0906 and HT0901) is different from the mean (34.9 Ma) of the marginal samples (US090, GT0803 and GT0804) with a confidence level of 80 %; for the central section the mean (30.0 Ma) of the central samples (WG0902, ZG0908 and ZG0904) is different from the mean (32.2 Ma) of the marginal samples (WT0901 and AT0911) with a confidence level of 85 %; for the western section the mean (25.3 Ma) of the central samples (TVT0809, ZT0902 and PT0802b) is different from the mean (30.2 Ma) of the marginal samples (TVT0801 and PT0820) with a confidence level of 99.9 %.

In addition we performed three two-tailed t-tests were to decide whether there is an east-west trend across the three sections. The mean (33.4 Ma) of the eastern section (US0902, US0905, US0906, HT0901, GT0803, GT0804) is different from the mean (30.9 Ma) of the central section (WT0901, WG0902, ZG0908, ZG0904, AT0911) with a confidence level of 90 %; the mean (26.8 Ma) of the western section (TVT0801, TVT0809, ZT0902, PT0802b, PT0820) is different from the mean (30.9

Ma) of the central section with a confidence level of 99.9 %; the mean (33.4 Ma) of the eastern section is different from the mean (26.8 Ma) of the western section with a confidence level of 99.999 %. Therefore we argue that both age trends, younging towards the centers of the sections and younging towards the west across all sections are geological meaningful.

4.9.2 Formation or cooling ages

Generally radiometric ages can be interpreted as either formation age, dating the time of magmatic, metamorphic, diagenetic, deformational or hydrothermal mineral formation, or as cooling age from a magmatic or metamorphic event, dating the time when volume diffusion of radiogenic nuclides out of the mineral has ceased mainly due to undercutting the closure temperature of a given isotope system (Dodsen, 1973). Microscopic petrography, mineral chemistry and thermobarometric estimations, with respect to the specific closure temperatures, are the main criterions for age interpretations. The age spectra itself might also give some hints, but it depends also on the tectono-metamorphic setting. Rather similar ages would be expected if the isotopic systematics were controlled by a discrete formation or recrystallization event, although syn-kinematic mineral formation might be possible over a prolonged interval if localized deformation is long-lasting (e.g. Pollington and Baxter, 2011; Schneider et al., 2013). Fast cooling from high temperatures (e.g. upper amphibolite-facies) would cause relatively uniform cooling ages. On the contrary, an observed age spread from a single hand specimen or a restricted working area could point to the progressive closing of an isotopic system, during slow cooling, which could be caused by the development of diffusion gradients of radiogenic nuclides across the effective diffusion domain of a given geochronometer (Willigers et al., 2001). In addition, if isotopic signatures of earlier events, e.g. magmatic formation are still preserved, interpretation as cooling ages is likely.

The zircon concordia ages vary between 290.3 and 296.5 Ma, all overlapping within their 2σ errors, and the zircon discordia (upper intercept) ages vary between 296 and 315 Ma, also overlapping within their 2σ errors. In agreement to previous studies (Vavra and Hansen 1991; von Quadt, 1992; Finger et al., 1993, 1997; Cesare et al., 2002; Veselá et al., 2008) presenting magmatic crystallization ages from the Zentralgneiss batholith, the zircon U-Pb ages above are interpreted as formation ages dating the emplacement of the Zentralgneiss batholith.

The paragneiss-sample GT0803 shows zircon cores having $^{206}Pb/^{238}U$ ages of ~338 and 653 Ma that are concordant (supplementary table 1). Two orthogneiss-samples US0905 and US0906 show each one zircon core having $^{206}Pb/^{238}U$ ages of 529±20 and 581±23 Ma, respectively, that are concordant (supplementary table 1). These few Carboniferous to Precambrian ages of the zircon cores are interpreted to reflect detrital zircons from the country rocks of the Zentralgneiss or from crustal fragments brought into the Zentralgneiss batholith by melt assimilation during pluton emplacement. The aplitic dike-sample GT0804 shows scattering $^{206}Pb/^{238}U$ zircon ages between ~239 and 595 Ma that are partly concordant and partly discordant, having a larger cluster of concordant ages at ~340 Ma (supplementary table 1). These ages might also reflect inherited ages from geological events preceding emplacement of the Zentralgneiss or they represent isotopically disturbed ages that we will not considered any further for the geological interpretation.

Apatite analyses scatter over a wide range and show two age clusters. A considerable number of apatite analyses of each sample reflect a relatively uniform age cluster varying between ~40-20 Ma. These age values define a plateau as reliable ages and are separated from the older age cluster by either a kink in the age-value trend (Figs. 6a, b, c, and k), by a logarithmic approximation (Pareto distribution, Figs. 6f, j, l, n, o, and p), or by a discrete offset in age value (Fig. 6d, g, h, i, and m). The ISOPLOT algorithm extracted median ages from this cluster due to their relatively low error

and their high frequency. The obtained apatite median ages of all samples vary between 36.1 and 25.3 Ma, whereat the majority (10 of 16 samples) vary between ~29 and 31 Ma (Fig. 7a). Three samples located in the center of the western section (ZT0902, PT0802b, and TVT0809) show younger median ages of ~25 and 26 Ma. Three samples (US0902, GT0803 and GT0804) of the eastern section, located at the margins or even outside of the transpressive belt (Fig. 1a) of the western Tauern Window, show older median ages of ~34 and 36 Ma. The median ages overlap with the time interval of Barrovian metamorphism in the Eastern Alps, suggesting a tectono-metamorphic relation (Lambert, 1970; Cliff et al., 1985; Selverstone, 1985; Grundmann and Morteani, 1985; von Blanckenburg and Villa, 1988; von Blanckenburg et al., 1989; Christensen et al., 1994; Inger and Cliff, 1994; Ratschbacher et al., 2004). The thermal climax of the Barrovian metamorphism of the analyzed samples was majoritarian >450 °C, therefore we interpret the median ages as cooling ages. However, in all cases the median ages reflect the youngest age values of the samples with relatively low scatter, no drop to younger age values from the median-age plateau is observed (Figs. 6a-p), therefore we exclude that the apatites are affected by remarkable Pb loss, either diffusional or due to fluid-mineral interactions, after isotopic resetting.

Samples WG0904 shows apatite age values that are >76 Ma, no median age could be extracted. Apatite analyses of sample US0902 show a young age cluster but the asymmetric error of the median age is maximal (31 %). Both these samples hail from locations where the thermal climax of the Barrovian overprint is ≤450 °C, suggesting that during metamorphism the samples were not heated completely through and therefore, not isotopically reset.

The second age cluster in all samples reveals age values scattering between ~300-40 Ma. The time span between pluton emplacement indicated by the zircon crystallization ages, and the younger age cluster is often covered by several age values of the apatite analyses (Figs. 6a-p), that are interpreted as partly reset. Four samples (HT0901, TVT0801, TVT0809 and WT0902) show a discrete jump between the partly reset age values (≥108 Ma) and the younger age cluster. The oldest apatite age values, if not excluded due to their high error by the ISOPLOT algorithm, overlap with the zircon crystallization ages from the same samples. The preservation of the age signal of the magmatic emplacement is an additional argument, that the apatites are affected by diffusional Pb loss during Alpine Barrovian metamorphism (Tauerncrystallization) rather than by recrystallization. Otherwise in case of metamorphic apatite growth this age signal would have been completely overprinted or not manifested at all.

4.9.3 Comparison to other geochronometers

The spatial age trends of the obtained cooling ages show remarkable accordance with the spatial age patterns of geochronometers (K/Ar biotite, Rb/Sr biotite, ZFT, and AFT) having lower closure temperatures (see compilation of Luth and Willingshofer, 2008). For six out of eighteen samples additional cooling ages (ZFT and/or AFT) were performed and are published elsewhere (Fig. 8, Bertrand et al., 2014). We calculated cooling rates (Fig. 8) for these six sample assuming closure temperatures of 450±50 °C for apatite U-Pb (Chamberlain and Bowring, 2000), of 230±20 °C for ZFT and of 120±20 °C for AFT (Reiners and Brandon, 2006). The sample GT0804 from outside the restraining bend yield a cooling rate of 10.4 K/Myr. The remaining five samples from the western sub-dome yield uniform cooling rates between 14.4 and 16.3 K/Myr, with a mean cooling rate of 15.2±1.5 K/Myr (2σ). Although the age spread of the U-Pb apatite cooling ages and the ZFT ages is relatively large (> 5 Myr), the specific cooling trends are remarkable uniform. The linear cooling trend overlaps with published cooling age ranges of biotite and muscovite (K/Ar and Rb/Sr, Fig. 8). We estimated the thermal climax of the Barrovian metamorphism for each sample

graphically from the sample location (Fig. 1b, Bousquet et al., 2012b). Using the specific cooling rates we calculated the specific timing of the thermal climax for each sample that resulted in an age range between 38 to 34 Ma (Fig. 8).

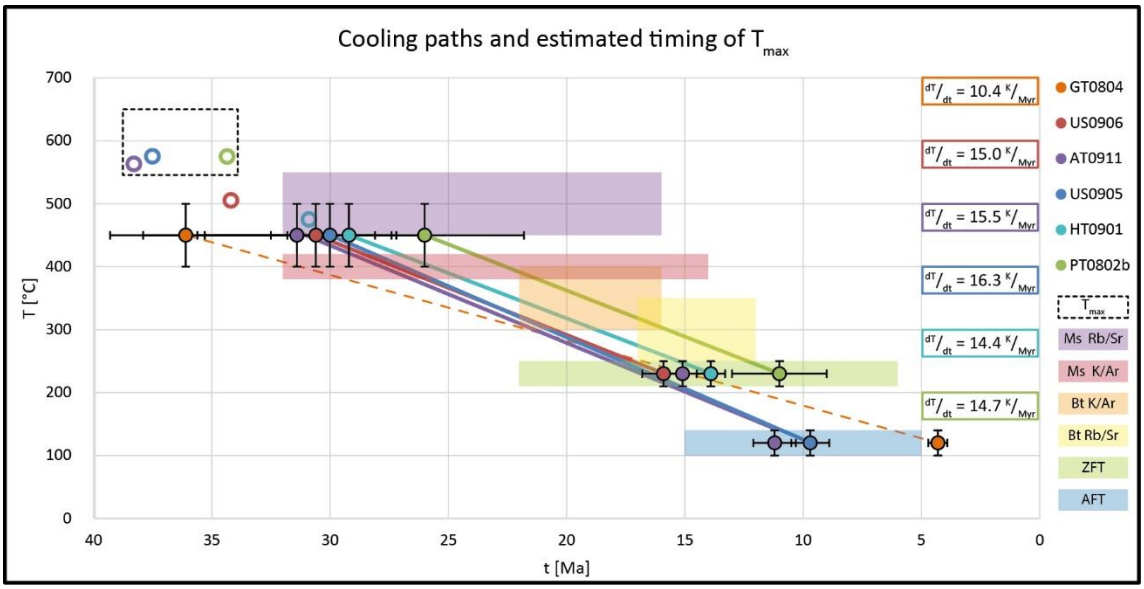

Figure 8: *Time-temperature diagram solid circles indicate the dated samples, open circles indicate the calculated time range of the thermal climax t(T_{max}), solid lines indicate the cooling rates of samples inside the western Tauern Window, dashed line indicates apparent cooling rate of a sample from the central Tauern Window, formulas show the specific cooling rates, colored semitransparent squares give the age ranges of different geochronometers (errors are not included), assumed closure temperatures: muscovite Rb/Sr 500±50 °C (Jäger et al., 1996), muscovite K/Ar 400±30 °C (Kirschner et al., 1996), apatite U-Pb 450±50 °C (Chamberlain and Bowring, 2000), biotite K/Ar 350±50 °C (Grove and Harrison, 1996); biotite Rb/Sr 300±50 °C (Jäger et al., 1969); ZFT 230±20 °C (Reiners and Brandon, 2006); AFT 120±20 °C (Reiners and Brandon, 2006), dashed box indicates thermal climax based on Bousquet et al., 2012b and extrapolated age data.*

4.9.4 Tectono-metamorphic implications

The timing of the Tauerncrystallization compared to the timing of the high-pressure metamorphism in the Eclogite Zone is one of the fundamental constrains for the tectono-metamorphic evolution of the Eastern Alps. Smye et al. (2011) argued for fast exhumation of the Eclogite Zones within 10 Myr (38-28 Ma) enhanced by mantle heat input. Our results indicate that simultaneously the thermal climax within the Tauern Window occurred at 38-34 Ma. A possible source for this heat input might by slab breakoff (Davies and von Blanckenburg, 1994) at ~35 Ma (Ratschbacher et al., 2004). The Periadriatic plutonism is discussed to be a manifestation of this heat input and lower crustal melting, recent U-Pb zircon ages point to magmatic emplacement at 42-30 Ma (Pomella et al., 2011 and references therein) overlapping with the timing of the thermal climax estimated in this study.

The U-Pb apatite cooling age distribution in map view shows two spatial trends. Along each of the three sections ages become younger towards the central area. This effect is most clearly seen in the western and eastern sections. Additionally a lateral, westward younging trend also exists. The age pattern in map view appears to be mirror-symmetric about a central plane striking ENE, but also the westward younging trend correlates with the differential shortening of the Dolomites indenter being highest in the west and decreasing eastward (Fig. 1a). This pattern resembles those of

geochronometers having lower closure temperatures (Fig. 7b, Luth and Willingshofer, 2008; Bertrand et al., 2014). The orientation and the location of this symmetry plane is almost identical to the hinge of the western Tauern dome (Schneider et al., 2014). Hence, erosional denudation after upright folding seems to explain cooling below ~450 °C, and this exhumation continued until the partial annealing zone (PAZ) for AFT is attained (Bertrand et al., 2014).

Younging of cooling ages towards the hinge of an antiform has been observed in thermal (Bertrand, 2013) and thermo-mechanical (Batt and Braun, 1997) numerical models, but also in other, natural examples of orogen-scale folding (Brandon et al., 1998). This age variation results from the combined effect of higher uplift and erosion rates in the hinge region compared to the limbs and to successive upward-bending of the isotherms in the hinge region during doming (Bertrand, 2013). The first process reduces the time needed for material particles in the hinge region to reach the Earth surface from the PAZ. The second process reduces the distance between the PAZ and the Earth surface. However, the cooling rates of the western Tauern Window obtained in this study are uniform, therefore the upward bending of the isotherms seems to dominate the exhumation process. However, this interpretation is preliminary base on five specific cooling rates. As shown by numerical, thermal models of a lithosphere undergoing shortening by folding and erosion, the oldest ages at the margins of the fold can be taken to date the initiation of folding. This suggests that the Tauern dome may have started to be exhumed already at ~36-35 Ma, hence much earlier than previously thought and possibly linked to the slab breakoff at ~35 Ma (Ratschbacher et al., 2004). All samples that are located within the restraining bend (Schneider et al., 2014) of the western sub-dome yield Oligocene cooling ages, whereas two sample (GT0803 and GT0804) outside this restraining bend yield Eocene cooling ages. This age jump in cooling ages across the restaining bend might date the onset of Dolomites Indentation to ~31-29 Ma that would be in agreement with deformation age data of the Giudicarie Belt (Müller et al., 2001) of the restraining bend in the western Tauern Window (Glodny et al., 2008; Pollington and Baxter, 2011; Schneider et al., 2013) and the SEMP Fault accommodating lateral extrusion (Peresson and Decker, 1997; Urbanek et al., 2002; Cole et al., 2007).

4.10 Conclusion

The ISOPLOT algorithm TuffZirc age extractor (Ludwig and Mundil, 2002) is a promising tool to decipher crystallization, partly reset and cooling ages of apatites that underwent amphibolite-facies metamorphism. Cooling ages dating the mid-range metamorphism (~400-500 °C) can be obtained from apatites due to their diffusion controlled Pb loss and their inert behavior to recrystallization. Differentiation of the apatite age spectra into crystallization, partly reset and cooling ages was supported by the U-Pb crystallization ages of zircons from the same samples and by combining the apatite U-Pb age data to a large data set that existed already in the literature (compilation by Luth and Willingshofer, 2008). Both age trends that were observed for cooling ages of geochronometers having lower closure temperatures (Luth and Willingshofer, 2008) could be positively confirmed by applying the unconventional U-Pb apatite geochronometer the first time in the Eastern Alps. In future studies analyses of larger amounts of grains (≥100) might achieve a higher significance level of the apatite median ages and therefore could better constrain the timing of isotopic closure.

Formation of the Tauern Window is largely related to doming caused by Adria-Europe collision causing Barrovian metamorphism in the Zentralgneiss batholith. The timing of the thermal climax in the Zentralgneiss batholith occurred at 38-34 Ma contemporaneously to high-pressure metamorphism in the eclogite zone and might be related to mantle-derived heat influx after slab breakoff at ~35 Ma. Ongoing shortening and detached upper crust might have promoted Dolomites

Indentation causing strain localization such as the restaining bend in the western Tauern Window and additional rock uplift starting at ~33 Ma. The remarkable coincidence of U-Pb apatite ages with the spatial distribution of geochronometers having lower closure temperatures indicate that from ~31-29 Ma on the western Tauern Window cooled with a cooling rate of 15.2±1.5 K/Myr due to erosional denudation. Samples that are outside of the restraining bend, cooled at 36-35 Ma, whereas samples that are inside of the restaining bend started to cool at 31-29 Ma below 450 °C. Therefore we argue that the onset of Dolomites indentation might have occurred at 31-29 Ma.

4.11 Acknowledgement

This study was funded by the DFG grant Ro2177/4. We acknowledge family Schwärzer, especially M. Schwärzer, G. Fankhauser and R. Emberger for field support and accommodation. For helpful discussions we thank A. Bertrand, S. Favaro, S. Garcia, M.R. Handy, L. Ratschbacher, D. Rutte, and M. Tichomirowa.

4.12 References

Batt, G., Braun, J., 1997. On the thermomechanical evolution of compressional orogens. Geophys. J. Int. 128, 364-382.

Bertrand, A., 2013 Chapter IV. 2D-thermal modelling of a structural and thermal dome based on a natural example, the Tauern Window (Eastern Alps), 123–158.

Bertrand, A., Rosenberg, C., Fügenschuh B., 2014. Exhumation mechanisms of the Tauern Window (Eastern Alps) inferred from Apatite and Zircon fission track thermochronology. Tectonics, (in review).

Blanckenburg, F.v., Villa, I.M., 1988. Argon retentivity and argon excess in amphiboles from the garbenschists of the Western Tauern Window, Eastern Alps. Contrib. Mineral. Petrol. 100, 1¬–11.

Blanckenburg, F.v., Villa, I.M., Baur, H., Morteani, G., Steiger, R.H., 1989. Time calibration of a PT path from the Western Tauern Window, Eastern Alps: the problem of closure temperatures. Contrib. Mineral. Petrol. 101, 1–11.

Borsi, S., Del Moro, A., Sassi, F.P., Zirpoli, G., 1973. Metamorphic evolution of the Austridic rocks to the south of the Tauern Window (Eastern Alps): radiometric and geopetrologic data. Mem. Soc. Geol. It., 12, 549– 571.

Borsi, S., Del Morro, A., Sassi, F., Zanferrari, A., Zirpoli, G. 1978. New geopetrologic and radiometric data on the alpine history of the Austridic continental margin South of the Tauern window (Eastern Alps). Memorie dell'Istituto della Regia Universitá di Padova 32, 1–20.

Bousquet, R., Oberhänsli, R., Goffé, B., Wiederkehr, M., Koller, F., Schmid, S. M., Martinotti, G. 2008. Metamorphism of metasediments at the scale of an orogen: a key to the Tertiary geodynamic evolution of the Alps*. Geol. Soc. Spec. Pub. 298, 393–411.

Bousquet, R., Schmid, S.M., Zeilinger, G., Oberhänsli, R., Rosenberg, C.L., Molli, G., Robert, C., Wiederkehr, M., Rossi, P., 2012a, Tectonic framework of the Alps, CCGM/CGMW

Bousquet, R., Oberhänsli, R., Schmid, S.M., Berger, A., Wiederkehr, M., Robert, C., Rosenberg, C.L., Koller, F., Molli, G., Zeilinger, G., 2012b, Metamorphic framework of the Alps, CCGM/CGMW

Brandon M.T., Roden-Tice, M.K., Garver, J.I., 1998. Late Cenozoic exhumation of the Cascadia accretionary wedge in the Olympic Mountains, northwest Washington State. GSA Bulletin 110, 985–1009.

Cesare, B., Rubatto, D., Hermann, J., Barzi, L., 2002. Evidence for Late Carboniferous subduction-type magmatism in ultra-mafic cumulates of the SW Tauern window (Eastern Alps), Contrib. Mineral. Petrol. 142, 449–464.

Chamberlain, K.R., Bowring, S.A., 2000. Apatite–feldspar U–Pb thermochronometer: a reliable, mid-range (~450°C), diffusion-controlled system. Chem. Geol. 172, 173–200.

Cherniak, D.J., Lanford, W.A., Ryerson, F.J., 1991. Lead diffusion in apatite and zircon using ion implantation and Rutherford backscattering techniques. Geochim. Cosmochim. Acta 55, 1663–1673.

Christensen, J.N., Selverstone, J., Rosenfeld, J.L., De Paolo, D.J., 1994. Correlation by Rb–Sr geochronology of garnet growth histories from different structural levels within the Tauern Window, Eastern Alps. Contrib. Mineral. Petrol. 118, 1–18.

Cliff, R.A., Droop, G.T.R., Rex, D.C., 1985. Alpine metamorphism in the south-east Tauern Window, Austria: 2. Rates of heating, cooling and uplift. J. metamorphic Geol. 3, 403–415.

Cole, J., Hacker, B., Ratschbacher, L., Dolan, J., Seward, G., Frost, E., Frank, W., 2007. Localized ductile shear below the seismogenic zone: Structural analysis of an exhumed strike-slip fault, Austrian Alps. J. Geophys Res. Sol. Ea., 1978–2012.

Corfu, F., Stone, D., 1998. The significance of titanite and apatite U-Pb ages: Constraints for the post-magmatic thermal-hydrothermal evolution of a batholithic complex, Berens River area, northwestern Superior Province, Canada. Geochim. Cosmochim. Acta, 62, 2979–2995.

Cornelius, H.P., 1940. Zur Auffassung der Ostalpen im Sinne der Deckenlehre. Z. Deutsch. Geol. Ges. 92, 271–312.

Davies, H.J., Blanckenburg, F.v., 1995. Slab breakoff: a model of lithosphere detachment and its test in the magmatism and deformation of collisional orogens. Earth Planet. Sci. Lett., 129, 85–102.

Dingledey, C., Dallmeyer, R.D., Koller, F., Massonne, H.-J., 1997. P-T-t history of the Lower Austroalpine Nappe Complex in the “Tarntaler Berge” NW of the Tauern Window: implications for the geotectonic evolution of the central Eastern Alps. Contrib. Mineral. Petr. 129, 1–19.

Dodson, M.H., 1973. Closure temperature in cooling geochronological and petrological systems. Contrib. Mineral. Petr., 40, 259–274.

Droop. G.T.R., 1981. Alpine metamorphism of pelitic schists in the south-east Tauern Window. Austria. Schweiz. Miner. Petrog. 61, 237–273.

Finger, F., Frasl, G., Haunschmid, B., Lettner, H., Quadt, A.v., Schermaier, A., Schindlmayr, A.O., Steyrer, H.P., 1993. The Zentralgneise of the Tauern Window (Eastern Alps): insight into an intra-alpine Variscan Batholith. In J.F. von Raumer and F. Neubauer (Eds.): Pre-Mesozoic Geology in the Alps, 375–391. Berlin: Springer.

Finger, F., Roberts, M.P., Haunschmid, B., Schermaier, A., Steyrer, H.P., 1997. Variscan granitoids of central Europe: their typology, potential sources and tectonothermal relations. Mineralogy and Petrology 61, 67–96.

Frei, D., Gerdes, A., 2009. Precise and accurate in situ U–Pb dating of zircon with high sample throughput by automated LA-SF-ICP-MS. Chem. Geol. 261, 261–270.

Fügenschuh, B., Seward, D., Mancktelow, N.S., 1997. Exhumation in a convergent orogen: the western Tauern Window. Terra Nova 9, 213–217.

Gerdes, A., Zeh, A., 2006. Combined U–Pb and Hf isotope LA-(MC)-ICP-MS analyses of detrital zircons: comparison with SHRIMP and new constraints for the provenance and age of an Armorican metasediment in Central Germany. Earth Planet. Sci. Lett. 249, 47–61.

Gerdes, A., Zeh, A., 2009. Zircon formation versus zircon alteration—new insights from combined U–Pb and Lu–Hf in-situ La-ICP-MS analyses of Archean zircons from the Limpopo Belt. Chem. Geol. 261, 228–241. doi:10.1016/j. chemgeo.2008.03.005.

Gleißner, P., Glodny, J., Franz, G., 2007. Rb–Sr isotopic dating of pseudomorphs after lawsonite in metabasalts from the Glockner nappe, Tauern Window, Eastern Alps. Eur. J. Mineral. 19, 723–734.

Glodny, J., Ring, U., Kühn, A., Gleissner, P., Franz, G., 2005. Crystallization and very rapid exhumation of the youngest Alpine eclogites (Tauern Window, Eastern Alps) from Rb/Sr mineral assemblage analysis. Contrib. Mineral. Petrol. 149, 699–712.

Glodny, J., Ring, U., Kühn, A., 2008. Coeval high-pressure metamorphism, thrusting, strike-slip, and extensional shearing in the Tauern Window, Eastern Alps. Tectonics 27, TC4004. http://dx.doi.org/10.1029/2007TC002193.

Grove, M., Harrison, M.T., 1996. Ar diffusion in Fe-rich biotite. Am. Mineral. 81, 940–951.

Grundmann, G., Morteani, G., 1985. The Young Uplift and Thermal History of the Central Eastern Alps (Austria/Italy), Evidence from Apatite Fission Track Ages. Jb. Geol. B.-A. 128, 197–216.

Harrison, M.T., Cathlos, E.J., Montel, J.-M., 2002. U-Th-Pb Dating of Phosphate Minerals. Rev. Minerl. Geochem. 48, 524–558.

Hoernes, S., Friedrichsen, H., 1974. Oxygen isotope studies on metamorphic rocks of the Western Hohe Tauern area (Austria). Schweiz. Mineral. Petrogr. 54, 769–788.

Höche. T., Moisescu, C, Avramov, I., Rüssel, C., 2001. Microstructures of SiO_2-Al_2O_3-CaO-P_2O_5-K_2O-F- Glass Ceramics. 1. Needlelike versus Isometric Morphology of Apatite Crystalls. Chem. Mater. 13, 1312–1319.

Höck, V., 1980. Distribution maps of minerals of the Alpine metamorphism in the Penninic Tauern window, Austria. Mitt. Österr. Geol. Ges. 71/72, 119–127.

Inger, S., Cliff, R.A., 1994. Timing of metamorphism in the Tauern Window, Eastern Alps: Rb-Sr ages and fabric formation. J. metamorphic Geol. 12, 695–707.

Jackson, S., Pearson, N.J., Griffin, W.L., Belousova, E.A., 2004. The application of laser ablation – inductively coupled plasma – mass spectrometry to in situ U–Pb zircon geochronology. Chem. Geol. 211,

Jäger, E., Karl, F., Schmidegg, O., 1969. Rubidium-Strontium-Altersbestimmungen an Biotit-Muskowit-Granitgneisen (Typus Augen- und Flasergneise) aus dem nördlichen Großvenedigerbereich (Hohe Tauern). Miner. Petrol., 13, 251–272.

Kennedy, A.K., Dante, K., 1997. SHRIMP measurement of U–Th–Pb ages of apatite from the Acropolis find ore prospect, South Australia. Joint Annual Meeting of the Geological Association of Canada and the Mineralogical Association of Canada (GAC-MAC), Abstract, A-77.

Kirschner, D., Cosca, M., Masson, H. Hunziker, J. 1996. Staircase $^{40}Ar/^{39}Ar$ spectra of fine-grained white mica; timing and duration of deformation and empirical constraints on argon diffusion. Geology 24(8), 747–750.

Košler, J., Sylvester, P.J., 2003. Present trends and the future of zircon in geochronology: laser ablation ICPMS. Rev. Mineral. Geochem. 53, 243–275.

Krogstad, E.J., Walker, R.J., 1994. High closure temperatures of the U–Pb system in large apatites from the Tin Mountain Pegmatite, Black Hills, South Dakota, USA. Geochim. Cosmochim. Acta 58, 3845–3853.

Kruhl, J.H., 1996. Prism- and basal-plane parallel subgrain boundaries in quartz: a microstructural geothermobarometer, J. metamorphic Geol. 14, 581–589.

Kurz, W., Handler, R., Bertoldi, C., 2008. Tracing the exhumation of the Eclogite Zone (Tauern Window, Easter Alps) by $^{40}Ar/^{39}Ar$ dating of white mica in eclogites. Swiss J. Geosci. 3, 1–16.

Laubscher, H., 1996. Shallow and deep rotations in the Miocene Alps. Tectonics, 15, 1022–1035.

Lambert, S. 1970. A Potassium-Argon Study of the Margin of the Tauernfenster at Döllach, Austria. Eclogae Geol. Helv. 63, 197–205.

Ludwig, K.R., 1998. On the treatment of concordant uranium-lead ages: Geochim. Cosmochim. Acta 62, 665–676.

Ludwig, K.R., 2009. User's Manual for ISOPLOT 3.70 A Geochronological Toolkit for Microsoft Excel, Berkeley Geochronology Center Special Publication No. 4, 1-78.

Ludwig K.R., Mundil, R., 2002. Extracting reliable U-Pb ages and errors from complex populations of zircons from Phanerozoic tuffs. J. Conf. Abstr. 12th Goldschmidt Conf. 2002.

Luth, S.W., Willingshofer, E., 2008. Mapping of the post-collisional cooling history of the Eastern Alps. Swiss J. Geosci. 101, 207–223.

Miller, C., Konzett, J., Tiepolo, M., Armstrong, R., Thöni, M., 2007. Jadeite-gneiss from the Eclogite Zone, Tauern Window, Eastern Alps, Austria: metamorphic, geochemical and zircon record of a sedimentary protolith. Lithos 93, 68–88.

Millionig, L.J., Gerdes, A., Groat, L.A., 2012. The effect of amphibolite facies metamorphism on the U–Th–Pb geochronology of accessory minerals from meta-carbonatites and associated meta-alkaline rocks. Chem. Geol. 353, 199–209.

Most, P., 2003. Late Alpine Cooling Histories of Tectonic Blocks along the Central Part of the Transalp-Traverse (Inntal–Gadertal): Constraints from Geochronology. Ph.D.-thesis. Eberhardt-Karls-Universität Tübingen, 1–151.

Müller, W., Prosser, G., Mancktelow, N.S., Villa, I.M., Kelley, S.P., Viola, G., Oberli, F., 2001. Geochronological constraints on the evolution of the Periadriatic Fault System (Alps). Int. J. Earth Sci., 90, 623–653.

Nagel, T.J., Herwartz, D., Rexroth, S., Münker, C., Froitzheim, N., Kurz, W., 2013. Lu–Hf dating, petrography, and tectonic implications of the youngest Alpine eclogites (Tauern Window, Austria). Lithos 170–171, 179–190.

Neufeld, K., Ring, U., Heidelbach, F., Dietrich, S., Neuser, R.D., 2008. Omphacite textures in eclogites of the Tauern Window: implications for the exhumation of the Eclogite Zone, Eastern Alps. J. Struct. Geol., 30, 976–992.

Oosthuyzen, E.J., Burger, A.J., 1973. The suitability of apatite as an age indicator by the uranium–lead isotope method. Earth Planet. Sci. Lett. 18, 29–36.

Peresson, H., Decker, K., 1997. The Tertiary dynamics of the northern Eastern Alps (Austria): changing palaeostresses in a collisional plate boundary. Tectonophysics, 272, 125–157.

Piccoli, P.M., Candela, P.A., 1994. Apatite in felsic rocks; a model for the estimation of initial halogen concentrations in the Bishop Tuff (Long Valley) and Tuolumne Intrusive Suite (Sierra Nevada Batholith) magmas. Am. J. Sci. 294, 92–135.

Piccoli, P.M., Candela, P.A., 2002. Apatite in Igneous Systems. Rev. Minerl. Geochem. 48, 255–292.

Pollington, A.D., Baxter, E.F., 2010. High resolution Sm–Nd garnet geochronology reveals the uneven pace of tectonometamorphic processes. Earth Planet. Sci. Lett. 293, 63–71.

Quadt, A.v., 1992. U-Pb zircon and Sm-Nd geochronology of mafic and ultramafic rocks from the central part of the Tauern Window (eastern Alps). Contrib. Mineral. Petrol 110, 57–67.

Raith, M., Raase, P., Kreuzer, P., Müller, P. 1978. The age of the Alpidic metamorphism in the Western Tauern Window, Austrian Alps, according to radiometric dating In: Cloos, H., Roeder, D. & Schmid, K. (Eds): Alps, Apennines, Hellenides, Inter-Union Commission on Geodynamics, 140–148.

Ratschbacher, L., Frisch, W., Linzer, H.-G., Merle, O., 1991. Lateral extrusion in the Eastern Alps, Part2: structural analysis. Tectonics 10, 257–271.

Ratschbacher, L., Dingeldey, C., Miller, C., Hacker, B.R., McWilliams, M.O., 2004. Formation, subduction, and exhumation of Penninic oceanic crust in the Eastern Alps: time constraints from $^{40}Ar/^{39}Ar$ geochronology. Tectonophysics 394, 155–170.

Reiners, P.W., Brandon, M.T., 2006. Using thermochronology to understand orogenic erosion. Annu. Rev. Earth Planet. Sci. 34, 419–66.

Rosenberg, C.L., Berger, A., 2009. On the causes and modes of exhumation and lateral growth of the Alps. Tectonics 28, pp. 1–16 http://dx.doi.org/10.1029/2008TC002442.

Rosenberg, C.L., Brun, J.-P., Gapais, D., 2004. An indentation model of the Eastern Alps and the origin of the Tauern Window. Geology 32, 997–1000.

Sander, B., 1911. Geologische Studien am Westende der Hohen Tauern (1. Bericht) Denkschr. Akad. Wiss. Wien, math. nat. Kl., 82, 257–319.

Sander, B., 1921 Geologische Studien am Westende der Hohen Tauern (2. Bericht) Jahrb. Geol. St.-A. Wien, 70, 273–296.

Sano, Y., Oyama, T., Terada, K., Hidaka, H., 1999. Ion micro-probe U–Pb dating of apatite. Chem. Geol. 153, 249–258.

Satir, M., 1975. Die Entwicklungsgeschichte der westlichen Hohen Tauern und der südlichen Ötztalmasse auf Grund radiometrischer Altersbestimmungen. PhD.-thesis, Società cooperativa tipografica, Padova, 1–84.

Satir, M., Friedrichsen, H., 1986. The origin and evolution of the Menderes Massif, W-Turkey: a rubidium/strontium and oxygen isotope study. Int. J. Earth Sci. 75, 703–714.

Satir, M., Morteani, G., 1982. Petrological study and radiometric age determination of the migmatites in the Penninic rocks of the Zillertaler Alpen (Tyrol/Austria). Tscher. Miner. Petrog. 30, 59-75.

Scharf, A., Handy, M.R., Favaro, S., Schmid, S.M., Bertrand, A., 2013. Modes of orogen-parallel stretching and extensional exhumation in response to microplate indentation and roll-back subduction (Tauern Window, Eastern Alps). Int. J. Earth Sci. 106, 1627–1654.

Schmid, S.M., Scharf, A., Handy, M.R., Rosenberg, C.L., 2013. The Tauern Window (Eastern Alps, Austria): a new tectonic map, with cross-sections and a tectonometamorphic synthesis. Swiss J. Geosci. 106, 1–32.

Schneider, S., Hammerschmidt, K., Rosenberg, C.L., 2013. Dating the longevity of ductile shear zones: Insight from $^{40}Ar/^{39}Ar$ in situ analyses. Earth Planet. Sci. Lett. 369, 43–58.

Schneider, S., Rosenberg, C.L., Scharf, A., Hammerschmidt, K., 2014. Translation of indentation into lateral extrusion across a restraining bend: The western Tauern Window, Eastern Alps, Tectonics (in review).

Selverstone, J., 1985. Petrologic constraints on imbrication, metamorphism, and uplift in the SW Tauern Window, Eastern Alps. Tectonics, 4, 687–704.

Smye, A.J., Bickle, M.J., Holland, T.J., Parrish, R.R., Condon, D.J., 2011. Rapid formation and exhumation of the youngest Alpine eclogites: a thermal conundrum to Barrovian metamorphism. Earth Planet. Sci. Lett., 306, 193–204.

Spear, F. S., Franz, G., 1986. PT evolution of metasediments from the Eclogite Zone, south-central Tauern Window, Austria. Lithos, 19, 219–234.

Stacey, J.S., Kramers, J.D., 1975. Approximation of terrestrial lead isotope evolution by a two-stage model. Earth Planet. Sci. Lett. 26, 207–221.

Steiger, R., Jäger, E., 1977. Subcommission on geochronology: convention on the use of decay constants in geo-and cosmochronology. Earth Planet. Sci. Lett., 36, 359–362.

Sylvester, P.J., Ghaderi, M., 1997. Trace element analysis of scheelite by excimer laser ablation inductively coupled plasma mass spectrometry (ELA-ICP-MS) using a synthetic glass standard. Chem. Geol. 141, 49–65.

Thomson, S.N., Gehrels, G.E., Ruiz, J., Buchwaldt. R., 2012. Routine low-damage apatite U-Pb dating using laser ablation–multicollector–ICPMS, Geochem. Geophy. Geosy. 13, Q0AA21, doi:10.1029/2011GC003928.

Thöni, M., 1980. Distribution of pre-Alpine and Alpine metamorphism of the southern Ötztal Mass and the Scarl Unit, based on K/Ar age determinations. Mitt. österr. geol. G., 71, 139–165.

Tiepolo, M., 2003. In situ Pb geochronology of zircon with laser ablation-inductively coupled plasma-sector field mass spectrometry. Chem. Geol. 199, 159–177.

Urbanek, C., Frank, W., Grasemann, B., Decker, K., 2002. Eoalpine Versus Tertiary Deformation: Dating of Heterogeneously Partitioned Strain (Tauern Window, Austria).PanGeo Austria 2002, abstract volume.

Vavra, G., Hansen, B.T., 1991. Cathodoluminescence studies and U/Pb dating of zircons in pre-Mesozoic gneisses of the Tauern Window implications for the Penninic basement evolution. Int. J. Earth Sci. 80, 703–715.

Veselá, P., Söllner, F., Finger, F., Gerdes, A., 2010. Magmato-sedimentary Carboniferous to Jurassic evolution of the western Tauern window, Eastern Alps (constraints from U-Pb zircon dating and geochemistry). Int. J. Earth Sci. 100, 993–1027.

Villa, I.M. 1998. Isotopic closure. Terra Nova 10, 42–47.

White, W.M., 2005. Geochemistry. Chapter 7: Trace Elements in Igneous Processes. 1–55.

Willigers, B.J.A., Krogstad, E.J., Wijbrans, J.R., 2001. Comparison of thermochronometers in a slowly cooled granulite terrain: Nagssugtoqidian Orogen, West Greenland. J. Petrol. 42, 1729 – 1749.

Willigers, B.J.A., Baker, J.A., Krogstad, E.J., Peate, D.W., 2002. Precise and accurate in situ Pb-Pb dating of apatite, monazite, and sphene by laser ablation multiple-collector ICP-MS. Geochim. Cosmochi. Acta, 66, 1051–1066.

Wolf, M.B., London, D. 1995. Incongruent dissolution of REE-and Sr-rich apatite in peraluminous granitic liquids: Differential apatite, monazite, and xenotime solubilities during anatexis. Am. Mineral. 80, 765-775.

Wyllie, P.J., Cox, K.G., Biggar, G.M., 1962. The habit of apatite in synthetic systems and igneous rocks. J. Petrol. 3, 238–243.

Zimmermann, R., Hammerschmidt, K., Franz, G., 1994. Eocene high pressure metamorphism in the Penninic units of the Tauern Window (Eastern Alps): evidence from ^{40}Ar–^{39}Ar dating and petrological investigations. Contrib. Mineral. Petrol. 117, 175–186.

4.13 Supplementary material

Table 1: LA-ICP-MS results of zircons

	Concentrations			Ratios							Ages (Ma)						Conc.
Analysis	**U (ppm)[a]**	**Pb (ppm)[a]**	**Th/U[a]**	**$^{207}Pb/^{235}U$[b]**	2σ (%) [c]	**$^{206}Pb/^{238}U$[b]**	2σ (%) [c]	**rho[d]**	**$^{207}Pb/^{206}Pb$[e]**	2σ (%) [c]	**$^{207}Pb/^{235}U$**	2σ	**$^{206}Pb/^{238}U$**	2σ	**$^{207}Pb/^{206}Pb$**	2σ	**(%)**
AT0911, anchored Discordia, upper intercept=300±18 Ma, MSWD=0.029																	
zcn 08	176	6.4	0.29	0.26	5.7	0.036	3.9	0.68	0.052	4.2	233	13	227.4	8.8	293	48	97
zcn 15	560	22	0.35	0.29	5.0	0.040	4.5	0.89	0.053	2.3	258	13	252	11	312	26	81
zcn 07	266	11	0.44	0.29	4.4	0.040	3.5	0.78	0.052	2.8	258	11	254.4	8.8	295	32	98
zcn 20	301	14	0.60	0.30	4.9	0.042	3.7	0.76	0.052	3.1	268	13	264.3	9.8	298	36	89
zcn 16	168	7.3	0.39	0.30	5.1	0.042	4.1	0.80	0.052	3.0	268	14	265	11	288	34	92
zcn 22	211	9.3	0.43	0.31	4.9	0.043	3.5	0.72	0.052	3.4	272	13	268.9	9.5	301	39	89
zcn 14	292	13	0.41	0.31	5.4	0.043	4.0	0.73	0.052	3.7	274	15	270	11	301	42	90
zcn 24	245	11	0.53	0.31	4.5	0.043	3.7	0.81	0.052	2.6	275	12	272	10	300	30	91
zcn 21	264	12	0.47	0.31	4.6	0.043	3.7	0.80	0.052	2.8	276	13	274	10	292	31	94
zcn 11	198	9.0	0.48	0.32	6.2	0.044	3.7	0.59	0.053	5.1	279	17	276	10	309	58	89
zcn 23	246	12	0.62	0.32	4.8	0.044	3.6	0.76	0.052	3.1	280	13	277	10	301	35	92
zcn 13	113	5.2	0.51	0.32	6.1	0.044	4.2	0.68	0.052	4.5	280	17	278	12	299	51	93
zcn 29	191	8.7	0.41	0.32	5.8	0.044	4.0	0.69	0.052	4.2	282	16	279	11	305	48	91
zcn 25	247	11	0.52	0.32	5.3	0.044	4.0	0.76	0.052	3.4	281	15	279	11	297	39	94
zcn 27	95	4.3	0.39	0.32	6.4	0.044	4.3	0.67	0.052	4.7	282	18	279	12	303	54	92
zcn 28	190	9.0	0.55	0.32	5.8	0.044	3.9	0.68	0.052	4.3	283	16	280	11	301	49	93
zcn 12	307	14	0.33	0.32	5.1	0.044	3.9	0.77	0.052	3.3	283	15	281	11	305	38	92
zcn 10	203	9.0	0.31	0.32	5.4	0.045	3.9	0.72	0.052	3.8	284	15	282	11	301	43	99
zcn 26	204	9.2	0.37	0.32	5.1	0.045	4.1	0.79	0.052	3.1	283	15	282	11	295	36	95
zcn 09	260	15	0.43	0.42	4.8	0.055	3.9	0.81	0.056	2.8	357	17	344	13	442	31	96
GT0803, Concordia age=296.5±3.9 Ma, MSWD=3.0, Probability=0.086																	
zcn 20, core	1677	52	0.86	0.23	4.4	0.032	4.3	0.96	0.052	1.3	212.9	9.5	205.1	8.7	301	15	68
zcn 36, rim	1221	50	0.85	0.32	6.1	0.043	3.7	0.61	0.053	4.9	279	17	274	10	320	55	86
zcn 07, rim	1152	48	0.11	0.32	4.0	0.044	3.4	0.86	0.054	2.0	285	11	276.5	9.5	353	23	97
zcn 16, rim	1666	69	0.35	0.32	4.1	0.044	3.7	0.91	0.052	1.7	280	11	277	10	306	19	90
zcn 12, rim	1194	50	0.68	0.33	3.8	0.045	3.5	0.92	0.053	1.5	289	11	287	10	311	17	92
zcn 10*, rim	1481	64	0.66	0.34	4.5	0.046	4.1	0.92	0.053	1.7	294	13	291	12	318	19	99
zcn 27*, rim	1011	44	1.3	0.34	4.2	0.047	3.9	0.92	0.053	1.7	296	13	294	11	311	19	95
zcn 14*, rim	1215	53	1.7	0.34	4.0	0.047	3.6	0.89	0.053	1.8	297	12	295	11	312	21	94
zcn 34*, rim	1465	64	1.0	0.34	3.8	0.047	3.6	0.96	0.052	1.1	296	11	295	11	304	13	97
zcn 25*, rim	934	41	0.74	0.34	4.6	0.047	4.1	0.90	0.052	2.0	298	14	297	12	301	22	99
zcn 23*, rim	1619	72	0.49	0.34	3.7	0.047	3.6	0.95	0.053	1.1	299	11	297	11	312	13	95
zcn 21*, rim	1123	49	0.80	0.34	3.8	0.047	3.4	0.90	0.052	1.7	298	11	298	10	292	19	102
zcn 29, rim	1124	50	1.1	0.35	4.1	0.048	3.5	0.86	0.053	2.1	305	12	302	11	328	24	92
zcn 09, core	283	17	0.42	0.40	4.2	0.054	3.6	0.85	0.054	2.2	341	14	338	12	364	25	99
zcn 24, core	902	62	2.5	0.52	4.1	0.067	3.7	0.90	0.056	1.8	424	17	417	15	459	20	91
zcn 26, core	511	39	0.88	0.55	4.0	0.071	3.5	0.87	0.056	2.0	445	18	444	16	450	22	99
zcn 22, core	429	30	2.1	0.58	4.8	0.074	3.7	0.76	0.056	3.1	463	22	462	17	468	35	99
zcn 08, core	368	28	0.60	0.59	4.2	0.076	3.6	0.87	0.056	2.1	469	20	474	17	448	23	101
zcn 15, core	376	29	1.2	0.61	4.5	0.077	3.9	0.87	0.057	2.2	481	21	480	19	483	25	99
zcn 13, core	264	22	0.97	0.73	4.9	0.082	4.3	0.87	0.064	2.4	555	27	507	22	755	25	67
zcn 37, core	327	28	1.3	0.72	4.9	0.089	3.8	0.77	0.059	3.1	551	27	547	21	565	33	97
zcn 11, core	300	32	0.99	0.76	4.4	0.094	3.7	0.85	0.059	2.3	577	25	577	21	575	25	100
zcn 28, core	379	42	0.29	0.80	4.3	0.096	3.7	0.86	0.061	2.2	598	26	591	22	626	23	94
zcn 33, core	119	13	0.86	0.90	5.8	0.11	3.5	0.59	0.061	4.7	652	38	651	22	655	50	99
zcn 35, core	463	55	0.35	0.91	5.2	0.11	3.9	0.76	0.062	3.3	658	34	653	26	673	36	97
GT0804, inherited ages																	
zcn 035	1781	64	0.043	0.27	6.3	0.038	4.7	0.74	0.052	4.2	244	15	239	11	293	48	81
zcn 008	406	18	0.47	0.31	4.8	0.044	3.9	0.82	0.052	2.8	278	13	275	11	300	32	92
zcn 029	980	50	0.70	0.33	8.3	0.045	4.2	0.51	0.052	7.1	288	24	286	12	301	81	95
zcn 028	312	16	0.13	0.42	5.3	0.052	4.2	0.81	0.059	3.1	358	19	329	14	552	34	60
zcn 033	650	34	0.030	0.41	7.8	0.055	4.6	0.59	0.054	6.3	349	27	347	16	357	71	97
zcn 020	1097	62	0.17	0.45	5.0	0.060	4.0	0.79	0.054	3.1	375	19	375	15	375	35	100
zcn 007	365	22	0.20	0.50	5.2	0.062	4.1	0.78	0.058	3.2	410	21	387	16	546	35	71
zcn 024	365	25	0.36	0.52	5.4	0.067	4.4	0.83	0.056	3.0	423	23	415	18	465	33	89
zcn 015	642	41	0.14	0.55	4.3	0.068	3.9	0.93	0.059	1.6	444	19	423	17	552	17	77
zcn 013	488	33	0.22	0.52	4.5	0.068	4.2	0.93	0.056	1.6	428	19	426	18	437	18	97
zcn 027	404	28	0.27	0.53	5.0	0.069	4.1	0.82	0.056	2.9	431	22	428	18	446	32	96
zcn 021	560	36	0.084	0.52	5.0	0.069	4.5	0.90	0.055	2.2	428	22	430	19	415	25	103
zcn 016	564	37	0.14	0.54	4.7	0.070	4.3	0.91	0.056	2.0	437	21	434	18	454	22	96
zcn 012	432	29	0.13	0.53	4.4	0.070	3.9	0.90	0.055	1.9	434	19	434	17	430	22	101
zcn 014	209	15	0.30	0.55	5.0	0.070	4.1	0.83	0.057	2.8	444	22	435	18	493	31	88
zcn 011	376	27	0.33	0.53	5.1	0.070	4.3	0.85	0.055	2.7	432	22	437	19	407	30	108
zcn 009	177	13	0.50	0.54	5.8	0.070	4.2	0.73	0.056	3.9	440	25	438	18	452	44	97
zcn 010	998	82	1.1	0.59	4.6	0.072	3.9	0.85	0.060	2.4	472	22	445	17	601	26	74
zcn 038	346	25	0.37	0.55	5.2	0.072	4.2	0.81	0.056	3.1	447	23	449	19	438	34	102
zcn 023	282	21	0.21	0.61	8.7	0.073	4.3	0.49	0.060	7.6	485	42	456	20	621	82	73
zcn 025	318	23	0.27	0.61	4.9	0.074	4.2	0.84	0.060	2.6	486	24	458	19	618	28	74
zcn 026	152	11	0.22	0.62	5.6	0.076	4.2	0.74	0.059	3.7	489	27	470	20	580	41	81
zcn 022	1335	117	0.15	0.76	4.3	0.092	4.1	0.96	0.060	1.2	572	24	566	23	595	13	95
zcn 037	679	77	1.1	0.79	7.2	0.095	4.1	0.57	0.060	5.9	591	43	587	24	604	64	97
zcn 036	382	36	0.20	0.80	4.7	0.096	4.1	0.87	0.061	2.3	597	28	590	24	622	24	95
zcn 034	150	16	0.78	0.79	5.7	0.097	4.4	0.77	0.060	3.6	594	34	595	26	590	39	101

Table 1: LA-ICP-MS results of zircons

	Concentrations			Ratios								Ages (Ma)						Conc.
Analysis	**U (ppm)[a]**	**Pb (ppm)[a]**	**Th/U[a]**	**$^{207}Pb/^{235}U$[b]**	2σ (%) [c]	**$^{206}Pb/^{238}U$[b]**	2σ (%) [c]	**rho[d]**	**$^{207}Pb/^{206}Pb$[e]**	2σ (%) [c]	**$^{207}Pb/^{235}U$**	2σ	**$^{206}Pb/^{238}U$**	2σ	**$^{207}Pb/^{206}Pb$**	2σ	**(%)**
HT0901, Concordia age=293.6±3.0 Ma, MSWD=0.14, Probability=0.71																	
zcn 25	2323	56	0.29	0.18	4.0	0.025	3.8	0.95	0.052	1.2	166.0	6.6	156.9	5.9	298	14	53
zcn 13	521	20	0.32	0.28	8.1	0.038	3.9	0.48	0.052	7.1	247	20	240.5	9.4	307	81	78
zcn 29	949	38	0.33	0.29	7.8	0.040	3.7	0.48	0.052	6.8	259	20	254.9	9.5	292	78	87
zcn 15	647	27	0.55	0.29	6.8	0.040	3.7	0.55	0.052	5.6	260	18	255.3	9.5	298	64	86
zcn 10	1182	48	0.26	0.30	5.9	0.041	4.1	0.69	0.052	4.3	263	16	259	11	292	49	99
zcn 38	298	12	0.18	0.30	4.6	0.041	3.9	0.84	0.052	2.5	264	12	260	10	299	28	87
zcn 14	1673	68	0.27	0.30	4.0	0.042	3.8	0.93	0.053	1.4	270	11	265	10	312	16	85
zcn 28	350	15	0.31	0.31	4.6	0.043	3.7	0.81	0.052	2.7	273	12	270	10	298	30	91
zcn 23	476	21	0.32	0.32	4.8	0.045	3.8	0.79	0.052	3.0	283	14	281	11	300	34	94
zcn 07	593	26	0.31	0.32	4.5	0.045	3.9	0.87	0.052	2.2	283	13	282	11	296	25	99
zcn 20*	342	16	0.37	0.33	4.5	0.046	3.5	0.78	0.052	2.8	289	13	288	10	291	32	99
zcn 11*	852	39	0.31	0.33	4.3	0.046	3.8	0.88	0.052	2.0	290	12	289	11	295	23	98
zcn 27*	323	16	0.62	0.33	4.5	0.046	3.9	0.87	0.052	2.3	291	13	289	11	302	26	96
zcn 34*	569	27	0.53	0.33	4.2	0.046	3.8	0.91	0.052	1.7	292	12	291	11	299	20	97
zcn 33*	443	22	0.64	0.34	4.3	0.047	3.5	0.82	0.052	2.4	294	13	293	10	301	28	98
zcn 08	175	8	0.28	0.34	5.7	0.047	3.6	0.63	0.053	4.4	296	17	294	11	310	51	99
zcn 22*	267	13	0.51	0.34	4.7	0.047	3.6	0.78	0.052	2.9	294	14	294	11	288	33	102
zcn 36*	583	28	0.57	0.34	4.3	0.047	3.8	0.88	0.052	2.0	295	13	294	11	303	23	97
zcn 37	333	16	0.51	0.34	4.5	0.047	3.7	0.81	0.052	2.6	294	13	295	11	289	30	102
zcn 09*	957	44	0.27	0.34	4.4	0.047	4.1	0.93	0.052	1.6	295	13	295	12	294	18	100
zcn 21*	407	20	0.50	0.34	4.7	0.047	3.5	0.75	0.052	3.1	296	14	295	10	303	36	97
zcn 39*	750	35	0.37	0.34	3.9	0.047	3.4	0.88	0.052	1.8	297	11	297	10	295	21	101
zcn 26*	276	13	0.35	0.34	4.4	0.047	3.7	0.85	0.052	2.3	298	13	298	11	295	26	101
zcn 35*	440	21	0.41	0.34	4.5	0.047	3.7	0.81	0.052	2.7	298	13	299	11	291	30	103
PT0802b, Concordia age=293.6±2.6 Ma, MSWD=0.013, Probability=0.91																	
zcn 38	1742	49	1.2	0.15	6.4	0.021	3.7	0.57	0.052	5.3	141.5	9.1	132.2	4.9	301	60	44
zcn 07	1946	42	0.27	0.16	4.3	0.022	3.9	0.91	0.052	1.8	146.7	6.3	137.2	5.3	304	21	93
zcn 16	2101	75	0.65	0.17	7.0	0.024	5.1	0.74	0.052	4.7	163	11	154.4	8.0	294	54	52
zcn 12	1456	41	0.26	0.21	5.2	0.028	4.7	0.89	0.053	2.4	190.0	9.9	179.7	8.4	321	27	56
zcn 33	1076	42	0.46	0.28	4.7	0.039	3.9	0.83	0.052	2.6	249	12	244.0	9.6	298	30	82
zcn 29	1068	41	0.32	0.28	4.0	0.039	3.4	0.85	0.052	2.1	253	10	249.3	8.4	291	24	86
zcn 35	690	29	0.38	0.30	4.2	0.042	3.6	0.87	0.052	2.1	268	11	265.8	9.6	285	24	93
zcn 39	807	38	0.94	0.31	4.5	0.042	3.6	0.80	0.053	2.7	272	12	267.1	9.5	318	31	84
zcn 08	1157	49	0.32	0.31	4.1	0.043	3.3	0.79	0.053	2.5	275	11	271.1	8.9	310	29	99
zcn 09	1213	54	0.37	0.32	4.1	0.044	3.7	0.90	0.052	1.8	281	11	279	10	292	20	99
zcn 11*	957	42	0.30	0.33	4.9	0.045	4.4	0.91	0.052	2.0	288	14	287	13	302	23	95
zcn 22*	557	24	0.21	0.33	4.1	0.046	3.4	0.82	0.052	2.4	288	12	287.8	9.8	294	27	98
zcn 21*	739	34	0.31	0.33	4.1	0.046	3.6	0.88	0.052	2.0	289	12	289	10	294	23	98
zcn 24*	637	29	0.30	0.33	4.2	0.046	3.6	0.86	0.052	2.1	290	12	290	10	293	24	99
zcn 28*	342	16	0.36	0.33	4.9	0.046	3.3	0.69	0.052	3.5	292	14	292.0	9.7	288	40	102
zcn 23*	557	25	0.21	0.33	4.1	0.046	3.4	0.82	0.052	2.4	292	12	292.1	9.9	294	27	99
zcn 37*	781	36	0.35	0.33	4.0	0.046	3.5	0.87	0.052	2.0	293	12	292	10	299	23	98
zcn 15*	950	44	0.34	0.34	4.6	0.047	4.2	0.90	0.052	2.0	296	14	296	12	296	23	100
zcn 25	1178	56	0.50	0.34	4.2	0.047	3.8	0.89	0.053	2.0	300	13	296	11	330	22	89
zcn 27*	820	38	0.33	0.34	4.1	0.047	3.5	0.85	0.052	2.2	297	12	296	10	300	25	99
zcn 34*	717	33	0.33	0.34	4.1	0.047	3.5	0.85	0.052	2.2	296	12	297	10	294	25	101
zcn 14*	649	30	0.26	0.34	4.3	0.047	3.4	0.78	0.052	2.7	296	13	297	10	291	30	102
zcn 13*	854	39	0.28	0.34	5.1	0.047	4.6	0.91	0.052	2.1	296	15	297	14	287	24	104
zcn 36*	173	9	0.68	0.34	5.1	0.047	3.7	0.73	0.052	3.5	298	15	298	11	295	40	101
zcn 10*	866	41	0.37	0.34	3.9	0.047	3.3	0.84	0.052	2.1	298	12	298.1	9.9	298	24	100
zcn 20*	899	42	0.33	0.34	3.9	0.047	3.5	0.90	0.052	1.7	298	12	299	10	291	19	103
PT0820, Concordia age=290.3±3.2 Ma, MSWD=0.109, Probability=0.74																	
zcn 36	3292	16	0.059	0.034	14	0.0047	3.9	0.28	0.052	13	33.6	4.7	30.1	1.2	285	154	11
zcn 09	4922	69	0.27	0.10	7.5	0.013	4.2	0.56	0.052	6.2	93.6	7.1	86.4	3.7	281	71	92
zcn 34	4317	65	0.26	0.11	6.2	0.015	4.4	0.71	0.052	4.4	104.4	6.5	96.0	4.2	300	50	32
zcn 35	1853	39	0.28	0.15	5.0	0.021	4.8	0.94	0.053	1.7	143.5	7.2	133.3	6.3	315	19	42
zcn 10	2075	65	0.21	0.24	5.0	0.032	4.7	0.93	0.053	1.8	216	11	205.8	9.7	332	20	95
zcn 29	1040	36	0.50	0.23	5.9	0.032	5.6	0.94	0.052	2.0	213	13	206	12	295	23	70
zcn 08	963	41	0.62	0.28	8.5	0.039	4.0	0.47	0.052	7.5	248	21	243.8	9.8	287	86	98
zcn 28	539	23	0.38	0.31	5.3	0.043	4.6	0.87	0.053	2.6	277	15	271	13	323	30	84
zcn 11	271	12	0.40	0.32	5.3	0.044	4.2	0.78	0.052	3.4	279	15	276	11	307	38	90
zcn 24*	316	14	0.33	0.32	5.0	0.044	4.1	0.82	0.052	2.9	280	14	279	11	292	33	96
zcn 26*	366	16	0.38	0.32	5.5	0.045	4.2	0.76	0.052	3.6	283	16	282	12	291	41	97
zcn 12*	629	31	0.68	0.32	5.3	0.045	4.6	0.88	0.052	2.5	285	15	284	13	288	28	99
zcn 20*	567	27	0.64	0.33	5.1	0.045	4.1	0.81	0.052	3.0	286	15	285	12	295	34	97
zcn 23*	337	16	0.57	0.33	5.3	0.046	4.6	0.87	0.052	2.6	289	15	288	13	297	30	97
zcn 27*	731	33	0.39	0.33	4.9	0.046	4.5	0.93	0.052	1.8	290	14	290	13	291	21	99
zcn 22*	324	15	0.39	0.33	5.3	0.046	3.9	0.74	0.052	3.6	290	15	290	11	285	41	102
zcn 16*	580	27	0.45	0.33	4.9	0.046	4.3	0.88	0.052	2.3	291	14	291	13	288	27	101
zcn 14*	411	19	0.38	0.33	5.0	0.046	4.3	0.85	0.052	2.6	292	15	292	12	298	30	98
zcn 33*	443	21	0.49	0.34	4.8	0.047	4.1	0.85	0.052	2.5	295	14	295	12	292	29	101
zcn 21*	388	19	0.45	0.34	5.6	0.047	4.2	0.75	0.052	3.7	297	17	296	12	300	43	99
zcn 07*	343	16	0.40	0.34	5.2	0.047	4.1	0.79	0.052	3.2	297	15	297	12	297	37	100
zcn 13*	249	12	0.50	0.34	5.3	0.047	4.2	0.80	0.052	3.2	298	16	298	13	301	37	99
zcn 25*	830	40	0.50	0.34	5.4	0.048	5.0	0.93	0.052	1.9	299	16	299	15	294	22	102

Table 1: LA-ICP-MS results of zircons

	Concentrations			Ratios							Ages (Ma)						Conc.
Analysis	U (ppm)[a]	Pb (ppm)[a]	Th/U[a]	$^{207}Pb/^{235}U$[b]	2σ (%)[c]	$^{206}Pb/^{238}U$[b]	2σ (%)[c]	rho[d]	$^{207}Pb/^{206}Pb$[e]	2σ (%)[c]	$^{207}Pb/^{235}U$	2σ	$^{206}Pb/^{238}U$	2σ	$^{207}Pb/^{206}Pb$	2σ	(%)
TVT0801, Concordia age=295.5±4.0 Ma, MSWD=0.029, Probability=0.87																	
zcn 15	1175	24	0.29	0.15	5.1	0.020	4.2	0.83	0.053	2.8	138.2	7.0	128.2	5.4	314	32	41
zcn 23	2672	56	0.32	0.15	4.8	0.021	3.9	0.80	0.052	2.9	146.0	7.0	136.4	5.3	306	33	45
zcn 22	1028	24	0.37	0.16	6.6	0.022	4.0	0.61	0.052	5.3	152	10	143.2	5.8	290	60	49
zcn 21	662	19	0.25	0.20	6.2	0.028	4.8	0.76	0.052	4.0	185	12	175.5	8.4	303	46	58
zcn 13	1351	41	0.24	0.22	5.8	0.031	5.5	0.95	0.052	1.9	203	12	195	11	306	21	64
zcn 25	2968	89	0.27	0.23	4.5	0.031	4.1	0.91	0.053	1.8	208.0	9.3	199.2	8.2	309	21	65
zcn 27	2424	78	0.27	0.24	5.3	0.033	5.2	0.97	0.052	1.3	216	12	208	11	297	15	70
zcn 12	1642	55	0.30	0.25	4.5	0.034	4.3	0.95	0.052	1.3	222.6	9.9	214.9	9.2	305	15	71
zcn 16	1143	48	0.73	0.27	4.3	0.038	3.9	0.90	0.052	1.9	244	11	239.1	9.3	294	22	81
zcn 07	1111	43	0.30	0.28	5.1	0.039	4.6	0.91	0.052	2.1	251	13	246	11	303	24	98
zcn 24	488	22	0.40	0.32	5.4	0.044	4.2	0.78	0.052	3.4	278	15	276	11	297	39	93
zcn 10*	505	26	1.00	0.33	9.3	0.045	3.7	0.40	0.052	8.5	287	27	287	11	287	97	100
zcn 14*	414	19	0.41	0.33	4.8	0.045	3.6	0.75	0.052	3.2	288	14	287	10	300	36	95
zcn 20*	463	22	0.45	0.34	4.6	0.047	3.5	0.77	0.052	3.0	297	14	297	10	297	34	100
zcn 28*	367	17	0.34	0.34	6.2	0.047	5.5	0.88	0.052	3.0	297	19	297	16	296	34	100
zcn 29*	708	33	0.34	0.34	4.9	0.047	4.5	0.91	0.052	2.0	297	15	298	13	294	23	101
zcn 33*	303	15	0.55	0.34	5.4	0.047	4.3	0.80	0.052	3.2	298	16	298	13	300	37	99
zcn 09*	979	45	0.22	0.34	4.6	0.048	3.8	0.83	0.052	2.6	299	14	300	11	294	30	100
zcn 08*	485	23	0.27	0.35	4.3	0.049	3.6	0.85	0.052	2.2	305	13	306	11	304	25	100
TVT0809, anchored Discordia, upper intercept 296±13 Ma, MSWD=0.32																	
zcn 09	9077	86	0.087	0.071	7.6	0.0099	6.7	0.88	0.052	3.7	69.3	5.3	63.3	4.2	284	42	91
zcn 22	3104	60	0.22	0.14	4.4	0.020	4.1	0.93	0.053	1.6	137.5	6.0	127.2	5.2	319	18	40
zcn 10	2096	45	0.16	0.16	8.3	0.022	7.8	0.94	0.053	2.9	153	13	141	11	348	32	92
zcn 21	5960	135	0.18	0.17	4.0	0.024	3.8	0.95	0.052	1.2	159.2	6.4	150.3	5.7	294	14	51
zcn 12	1105	30	0.27	0.20	9.5	0.027	9.0	0.95	0.052	2.9	183	17	175	16	296	34	59
zcn 08	3336	108	0.22	0.24	4.5	0.033	4.0	0.89	0.052	2.1	219.6	9.9	212.3	8.5	298	24	97
zcn 23	993	36	0.36	0.26	4.1	0.036	3.6	0.88	0.052	2.0	232.4	9.6	227.1	8.3	287	22	79
zcn 24	1939	73	0.27	0.28	4.2	0.039	3.9	0.93	0.052	1.6	248	10	244.0	9.4	285	18	86
zcn 28	536	20	0.20	0.28	4.6	0.040	3.7	0.79	0.052	2.8	254	12	250.3	9.2	289	32	87
zcn 11	774	32	0.34	0.29	4.6	0.041	4.0	0.85	0.052	2.4	261	12	257	10	301	27	85
zcn 07	358	15	0.34	0.29	5.8	0.041	4.1	0.70	0.052	4.1	262	15	259	11	292	47	99
zcn 27	493	21	0.44	0.30	4.7	0.042	4.1	0.88	0.052	2.2	266	12	263	11	291	25	90
zcn 25	403	17	0.33	0.31	4.8	0.043	4.0	0.82	0.052	2.7	273	13	271	11	292	31	93
zcn 16	421	20	0.70	0.31	4.7	0.044	3.6	0.77	0.052	3.0	276	13	274.8	9.9	287	34	96
zcn 14	1001	43	0.23	0.32	4.1	0.044	3.6	0.88	0.052	1.9	280	12	279	10	290	22	96
zcn 29	155	6.9	0.36	0.32	5.1	0.045	4.0	0.79	0.052	3.1	284	14	283	11	289	36	98
zcn 20	394	19	0.59	0.34	4.5	0.047	3.7	0.82	0.052	2.6	296	13	296	11	290	30	102
US0901, anchored Discordia, upper intercept 315±13 Ma, MSWD=0.24																	
zcn 16	1088	38	0.51	0.24	11	0.033	4.3	0.39	0.052	10	215	24	208.4	9.0	282	117	74
zcn 08	536	21	0.68	0.27	11	0.038	3.6	0.33	0.052	10	245	26	241.4	8.7	281	116	98
zcn 07	601	26	0.61	0.28	5.7	0.039	4.2	0.73	0.052	3.9	251	14	247	10	284	45	99
zcn 26	702	30	0.36	0.30	4.9	0.042	4.2	0.86	0.052	2.5	268	13	264	11	302	29	87
zcn 35	489	23	0.47	0.32	9.5	0.044	4.0	0.42	0.052	8.7	278	27	276	11	297	99	93
zcn 22	1105	48	0.34	0.32	4.1	0.044	3.8	0.93	0.053	1.5	283	12	277	11	330	17	84
zcn 15	1184	53	0.29	0.33	4.5	0.045	4.0	0.89	0.053	2.0	290	13	285	11	329	23	87
zcn 13	665	31	0.53	0.33	4.1	0.046	3.6	0.87	0.053	2.1	291	12	288	10	319	23	90
zcn 38	734	37	0.61	0.33	9.0	0.046	3.9	0.44	0.052	8.1	293	26	291	11	302	92	97
zcn 20	605	40	1.3	0.33	9.6	0.046	4.0	0.41	0.052	8.8	291	28	292	12	289	100	101
zcn 11	728	39	0.39	0.33	12	0.046	3.9	0.31	0.052	12	292	36	292	11	287	134	102
zcn 09	170	7.9	0.34	0.33	4.8	0.046	3.8	0.80	0.052	2.9	292	14	293	11	286	33	100
zcn 10	327	16	0.51	0.34	4.7	0.047	3.8	0.81	0.052	2.7	296	14	295	11	305	31	100
zcn 34	413	22	0.30	0.35	7.1	0.049	3.6	0.51	0.053	6.1	308	22	306	11	323	69	95
US0902, Concordia age=295.8±5.7 Ma, MSWD=0.015, Probability=0.90																	
zcn 47	3551	39	0.17	0.07	18	0.010	4.6	0.26	0.052	17	73	13	66.2	3.0	298	195	22
zcn 54	4326	56	0.10	0.078	26	0.011	25	0.98	0.053	5.4	77	20	69	18	311	61	22
zcn 50	2462	47	0.22	0.13	9.9	0.017	4.6	0.47	0.053	8.7	121	12	111.2	5.2	321	99	35
zcn 46	1140	30	1.2	0.14	13	0.020	4.8	0.38	0.052	12	137	17	128.3	6.1	291	134	44
zcn 62	1727	41	0.59	0.15	12	0.021	5.6	0.47	0.052	11	143	17	134.7	7.6	283	122	48
zcn 53	2221	50	0.43	0.16	9.7	0.022	6.3	0.65	0.052	7.3	147	14	137.9	8.7	292	84	47
zcn 49	1187	33	0.79	0.17	15	0.024	7.5	0.49	0.052	13	161	24	152	11	288	151	53
zcn 68	1349	44	0.30	0.19	12	0.026	4.5	0.37	0.052	11	176	21	166.7	7.5	303	127	55
zcn 60	2213	65	0.25	0.22	7.8	0.030	4.5	0.57	0.052	6.4	200	16	191.7	8.6	296	73	65
zcn 51	1797	59	0.35	0.23	7.7	0.032	4.0	0.52	0.052	6.6	212	16	206.2	8.3	280	75	74
zcn 63	1830	83	0.27	0.26	11	0.036	6.7	0.60	0.052	9.1	234	26	228	15	296	103	77
zcn 48*	801	39	0.72	0.33	9.2	0.046	4.9	0.53	0.052	7.8	290	27	290	14	289	90	100
zcn 65*	1613	72	0.23	0.34	9.3	0.046	4.6	0.49	0.053	8.1	295	28	292	13	314	92	93
zcn 66*	437	21	0.46	0.34	5.6	0.047	4.1	0.73	0.052	3.8	294	16	295	12	292	43	101
zcn 52*	1724	97	0.78	0.34	9.8	0.047	5.0	0.51	0.052	8.4	297	29	296	15	298	96	99
zcn 61*	610	28	0.18	0.35	5.2	0.048	4.1	0.79	0.052	3.2	303	16	303	12	303	36	100

Table 1: LA-ICP-MS results of zircons

	Concentrations			Ratios							Ages (Ma)						Conc.
Analysis	**U (ppm)[a]**	**Pb (ppm)[a]**	**Th/U[a]**	**$^{207}Pb/^{235}U$[b]**	2σ (%) [c]	**$^{206}Pb/^{238}U$[b]**	2σ (%) [c]	**rho[d]**	**$^{207}Pb/^{206}Pb$[e]**	2σ (%) [c]	**$^{207}Pb/^{235}U$**	2σ	**$^{206}Pb/^{238}U$**	2σ	**$^{207}Pb/^{206}Pb$**	2σ	**(%)**
US0905, Concordia age=295.8±2.6 Ma, MSWD=0.018, Probability=0.68																	
zcn 07	1624	70	0.50	0.29	4.1	0.041	3.8	0.93	0.052	1.4	261	11	257.1	9.8	300	16	98
zcn 22, core	724	31	0.28	0.31	3.8	0.043	3.5	0.92	0.052	1.5	272	10	268.9	9.4	296	17	91
zcn 08, core	744	37	0.97	0.32	5.4	0.044	5.0	0.92	0.053	2.2	282	15	279	14	309	25	99
zcn 36	240	11	0.39	0.32	4.8	0.044	3.6	0.75	0.052	3.2	282	13	279.2	9.9	301	36	93
zcn 38	239	11	0.41	0.32	4.8	0.045	3.4	0.72	0.052	3.3	283	13	280.9	9.7	297	38	95
zcn 23, rim	291	13	0.34	0.32	5.3	0.045	3.6	0.68	0.052	3.9	282	15	281	10	291	45	97
zcn 09, rim	687	33	0.48	0.33	4.5	0.045	3.7	0.82	0.052	2.6	286	13	284	10	297	30	100
zcn 37	602	30	0.60	0.33	4.2	0.045	3.7	0.88	0.052	2.0	287	12	285	10	305	22	93
zcn 39*	630	31	0.62	0.33	5.4	0.046	3.8	0.70	0.052	3.9	288	16	288	11	288	44	100
zcn 16*	575	29	0.59	0.33	4.3	0.046	3.5	0.82	0.052	2.5	292	13	291	10	299	28	98
zcn 21*	376	18	0.46	0.33	4.8	0.046	3.9	0.82	0.052	2.8	292	14	291	12	301	31	97
zcn 15*	263	13	0.43	0.33	5.2	0.046	3.5	0.67	0.052	3.9	292	15	293	10	289	44	101
zcn 34*	298	14	0.41	0.34	4.5	0.047	3.6	0.80	0.052	2.7	294	13	294	11	294	31	100
zcn 11*	259	12	0.38	0.34	4.5	0.047	3.5	0.78	0.052	2.8	295	13	295	10	299	32	98
zcn 35*	246	12	0.37	0.34	4.8	0.047	3.8	0.79	0.052	2.9	296	14	296	11	296	33	100
zcn 10*	493	23	0.34	0.34	4.9	0.047	4.1	0.82	0.052	2.8	296	15	296	12	296	32	100
zcn 20*	569	28	0.50	0.34	4.3	0.047	3.6	0.82	0.052	2.4	297	13	296	11	306	28	97
zcn 12*	249	12	0.41	0.34	4.7	0.047	3.6	0.77	0.052	3.0	298	14	298	11	300	34	99
zcn 27*	300	14	0.38	0.34	4.8	0.047	3.9	0.82	0.052	2.8	297	14	298	12	289	32	103
zcn 13*	625	31	0.48	0.34	4.7	0.047	4.0	0.85	0.052	2.4	298	14	298	12	293	28	102
zcn 14*	159	8	0.45	0.34	6.2	0.047	3.6	0.58	0.052	5.0	299	18	299	11	300	57	100
zcn 28*	338	17	0.44	0.34	4.8	0.047	3.7	0.78	0.052	3.0	299	14	299	11	303	34	98
zcn 26*	625	31	0.51	0.34	4.2	0.047	3.7	0.90	0.053	1.8	300	12	299	11	309	21	97
zcn 25*, rim	316	15	0.38	0.34	5.5	0.048	4.0	0.73	0.052	3.7	299	16	299	12	300	43	100
zcn 33*	417	20	0.41	0.34	4.4	0.048	3.7	0.84	0.052	2.4	300	13	299	11	301	27	99
zcn 24, core	419	34	0.17	0.70	4.6	0.086	3.7	0.81	0.059	2.7	538	25	529	20	579	29	91
US0906, Concordia age=295.1±4.2 Ma, MSWD=0.46, Probability=0.50																	
zcn 047	3076	48	0.24	0.11	7.8	0.016	5.3	0.69	0.052	5.7	108.0	8.4	99.5	5.3	299	65	92
zcn 048	1856	45	0.32	0.17	11	0.024	3.9	0.37	0.052	10	161	17	151.8	6.0	300	114	94
zcn 063, rim	2058	55	0.28	0.20	6.9	0.027	4.1	0.60	0.053	5.5	184	13	174.2	7.2	313	62	95
zcn 049	1139	39	0.61	0.25	5.1	0.034	4.5	0.89	0.053	2.3	226	12	218.5	9.9	309	27	97
zcn 062, rim	1463	50	0.22	0.25	4.8	0.035	4.2	0.88	0.052	2.2	228	11	221.3	9.3	296	26	97
zcn 060	1414	54	0.47	0.27	5.1	0.037	4.7	0.92	0.053	2.0	239	12	232	11	314	22	97
zcn 050	1866	75	0.31	0.30	4.1	0.041	3.8	0.91	0.052	1.7	263	11	258.1	9.7	302	19	98
zcn 066	474	19	0.34	0.29	5.0	0.041	4.2	0.85	0.052	2.6	262	13	259	11	292	30	99
zcn 064	1367	58	0.29	0.31	4.7	0.043	4.1	0.87	0.053	2.3	276	13	271	11	318	26	98
zcn 046	1293	55	0.23	0.32	4.9	0.044	4.3	0.88	0.052	2.3	280	14	277	12	302	26	99
zcn 067*	1349	60	0.22	0.33	4.2	0.046	3.8	0.90	0.052	1.8	290	12	288	11	302	21	99
zcn 053	855	41	0.56	0.34	4.9	0.046	4.2	0.85	0.053	2.6	296	15	291	12	342	29	98
zcn 059	1642	74	0.26	0.34	4.2	0.046	3.8	0.90	0.053	1.8	296	12	292	11	331	20	99
zcn 068*	881	41	0.31	0.33	4.5	0.046	3.9	0.86	0.052	2.3	293	13	292	11	294	26	100
zcn 054*	633	29	0.32	0.34	5.3	0.046	4.1	0.77	0.052	3.4	294	16	293	12	303	39	100
zcn 051*	832	40	0.43	0.34	4.7	0.047	3.9	0.84	0.053	2.5	298	14	297	12	308	29	100
zcn 055*	628	29	0.23	0.34	4.7	0.047	4.0	0.86	0.052	2.4	297	14	297	12	291	27	100
zcn 065*	1221	56	0.22	0.34	4.2	0.047	3.8	0.91	0.052	1.8	298	12	298	11	304	20	100
zcn 052*	1030	47	0.24	0.34	4.5	0.047	4.0	0.90	0.052	1.9	299	13	299	12	305	22	100
zcn 061, core	280	25	0.17	0.78	4.7	0.094	3.9	0.83	0.060	2.6	586	27	581	23	605	28	99
WG0902, Concordia age=295.8±4.0 Ma, MSWD=0.114, Probability=0.74																	
zcn 62	1856	50	0.23	0.19	4.8	0.027	3.4	0.71	0.053	3.4	179.1	8.6	169.5	5.8	308	39	55
zcn 66	1067	31	0.29	0.21	5.0	0.029	4.2	0.84	0.052	2.7	193	10	184.5	7.8	300	31	61
zcn 59	2549	73	0.26	0.21	5.5	0.029	5.2	0.95	0.053	1.8	194	11	185	10	312	20	59
zcn 55	1976	62	0.24	0.23	6.5	0.032	3.7	0.57	0.052	5.4	209	14	201.3	7.5	296	61	68
zcn 76	2371	75	0.27	0.23	5.0	0.032	3.5	0.70	0.052	3.5	213	11	205.2	7.1	300	40	68
zcn 46	2069	69	0.51	0.23	7.3	0.032	3.3	0.46	0.052	6.5	213	16	205.3	6.8	302	74	96
zcn 51	1475	49	0.22	0.23	5.9	0.033	3.5	0.59	0.052	4.8	214	13	206.5	7.2	301	55	69
zcn 50	1291	48	0.32	0.27	4.8	0.037	4.5	0.93	0.052	1.8	241	12	234	10	304	20	77
zcn 79	1311	51	0.30	0.28	5.8	0.038	3.3	0.58	0.052	4.7	248	14	242.8	8.1	299	54	81
zcn 68	1533	59	0.24	0.28	3.8	0.040	3.5	0.92	0.052	1.4	253.3	9.5	250.5	8.7	280	16	90
zcn 77	1465	60	0.35	0.30	4.0	0.041	3.4	0.84	0.052	2.2	263	11	259.5	8.8	291	25	89
zcn 52	1253	51	0.25	0.30	4.2	0.042	3.6	0.86	0.052	2.1	268	11	264	10	301	24	88
zcn 63	1118	47	0.37	0.30	3.9	0.042	3.2	0.82	0.052	2.3	269	11	264.7	8.5	304	26	87
zcn 48	343	15	0.32	0.31	4.4	0.043	3.2	0.72	0.053	3.0	277	12	273.0	8.6	311	34	99
zcn 74	714	31	0.24	0.32	3.6	0.044	3.1	0.85	0.052	1.9	281	10	279.4	8.6	296	22	94
zcn 60	1359	61	0.38	0.32	4.8	0.045	3.1	0.64	0.052	3.7	283	14	281.1	8.7	300	42	94
zcn 75	1754	77	0.32	0.32	4.5	0.045	3.9	0.86	0.053	2.3	284	13	281	11	308	26	91
zcn 54	1347	60	0.32	0.33	4.2	0.045	3.5	0.83	0.053	2.4	289	12	287	10	313	27	92
zcn 49*	736	33	0.21	0.33	4.5	0.046	3.5	0.78	0.053	2.8	293	13	291	10	308	32	99
zcn 47*	654	30	0.26	0.34	4.3	0.047	3.4	0.78	0.052	2.7	295	13	294.4	9.9	296	31	100
zcn 73*	521	24	0.25	0.34	4.4	0.047	3.6	0.81	0.052	2.6	294	13	295	11	288	29	102
zcn 67*	1083	50	0.31	0.34	3.8	0.047	3.2	0.85	0.052	2.0	296	11	295.2	9.6	306	22	97
zcn 53*	1343	61	0.24	0.34	3.8	0.047	3.4	0.89	0.052	1.7	296	11	296	10	297	20	100
zcn 64*	475	25	0.56	0.35	4.3	0.048	3.5	0.80	0.052	2.6	304	13	304	11	302	30	100

Table 1: LA-ICP-MS results of zircons

	Concentrations			Ratios							Ages (Ma)						Conc.
Analysis	U (ppm)[a]	Pb (ppm)[a]	Th/U[a]	$^{207}Pb/^{235}U$[b]	2σ (%)[c]	$^{206}Pb/^{238}U$[b]	2σ (%)[c]	rho[d]	$^{207}Pb/^{206}Pb$[e]	2σ (%)[c]	$^{207}Pb/^{235}U$	2σ	$^{206}Pb/^{238}U$	2σ	$^{207}Pb/^{206}Pb$	2σ	(%)
WG0904, anchored Discordia, upper intercept 304±17 Ma, MSWD=0.19																	
zcn 59	3473	39	0.24	0.077	7.1	0.011	4.1	0.59	0.052	5.7	75.4	5.3	68.5	2.8	302	65	23
zcn 52	2505	41	0.28	0.12	5.8	0.016	4.0	0.68	0.052	4.3	110.7	6.5	102.4	4.0	291	49	35
zcn 55	1715	54	0.28	0.23	5.3	0.032	3.5	0.66	0.052	4.0	210	11	202.5	7.1	295	46	69
zcn 66	1838	64	0.28	0.24	6.8	0.033	3.2	0.46	0.052	6.0	215	15	208.3	6.6	294	69	71
zcn 53	983	34	0.28	0.25	5.1	0.035	4.5	0.88	0.053	2.4	228	12	220.3	9.8	309	27	71
zcn 61	968	40	0.27	0.30	3.6	0.041	3.1	0.85	0.053	1.9	268	10	261.6	8.0	326	21	80
zcn 67	1090	44	0.23	0.30	3.8	0.042	3.2	0.83	0.053	2.1	268	10	262.3	8.3	313	24	84
zcn 51	759	34	0.48	0.30	3.8	0.042	3.0	0.79	0.052	2.3	267	10	263.9	7.9	291	26	91
zcn 62	772	34	0.32	0.32	4.0	0.044	3.3	0.81	0.052	2.3	282	11	279.6	9.1	303	27	92
zcn 48	675	30	0.38	0.32	4.6	0.044	3.1	0.68	0.053	3.4	284	13	279.7	8.8	322	38	87
zcn 68	960	45	0.48	0.32	4.1	0.045	3.3	0.82	0.052	2.4	281	12	280.7	9.4	286	27	98
zcn 63	142	6.4	0.35	0.32	5.7	0.045	3.5	0.60	0.052	4.6	285	16	285.7	9.9	282	52	101
zcn 46	842	38	0.27	0.33	4.1	0.046	3.1	0.76	0.052	2.7	289	12	287.6	8.8	299	30	96
zcn 54	615	29	0.24	0.34	5.9	0.047	4.8	0.81	0.052	3.4	298	18	299	14	292	39	103
ZG0904, Concordia age=295.1±2.9 Ma, MSWD=0.012, Probability=0.97																	
zcn 53	6136	152	0.18	0.18	10	0.025	9.8	0.96	0.052	2.9	168	17	159	16	298	33	53
zcn 73	3225	125	0.14	0.24	3.7	0.032	3.2	0.85	0.053	2.0	215.4	8.1	203.7	6.5	345	22	59
zcn 66	6131	272	0.16	0.25	4.5	0.034	4.3	0.94	0.053	1.6	223	10	213.6	9.1	329	18	65
zcn 50	4455	165	0.24	0.27	4.2	0.037	3.7	0.87	0.052	2.1	243	10	237.3	8.7	298	24	80
zcn 60	4431	186	0.24	0.30	3.5	0.042	3.3	0.92	0.052	1.4	265.8	9.4	262.6	8.6	294	16	89
zcn 59	1475	66	0.43	0.32	4.0	0.044	3.4	0.85	0.053	2.1	280	11	275.6	9.5	321	24	86
zcn 48	445	21	0.48	0.33	4.0	0.046	3.0	0.75	0.053	2.7	290	12	287.4	8.7	310	30	93
zcn 47*	1531	71	0.41	0.33	3.9	0.046	3.0	0.77	0.052	2.5	291	11	290.8	8.9	293	28	99
zcn 61*	820	38	0.33	0.33	4.0	0.046	3.4	0.86	0.052	2.0	292	12	290.8	9.9	304	23	96
zcn 72*	1335	61	0.30	0.33	3.8	0.046	3.3	0.86	0.052	1.9	291	11	291.7	9.5	287	22	102
zcn 46*	600	28	0.38	0.34	4.1	0.047	3.1	0.74	0.052	2.8	295	12	294.5	9.0	298	32	99
zcn 49*	585	28	0.45	0.34	4.8	0.047	3.4	0.72	0.052	3.3	295	14	295	10	297	38	99
zcn 52*	407	19	0.22	0.34	3.9	0.047	2.8	0.70	0.052	2.8	294	12	296.1	8.2	282	32	105
zcn 51*	668	30	0.21	0.34	3.8	0.047	3.3	0.86	0.052	2.0	297	11	297	10	298	22	100
zcn 65*	1008	52	0.74	0.34	4.1	0.047	3.2	0.79	0.052	2.5	296	12	296.8	9.5	292	29	101
zcn 63*	739	36	0.50	0.34	3.9	0.047	3.2	0.82	0.052	2.2	297	12	297.7	9.6	291	26	102
zcn 64*	773	36	0.24	0.35	3.9	0.048	3.1	0.80	0.053	2.3	302	12	300.9	9.3	310	26	97
zcn 74	501	24	0.27	0.35	4.5	0.048	2.8	0.63	0.052	3.5	304	14	305.2	8.6	295	40	103
ZG090, Concordia age=291.2±2.9 Ma, MSWD=0.23, Probability=0.63																	
zcn 50	9999	122	0.063	0.079	17	0.011	16	0.96	0.052	4.5	77	13	71	11	282	52	25
zcn 73	5956	160	0.19	0.20	3.5	0.027	3.3	0.93	0.053	1.3	182.9	6.5	173.1	5.7	312	15	56
zcn 54	2749	86	0.28	0.23	3.8	0.032	3.5	0.91	0.052	1.6	210.5	8.1	203.3	7.1	292	18	70
zcn 76	4887	167	0.25	0.25	4.0	0.035	3.7	0.93	0.052	1.5	227.4	9.1	220.3	8.2	302	17	73
zcn 60	2499	95	0.23	0.28	3.7	0.039	3.3	0.90	0.052	1.6	250.5	9.2	245.1	8.0	301	19	81
zcn 49	669	29	0.62	0.28	8.7	0.039	3.7	0.43	0.052	7.9	251	22	248.4	9.2	281	90	88
zcn 74	702	30	0.26	0.31	3.8	0.043	2.9	0.77	0.052	2.4	274	10	270.7	7.9	300	27	90
zcn 64	977	44	0.45	0.31	4.1	0.044	3.4	0.82	0.052	2.3	276	11	274.5	9.3	293	27	94
zcn 75	1468	63	0.24	0.31	3.6	0.044	3.2	0.88	0.052	1.7	277	10	274.7	8.7	296	20	93
zcn 51	1046	45	0.28	0.31	3.7	0.044	3.0	0.79	0.052	2.3	277	10	274.7	8.1	297	26	92
zcn 66	458	20	0.29	0.32	4.2	0.044	2.9	0.70	0.052	3.0	280	12	277.6	8.1	301	34	92
zcn 68	1344	65	0.65	0.32	3.5	0.044	3.0	0.84	0.053	1.9	282	10	277.9	8.2	314	22	89
zcn 72*	926	42	0.34	0.32	4.3	0.045	3.4	0.77	0.052	2.7	284	12	282.4	9.5	293	31	96
zcn 53*	271	12	0.29	0.33	4.4	0.046	2.8	0.65	0.052	3.3	289	13	288.2	8.2	294	38	98
zcn 46*	747	35	0.39	0.33	4.1	0.046	3.1	0.77	0.052	2.6	292	12	291.2	9.1	296	30	98
zcn 48*	422	20	0.36	0.33	4.4	0.046	3.3	0.75	0.052	2.9	292	13	291.7	9.7	295	33	99
zcn 47*	1074	49	0.33	0.33	4.1	0.046	3.3	0.80	0.052	2.5	293	12	292.2	9.6	300	28	97
zcn 63*	1333	66	0.55	0.33	4.4	0.046	3.6	0.82	0.052	2.5	293	13	293	10	292	29	100
zcn 59*	1471	68	0.30	0.34	3.9	0.047	3.6	0.92	0.052	1.6	294	12	294	11	298	18	99
zcn 62*	514	25	0.51	0.34	4.1	0.047	2.9	0.71	0.052	2.9	295	12	293.7	8.5	303	32	97
zcn 65*	1502	73	0.52	0.34	3.5	0.047	3.0	0.85	0.052	1.8	296	10	295.9	8.8	296	21	100
zcn 61*	617	30	0.42	0.34	4.1	0.047	3.4	0.83	0.052	2.3	297	12	298	10	291	26	102
ZT0902, anchored Discordia, upper intercept 305±11 Ma, MSWD=0.27																	
zcn 51	7147	40	0.36	0.036	10.1	0.006	5.5	0.55	0.047	8.4	35.7	3.6	35.4	2.0	60	100	59
zcn 62	3339	37	0.07	0.076	7.6	0.012	3.9	0.51	0.047	6.5	74.5	5.7	75.1	2.9	54	78	139
zcn 55	1409	30	0.41	0.16	6.9	0.022	6.6	0.95	0.052	2.1	148	10	138.7	9.1	296	24	47
zcn 66	3579	85	0.19	0.18	6.7	0.025	6.5	0.96	0.053	1.8	168	11	158	10	309	21	51
zcn 59	5575	141	0.25	0.19	4.3	0.026	4.0	0.92	0.052	1.7	174.9	7.6	165.4	6.6	305	19	54
zcn 52	807	30	0.24	0.27	5.2	0.037	4.1	0.80	0.053	3.1	242	13	235	10	312	36	75
zcn 47	1686	61	0.28	0.27	3.6	0.038	3.0	0.84	0.053	2.0	245.0	8.9	237.4	7.2	319	23	74
zcn 63	925	34	0.38	0.27	4.3	0.038	3.7	0.88	0.052	2.0	245	10	239.1	8.9	299	23	80
zcn 68	1832	68	0.22	0.27	4.2	0.038	3.7	0.88	0.053	2.0	247	10	239.8	8.9	312	23	77
zcn 46	745	28	0.25	0.28	5.5	0.038	4.9	0.89	0.052	2.5	248	14	243	12	298	28	81
zcn 65	2178	83	0.22	0.28	4.0	0.039	3.6	0.89	0.052	1.8	249	10	244.1	8.8	299	21	82
zcn 67	758	30	0.45	0.28	4.3	0.039	3.7	0.85	0.053	2.3	253	11	247.5	9.1	307	26	81
zcn 53	1047	43	0.37	0.30	5.5	0.041	5.3	0.95	0.053	1.7	264	15	259	14	314	20	83
zcn 54	500	21	0.20	0.30	4.1	0.042	3.2	0.80	0.052	2.5	269	11	266.6	8.6	294	28	91
zcn 60	896	39	0.29	0.31	4.2	0.044	3.1	0.75	0.052	2.8	278	12	275.3	8.7	300	32	92
zcn 49	3672	161	0.28	0.32	3.7	0.044	3.5	0.94	0.052	1.3	281	11	280	10	292	15	96
zcn 61	1220	54	0.30	0.33	3.9	0.045	3.5	0.89	0.053	1.7	290	11	284	10	332	20	86
zcn 64	1878	85	0.32	0.33	3.6	0.046	3.1	0.86	0.052	1.8	289	10	288.1	9.0	292	21	99
zcn 48	972	44	0.24	0.33	4.2	0.046	3.6	0.86	0.052	2.1	293	12	292	11	304	24	96
zcn 50	97	4.7	0.47	0.35	7.7	0.048	4.6	0.60	0.052	6.2	302	23	304	14	287	71	106

Table 1: LA-ICP-MS results of zircons

	Concentrations			Ratios							Ages (Ma)						Conc.
Analysis	**U (ppm)[a]**	**Pb (ppm)[a]**	**Th/U[a]**	**$^{207}Pb/^{235}U$[b]**	2σ (%) [c]	**$^{206}Pb/^{238}U$[b]**	2σ (%) [c]	**rho[d]**	**$^{207}Pb/^{206}Pb$[e]**	2σ (%) [c]	**$^{207}Pb/^{235}U$**	2σ	**$^{206}Pb/^{238}U$**	2σ	**$^{207}Pb/^{206}Pb$**	2σ	**(%)**
Age-standard																	
Peisovice[f]	999	52	0.16	0.40	0.0090	0.054	0.0011	0.78	0.053	0.00038	339.2	6.5	339.3	6.7	339	16	100

[a] U and Pb concentrations and Th/U ratios are calculated relative to GJ-1 reference zcn

[b] Corrected for background and within-run Pb/U fractionation and normalised to reference zcn GJ-1 (ID-TIMS values/measured value);

$^{207}Pb/^{235}U$ calculated using ($^{207}Pb/^{206}Pb$)/($^{238}U/^{206}Pb$ * 1/137.88)

[c] Quadratic addition of within-run errors (2 SD) and daily reproducibility of GJ-1 (2 SD)

[d] Rho is the error correlation defined as the quotient of the propagated errors of the $^{206}Pb/^{238}U$ and the $^{207}/^{235}U$ ratio

[e] Corrected for mass-bias by normalising to GJ-1 reference zcn (~0.6 per atomic mass unit) and common Pb using the model Pb composition of Stacey & Kramers (1975)

[f] Accuracy and reproducibilty was checked by repeated analyses (n = 25) of reference zcn Plesovice, Griedel, and 91500 ;
data given as mean with 2 standard deviation uncertainties

Conc. = Concordance of of the $^{206}Pb/^{238}U$ and the $^{207}/^{235}U$ ages

Table 2: LA-ICP-MS results of apatites

	Concentrations						Ratios					Ages (Ma)			
Analysis	**^{206}Pb (cps)^{a}**	**U (ppm)^{b}**	**Pb (ppm)^{b}**	**Th/U^{b}**	**^{206}Pbc (%)^{c}**	**^{208}Pbc (%)^{c}**	**^{206}Pb/^{238}U^{d}**	**2σ (%) ^{d}**	**^{207}Pb/^{235}U^{d}**	**2σ (%) ^{d}**	**rho^{e}**	**^{207}Pb/^{235}U**	**2σ**	**^{206}Pb/^{238}U**	**2σ**
AT0911, Median Age=31.4+6.5/-3.3 Ma, 97% confidence from coherent group of 18															
ap 112*	15139	4.9	1.6	0.62	94	100	0.0032	101	0.028	112	0.91	28	31	20	21
ap 105*	24440	0.89	2.7	0.027	94	100	0.0037	54	0.053	72	0.74	53	38	24	13
ap 90*	14238	14	1.5	0.21	88	100	0.0038	24	0.035	91	0.27	35	32	24.6	6.0
ap 83*	18034	4.4	2.0	1.6	89	100	0.0041	50	0.061	72	0.70	60	43	27	13
ap 101*	17977	12	1.9	1.3	90	99	0.0043	51	0.028	99	0.52	28	27	28	14
ap 106*	22011	79	2.1	1.5	78	92	0.0046	6.9	0.033	69	0.10	33	22	29.4	2.0
ap 87*	18624	9.3	2.0	1.3	84	99	0.0047	68	0.050	102	0.66	50	51	30	20
ap 98*	16923	24	1.8	0.75	90	99	0.0047	26	0.047	110	0.24	47	52	30.5	8.0
ap 92*	16521	13	1.9	1.2	92	99	0.0048	33	0.039	95	0.35	38	37	31	10
ap 108*	18972	23	2.0	0.48	88	99	0.0049	14	0.024	84	0.17	24	20	31.7	4.6
ap 97*	18859	8.0	2.0	0.47	90	100	0.0050	37	0.045	96	0.38	44	43	32	12
ap 99*	15376	6.2	1.6	0.73	88	100	0.0057	38	0.035	62	0.61	35	21	37	14
ap 84*	15384	20	1.7	0.52	80	99	0.0058	21	0.056	49	0.42	56	27	37.1	7.7
ap 109*	14373	13	1.5	1.3	89	98	0.0059	15	0.067	93	0.17	66	61	38.0	5.9
ap 111*	15985	3.8	1.7	1.7	93	99	0.0060	71	0.029	111	0.64	29	32	39	28
ap 107*	18050	10	1.9	1.7	91	99	0.0061	32	0.041	99	0.33	41	41	39	13
ap 91*	19164	13	1.9	1.3	82	98	0.0066	29	0.055	98	0.30	55	54	42	12
ap 104*	15619	3.5	1.7	0.41	93	100	0.0071	55	0.12	92	0.60	113	103	45	25
ap 82	17176	8.1	1.8	1.7	83	98	0.010	10	0.098	95	0.10	95	90	66.5	6.4
ap 113	44088	47	2.5	0.26	55	98	0.014	7.7	0.083	26	0.30	81	20	89.9	6.9
ap 86	20597	18	2.2	0.91	77	96	0.016	4.7	0.10	89	0.053	98	86	105.0	4.9
ap 96	19324	8.9	2.1	1.9	82	96	0.017	18	0.09	98	0.18	86	83	112	20
ap 89	19887	7.0	2.1	1.7	82	97	0.021	20	0.16	79	0.25	155	120	133	26
ap 93	17884	11	1.9	1.3	76	95	0.023	12	0.18	63	0.20	170	103	147	18
ap 95	41513	15	1.7	1.1	63	92	0.024	5.8	0.17	77	0.075	159	120	153.7	8.8
ap 88	18993	12	2.0	1.5	71	92	0.028	7.9	0.30	63	0.13	270	161	179	14
ap 94	19416	8.7	2.2	1.8	83	94	0.028	11	0.12	53	0.21	119	62	181	20
ap 102	20659	9.3	2.4	2.5	74	91	0.030	7.2	0.35	81	0.090	304	238	190	14
ap 85	20747	11	2.3	1.6	72	90	0.039	4.0	0.18	60	0.067	167	97	244.4	9.6
ap 100	21931	8.3	2.3	1.8	68	90	0.048	7.7	0.45	72	0.11	376	254	305	23
GT0803, Median Age=35.3+1.2/-3.9 Ma, 96% confidence from coherent group of 9															
ap 64*	38729	25	3.8	0.026	73	100	0.0048	14	0.029	40	0.35	29	11	30.7	4.3
ap 50*	50899	9.4	2.7	0.68	90	100	0.0049	27	0.045	85	0.32	45	38	31.3	8.4
ap 57*	32743	65	3.2	0.022	70	100	0.0052	11	0.034	48	0.23	34	16	33.1	3.7
ap 72*	33525	15	3.6	1.4	85	99	0.0054	8.2	0.035	88	0.093	35	30	34.5	2.8
ap 63*	20584	9.4	2.3	0.83	89	100	0.0055	17	0.034	132	0.13	34	45	35.2	5.9
ap 81*	29824	25	3.1	0.16	83	100	0.0056	15	0.033	107	0.14	33	35	35.9	5.2
ap 53*	24717	13	2.5	0.43	72	100	0.0056	22	0.037	44	0.49	37	16	36.0	7.8
ap 46*	60199	38	2.9	0.021	81	100	0.0057	8.2	0.034	57	0.14	34	19	36.4	3.0
ap 78*	22124	9.6	2.1	1.0	86	99	0.0060	24	0.040	50	0.48	40	20	38.8	9.4
ap 51	62788	24	2.8	0.022	80	100	0.0091	8.2	0.057	44	0.18	56	24	58.6	4.8
ap 56	36459	33	3.2	0.45	75	99	0.010	3.3	0.069	30	0.11	68	20	65.8	2.2
ap 73	33377	12	3.5	0.038	78	100	0.011	13	0.079	76	0.17	77	58	72.9	9.3
ap 77	23781	14	2.2	0.47	78	99	0.013	6.0	0.085	50	0.12	82	40	80.1	4.8
ap 60	40163	21	4.3	0.32	80	99	0.017	5.3	0.11	54	0.10	104	55	106.0	5.6
ap 48	54906	22	2.5	0.29	65	98	0.019	5.4	0.13	25	0.21	127	30	124.0	6.6
ap 62	32747	20	3.1	0.15	69	99	0.020	3.6	0.13	35	0.10	127	42	128.9	4.6
ap 58	19697	11	2.0	0.087	74	100	0.020	6.5	0.13	68	0.097	128	85	130.2	8.4
ap 74	24038	13	2.2	0.28	65	99	0.026	3.8	0.18	35	0.11	167	56	168.2	6.3
ap 55	26554	18	2.6	0.49	64	97	0.026	3.9	0.18	25	0.15	168	40	168.5	6.5
ap 76	30936	17	3.2	0.53	62	98	0.029	11	0.25	130	0.081	224	303	184	19
ap 49	43962	9.6	2.2	0.64	70	98	0.030	5.5	0.15	249	0.022	146	410	193	11
ap 79	35502	28	2.8	0.41	53	95	0.033	3.2	0.23	17	0.18	212	34	209.3	6.6
ap 75	26785	18	2.4	0.14	54	99	0.034	4.0	0.24	24	0.17	218	48	214.6	8.5
ap 66	22095	11	2.2	0.38	66	98	0.038	3.2	0.28	48	0.067	247	110	238.3	7.5
ap 47	61783	20	2.8	0.71	54	93	0.040	3.1	0.28	31	0.098	249	71	253.1	7.6
ap 80	100523	126	7.0	0.82	6.6	48	0.042	2.4	0.30	4.1	0.58	263.2	9.6	263.7	6.2
ap 52	148006	187	10	0.35	10	74	0.042	2.4	0.31	3.3	0.70	272.1	8.0	266.6	6.1
ap 61	75729	93	4.6	0.077	8.0	90	0.044	2.4	0.32	4.1	0.59	278	10	279.2	6.6
ap 54	54844	64	4.0	0.22	10	87	0.045	2.5	0.33	6.1	0.40	288	15	284.1	6.9
ap 65	33942	25	3.0	0.39	46	94	0.045	2.9	0.33	14	0.21	287	36	286.4	8.2

Table 2: LA-ICP-MS results of apatites

	Concentrations						Ratios					Ages (Ma)			
Analysis	**^{206}Pb (cps)^{a}**	**U (ppm)^{b}**	**Pb (ppm)^{b}**	**Th/U^{b}**	**^{206}Pbc (%)^{c}**	**^{208}Pbc (%)^{c}**	**^{206}Pb/^{238}U^{d}**	**2σ (%) ^{d}**	**^{207}Pb/^{235}U^{d}**	**2σ (%) ^{d}**	**rho^{e}**	**^{207}Pb/^{235}U**	**2σ**	**^{206}Pb/^{238}U**	**2σ**
GT0804, Median Age=36.1+3.2/-4.3 Ma, 94% confidence from coherent group of 11															
ap 38*	38716	8.6	4.4	0.13	88	100	0.0046	31	0.035	93	0.33	35	32	29.8	9.2
ap 12*	39751	11	4.8	0.11	89	100	0.0049	28	0.028	56	0.50	28	15	31.3	8.7
ap 32*	31505	5.0	3.8	0.10	87	100	0.0049	22	0.028	51	0.43	28	14	31.8	6.9
ap 10*	41657	10	5.2	0.06	91	100	0.0051	39	0.031	141	0.27	31	43	33	13
ap 16*	85675	7.8	4.8	0.12	93	100	0.0055	30	0.048	69	0.43	48	33	35	10
ap 06*	31990	5.1	4.0	0.20	89	100	0.0056	23	0.055	64	0.36	54	34	36.1	8.3
ap 11*	49367	44	6.0	0.08	89	100	0.0057	12	0.041	100	0.12	41	41	36.6	4.5
ap 09*	35533	54	4.3	0.08	78	100	0.0060	7.0	0.051	36	0.20	51	18	38.3	2.7
ap 27*	100138	4.4	5.7	0.23	86	100	0.0061	22	0.040	299	0.073	40	125	39.2	8.5
ap 40*	85795	27	11	0.15	85	100	0.0061	23	0.014	787	0.029	14	116	39.4	9.0
ap 20*	52248	13	6.2	0.05	88	100	0.0069	24	0.049	106	0.23	48	51	45	11
ap 14	149393	46	7.2	<0.01	77	100	0.010	7.1	0.065	29	0.24	64	18	66.3	4.7
ap 18	60424	5.7	3.3	<0.01	88	100	0.014	19	0.089	72	0.26	87	62	87	16
ap 29	87283	11	4.6	0.088	87	100	0.015	6.5	0.11	63	0.10	103	64	93.1	6.0
ap 31	40151	14	4.7	0.073	75	100	0.017	8.0	0.10	77	0.10	100	76	107.0	8.5
ap 19	56031	41	5.7	0.070	65	100	0.017	3.3	0.11	24	0.14	106	25	107.5	3.6
ap 07	49408	21	5.8	0.16	77	100	0.019	6.0	0.13	46	0.13	123	55	123.7	7.3
ap 28	94637	5.8	5.2	0.21	88	100	0.022	15	0.21	74	0.21	190	137	137	21
ap 23	97024	6.7	5.4	0.29	89	100	0.024	10	0.16	59	0.17	147	84	150	15
ap 24	39591	14	4.7	0.12	67	100	0.029	6.7	0.19	39	0.17	173	63	186	12
ap 30	28406	8.6	3.3	0.27	85	99	0.031	7.1	0.19	86	0.083	174	147	199	14
ap 25	50965	23	5.6	0.13	55	99	0.033	5.6	0.20	44	0.13	184	76	212	12
ap 13	39014	4.4	5.1	0.48	88	100	0.037	16	0.26	50	0.33	237	110	232	37
ap 17	57988	27	6.3	0.058	69	100	0.039	4.2	0.25	37	0.11	224	78	248	10
ap 08	64559	36	7.0	0.052	56	100	0.039	3.5	0.28	24	0.14	252	56	248.3	8.6
ap 21	70850	40	7.7	0.050	56	100	0.042	2.9	0.29	21	0.14	258	48	263.0	7.6
HT0901, Median Age=29.2+6.4/-1.8 Ma, 75% confidence from coherent group of 3															
ap 184*	16098	4.4	1.9	2.2	90	99	0.0043	45	0.023	60	0.74	23	14	27	12
ap 179*	23841	28	2.8	1.5	88	98	0.0045	43	0.020	60	0.71	20	12	29	13
ap 186*	21094	15	2.4	1.3	89	99	0.0055	14	0.044	172	0.08	44	76	35.6	5.0
ap 183	25743	19	2.7	1.6	67	92	0.022	3.9	0.14	23	0.17	136	30	137.4	5.3
ap 160	15501	5.9	2.0	1.2	82	97	0.024	7.4	0.18	22	0.34	165	34	155	11
ap 185	16127	5.1	1.9	1.7	72	96	0.030	6.7	0.33	46	0.15	291	122	193	13
ap 171	19598	6.9	2.4	1.6	79	95	0.032	7.6	0.25	64	0.12	230	141	200	15
ap 180	487471	33	6.5	0.84	54	93	0.037	2.6	0.28	3.1	0.85	249.1	6.9	236.2	6.1
ap 182	18487	4.8	2.4	1.9	79	96	0.039	23	0.38	57	0.41	330	175	247	57
ap 173	17648	5.4	2.1	1.5	76	95	0.042	5.2	0.44	57	0.09	367	193	263	13
ap 165	22284	14	2.4	0.54	58	95	0.044	3.5	0.36	23	0.15	310	64	277.1	9.4
PT0802b, No useful Median Age, one analyses=26.0±4.2															
ap 89*	215730	102	26	0.033	95	100	0.0040	16	0.039	108	0.15	39	42	26.0	4.2
ap 76	880314	21	108	0.036	96	100	0.0072	102	0.074	112	0.92	72	81	46	48
ap 88	758932	9.8	93	0.051	97	100	0.019	138	0.24	147	0.94	220	343	122	169
ap 107	400937	10	48	0.007	96	100	0.031	28	0.35	71	0.40	302	205	199	55
ap 108	664367	24	81	0.019	96	100	0.034	16	0.24	49	0.33	220	102	213	34
ap 75	629712	20	78	0.42	94	100	0.039	35	0.20	94	0.37	182	171	246	84
ap 78	484031	16	60	0.12	95	100	0.039	17	0.22	54	0.31	205	105	248	41
ap 86	654092	7.6	80	0.20	96	100	0.041	54	0.84	82	0.66	621	478	256	138
ap 92	542264	22	67	0.091	96	100	0.047	16	0.41	37	0.42	352	117	294	45
ap 83	675471	23	83	0.029	95	100	0.047	13	0.66	43	0.31	515	190	295	39
ap 93	656844	20	81	0.010	96	100	0.052	16	0.54	68	0.23	436	276	324	50
ap 79	766015	20	95	0.021	93	100	0.053	16	0.66	73	0.22	512	346	335	53
PT0820, Median Age=29.4+4.1/-3.5 Ma, 98% confidence from coherent group of 10															
ap 228*	20950	11	1.4	0.31	85	100	0.0040	26	0.032	37	0.68	32	12	25.8	6.6
ap 212*	24479	4.1	3.1	0.52	92	100	0.0040	35	0.021	46	0.76	21	10	25.9	9.1
ap 225*	21264	13	1.7	0.74	83	99	0.0042	25	0.018	52	0.47	18	10	27.3	6.7
ap 218*	41256	29	1.9	0.37	78	99	0.0044	14	0.034	57	0.24	34	19	28.4	3.9
ap 214*	43806	10	3.1	0.70	92	100	0.0045	28	0.035	54	0.52	35	19	28.8	8.0
ap 230*	18739	18	2.1	0.61	87	99	0.0047	34	0.032	52	0.67	32	17	30	10
ap 207*	26234	8.5	2.2	0.39	88	100	0.0047	19	0.031	34	0.55	31	10	30.4	5.7
ap 215*	19175	5.0	1.4	2.0	89	99	0.0051	23	0.032	52	0.45	32	17	32.8	7.6
ap 235*	18906	11	1.4	0.065	80	100	0.0052	25	0.044	60	0.42	44	26	33.6	8.4
ap 202*	59497	12	2.8	0.15	88	100	0.0062	19	0.046	47	0.42	46	21	40.0	7.8
ap 226	45247	7.9	2.1	1.1	86	99	0.0082	24	0.028	50	0.47	28	14	53	12
ap 221	22000	5.2	1.6	0.72	89	99	0.0083	44	0.13	64	0.68	124	78	53	23
ap 211	21201	6.5	0.94	1.2	83	98	0.0090	16	0.057	33	0.47	56	18	57.6	9.0
ap 232	22082	12	2.3	0.97	86	98	0.011	23	0.13	60	0.39	126	74	72	17
ap 227	50012	11	2.3	1.1	85	98	0.012	14	0.080	42	0.34	78	32	79	11
ap 223	41086	5.8	2.0	0.84	88	99	0.013	28	0.17	44	0.63	158	67	83	23
ap 217	57526	15	2.6	0.61	74	97	0.023	9.1	0.18	29	0.32	169	46	146	13
ap 204	716316	15	36	0.57	92	100	0.025	36	0.14	70	0.52	133	92	161	58
ap 224	104583	69	3.0	0.20	37	92	0.026	4.6	0.19	19	0.25	177	31	168.1	7.6
ap 234	41690	6.5	2.1	1.2	76	97	0.027	9.1	0.20	52	0.18	186	91	171	15
ap 216	45863	5.2	2.2	1.8	83	96	0.027	11	0.13	59	0.19	123	70	171	19
ap 208	48349	5.3	2.4	1.2	80	98	0.030	13	0.17	60	0.22	156	91	188	25
ap 222	26514	2.8	1.4	0.0033	81	100	0.032	68	0.46	90	0.76	383	336	203	137
ap 229	20310	5.7	2.1	1.5	64	94	0.042	10	0.44	36	0.28	368	118	266	26
ap 233	64629	5.8	3.2	0.84	76	98	0.047	13	0.53	52	0.26	429	200	294	39
ap 219	25813	0.42	1.3	0.012	94	100	0.068	44	0.79	54	0.81	590	274	423	181

Table 2: LA-ICP-MS results of apatites

	Concentrations						Ratios					Ages (Ma)			
Analysis	^{206}Pb (cps)[a]	U (ppm)[b]	Pb (ppm)[b]	Th/U[b]	^{206}Pbc (%)[c]	^{208}Pbc (%)[c]	^{206}Pb/^{238}U[d]	2σ (%) [d]	^{207}Pb/^{235}U[d]	2σ (%) [d]	rho[e]	^{207}Pb/^{235}U	2σ	^{206}Pb/^{238}U	2σ
TVT0801, Median Age=30.1+4.6/-6.1 Ma, 94% confidence from coherent group of 5															
ap 42*	18539	8.0	2.5	0.72	92	100	0.0037	31	0.019	43	0.71	19.4	8.4	24.0	7.4
ap 18*	21464	16	3.1	0.41	92	100	0.0044	20	0.025	38	0.54	25.5	9.5	28.1	5.7
ap 14*	22517	33	3.2	0.66	78	99	0.0047	23	0.023	41	0.57	23.1	9.5	30.1	7.0
ap 45*	9820	12	1.3	0.71	83	99	0.0052	26	0.024	56	0.47	24	13	33.2	8.8
ap 40*	18892	48	2.9	0.26	74	99	0.0054	23	0.029	43	0.53	29	12	34.6	7.9
ap 44	20130	6.1	2.9	2.2	86	97	0.018	16	0.16	56	0.30	150	81	113	18
ap 25	19138	5.3	2.8	1.7	85	97	0.026	12	0.28	61	0.20	249	143	168	20
ap 43	18571	7.1	2.7	2.6	75	93	0.031	20	0.18	49	0.40	169	80	196	39
ap 31	21688	14	2.9	2.1	59	87	0.034	7.1	0.27	37	0.19	246	84	216	15
ap 38	17397	3.3	2.5	2.1	86	97	0.037	19	0.09	62	0.30	86	53	231	43
ap 24	30787	29	3.8	1.4	35	84	0.037	4.5	0.26	24	0.19	235	51	236	11
ap 27	24480	15	3.3	1.7	54	89	0.039	6.8	0.28	34	0.20	252	78	245	16
ap 10	43724	16	3.9	1.8	71	89	0.043	9.4	0.44	32	0.30	369	103	269	25
ap 23	10529	17	3.8	2.9	55	79	0.044	7.7	0.33	25	0.30	293	67	280	21
ap 13	20784	3.8	3.1	2.0	85	96	0.045	13	0.35	41	0.32	303	115	283	36
ap 29	27957	23	3.5	0.70	13	91	0.046	3.5	0.32	24	0.15	281	60	287.3	9.9
ap 32	23064	5.0	3.4	2.7	80	94	0.048	11	0.40	44	0.26	344	139	300	34
ap 07	20533	4.4	3.1	1.1	79	97	0.054	13	0.42	35	0.38	353	108	340	44
ap 08	18118	3.0	2.8	1.6	81	96	0.066	16	1.5	40	0.40	930	276	411	64
ap 16	19882	6.8	3.1	2.1	5.2	88	0.073	7.2	0.75	34	0.21	566	159	456	32
TVT0809, Median Age=26.2+6.4/-3.2 Ma, 75% confidence from coherent group of 3															
ap 130*	53641	511	36	2.4	79	96	0.0036	24	0.025	26	0.93	25.1	6.4	23.0	5.5
ap 131*	57407	256	34	2.5	75	98	0.0041	20	0.029	25	0.82	29.2	7.2	26.1	5.3
ap 152*	46104	23	2.4	0.17	86	100	0.0051	20	0.030	44	0.47	30	13	32.5	6.7
ap 139	71250	15	3.7	0.60	84	99	0.017	11	0.099	32	0.34	96	30	108	12
ap 136	45284	3.8	2.6	0.90	82	99	0.027	16	0.26	41	0.40	235	89	175	28
ap 153	43802	10	2.8	0.21	65	99	0.035	30	0.32	43	0.68	281	112	224	66
ap 127	39851	3.7	3.6	0.20	77	100	0.053	18	0.48	38	0.47	397	133	333	58
ap 159	58422	1.4	3.1	0.34	89	100	0.059	20	0.40	38	0.52	339	117	368	72
US0902, Median Age=34.0+8.4/-10.4 Ma, 97% confidence from coherent group of 6															
ap 127*	233088	9.8	12	3.5	94	100	0.0037	60	0.020	99	0.60	20	20	24	14
ap 120*	68866	9.6	3.3	1.5	89	99	0.0043	60	0.029	82	0.73	29	24	28	17
ap 115*	78325	9.6	3.8	2.1	89	99	0.0049	73	0.025	88	0.83	25	22	31	23
ap 122*	84646	11	4.1	3.0	90	99	0.0057	34	0.032	53	0.65	32	17	37	13
ap 141*	91096	8.3	4.7	2.4	91	99	0.0060	68	0.023	122	0.56	23	28	38	26
ap 118*	100188	20	11	2.3	94	99	0.0066	53	0.043	66	0.80	43	28	42	22
ap 137	89254	7.0	4.6	4.5	89	98	0.013	30	0.063	83	0.36	62	51	86	26
ap 138	66740	8.5	3.4	2.4	83	97	0.019	12	0.11	58	0.20	109	62	120	14
ap 114	68478	11	3.2	1.6	83	97	0.021	9.5	0.12	68	0.14	117	78	136	13
ap 129	66722	8.4	3.4	3.6	79	94	0.022	10	0.15	50	0.20	145	69	142	14
ap 119	33573	14	3.7	2.9	76	93	0.023	13	0.20	42	0.30	186	75	148	18
ap 124	87578	6.2	4.6	3.9	89	96	0.025	11	0.19	43	0.26	175	72	157	17
ap 117	40076	13	4.3	2.5	81	95	0.025	8.0	0.14	31	0.26	132	39	160	13
ap 125	83977	10	4.1	1.8	79	96	0.027	8.8	0.16	42	0.21	148	59	175	15
ap 140	73598	8.4	3.7	2.8	80	95	0.030	10	0.20	77	0.13	183	138	190	19
ap 116	71311	12	3.6	2.2	77	93	0.031	6.8	0.18	68	0.10	165	109	199	13
ap 126	73368	12	3.5	2.2	71	93	0.032	5.7	0.14	46	0.12	133	59	202	11
ap 121	77260	9.0	3.9	2.9	80	93	0.035	7.3	0.23	49	0.15	209	98	219	16
ap 130	68315	15	3.2	1.8	66	91	0.037	4.5	0.21	35	0.13	194	64	237	11
ap 139	85180	10	4.7	4.3	81	91	0.039	11	0.34	33	0.34	297	90	244	27
ap 134	92926	12	4.7	2.2	77	94	0.039	4.7	0.26	46	0.10	237	102	245	11
ap 128	73692	8.7	3.6	2.0	79	94	0.041	4.8	0.28	36	0.13	254	86	259	12
ap 135	78579	12	4.0	1.8	73	93	0.042	6.5	0.33	32	0.20	290	85	267	17
US0905, Median Age=30.0+5.3/-2.8 Ma, 94% confidence from coherent group of 14															
ap 39*	15870	7.0	2.0	2.0	95	100	0.0022	130	0.0091	174	0.75	9	16	14	19
ap 42*	14138	5.5	2.6	1.9	90	100	0.0037	121	0.039	197	0.61	39	79	24	29
ap 23*	34818	19	4.4	1.6	89	99	0.0040	64	0.025	106	0.60	25	27	26	16
ap 44*	16336	16	1.9	4.3	87	96	0.0042	66	0.038	92	0.72	38	35	27	18
ap 11*	14814	9.1	2.0	2.1	90	99	0.0045	76	0.046	113	0.68	45	51	29	22
ap 38*	16086	6.4	2.0	2.1	86	99	0.0045	56	0.043	122	0.46	42	52	29	16
ap 25*	23702	14	3.1	1.6	86	99	0.0046	48	0.044	71	0.67	43	31	29	14
ap 08*	10832	8.4	1.5	2.0	89	99	0.0048	43	0.067	59	0.72	66	38	31	13
ap 30*	11599	3.1	0.7	1.9	89	99	0.0051	85	0.043	104	0.82	43	45	33	28
ap 21*	35420	6.9	2.0	1.9	89	99	0.0052	45	0.039	101	0.45	39	40	33	15
ap 07*	28704	27	4.0	1.3	90	99	0.0055	24	0.039	56	0.42	38	21	35.3	8.3
ap 17*	14111	8.2	2.0	2.2	95	98	0.0061	42	0.054	72	0.58	53	38	39	16
ap 16*	15316	8.0	2.1	1.9	85	98	0.0093	41	0.051	56	0.72	51	28	60	24
ap 13*	12828	5.8	1.7	1.4	67	99	0.010	55	0.17	104	0.52	162	170	67	36
ap 32	8907	4.3	1.2	1.3	86	99	0.011	32	0.15	86	0.38	138	118	68	22
ap 31	26141	3.3	3.5	1.6	70	100	0.011	151	0.077	153	0.99	75	118	72	109
ap 09	14365	11	2.1	0.98	87	98	0.012	18	0.40	66	0.27	343	212	78	14
ap 43	16065	7.6	2.1	1.8	90	97	0.018	17	0.12	92	0.18	116	106	115	19
ap 12	16212	10	2.3	2.3	81	94	0.021	14	0.28	66	0.22	249	156	133	19
ap 28	26159	10	3.6	1.5	84	97	0.023	17	0.25	104	0.16	224	235	145	24
ap 29	20344	10	2.5	1.9	82	94	0.025	11	0.14	39	0.30	130	48	157	18
ap 26	19303	12	2.4	2.3	71	90	0.029	6.3	0.20	48	0.13	187	85	184	11
ap 10	18542	8.6	2.5	2.2	78	93	0.029	12	0.20	54	0.23	187	96	185	23
ap 22	35031	7.1	2.2	2.1	74	92	0.041	7.4	0.34	47	0.16	300	130	258	19
ap 06	24486	7.2	1.5	1.5	64	90	0.043	4.4	0.25	56	0.08	229	123	270	12

Table 2: LA-ICP-MS results of apatites

	Concentrations						Ratios					Ages (Ma)			
Analysis	**^{206}Pb (cps)[a]**	**U (ppm)[b]**	**Pb (ppm)[b]**	**Th/U[b]**	**^{206}Pbc (%)[c]**	**^{208}Pbc (%)[c]**	**^{206}Pb/^{238}U[d]**	**2σ (%) [d]**	**^{207}Pb/^{235}U[d]**	**2σ (%) [d]**	**rho[e]**	**^{207}Pb/^{235}U**	**2σ**	**^{206}Pb/^{238}U**	**2σ**
US0906, Median Age=30.6+1.9/-4.8 Ma, 94% confidence from coherent group of 14															
ap 54*	398884	38	50	1.0	90	100	0.0036	54	0.040	89	0.61	40	35	23	12
ap 46*	249904	20	31	0.19	89	100	0.0037	23	0.026	51	0.46	26	13	24.0	5.6
ap 41*	24023	11	2.9	0.086	91	100	0.0038	40	0.024	68	0.60	24	16	24.6	9.9
ap 60*	294044	8.0	37	1.7	93	100	0.0040	55	0.027	61	0.89	27	16	26	14
ap 49*	286925	12	37	1.1	93	100	0.0040	32	0.040	66	0.49	40	26	25.8	8.3
ap 63*	30349	14	3.6	1.1	89	99	0.0046	22	0.047	62	0.36	46	29	29.4	6.5
ap 56*	26776	14	3.3	1.0	91	99	0.0047	13	0.042	61	0.21	42	25	30.3	3.9
ap 47*	183073	20	23	0.42	86	100	0.0048	32	0.028	69	0.46	28	19	30.8	9.8
ap 66*	156338	7.5	20	0.28	90	100	0.0049	43	0.024	72	0.59	24	17	32	14
ap 45*	27434	14	3.4	1.0	91	99	0.0050	20	0.036	75	0.27	36	27	32.1	6.4
ap 53*	179673	32	25	2.0	92	99	0.0051	29	0.031	55	0.53	31	17	32.5	9.3
ap 72*	149004	192	18	1.9	84	97	0.0053	9.8	0.039	45	0.22	39	17	33.9	3.3
ap 64*	304566	8.8	38	0.20	90	100	0.0060	50	0.032	182	0.28	32	59	39	19
ap 55*	16350	7.2	2.0	1.3	90	99	0.0069	23	0.072	58	0.39	70	41	44.1	9.9
ap 48	147415	4.9	19	0.11	88	100	0.010	17	0.058	48	0.36	58	27	67	12
ap 62	41360	42	4.7	1.0	74	97	0.012	8.9	0.057	71	0.13	56	39	75.0	6.6
ap 65	164377	7.5	20	0.045	89	100	0.012	53	0.099	143	0.37	96	140	78	41
ap 74	186797	9.5	23	0.33	88	100	0.017	20	0.36	68	0.29	312	203	107	21
ap 43	21172	27	1.4	0.16	39	97	0.023	4.0	0.14	17	0.24	135	21	144.3	5.8
ap 59	521627	34	66	0.26	68	100	0.027	10	0.21	63	0.16	194	118	171	17
ap 42	126035	4.2	16	0.066	83	100	0.030	9.3	0.20	52	0.18	189	94	190	17
ap 73	78334	78	6.6	0.34	57	94	0.032	3.0	0.22	18	0.16	201	34	204.1	6.1
ap 52	25083	34	1.6	0.39	36	57	0.040	2.7	0.28	7.2	0.37	254	16	252.0	6.6
WG0902, Median Age=28.8+3.2/-4.4 Ma, 94% confidence from coherent group of 14															
ap 136*	23606	29	2.7	1.1	84	99	0.0034	20	0.022	48	0.42	22	11	22.1	4.4
ap 154*	24103	12	3.3	1.9	90	99	0.0037	58	0.029	64	0.92	29	19	23	14
ap 129*	22013	11	2.4	1.4	94	99	0.0037	21	0.017	53	0.40	17.0	9.0	23.5	5.0
ap 159*	20953	6.8	2.6	1.5	90	100	0.0037	38	0.026	44	0.87	26	11	24.1	9.2
ap 157*	17757	24	2.1	0.59	84	99	0.0040	35	0.058	149	0.23	58	87	25.6	9.0
ap 149*	19226	5.5	2.3	1.3	90	100	0.0044	22	0.034	49	0.45	34	16	28.1	6.1
ap 151*	17198	9.0	2.0	1.8	86	99	0.0045	18	0.026	42	0.42	26	11	28.6	5.1
ap 125*	20009	11	2.3	1.1	89	99	0.0045	20	0.024	38	0.54	24.5	9.1	28.9	5.8
ap 127*	21355	5.5	2.5	1.6	82	100	0.0048	24	0.029	43	0.56	29	12	31.1	7.5
ap 135*	20268	9.9	2.3	1.5	86	99	0.0049	27	0.032	42	0.63	32	13	31.4	8.4
ap 138*	20806	17	2.4	1.5	86	98	0.0050	28	0.026	44	0.63	26	11	31.9	8.9
ap 155*	21094	15	2.3	1.3	87	99	0.0058	61	0.053	182	0.33	52	98	37	23
ap 140*	16572	9.2	2.0	1.3	86	99	0.0062	34	0.046	45	0.76	46	20	40	13
ap 156*	17097	5.7	2.1	0.78	90	100	0.0067	39	0.14	129	0.30	129	171	43	17
ap 123	23464	59	2.6	0.78	71	96	0.0069	24	0.050	45	0.54	50	22	44	11
ap 132	23024	26	2.5	0.14	73	99	0.011	36	0.047	61	0.59	46	28	72	26
ap 128	16145	12	2.0	0.90	83	98	0.012	26	0.18	48	0.55	165	75	79	20
ap 142	40907	65	4.5	0.86	66	95	0.013	3.5	0.074	36	0.10	72	26	82.2	2.9
ap 124	24285	17	2.8	1.2	77	97	0.014	29	0.11	67	0.43	102	67	87	25
ap 148	19831	6.6	2.3	1.6	81	98	0.014	36	0.15	61	0.59	143	84	88	31
ap 152	7166	8.4	0.96	1.7	62	93	0.014	6.2	0.093	6.9	0.89	90.0	5.9	88.9	5.4
ap 130	19561	7.9	2.3	1.2	84	98	0.014	16	0.096	43	0.37	93	39	90	14
ap 150	17711	7.2	2.1	0.34	85	99	0.016	14	0.13	178	0.08	126	236	105	14
ap 122	21204	8.5	2.5	1.4	87	98	0.017	10	0.12	85	0.12	112	94	107	11
ap 134	21832	12	2.5	1.1	71	97	0.020	7.5	0.10	44	0.17	94	41	126.1	9.4
ap 141	21537	9.8	2.5	1.2	73	97	0.022	6.2	0.19	34	0.18	174	56	139.3	8.5
ap 139	23565	24	2.9	0.74	67	95	0.025	17	0.26	61	0.27	238	139	157	26
ap 131	25321	9.6	3.1	1.6	82	96	0.027	5.8	0.16	64	0.09	154	96	171.6	9.8
ap 153	24602	7.1	3.0	1.2	82	98	0.029	26	0.47	152	0.17	392	677	183	47
ap 133	21170	4.3	2.6	2.2	86	97	0.029	10	0.21	76	0.13	197	145	185	18
ap 158	22438	7.9	2.9	1.4	76	94	0.046	4.9	1.4	15	0.34	903	91	292	14
WG0904, No useful Median Age															
ap 113	101785	4.0	12	1.1	83	100	0.012	183	0.11	208	0.88	103	228	76	139
ap 114	24798	11	2.6	0.82	71	98	0.023	8.7	0.20	34	0.26	183	58	147	13
ap 110	64636	51	6.1	0.76	63	93	0.029	3.8	0.20	43	0.088	185	76	186.6	7.0
ap 111	33670	24	3.1	0.13	43	99	0.032	3.7	0.25	26	0.14	227	54	205.0	7.4
ap 112	35426	26	3.4	1.0	61	91	0.033	4.6	0.24	21	0.22	214	42	207.7	9.5
ap 117	36974	28	3.7	0.87	57	91	0.038	3.1	0.30	17	0.18	266	40	241.3	7.3

Table 2: LA-ICP-MS results of apatites

	Concentrations						Ratios					Ages (Ma)			
Analysis	**^{206}Pb (cps)^{a}**	**U (ppm)^{b}**	**Pb (ppm)^{b}**	**Th/U^{b}**	**^{206}Pbc (%)^{c}**	**^{208}Pbc (%)^{c}**	**^{206}Pb/^{238}U^{d}**	2σ (%) ^{d}	**^{207}Pb/^{235}U^{d}**	2σ (%) ^{d}	**rho^{e}**	**^{207}Pb/^{235}U**	2σ	**^{206}Pb/^{238}U**	2σ
WT0901, Median Age=31.4+6.5/-4.2 Ma, 97% confidence from coherent group of 6															
ap 175*	34736	48	3.8	0.12	72	100	0.0042	26	0.028	45	0.57	28	13	27.2	7.0
ap 184*	168371	51	19	0.30	92	100	0.0043	40	0.036	62	0.65	36	22	28	11
ap 200*	189731	89	25	0.20	90	100	0.0048	27	0.033	72	0.38	33	23	30.7	8.4
ap 201*	53077	38	6.1	2.3	89	98	0.0050	17	0.036	58	0.30	36	20	32.1	5.6
ap 164*	60223	39	7.0	0.37	89	100	0.0052	18	0.058	44	0.42	57	24	33.4	6.2
ap 165*	50809	60	6.1	0.52	84	99	0.0059	13	0.025	35	0.38	24.6	8.5	38.0	5.0
ap 167	48836	19	5.5	1.2	75	97	0.023	11	0.13	37	0.30	120	43	147	16
ap 189	37349	12	4.1	0.86	79	98	0.025	11	0.15	35	0.30	141	47	156	16
ap 171	92797	24	10	0.84	81	98	0.025	13	0.25	35	0.36	223	73	156	20
ap 197	478832	44	54	0.90	93	99	0.026	22	0.29	57	0.38	258	138	165	36
ap 185	55996	12	6.2	1.0	85	98	0.028	12	0.14	42	0.28	135	55	180	21
ap 186	79137	24	8.6	0.87	68	98	0.031	8.9	0.24	34	0.26	222	71	200	18
ap 169	46937	23	5.4	1.5	69	93	0.032	8.2	0.29	40	0.21	255	94	201	16
ap 179	44931	20	4.6	0.72	64	96	0.032	7.8	0.22	39	0.20	204	74	203	16
ap 177	63195	34	6.6	0.87	54	95	0.034	7.4	0.27	36	0.20	246	83	215	16
ap 163	158759	17	8.1	1.0	82	98	0.035	11	0.23	37	0.29	208	73	219	23
ap 183	40261	15	4.1	0.93	63	96	0.036	8.3	0.28	39	0.22	247	88	230	19
ap 176	29326	4.4	3.3	0.79	84	99	0.037	15	0.26	53	0.28	236	118	234	34
ap 161	82804	15	4.1	1.2	69	95	0.037	7.9	0.22	48	0.17	198	89	237	18
ap 162	93199	18	4.3	0.92	56	95	0.039	7.5	0.28	23	0.33	251	53	244	18
ap 168	68775	24	7.7	1.1	61	96	0.039	8.8	0.32	39	0.22	283	102	246	21
ap 178	45400	18	4.7	1.1	68	94	0.039	8.8	0.32	30	0.29	278	75	250	22
ap 195	35417	8.0	3.9	0.95	79	98	0.040	10	0.27	43	0.24	240	96	251	26
ap 182	38313	14	4.0	0.92	59	95	0.041	7.1	0.25	33	0.22	230	70	258	18
ap 196	48981	28	4.9	0.95	36	91	0.043	4.9	0.28	32	0.15	252	74	270	13
ap 174	45615	23	4.6	0.80	47	94	0.043	6.0	0.31	30	0.20	275	76	274	16
ap 190	63169	35	6.3	1.4	35	87	0.044	4.6	0.31	16	0.29	275	39	279	13
ap 170	58793	36	8.0	0.68	48	95	0.044	5.8	0.30	21	0.27	267	51	280	16
ap 188	41801	17	4.5	0.94	49	94	0.045	6.3	0.35	33	0.19	301	90	283	18
ap 166	40047	14	4.3	1.0	74	95	0.045	8.5	0.31	39	0.22	271	96	283	24
ap 162	92820	18	4.5	0.93	49	94	0.045	7.3	0.37	39	0.19	316	113	284	20
ap 172	43567	24	4.5	0.79	33	93	0.046	5.1	0.32	32	0.16	279	80	288	14
ap 181	40512	16	4.3	1.2	53	93	0.046	6.5	0.31	25	0.26	274	63	288	18
ap 180	53353	21	5.8	1.4	53	91	0.047	6.2	0.36	23	0.27	309	62	295	18
ap 173	44458	15	4.8	1.0	69	95	0.047	7.9	0.32	35	0.23	286	91	297	23
ap 198	85038	44	8.2	1.6	46	83	0.051	6.2	0.44	23	0.27	373	74	319	19
ZG0904, Median Age=30.0+5.4/-4.1 Ma, 96% confidence from coherent group of 12															
ap 85*	31276	11	1.9	1.1	91	99	0.0034	33	0.023	41	0.82	22.7	9.2	22.0	7.3
ap 75*	30642	31	2.8	0.71	82	99	0.0040	15	0.30	18	0.82	266	43	25.7	3.7
ap 51*	13716	10	2.0	0.29	90	100	0.0040	20	0.025	35	0.58	25.5	8.9	25.9	5.3
ap 50*	20388	14	2.9	0.94	89	99	0.0042	19	0.021	45	0.43	20.8	9.3	26.8	5.2
ap 64*	15297	20	2.1	0.88	87	99	0.0042	24	0.025	53	0.45	25	13	27.2	6.5
ap 65*	17121	21	2.3	1.0	87	99	0.0044	23	0.040	59	0.39	40	23	28.5	6.6
ap 76*	23421	13	2.3	0.23	87	100	0.0049	26	0.035	38	0.67	35	13	31.6	8.1
ap 77*	30378	37	2.9	0.33	83	99	0.0050	18	0.028	32	0.58	27.6	8.7	32.2	5.9
ap 66*	24174	21	2.5	0.36	86	99	0.0053	36	0.040	66	0.56	39	26	34	13
ap 83*	28593	8.3	1.7	0.31	90	100	0.0055	21	0.043	51	0.40	43	22	35.5	7.3
ap 49*	36253	42	2.8	0.23	65	99	0.0056	34	0.031	48	0.71	31	15	36	12
ap 60*	12700	12	1.8	0.57	88	99	0.0057	31	0.039	51	0.61	39	20	36	11
ap 74	15693	11	2.1	1.5	85	98	0.0077	16	0.041	57	0.27	41	23	49.6	7.7
ap 48	22055	47	2.7	0.89	67	96	0.0082	20	0.045	32	0.62	44	14	53	10
ap 81	36552	11	2.2	1.2	86	98	0.0099	24	0.12	51	0.46	113	56	63	15
ap 59	17788	12	2.4	1.4	81	97	0.013	29	0.20	42	0.70	185	74	85	25
ap 63	26205	5.9	2.5	0.85	82	99	0.017	15	0.22	43	0.36	203	81	106	16
ap 57	29789	14	2.7	0.92	69	97	0.018	23	0.18	39	0.59	164	60	113	26
ap 73	14134	6.1	2.0	1.5	83	97	0.020	42	0.21	64	0.66	194	119	125	52
ap 84	66837	45	2.9	2.4	34	61	0.023	6.3	0.11	47	0.13	109	49	149.1	9.3
ap 55	33904	12	3.1	1.4	77	96	0.024	17	0.19	35	0.47	174	58	150	25
ap 80	37238	6.3	2.3	1.4	81	97	0.024	11	0.27	29	0.38	247	66	155	17
ap 72	19648	8.8	2.6	1.4	58	96	0.025	11	0.22	38	0.29	203	72	157	17
ap 56	33254	18	3.2	1.5	49	93	0.025	10	0.40	38	0.26	344	118	158	16
ap 53	41075	25	3.0	0.44	51	97	0.025	9.6	0.17	22	0.43	161	34	159	15
ap 62	37754	40	3.8	2.4	29	74	0.026	8.1	0.15	38	0.21	142	52	163	13
ap 82	33674	4.5	2.1	1.9	82	96	0.031	11	0.32	29	0.37	285	75	199	21
ap 46	17084	12	2.5	0.79	64	95	0.033	12	0.32	34	0.34	282	88	208	24
ap 54	30037	9.9	3.3	2.3	78	91	0.039	28	0.30	36	0.79	268	88	246	68
ap 79	24982	2.4	1.5	0.96	50	96	0.078	12	0.96	41	0.28	685	229	485	55
ap 47	15863	4.2	2.5	1.5	34	93	0.089	14	0.63	24	0.58	497	99	552	74

Table 2: LA-ICP-MS results of apatites

	Concentrations						Ratios					Ages (Ma)			
Analysis	**^{206}Pb (cps)[a]**	**U (ppm)[b]**	**Pb (ppm)[b]**	**Th/U[b]**	**^{206}Pbc (%)[c]**	**^{208}Pbc (%)[c]**	**^{206}Pb/^{238}U[d]**	**2σ (%) [d]**	**^{207}Pb/^{235}U[d]**	**2σ (%) [d]**	**rho[e]**	**^{207}Pb/^{235}U**	**2σ**	**^{206}Pb/^{238}U**	**2σ**
ZG0908, Median Age=30.4+4.0/-5.3 Ma, 96% confidence from coherent group of 9															
ap 121*	16018	34	2.1	0.36	83	99	0.0036	40	0.037	47	0.84	37	17	23.3	9.2
ap 95*	34589	35	4.5	0.37	88	100	0.0039	23	0.058	61	0.38	57	35	25.1	5.8
ap 123*	10239	16	1.2	0.25	80	100	0.0041	19	0.057	33	0.58	56	18	26.1	4.9
ap 116*	34478	62	1.8	0.78	55	96	0.0045	10	0.027	42	0.25	27	11	28.8	3.0
ap 091*	15883	13	1.9	0.68	88	99	0.0047	20	0.034	47	0.42	34	16	30.4	6.0
ap 98*	25437	8.7	1.5	0.64	90	99	0.0050	21	0.028	42	0.51	28	12	32.3	6.9
ap 93*	18218	71	2.2	0.82	65	95	0.0052	14	0.060	43	0.33	59	25	33.3	4.7
ap 122*	14300	9.1	1.7	0.91	88	99	0.0054	23	0.033	39	0.59	33	13	34.4	7.9
ap 111*	15951	14	1.9	0.74	87	99	0.0054	36	0.059	53	0.68	58	30	35	12
ap 101	24407	18	2.2	0.59	81	99	0.0064	18	0.044	38	0.48	43	16	41.0	7.5
ap 108	11909	5.0	1.5	1.7	89	98	0.0089	24	0.163	60	0.40	153	89	57	14
ap 112	14013	6.1	1.7	2.1	88	98	0.010	22	0.137	46	0.47	130	58	64	14
ap 96	12615	6.0	1.6	1.4	90	98	0.011	18	0.091	44	0.40	89	38	70	12
ap 100	24806	9.1	2.1	1.0	88	98	0.011	16	0.096	51	0.32	93	46	71	12
ap 94	19833	19	2.3	1.3	78	95	0.014	10	0.059	52	0.19	58	30	86.6	8.6
ap 115	33328	7.7	1.8	1.6	82	97	0.014	20	0.095	52	0.39	92	47	88	18
ap 97	23770	3.5	1.3	1.6	88	98	0.014	24	0.12	45	0.53	112	50	93	22
ap 99	14809	3.8	1.9	1.8	87	98	0.015	27	0.15	54	0.50	145	75	99	27
ap 92	16826	4.2	2.2	1.3	89	99	0.016	27	0.12	36	0.74	117	41	105	28
ap 118	19295	15	2.4	1.7	67	93	0.018	13	0.094	60	0.21	91	54	117	15
ap 90	29580	5.8	1.7	1.2	83	98	0.018	11	0.14	48	0.24	133	61	118	13
ap 87	18549	7.2	2.4	2.0	86	95	0.024	12	0.24	44	0.28	217	90	151	18
ap 117	17959	7.0	2.2	2.0	79	95	0.025	22	0.26	44	0.50	233	96	157	34
ap 114	52524	22	2.3	0.22	48	97	0.034	5.7	0.22	24	0.23	200	45	215	12
ap 110	15442	4.6	2.2	1.8	66	93	0.052	17	0.36	29	0.58	314	82	330	54
ZT0902, Median Age=25.1+3.5/-1.2 Ma, 95% confidence from coherent group of 29															
ap 25*	58946	84	7.4	2.6	86	97	0.0024	25	0.019	160	0.16	19	30	15.7	4.0
ap 30*	53855	52	8.0	2.1	94	99	0.0029	59	0.030	100	0.60	30	30	19	11
ap 15*	101004	104	6.0	2.3	81	96	0.0030	23	0.019	113	0.20	19	22	19.5	4.4
ap 56*	70754	66	8.5	1.9	92	99	0.0031	30	0.018	310	0.098	18	57	20.2	6.1
ap 18*	105831	57	14	1.4	95	99	0.0032	43	0.025	96	0.45	25	24	20.6	8.9
ap 53*	96561	64	12	1.8	94	99	0.0033	29	0.032	189	0.15	32	62	21.0	6.2
ap 44*	49502	54	6.5	5.1	90	90	0.0033	16	0.046	82	0.20	46	37	21.1	3.4
ap 55*	81140	50	9.5	1.6	90	98	0.0034	20	0.030	216	0.09	30	65	22.1	4.5
ap 74*	69356	124	7.6	1.3	89	98	0.0035	15	0.027	178	0.09	27	49	22.5	3.4
ap 43*	60449	113	6.8	0.20	83	99	0.0037	13	0.028	65	0.20	28	18	23.7	3.1
ap 52*	82308	68	10	4.2	94	97	0.0037	45	0.033	255	0.18	33	88	24	11
ap 63*	74032	75	9.3	3.3	92	97	0.0037	27	0.033	279	0.098	33	95	24.1	6.6
ap 12*	136445	106	8.3	3.3	88	95	0.0038	14	0.018	121	0.12	18	22	24.2	3.4
ap 41*	29221	26	3.4	1.3	96	99	0.0038	75	0.040	151	0.50	40	61	25	18
ap 65*	69483	69	8.0	1.7	80	96	0.0039	15	0.025	50	0.30	25	13	24.9	3.8
ap 48*	59318	72	9.0	2.2	92	98	0.0039	22	0.034	142	0.15	34	48	25.1	5.4
ap 60*	87420	64	10	2.9	94	98	0.0039	24	0.026	165	0.14	26	42	25.3	5.9
ap 31*	55144	45	7.1	3.4	74	94	0.0040	14	0.020	76	0.19	20	15	25.5	3.7
ap 64*	49225	92	5.7	3.5	89	93	0.0041	22	0.035	62	0.35	35	22	26.2	5.7
ap 23*	73001	82	9.6	3.3	85	96	0.0042	33	0.037	95	0.35	37	35	26.9	9.0
ap 58*	47204	50	5.5	1.8	91	98	0.0044	22	0.038	192	0.12	38	75	28.5	6.3
ap 73*	67829	31	7.6	1.3	91	99	0.0046	39	0.027	90	0.44	27	24	29	11
ap 08*	83383	89	12	4.4	92	95	0.0047	19	0.033	197	0.096	33	66	30.0	5.7
ap 72*	61068	41	6.8	1.0	93	99	0.0047	24	0.031	311	0.08	31	101	30.1	7.3
ap 19*	360445	53	56	4.1	91	99	0.0047	35	0.021	77	0.45	21	16	30	10
ap 57*	33610	26	4.9	0.80	91	99	0.0047	38	6.6	39	0.96	2058	424	30	12
ap 47*	21471	30	2.7	5.1	83	92	0.0048	33	0.098	121	0.28	95	116	31	10
ap 20*	67931	60	9.8	0.68	84	99	0.0048	19	0.032	101	0.19	32	32	31.1	5.8
ap 13*	98053	47	6.4	0.91	90	99	0.0049	26	0.028	69	0.37	28	19	31.6	8.1
ap 54	136749	59	18	3.4	94	96	0.0052	33	0.082	126	0.26	80	102	33	11
ap 29	66101	53	8.6	4.9	91	95	0.0052	25	0.086	122	0.21	84	103	33.7	8.4
ap 27	93653	16	12	0.55	95	100	0.0053	66	0.074	138	0.48	72	101	34	22
ap 49	71123	66	9.1	2.2	89	97	0.0054	17	0.044	119	0.14	44	53	35.0	5.9
ap 38	40924	56	5.4	3.0	91	94	0.0058	17	0.053	164	0.11	53	88	37.2	6.5
ap 07	66557	48	9.9	1.0	93	99	0.0059	23	0.063	131	0.18	62	82	37.9	8.7
ap 51	20059	8.7	2.4	3.4	93	98	0.0061	68	0.013	995	0.068	13	136	40	27
ap 45	110458	77	15	1.9	87	98	0.0071	25	0.19	59	0.43	173	99	45	12
ap 21	50022	70	7.0	2.7	84	91	0.011	25	0.079	71	0.35	77	54	67	17
ap 62	173334	107	23	2.1	89	97	0.011	33	0.075	50	0.66	73	36	68	22
ap 14	75495	17	10	2.2	92	98	0.014	50	0.13	151	0.33	125	195	92	46
ap 28	139281	48	18	2.0	92	98	0.015	19	0.15	213	0.088	145	339	99	18
ap 24	24998	17	3.4	1.1	88	97	0.018	27	0.15	96	0.28	139	133	114	30
ap 32	114420	30	15	0.81	91	99	0.025	22	0.57	271	0.080	460	4373	158	34
ap 66	442856	117	57	0.31	0	54	0.046	9.4	0.33	10	0.99	288	24	290	27
ap 11	30112	3.0	4.3	2.0	88	98	0.054	43	1.4	81	0.53	870	634	337	142
Age-standards															
Pleisovice	73330	676	35	0.11	0.88	29	0.394	0.0	0.05	0.0	0.59	337.5	8.4	339.4	5.8
Griedel[f]	5811	48	0.46	1.1	17	41	0.0263	0.0	0.004	0	0.35	26.3	2.8	26.4	1.3
91500[f]	177146	56	10	0.35	0.53	8.3	1.85	0.0	0.2	0.0	0.76	1064	15	1060	17

Notes:

Spot size = 50 to 75 µm; depth of crater ~15µm. $^{206}Pb/^{238}U$ error is the quadratic additions of the within run precision (2 SE) and the external reproducibility (2 SD) of the reference zircon. $^{207}Pb/^{206}Pb$ error propagation (^{207}Pb signal dependent) following Gerdes & Zeh (2009). $^{207}Pb/^{235}U$ error is the quadratic addition of the $^{207}Pb/^{206}Pb$ and $^{206}Pb/^{238}U$ uncertainty.

[a] Within run background-corrected mean ^{207}Pb signal in cps (counts per second).

[b] U and Pb content and Th/U ratio were calculated relative to GJ-1 reference zircon.

[c] percentage of the common Pb on the ^{206}Pb. b.d. = below dectection limit.

[d] corrected for background, within-run Pb/U fractionation (in case of $^{206}Pb/^{238}U$) and common Pb using Stacy and Kramers (1975) model Pb and subsequently normalised to GJ-1 (ID-TIMS value/measured value); $^{207}Pb/^{235}U$ calculated using $^{207}Pb/^{206}Pb/(^{238}U/^{206}Pb * 1/137.88)$.

[e] rho is the $^{206}Pb/^{238}U/^{207}Pb/^{235}U$ error correlation coefficient.

[f] Accuracy and reproducibilty was checked by repeated analyses (n = 16) of reference zircon Plesovice, Griedel, and 91500; data given as mean with 2 standard deviation uncertainties

5. The dynamic evolution of the Tauern Window: a crustal scale expression of upper mantle dynamics

5.1 Methodological conclusions

Based on comprehensive and detailed structural mapping of the western Tauern Window and on a structural compilation covering the entire window, we reassessed the position and the links between Cenozoic faults systems and shear zones, to discriminate between different kinematic models and to propose a new one. The compilation of main foliations covering the entire Tauern Window visualize the first order differences between the western, central and eastern Tauern Window that are also manifested by first order geochronological differences.

The ISOPLOT algorithm TuffZirc age extractor (Ludwig and Mundil, 2002) is a promising tool to decipher crystallization, partly reset and cooling ages of apatites that underwent amphibolite-facies metamorphism. Cooling ages dating the mid-range metamorphism (~450 °C) can be obtained from apatites due to their diffusion controlled Pb loss and their inert behavior to recrystallization. Differentiation of the apatite age spectra into crystallization, partly reset and cooling ages was supported by the U-Pb crystallization ages of zircons from the same samples. In future studies analyses of larger amounts of grains (≥100) might achieve a higher significance level of the apatite median ages and therefore, could better constrain the timing of isotopic closure.

In situ dating of microstructurally defined pre-, syn-, and post-kinematic minerals confirms the relative age sequence assessed by textural arguments and allows us to attribute absolute ages to ductile shear. Although pre-kinematic minerals appear to be affected by extraneous Ar, syn-kinematic and post-kinematic minerals yield reliable formation ages. Age differences of syn-kinematic minerals indicate different increments of a long lasting deformation history. Therefore, these ages can be interpreted to define longevities of ductile shear zones. Since post-kinematic phengite ages coincide with the youngest syn-kinematic formation ages of the same microstructural site in one sample, the termination of ductile deformation is interpreted to be identical with the age of post-kinematic phengites. The initiation of deformation cannot be constrained as precisely as its termination. This result is a first step to assess how and when orogen-scale shear zone networking was active, hence to understand how deformation is accommodated and partitioned in space and time.

5.2 Geological conclusions

The results of this study show that the western Tauern Window was deformed by a transpressive belt consisting of upright folds and sinistral shear zones that has the scale of an orogen. It forms a restraining bend by crustal buckling linking the sinistral, transpressive Giudicarie Belt, with the sinistral SEMP Fault. ~58 km of north-directed shortening caused by the Dolomites Indenter were accommodated by upright folds (~38 km) and partly by sinistral shear zones attaining ~26-31 km of bulk sinistral displacement, i.e. ~16-24 km east-west extension. The SEMP Fault as major strike-slip fault north of the central sub-dome accommodated ~60 km of sinistral displacement contributing ~58 km to lateral extrusion. North-south shortening in the central Tauern Window decreases, as seen from the lower amplitude of folds, the absence of interconnected networks of shear zones, and preserved, higher tectonostratigraphic units. These observations are consistent with the larger exposure of Austroalpine Units south of the Tauern Window and the more southerly position of the indenter margin.

The obtained cooling pattern from the U-Pb apatite ages indicates a dome structure in agreement with earlier studies. The novel aspect is that an early stage of this cooling event in the Lower Oligocene epoch was dated. Hence, the duration of cooling and the driving processes causing it were substantially extended. The remarkable coincidence of U-Pb apatite ages with the spatial distribution of geochronometers having lower closure temperatures indicate that from ~31-29 Ma on the western Tauern Window cooled with a cooling rate of 15.2±1.5 K/Myr due to erosional denudation. Samples that are outside of the restraining bend, cooled at 36-35 Ma, whereas samples that are inside of the restaining bend started to cool at 31-29 Ma below 450 °C. Therefore we argue that the onset of Dolomites Indentation might have occurred at 31-29 Ma.

The longevity of sinistral shear zones comprises for all dated structures several million years. The termination of those structures was precisely figured out in some cases. Localized deformation initiated within the entire western sub-dome contemporaneously to the cooling mentioned above. Our results suggest that the three large-scale shear zones investigated were partly coeval each of them acting for time intervals of 19 Myr, 13 Myr and 22 Myr, respectively. The northernmost Ahorn Shear Zone was active under greenschist-facies conditions between 33 and 15 Ma and might have terminated at 15.7±5.8 Ma. The Tuxer Shear Zones were active under greenschist to amphibolite facies conditions between 24 and 12 Ma and terminated at 12.4±1.0 Ma. The Greiner Shear Zone was active under amphibolite facies conditions between 28 and 7 Ma (Pollington and Baxter, 2010; Schneider et al., 2013). Localized deformation continued until the Upper Miocene and followed the cooling of the dome from the margins to the center. The sinistral shear zones and for this reason the entire transpressive belt dominated the uplift and exhumation of the western Tauern Window.

5.3 Geodynamic implications

Upright folding in the western Tauern Window is the surface expression of an extraordinary localized process of crustal buckling. In contrast to all other parts of the Alpine Chain, the site of accretion of new nappes of European basement did not shift towards the foreland, hence erosion eliminated more than 30 km of a crustal column in the hinge area of this antiformal stack, allowing for the exhumation of deep crust. This process was coeval with orogen-parallel extrusion, which localized along normal faults forming the western and eastern margins of the Tauern Window and a network of sinistral shear zones in the western sub-dome, decoupling it from central and eastern sub-domes.

Therefore, the western sub-dome experienced a different structural evolution compared to the central and eastern ones. In the former, the widespread association of high-amplitude, tight upright folds and sinistral shear zones, testifies a larger amount of orogen-perpendicular shortening and a peculiar position linking the Giudicarie Belt, hence indentation to the SEMP Fault, hence lateral extrusion. Against previous interpretations suggesting that exhumation of the western Tauern Window results from tectonic unroofing, emphasizing extensional tectonics, we showed that the fault pattern and the relative displacements on the faults required by such models do not match with the structures of the western Tauern Window. In contrast this fault pattern and the inferred displacements are consistent with exhumation dominated by erosional denudation during upright folding and sinistral shearing.

Formation of the Tauern Window is largely related to doming caused by Adria-Europe collision causing Barrovian metamorphism in the Zentralgneiss batholith. The timing of the thermal climax in the Zentralgneiss batholith occurred at 38-34 Ma contemporaneously to high-pressure metamorphism in the eclogite zone and might be related to mantle-derived heat influx after slab breakoff at ~35 Ma (Ratschbacher et al., 2004), which coincides with the main phase of Periadriatic plutonism ~34 Ma (42-30 Ma, cf. Pomella et al., 2011). Ongoing shortening and detached upper crust might have promoted Dolomites Indentation causing strain localization such as the restaining bend in the western Tauern Window and additional rock uplift starting at ~33 Ma, confirmed by the

oldest deformation ages obtained in this study and in agreement with eclogite-facies ductile shear at ~32 Ma (Kurz et al., 2008).

Recent findings of upper mantle anisotropy beneath the Eastern Alps measured by fast orientations of shear-wave splitting parameters indicate the presence of a more-or-less mountain chain-parallel seismic anisotropy in the upper mantle under the Western and Central Alps (Bokelmann et al., 2013). However, in the Eastern Alps, fast orientations jump by about 45° across the Tauern Window. For the easternmost stations yet record a shear-wave splitting of similar size, Bokelmann et al. (2013) found that fast directions agree closely with those predicted by the relative motion of the surface (GPS) with respect to the Central Alps. This suggests that the authors may have observed a mantle deformation signal of the eastward extrusion. In that case, the entire lithosphere takes part in the lateral escape toward the Pannonian basin. The restaining bend in the western Tauern Window and the decoupling of the central and eastern Tauern Window coinciding with this deep seismic signal may be the surface expression of this crustal-scale flip.

6. What will be next?

When I visited one of my new colleagues in Freiberg for some administrative questions, I read a very interesting proverb stuck to the monitor of his computer. At first I forgot it, but later on it came back into my mind and I really started to like it. It says: "The solution to a problem is half completed when the question to it is carefully worded" Therefore I will ask some question that might be interesting on the base of this thesis.

6.1 Methodological focus

6.1.1 How can we improve the $^{40}Ar/^{39}Ar$ geochronometer?

There are some set screws to refine in situ $^{40}Ar/^{39}Ar$ geochronology. First of all the quality of all isotopic measurements is directly proportional to the blank analyses. Thanks to Dr. Jörg Pfänder (Technische Universität Bergakademie Freiberg) the ARGUS VI mass spectrometer has a very low volume of the central unit and therefore internal instrument surfaces where blank gas can be attached to or released from is very low. In addition, a high percentage of the ablated gas enters the mass spectrometer yielding good intensities even from small ablation volumes. Therefore, the conditions for high-precision noble gas measurements with high spatial resolution are unrivaled in Freiberg. Another factor that directly influences the quality of $^{40}Ar/^{39}Ar$ data is the J-value, a parameter describing the neutron fluence that a given sample was exposed to during rotational neutron irradiation. The axial variability of this value is already described in the literature, but the radial variability is believed to be minor or negligible. On the contrary, new findings of PhD-student Daniel Rutte (Technische Universität Bergakademie Freiberg) showed that radial variability of the J-value might have been underestimated in the past. By better monitoring this value or better adjustment of the samples holder geometry the control of this variable could be improved. Maybe the biggest weakness $^{40}Ar/^{39}Ar$ geochronology or the laser ablation approach in general is that scientists have no direct measure of the isotopic concentrations since the ablated volume is hard to constrain and depends on several parameters like mineral phase, crystal structure, laser power and chosen ablation mode. The methodological improvement of direct excess to the Ar concentrations of the in situ analyses could facilitate microtectonic or geochemical interpretations in terms of mass-transfer, excess Ar, Ar loss or composition of metamorphic fluids.

6.1.2 Can we use other noble gases to understand orogenic processes?

Noble gases such as Helium, Neon, Argon and Xenon have been used to understand early differentiation processes of volatile accretion in the Earth's mantle. It has been shown that the noble gas signature of OIBs is less radiogenic compared to the one of MORBs. There is an ongoing discussion whether atmospheric Xenon was recycled to the mantle by subduction or whether there exists a relatively undegassed primitive deep-mantle reservoir. What exactly is happening to the noble gases during subduction is less understood and the data are ambivalent. A systematic comparison of the isotopic composition of noble gas in ophiolites and eclogites compared to present day MORB signatures might give a hint of which fraction of noble gases is recycled to the mantle during subduction, exhumation and/or eclogite formation.

6.2 Microstructural focus

6.2.1 How can we better understand major-element mass-transfer?

Breakdown and formation of minerals within shear and fault zones are the manifestation of differential stress and rock failure under certain PT conditions. Usually metamorphic fluids are involved in mineral reactions during deformation. The Ar concentration of metamorphic fluids is highly divers and the Ar isotope composition of such fluids is poorly understood. However, the presence and mobility of fluids a directly linked to the porosity and permeability of the rocks. Recent findings by Dr. Florian Fusseis (University of Edinburgh) showed that in mylonites a significant volume of porosity is present. He and his colleagues showed in analogue models that this porosity is formed syn-kinematically. Systematic sampling across fault and shear zone for analyses of K and Ar concentration, for Ar isotopic composition in contrast to porosity and permeability might give new insights to metamorphic fluids, their composition and distribution during deformation.

6.2.2 What tell us trace element distributions?

Several elements are consumed or released during metamorphic mineral reactions. Especially trace elements are highly mobile and might indicate fluid rock interactions. Recent findings of Dr. Matthias Konrad-Schmolke (University of Potsdam) showed that Li and B budgets are fluid-controlled in eclogite-facies rocks that suffered a deformation induced overprint, thus acting as tracers for fluid–rock interaction processes. On the contrary, other trace elements e.g. Sr and Pb were controlled by breakdown reactions of epidote. Looking at trace element distributions greenschist- to amphibolite-facies shear zones in combination to the above mentioned approaches might strengthen the link between metamorphic fluid infiltration and syn-kinematic mineral formation.

6.2.3 Do structural elements act the same or are there fundamental differences?

Mylonitic shear zones are mainly expressions of rock failure and stress release. Other structures more related to compression are folds. During folding recrystallization and syn-kinematic mineral formation also occurs. First results during this study that were not presented in this thesis due to their preliminary character show that there are also systematic age distribution in samples that are folded. In dependence on the second chapter presented in this study where the longevity of ductile shear zones was dated, the formation and longevity of folds might also be analyzed. Especially in transpressional or transtensional regimes where shear zones are linked to folds systematic analyses of both structural elements might reveals a more complete structural evolution of the area of interest.

6.3 Focus on Regional Geology

This study in agreement with earlier published literature showed that ductile shear zones might be active over millions of years and might evolve in space and time, especially if they are km-scale structures. This major result opens up the possibility to study the temporal evolution of major shear zones in the European Alps, in the Pamir Mountains, or in the Himalayas from the perspective of kinematic endurance and propagation of localized ductile deformation. A complication to this approach is the common field observation, that usually strain across a given shear zone system does not increase or decrease monotonous into one direction. Shear zones are webbed into networks, they interact and overprint themselves; and strain might be distributed or localized. Systematic sampling strategies for in situ $^{40}Ar/^{39}Ar$ dating across well- or un-known major fault and shear zones might illuminate tectonic processes and might also improve spatial plate restoration.

U-Pb ages of apatite were performed for the first time in the Eastern Alps. The results show remarkably consistent median ages and makes the U-Pb apatite geochronometer a promising tool. The precision could be improved by analyzing more grains which would not be extraordinary time-consuming. To better understand the thermal history of the entire Tauern Window, similar analyses could be performed in the central and eastern Tauern Window. The discussion of white mica cooling age vs. formation age could be circumvent by this approach since apatite U-Pb in the western Tauern Window are certainly cooling ages which is also likely for the central and eastern Tauern Window.